UNIVERSITY OF LIVERPOOL

Engineered High-k Oxides

Thesis submitted in accordance with the requirements of the University of Liverpool for the degree of Doctor in Philosophy in the Faculty of Science and Engineering by

Don Ayendra Dilshan Chathuranga Weerakkody

June 2016

Department of Electrical Engineering and Electronics

Abstract

Engineered High-k oxides

Don Ayendra Dilshan Chathuranga Weerakkody

The evolution of integrated circuit technology over the five decades resulted in scaling down the minimum feature size of a transistor from 10 μm to ~14 nm. The high-k dielectrics were identified as potential candidates to replace SiO_2 from 2007 due to the large leakage current observed when scaling down SiO_2. These materials captured the attention of many researchers and led them to focus on many emerging applications in addition to metal oxide semiconductor field effect transistors (MOSFET). In this thesis, two emerging applications of high-k dielectrics were investigated: (i) germanium based MOSFETs and (ii) high frequency high speed rectifiers for optical rectennas.

Ge is identified as a high mobility non-silicon channel material to replace Si in MOSFETs in order to enhance the device performance. However, the native oxide of Ge decomposes to GeO_x sub-oxide which is not stable. Therefore in this work, high-k materials such as Y_2O_3, Tm_2O_3, Al_2O_3 and GeO_2 are used to passivate the Ge surface. These structures are optically characterised by performing variable angle spectroscopic elliposometry (VASE) to extract the band gap values and analyse sub-band gap absorption peaks. The VASE results are correlated to X-ray photoelectron spectroscopy (XPS) to evaluate the conduction band offset (CBO). Y_2O_3/Ge, Tm_2O_3/Ge and GeO_2/Ge demonstrated sufficiently large CBO and valence band offset values to adequately suppress leakage current in real applications. The presence of GeO_x was evident for GeO_2/Ge and Y_2O_3/Ge stacks deposited at 225 °C. The optimal deposition temperature for Y_2O_3/Ge was in the higher range, at ~ 400 °C, as this allowed for more uniform germanate layer at the interface with better passivation properties; Moreover, Al_2O_3 and Tm_2O_3 showed low reactivity with Ge, and negligible interfacial layers. The study in this thesis points unambiguously to the barrier role of both Al_2O_3 and Tm_2O_3 interlayers, which could suppress the growth of unstable GeO_x and bring effective passivation route in future Ge-based complementary metal oxide (CMOS) devices.

A comprehensive research study has been conducted on single and multi-barrier metal insulator metal structures for potential infrared energy harvesting applications. Electrical characterisation demonstrated the dominance of quantum mechanical tunnelling in thin (< 5 nm) Ta_2O_5 and Nb_2O_5. The Ta_2O_5/Al_2O_3 and Nb_2O_5/Al_2O_3 based structures were fabricated with thickness ratio (in nm) of 4:1, derived from theoretical model, in order to observe the dominance of resonant tunnelling below 1 V. The ultra-thin (1-6 nm) insulator layers were

deposited by atomic layer deposition (ALD) or radio frequency magnetron sputtering with Al, Ta, Nb, Ag, Cr and W as metal contacts. Variable angle spectroscopic ellipsometry was performed to extract the optical properties and band gap of insulator layers while the surface roughness of the metal electrodes was measured by atomic force microscopy. The metal electrode work function and band line up were estimated from experimental results obtained by X-ray photoelectron spectroscopy, inverse photoemission spectroscopy and Fowler-Nordheim analysis. Superior low voltage large signal and small signal non-linearities such as asymmetry of 18 at 0.35 V, rate of change of non-linearity of 7.5 V^{-1}, and responsivity of 9 A/W at 0.2 V were observed for Al/Ta_2O_5/Al_2O_3/Al and Al/Nb_2O_5/Al_2O_3/Al metal-insulator-insulator-metal (MIIM) devices respectively. The MIIM device based on Nb/Nb_2O_5/Al_2O_3/Ag showed further increase of asymmetry in low voltage range, i.e. 35 at 0.1 V, a state-of-the-art value.

A fingerprint of resonant tunnelling can be found from a change of curvature and significant increase of current in current voltage characteristics. The resonant tunnelling was experimentally observed at ~0.6 V for MIIM devices, at ~0.35 V for non-cascaded MIIIM and ~ 1 V for cascaded MIIIM devices. Although the resonant tunnelling had an impact on enhanced forward biased current levels and increased asymmetry at higher voltages, the highest low-voltage asymmetry and responsivity were observed for MIIM and non-cascaded MIIIM where the effect of direct and step tunnelling dominate current transport. In summary, the novelty of this thesis is in demonstrating experimentally, enhanced asymmetry and low-voltage non-linearity in ALD nanometer scale double and triple tunnel-barrier rectifiers for their future use in optical rectennas.

Acknowledgments

I would like to express my utmost gratitude to my primary supervisor, Dr. Ivona Z. Mitrovic for giving me the golden opportunity to conduct this research study and for her supervision and perseverance throughout the Ph.D study. Moreover, I am forever in debt to her for proof reading my thesis and helping me to minimise the errors.

My special thanks also to my secondary supervisor, Prof. Steve Hall for all his guidance and advice throughout my Ph.D and for his extensive proof reading of this thesis.

I would like to express my deepest respect and appreciation to Dr. Naser Sedghi for the immense support and advice given since the beginning of my Ph.D and also for the simulation results provided.

I would like to take this opportunity to thank Dr. Jaqueline Wrench for growing high-k dielectrics for the device structures by ALD. Next, we could not have used the ALD facilities without Prof. Paul Chalker's permission; therefore I would like to express my sincere gratitude for him. A special thanks goes to Dr. Zhenhua Luo for letting me use the sputtering facilities in Southampton University. Next, I wish to thank Dr. Jidong Jin for helping me to improve my device fabrication process and for the advice given when compiling this thesis.

I am very grateful to Dr. Vin Dhanak in Stephenson Institute, University of Liverpool for letting me use his lab facilities to perform XPS and guidance given throughout the analysis stages. I must also thank Dr. Mohammed Althobaiti and Dr. David Hesp for performing the XPS measurements for us.

I am truly grateful to Dr. Robert Treharne for helping me with the sputtering process and being a very good friend all the time. I would also to thank Dr. Laurie Phillips and Prof. Ken Duros for letting me use their sputtering kit in Stephenson Insitutue, University of Liverpool. A special thanks goes to my colleagues in solid state electronics group for being supportive throughout the Ph.D.

I am forever indebted to my loving parents, Ayesh and Sonali to whom this thesis is dedicated to, for supporting whatever I choose to do. I would also like to thank my sister, Ayendri and all the family members and friends who have supported me to reach my targets.

Table of Contents

List of Figures viii

List of Tables xvi

Abbreviations xvii

Contribution from this work xx

1. Introduction 2

1.1 Background of high-k materials 2

1.2 Background of Ge as a channel material 6

1.3 Background of the rectenna 7

1.4 Thesis outline 13

2. Experimental techniques 19

2.1 Material deposition 19

2.1.1 Atomic layer deposition 19

2.1.2 Sputter deposition 20

2.1.3 Thermal evaporation process 21

2.2 Physical characterisation techniques 22

2.2.1 Variable angle spectroscopic ellipsometry (VASE) 22

2.2.1.1 The modelling process 26

2.2.2 X-Ray photoelectron spectroscopy (XPS) 28

2.2.2.1 Element identification 29

2.2.2.2 Chemical shift 29

2.2.2.3 Work function (Φ) estimation 30

2.2.2.4 Work function in semiconductors 32

2.2.3 Atomic Force Microscopy (AFM) 33

2.3 Electrical characterisation techniques 35

3. Optical properties of high-k oxides on germanium 38

3.1 Y_2O_3/Ge, Al_2O_3/Ge and GeO_2/Ge band line-up study 40

3.2 Tm_2O_3/Ge band line-up study 52
3.3 Discussion and Conclusion 56
4. Experimental methods for metal-insulator-metal and metal-multi insulator-metal devices 64
4.1 Device fabrication 65
4.1.1 Sample preparation 65
4.1.2 Material deposition 65
4.1.3 Device patterning techniques 66
4.1.3.1 Photolithography process 66
4.1.3.2 Shadow mask process 68
4.2 Physical characterisation 68
4.2.1 Surface roughness estimation of bottom metal electrode 68
4.2.2 Uniformity, thickness and band gap estimation by VASE 69
4.2.3 X-Ray photoelectron spectroscopy (XPS) 74
4.2.3.1 XPS CL fittings for Bulk Al_2O_3 sample 75
4.2.3.2 XPS CL fittings for Bulk Ta_2O_5 sample 76
4.2.3.3 XPS CL fittings for interface Ta_2O_5/Al_2O_3 samples 77
4.2.3.4 Valence band offset estimation for Ta_2O_5/Al_2O_3 samples 78
4.2.3.5 XPS CL fittings for Bulk Nb_2O_5 sample 79
4.2.3.6 XPS CL fittings for interface Nb_2O_5/Al_2O_3 sample 80
4.2.3.7 VBO estimation of Nb_2O_5/Al_2O_3 sample 82
4.2.3.8 Electron affinity estimation for Al_2O_3, Nb_2O_5 and Ta_2O_5 82
4.3 Work function estimation of Al, Nb, Ta, W and Ag 84
4.3.1 Barrier height at the interface of Al/Nb_2O_5 84
4.3.2 Barrier height at the interface of Nb/5 nm Nb_2O_5 85
4.3.3 Barrier height at the interface of Al/Ta_2O_5 86
4.3.4 Barrier height at the interface of Ta/Ta_2O_5 86
4.3.5 Barrier height at the interface of W/Nb_2O_5 and W/Ta_2O_5 87
4.3.6 Barrier height at the interface of Ag/Ta_2O_5 88

4.3 Discussion and Summary 88

5. Metal-insulator-metal (MIM) devices 93

5.1 Dominant conduction in dielectrics 99

5.1.1 Dominant conduction mechanism(s) in Ta_2O_5 99

5.1.2 Dominant conduction mechanism(s) in Nb_2O_5 106

5.2 Rectification properties of MIM structures 107

5.2.1 Al/1.6 nm AlO_x/5 nm Ta_2O_5/Al device rectification properties 107

5.2.2 Al/1.6 nm AlO_x/5 nm Nb_2O_5/Al device rectification properties 109

5.2.3 Ta/5 nm Ta_2O_5/Ta device rectification properties 110

5.2.4 Nb/5 nm Nb_2O_5/Nb device rectification properties 112

5.3 Discussion and conclusion 113

6. Resonant tunnelling in Metal-Insulator-Insulator-Metal (MIIM) structures 120

6.1 Theoretical considerations 124

6.2 Experimental 131

6.2.1 Al-based MIIM structures with the same metal electrodes 132

6.2.1.1 Al/1 .6 nm AlO_x/1 nm Al_2O_3/4 nm Ta_2O_5/Al device 132

6.2.1.2 Al/1.6 nm AlO_x/1 nm Al_2O_3/4 nm Nb_2O_5/Al device 136

6.2.2 MIIM structures with different metal electrodes 139

6.2.2.1 Ta/4 nm Ta_2O_5/1 nm Al_2O_3/Ta device 140

6.2.2.2 Ta/4 nm Ta_2O_5/1 nm Al_2O_3/Ag device 143

6.2.2.3 Ta/4 nm Ta_2O_5/1 nm Al_2O_3/Cr device 146

6.2.2.4 Nb/4 nm Nb_2O_5/1 nm Al_2O_3/Nb device 149

6.2.2.5 Nb/4 nm Nb_2O_5/1 nm Al_2O_3/Ag device 152

6.2.2.6 Nb/4 nm Nb_2O_5/1 nm Al_2O_3/W device 155

6.3 Discussion and summary 158

7. Metal-Insulator-Insulator-Insulator-Metal (MIIIM) structures. 166

7.1 Theoretical calculations 168
7.2 Experimental 170
7.2.1 Non-Cascaded MIIIM structures 171
7.2.1.1 Al/ 1 nm Al_2O_3/3 nm Nb_2O_5/1 nm Ta_2O_5/Al device 171
7.2.1.2 Al/1 nm Al_2O_3/2.5 nm Nb_2O_5/1.5 nm Ta_2O_5/Al device 175
7.2.1.3 Al/1 nm Al_2O_3/2 nm Nb_2O_5/2 nm Ta_2O_5/Al device 177
7.3.2 Cascaded MIIM structures 180
7.3.2.1 Al/1 nm Al_2O_3/3 nm Ta_2O_5/1 nm Nb_2O_5/Al 180
7.4 Discussion and summary 184
8. Conclusion and future Work 187

List of Figures

Figure 1.1: Rectenna block diagram……..……8

Figure 1.2: The spectra of incoming solar radiation and outgoing infrared radiation 10

Figure 2.1: (a) Schematic of sputtering chamber and (b) AJA sputtering system……...…....20

Figure 2.2: Linearly (top) and circularly (bottom) polarised light……...…..…...23

Figure 2.3: Schematic of Ellipsometry measurements done on a thin-film sample...……...…24

Figure 2.4: Flow chart of the modelling process using the general oscillator layer..…...…….27

Figure 3.1: Experimental and modelled Δ and ψ against photon energy for Y_2O_3/Ge deposited at 225 ºC……..……..…...…41

Figure 3.2: (a) Real part of the dielectric constant and (b) imaginary part of the dielectric constant for Y_2O_3/Ge structures deposited at 225 ºC and 400 ºC, and also GeO_2/Ge with and without the capping Al_2O_3 layer……...…….…….....43

Figure 3.3: The absorption coefficient vs photon energy plots for (a) Y_2O_3 and (b) Al_2O_3. Tauc plots for (c) Y_2O_3 (225 ºC and 400 ºC) and (d) Al_2O_3 for indirect band gap approximation. The inset in (a) shows logarithmic absorption coefficient vs photon energy. The insets of (c) and (d) show Tauc plots for direct band gap approximation……...……...44

Figure 3.4: XRD spectra of (a) Y_2O_3/Ge deposited at two temperatures: 225 ºC and 400 ºC and (b) reference Y_2O_3 …….……...46

Figure 3.5 (a) Ge 3d, (b) Y 3d and (c) O 1s XPS core levels for Y_2O_3/Ge samples deposited at 225 ºC and 400 ºC with GeO_2/Ge and Y_2O_3 foil as reference samples……..…...47

Figure 3.6: Ge 3d core levels for Y_2O_3/Ge deposited at 225 ºC and 400 ºC after *in situ* anneal from 450 ºC to 750 ºC, in steps of 25 ºC…….....……...48

Figure 3.7: Ge 3d XPS core level fitting after in-situ anneal for two different Y_2O_3/Ge gate stacks deposited at: (a) 225°C, and (b) 400°C……...…….49

Figure 3.8: Ge 3d core level fitting for the (a) GeO_2/Ge (b) Al_2O_3/3.2 nm GeO_2/Ge (c) Al_2O_3/7.2 nm GeO_2/Ge and (d) Al_2O_3/Ge samples…..……..……...…….…...50

Figure 3.9: (a) Al 2p and (b) O 1s XPS core level spectra for GeO_2/Ge with and without Al_2O_3 capping layer and Al_2O_3/Ge samples……...…….....51

Figure 3.10: High frequency capacitance voltage characteristics for 10 nm (nominal) Y_2O_3/n-Ge gate stacks deposited at (a) 225 ºC and (b) 400 ºC……...…52

Figure 3.11: Current density vs voltage characteristics for 10 nm (nominal) Y_2O_3/Ge stacks deposited at (a) 225 ºC and (b) 400 ºC…….……..……...52

Figure 3.12: Tauc plots for Tm_2O_3/Si, Tm_2O_3/Ge and GeO_2/Ge samples assuming (a) direct (b)-(c) indirect band gap approximation and (d) absorption coefficient of Tm_2O_3/Ge and GeO_2/Ge samples……..…….53

Figure 3.13: Logarithmic scale plots of ε_2 for Tm_2O_3 deposited on Si and Ge, with GeO_2/Ge as a reference spectrum…….…...54

Figure 3.14: (a) Tm 4d core level fitting, (b) Valence band spectra for Bulk Tm_2O_3/Ge, (c) Tm 4d core level fitting, (d) Ge 3p core level fitting for interfacial Tm_2O_3/Ge and (e) Ge 3p core level fitting, (f) Valence band spectra for Ge substrate……..……..…...…55

Figure 3.15: HRTEM images for (a) Tm_2O_3/Ge and (b) Tm_2O_3/Si…….……..…...56

Figure 4.1: A schematic of bottom contact masks designed for (a) wet etching and (b) dry etching ……...……...…….……66

Figure 4.2: Schematic of top contact mask (a) full mask and (b) magnified view……...…....67

Figure 4.3: Final device structure: (a) mask design and (b) fabricated device…….....…...67

Figure 4.4: Shadow mask design: (a) bottom contacts and (b) top contacts…..….……..…...68

Figure 4.5: AFM images of the Al blanket films (a) before, and (b) after optimizing the thermal evaporation and cleaning processes. The scanned area is 40 $\mu m \times$ 40 μm……...69

Figure 4.6: Thicknesses measured by VASE (a) 5 nm (nominal) Ta_2O_5, (b) 5 nm (nominal) Nb_2O_5, (c) 1 nm (nominal) Al_2O_3 and 4 nm (nominal) Ta_2O_5..…….....…...……70

Figure 4.7: Optical constants (n, k) vs photon energy extracted from VASE modelling for: (a) Ta_2O_5, (b) Nb_2O_5 and (c) absorption coefficient vs photon energy for both Nb_2O_5 and Ta_2O_5. The nominal thickness of Ta_2O_5 and Nb_2O_5 samples was 20 nm……...……...…71

Figure 4.8: Temperature dependence of (a) extinction coefficient and (b) absorption coefficient……...72

Figure 4.9: The thickness profile of (a) and (b) 20 nm (nominal) RF sputtered Al_2O_3 on glass as deposited and etched respectively (c) RF sputtered 18 nm (nominal) Al_2O_3 on Si and (d) ALD deposited 40 nm (nominal) Nb_2O_5 on Si…….....73

Figure 4.10: Core level fittings (a) Al 2p core level of bulk Al_2O_3, (b) O 1s core level of bulk Al_2O_3.....75

Figure 4.11: (a) VBM extraction and (b) electron energy loss spectrum of Al_2O_3/Si sample……75

Figure 4.12: Core level fittings (a) Ta 4f core level of bulk Ta_2O_5, (b) Ta 4d core level of bulk Ta_2O_5 and (c) O 1s core level of bulk Ta_2O_5……...…….…....76

Figure 4.13: (a) VBM extraction and (b) electron energy loss spectrum of bulk Ta_2O_5…….…...77

Figure 4.14: Core level fittings (a) Ta 4f core level of 2.7 nm Ta_2O_5/1 nm Al_2O_3, (b) Al 2p core level of 2.7 nm Ta_2O_5/1 nm Al_2O_3 and (c) O 1s core level of 2.7 nm Ta_2O_5/1 nm Al_2O_3……...78

Figure 4.15 (a) Nb 3d CL fitting, (b) O 1s CL fitting, (c) VBM and (d) electron energy loss spectrum of bulk Nb_2O_5…….……..….……...80

Figure 4.16: XPS CL fittings for (a) Nb 3d, (b) Al 2p and (c) O 1s of interface 3.8 nm Nb_2O_5/Al_2O_3 sample…….……..81

Figure 4.17 XPS spectra of (a, c, e) secondary cut-off and (b, d, f) valence band maximum of bulk Al_2O_3, Nb_2O_5 and Ta_2O_5…….....…….83

Figure 4.18: Fowler-Nordheim plots for (a) limited range (b) full range of Al/1.6 nm AlO_x/5 nm Nb_2O_5/Al……..……85

Figure 4.19: Fowler-Nordheim plots for (a) limited range (b) full range of Nb/5 nm Nb_2O_5/Nb……85

Figure 4.20: Fowler-Nordheim plots for (a) limited range (b) full range of Al/1.6 nm AlO_x/5 nm Ta_2O_5/Al……86

Figure 4.21: Fowler-Nordheim plots for (a) limited range (b) full range of Ta/5 nm Ta_2O_5/Ta…….…….....86

Figure 4.22: Fowler-Nordheim plot of (a) W/5 nm Nb_2O_5/W and (b) W/5 nm Ta_2O_5/W for a limited range, (c) W/ 5 nm Nb_2O_5/W and (d) W/5 nm Ta_2O_5/W for full range…….,.....87

Figure 4.23: Fowler-Nordheim plots for (a) limited range (b) full range of Ag/5 nm Ta_2O_5/Ag…….……,……...88

Figure 5.1: Energy band diagrams for (a) direct tunnelling, (b) Fowler-Nordheim tunnelling, (c) Schottky emission and (d) Poole-Frenkel emission……..…..93

Figure 5.2: Image force barrier lowering…….....95

Figure 5.3: Band diagram for MIMs with same metals and different metals……...…...…..…98

Figure 5.4: Two oxides are considered as two capacitors connected in series…..…...…....100

Figure 5.5: The cross-sections of Al-Al_2O_3-Ta_2O_5-Al devices without (a) and with (b) intentionally deposited 1 nm Al_2O_3 layer……..…...……..…101

Figure 5.6: Temperature dependent *JV* plots of (a) MIIM-1, (b) MIIM-2 devices and (c) MIIM-1 different device area……...……....…...102

Figure 5.7: Temperature dependent PF plots of (a) MIIM-1, and (b) MIIM-2 devices…....102

Figure 5.8: Temperature dependent Schottky plots of (a) MIIM-1 and (b) MIIM-2 devices……...103

Figure 5.9: Arrhenius plots for Schottky emission conduction for (a) MIIM-1 and (b) MIIM-2 devices……..…..…104

Figure 5.10: Experimental and calculated *JV* plots (DT, FNT and SE) for (a) MIIM-1 and (b) MIIM-2 structures……..……...105

Figure 5.11: Al/1.6 nm AlO_x/5 nm Ta_2O_5/Al (a) Device cross-section (b) High temperature *JV* characteristics, inset of (b) is FN plot of Al/Ta_2O_5/Al (A = 10^{-8} m^2)……..…….……106

Figure 5.12: Device (a) cross-section and (b) *JV* characteristics for Al/1.6 nm AlO_x/1 nm Al_2O_3/4 nm Nb_2O_5/Al (A = 10^{-8} m^2) ……..……107

Figure 5.13: Device (a) JV characteristics (Inset-Device corss-section), (b) asymmetry, (c) responsivity, (d) non-linearity and (e) dynamic resistance for Al/1.6 nm AlO_x/5 nm Ta_2O_5/Al. The device area = 1×10^{-8} m^2……..……108

Figure 5.14: Device (a) JV characteristics (Inset-Device corss-section), (b) asymmetry, (c) responsivity, (d) non-linearity and (e) dynamic resistance for Al/1.6 nm AlO_x/5 nm Nb_2O_5/Al. The device area = 1×10^{-8} m^2…..……..109

Figure 5.15: Device (a) JV characteristics (Inset - Device cross-section), (b) asymmetry, (c) responsivity, (d) non-linearity and (e) Dynamic resistance for Ta/5 nm Ta_2O_5/Ta. The device area = 1×10^{-8} m^2…….……..……..111

Figure 5.16: Device (a) JV characteristics (Inset - Device cross-section), (b) asymmetry, (c) responsivity, (d) non-linearity and (e) dynamic resistance for Nb/5 nm Nb_2O_5/Nb. The device area = 1×10^{-8} m^2……..……...……...113

Figure 6.1: Energy band diagram of the MIIM structure when a positive voltage is applied to metal 2……..……120

Figure 6.2: The energy band diagrams at (a) zero bias, (b) 0.5 V and (c) 1 V for Nb/4 nm Nb_2O_5/1 nm Al_2O_3/Nb device…….…..……..126

Figure 6.3: Tunnelling probability and transmittance for bias voltages: (a) 0.5 V with the Fermi-Dirac-like distribution (black line), (b) 0.5 V and -0.5 V, and (c) 1 V and -1 V for Nb/4 nm Nb_2O_5/1 nm Al_2O_3/Nb ……...……...……...127

Figure 6.4: The band diagram of Nb/4 nm Nb_2O_5/1 nm Al_2O_3/M where M is a different metal……..189

Figure 6.5: Arrhenius plots for (a) Al/ native AlO_x/4 nm Ta_2O_5/Al, (b) Al/ native AlO_x/1 nm Al_2O_3/4 nm Nb_2O_5/Al and (c) Al/ native AlO_x/5 nm Ta_2O_5/Al. ALD purge time in (a) was 4 seconds whereas the purge time was 10 seconds for (c) while depositing Ta_2O_5…....…….129

Figure 6.6: Two oxides are considered as two capacitors connected in series…....……..131

Figure 6.7: Device (a) cross-section and (b) energy band diagram for Al/1.6 nm AlO_x/1 nm Al_2O_3/4 nm Ta_2O_5/Al…….……...132

Figure 6.8: Calculated energy band diagrams of Al/1.6 nm AlO_x + 1 nm Al_2O_3/4 nm Ta_2O_5/Al MIIM tunnel rectifier depicting various conduction scenarios being dependent on external bias: (a)-(c) positive voltages; (d)-(e) negative voltages. DT, FN, ST, and RT refer to direct, Fowler-Nordheim, step and resonant tunneling, respectively…….....134

Figure 6.9: Device (a) JV characteristics (logarithmic scale), (b) asymmetry, (c) responsivity, (d) non-linearity, (e) JV characteristics with breakdown region, (f) dynamic resistance for Al/1 nm Al_2O_3/4 nm Ta_2O_5/Al. The device area =1×10^{-8} m^2……..…….……135

Figure 6.10: Device (a) cross-section and (b) energy band diagram for Al/1.6 nm AlO_x/1 nm Al_2O_3/4 nm Nb_2O_5/Al…….…….……..136

Figure 6.11: Energy band diagrams for A/1.6 nm AlO_x/1 nm Al_2O_3/4 nm Nb_2O_5/Al (a) flat band condition, (b), (c) and (d) conduction in forward bias (e), (f) conduction in reverse bias……137

Figure 6.12: Device (a) JV Characteristics, (b) asymmetry, (c) responsivity, (d) non-linearity, (e) rectification reversal and (f) dynamic resistance for Al/1.6 nm AlO_x/1 nm Al_2O_3/4 nm Nb_2O_5/Al. The device area = 1×10^{-8} m^2…….……...…….138

Figure 6.13: Device (a) cross-section and (b) energy band diagram for Ta/1 nm Al_2O_3/4 nm Ta_2O_5/Ta…….....…...140

Figure 6.14: Energy band diagrams of Ta/1 nm Al_2O_3/4 nm Ta_2O_5/Ta MIIM tunnel rectifier depicting various conduction scenarios being dependent on external bias: (a) flat band condition (b)-(d) positive voltages; (e)-(f) negative voltages…….....……141

Figure 6.15: Device (a) JV Characteristics, (b) asymmetry, (c) responsivity, (d) non-linearity, (e) rectification reversal and (f) dynamic resistance for Ta/4 nm Ta_2O_5/1 nm Al_2O_3/Ta. The device area = 1×10^{-8} m^2…….…….…….142

Figure 6.16: Device (a) cross-section and (b) energy band diagram for Ta/1 nm Al_2O_3/4 nm Ta_2O_5/Ag……..…….…143

Figure 6.17: Energy band diagrams of Ta/1 nm Al_2O_3/4 nm Ta_2O_5/Ag MIIM tunnel rectifier depicting various conduction scenarios being dependent on external bias: (a) zero bias (b) flat band condition (c)-(e) positive voltages; (f)-(g) negative voltages. ……..144

Figure 6.18: Device (a) JV characteristics, (b) asymmetry, (c) responsivity, (d) non-linearity, (e) rectification reversal and (f) dynamic resistance for Ta/1 nm Al_2O_3/4 nm Ta_2O_5/Ag. The device area = 1×10^{-8} m^2……...…….……145

Figure 6.19: Device (a) cross-section and (b) energy band diagram for Ta/1 nm Al_2O_3/4 nm Ta_2O_5/Cr……...…….....146

Figure 6.20: Energy band diagrams of Ta/1 nm Al_2O_3/4 nm Ta_2O_5/Cr MIIM tunnel rectifier depicting various conduction scenarios being dependent on external bias: (a) zero bias, (b) flat band condition, (c)-(e) positive voltages, (f)-(g) negative voltages. ……..……..…….…147

Figure 6.21: Device (a) JV characteristics, (b) asymmetry, (c) responsivity, (d) non-linearity, (e) rectification reversal and (f) dynamic resistance for Ta/1 nm Al_2O_3/4 nm Ta_2O_5/Cr. The device area = 1×10^{-8} m^2……..…….……..148

Figure 6.22: Device (a) cross-section and (b) energy band diagram for Nb/1 nm Al_2O_3/4 nm Nb_2O_5/Nb…….….149

Figure 6.23: Energy band diagrams of Nb/1 nm Al_2O_3/4 nm Nb_2O_5/Nb (a) flat band condition, (b), (c) and (d) conduction in forward bias (e), (f) conduction in reverse bias.....150

Figure 6.24: Device (a) JV characteristics (logarithmic scale), (b) asymmetry, (c) responsivity, (d) non-linearity, (e) rectification reversal and (f) dynamic resistance for Nb/1 nm Al_2O_3/4 nm Nb_2O_5/Nb. The device area = 1×10^{-8} m^2…….……...151

Figure 6.25: Device (a) cross-section and (b) energy band diagram for Nb/1 nm Al_2O_3/4 nm Nb_2O_5/Ag……..152

Figure 6.26: Energy band diagrams of Nb/1 nm Al_2O_3/4 nm Nb_2O_5/Ag MIIM tunnel rectifier depicting various conduction scenarios being dependent on external bias: (a) zero bias, (b) flat band condition, (c)-(e) positive voltages, (f)-(g) negative voltages…...……....153

Figure 6.27: Device (a) JV characteristics (logarithmic scale), (b) asymmetry, (c) responsivity, (d) non-linearity, (e) rectification reversal and (f) dynamic resistance for Nb/1 nm Al_2O_3/4 nm Nb_2O_5/Ag. The device area = 1×10^{-8} m^2…..……...154

Figure 6.28: Device (a) cross-section and (b) energy band diagram for Nb/1 nm Al_2O_3/4 nm Nb_2O_5/W…….…155

Figure 6.29: Energy band diagrams of Nb/1 nm Al_2O_3/4 nm Nb_2O_5/W MIIM tunnel rectifier depicting various conduction scenarios being dependent on external bias: (a) zero bias, (b) flat band condition, (c)-(e) positive voltages and (f)-(g) negative voltages. ……..……156

Figure 6.30: Device (a) JV characteristics (logarithmic scale), (b) asymmetry, (c) responsivity, (d) non-linearity, (e) rectification reversal and (f) dynamic resistance for Nb/1 nm Al_2O_3/4 nm Nb_2O_5/Ag. The device area = 1×10^{-8} m^2…….……..…….……157

Figure 6.31: Rectification reversal of Al/4 nm Ta_2O_5/1 nm Al_2O_3/Al and Ta/4 nm Ta_2O_5/1 nm Al_2O_3/Ta……...…….…….158

Figure 6.32: Rectification reversal (a) Simulated Ta/4 nm Ta_2O_5/1 nm Al_2O_3/M (Ta, Cr and Ag) (b) Simulated Nb/4 nm Nb_2O_5/1 nm Al_2O_3/M (Nb, W, and Ag) (c) experimental Ta/4 nm Ta_2O_5/1 nm Al_2O_3/M (Ta, Cr, and Ag) (d) experimental Nb/4 nm Nb_2O_5/1 nm Al_2O_3/M (Nb, W, and Ag)……..……..159

Figure 7.1: Energy band diagram of the MIIIM structure……..…….……161

Figure 7.2: Transmittance peaks at (a) 0.25 V and -0.25 V, (b) 0.35 V and -0.35 V for Al/0.8 nm Ta_2O_5/3.6 nm Nb_2O_5/1 nm Al_2O_3/Al……...……..…..……168

Figure 7.3: Transmittance peaks at 1.2V for Al/0.8 nm Ta_2O_5/3.6 nm Nb_2O_5/1 nm Al_2O_3/Al……...…….....169

Figure 7.4: (a) Transmittance peaks at 0.05 V, (b) band diagram for Nb/1 nm Ta_2O_5/4 nm Nb_2O_5/1 nm Al_2O_3/Nb……...170

Figure 7.5: (a) A device cross-section and (b) energy band diagram of Al/native AlO_x/1 nm Al_2O_3/3 nm Nb_2O_5/1 nm Ta_2O_5/Al……...…….….171

Figure 7.6: Conduction (a) at flat band condition, (b), (c) and (d) forward bias, (e) and (f) in reverse bias for Al/native AlO_x/1 nm Al_2O_3/3 nm Nb_2O_5/1 nm Ta_2O_5/Al device…….....172

Figure 7.7: Device (a) JV characteristics, (b) asymmetry, (c) responsivity, (d) non-linearity, (e) rectification reversal and (f) dynamic resistance for Al/~1.6 nm AlO_x/1 nm Al_2O_3/3 nm Nb_2O_5/1 nm Ta_2O_5/Al. The device area = 1×10^{-8} m^2…….....174

Figure 7.8: Conduction in Al/1.6 nm AlO_x/1 nm Al_2O_3/2.5 nm Nb_2O_5/1.5 nm Ta_2O_5/Al (a) Flat band condition, (b), (c) and (d) conduction in forward bias, (d) and (e) conduction in reverse bias……..…….…….175

Figure 7.9: Device (a) JV characteristics, (b) asymmetry, (c) responsivity, (d) non-linearity, (e) rectification reversal and (f) dynamic resistance for Al/~1.6 nm AlO_x/1 nm Al_2O_3/2.5 nm Nb_2O_5/1.5 nm Ta_2O_5/Al. The device area = 1×10^{-8} m^2…….……...…..176

Figure 7.10: Conduction in Al/1.6 nm AlOx/1 nm Al_2O_3/2 nm Nb_2O_5/2 nm Ta_2O_5/Al (a) flat band condition, (b), (c) and (d) conduction in forward bias, (e) and (f) conduction in reverse bias.……...……....178

Figure 7.11: Device (a) JV characteristics, (b) asymmetry, (c) responsivity, (d) non-linearity and (e) dynamic resistance for Al/~1.6 nm AlO_x/1 nm Al_2O_3/2 nm Nb_2O_5/2 nm Ta_2O_5/. The device area = 1×10^{-8} m^2……...…….179

Figure 7.12: (a) A device cross-section and (b) energy band diagram for Al/1.6 nm AlO_x/1 nm Al_2O_3/3 nm Ta_2O_5/1 nm Nb_2O_5/Al……..…….……180

Figure 7.13: Conduction in Al/1.6 nm AlOx/1 nm Al_2O_3/3 nm Ta_2O_5/1.nm Nb_2O_5/Al (a) flat band condition, (b), (c) and (d) conduction in forward bias, (e) and (f) conduction in reverse bias…….…….…..181

Figure 7.14: Device (a) JV characteristics, and (b) asymmetry for Al/~1.6 nm AlOx/1 nm Al_2O_3/3 nm Ta_2O_5/1 nm Nb_2O_5/Al. ……...…….…….…..…182

Figure 7.15: Device (a) JV Characteristics, (b) asymmetry, (c) responsivity, (d) non-linearity, (e) rectification reversal and (f) dynamic resistance for Al/~1.6 nm AlO_x/1 nm Al_2O_3/3 nm

Ta_2O_5/1 nm Nb_2O_5/Al. The inset of (b) represents the asymmetry considering the ratio of reverse to forward bias current. The device area = 1×10^{-8} m^2……...….……183

List of Tables

Table 3.1: Summary of thickness and band gap values extracted by VASE……..….....42
Table 4.1: Summary of thickness and band gap values extracted from VASE measurements……..72
Table 4.2: A summary CL binding energy values of key CLs for Ta_2O_5/Al_2O_3 samples.....78
Table 4.3: A summary CL binding energy values of key CLs for Nb_2O_5/Al_2O_3 samples….....81
Table 4.4: Comparison between experimentally obtained and reported work function and electron affinity values…….....……..89
Table 5.1: Sample specifications……..……..….....99
Table 5.2: Summarised rectification properties…….…116
Table 6.1: Band gap and electron affinity values of Al_2O_3, Ta_2O_5 and Nb_2O_5 extracted in chapter 4……..….....121
Table 6.2: Summary of theoretical and experimental rectification reversal values for MIIM structures ……...……...160
Table 6.3: Summarised rectification properties of MIIM structures fabricated in this work……..….……161
Table 7.1: Sample specifications with nominal thickness values for MIIIM devices……..…….…...167
Table 7.2: Summary of rectification properties of the MIIIM structures…….……...…184

Abbreviations

AC – Alternate current

ADS – Advanced design system

AFM – Atomic force microscopy

Ag – Silver

Al – Aluminium

Al_2O_3 – Aluminium oxide

AlO_x – native aluminium oxide

ALD – Atomic layer deposition

Ar – Argon

BE - Binding energy

C – Capacitance

CB – Conduction band

CBO – Conduction band offset

CMOS – Complementary metal oxide semiconductor

CV – Capacitance-voltage

Cr – Chromium

DC – Direct current

DI – Deionized

DT – Direct tunnelling

EOT – Equivalent oxide thickness

FNT – Fowler-Nordheim tunnelling

FWHM – Full width at half maximum

Ge - Germanium

GeO_2 – Germanium dioxide

GeO_x – Germanium oxide

I - Current

IC – Integrated circuits

IE – Ionisation Energy

IP – Ionisation potential

IR – Infrared

ITRS - International technology roadmap for semiconductors

IV- Current-voltage

JV- Current density-voltage

KE – Kinetic energy

KK - Kramers-Kronig

MBE – Molecular beam epitaxy

MIM – Metal-insulator-metal

MIIM – Metal- insulator-insulator-metal

MIIIM – Metal-insulator-insulator-insulator-metal

MOSFET – Metal oxide semiconductor field effect transistor

MSE – Mean standard error

Nb – Niobium

Nb_2O_5 – Niobium oxide

$Nb(OEt)_5$ – Niobium ethoxide

Ni – Nickel

NiO- Nickel oxide

PF - Poole-Frenkel

PV – Photovoltaics

PVD – Physical vapour deposition

QTH – Quartz tungsten halogen

R – Resistance

RF – Radio frequency

RMS – Root mean square

RT – Resonant tunnelling

SE - Schottky emission

Si – Silicon

ST – Step tunnelling

Ta – Tantalum

Ta_2O_5 – Tantalum oxide

$Ta(OEt)_5$ – Tantalum ethoxide

Tm_2O_3 – Thulium oxide

TMA - try-methyl-aluminium

UV – Ultraviolet

VASE – Variable angle spectroscopic Ellipsometry

VB – Valence band

VBM – Valence band maximum

VBO – Valence band offset

W – Tungsten

WKB - Wentzel-Kramers-Brillouin

XPS – X-ray photoelectron spectroscopy

XRD – X-ray diffraction

Y – Yttrium

Y_2O_3 – Yttrium oxide

Contribution from this work

Journal papers

1. I. Z. Mitrovic, **A. D. Weerakkody**, N. Sedghi, S. Hall, J. F. Ralph, J. S. Wrench, P. R. Chalker, Z. Luo, S. Beeby, "Tunnel-barrier rectifiers for optical nantennas", ECS Trans., 72 (2), 287 (2016)

2. L. J. Phillips, A. M. Rashed, R. E. Treharne, J. Kay, P, Yates, I. Z. Mitrovic, **A. Weerakkody**, S. Hall, K. Durose, "Maximizing the optical performance of planar $CH_3NH_3PbI_3$ hybrid perovskite heterojunction stacks", Solar Energy Mat., 147, 327 (2016)

3. L. J. Phillips, A. M. Rashed, R. E. Treharne, J. Kay, P, Yates, I. Z. Mitrovic, **A. Weerakkody**, S. Hall, K. Durose, "Dispersion relation data for methyl-ammonium lead triiodide perovskite deposited on a (100) silicon wafer using a two-step vapour-phase reaction process", Data in brief, 5, 926 (2015)

4. **A.D. Weerakkody**, N. Sedghi, I.Z. Mitrovic, H. van Zalinge, I. NemrNoureddine, S. Hall, J.S. Wrench, P.R. Chalker, L.J. Phillips, R. Treharne, K. Durose, "Enhanced low voltage nonlinearity in resonant tunnelling metal–insulator–insulator–metal nanostructures", Microelec. Eng. , 147, 298 (2015)

5. I.Z. Mitrovic, S. Hall, M. Althobaiti, D. Hesp, V.R. Dhanak, A. Santoni, **A.D. Weerakkody**, N. Sedghi, P.R. Chalker, C. Henkel, E. Dentoni Litta, P.-E. Hellström, M. Östling, H. Tan, S. Schamm-Chardon, "Atomic layer deposited thulium oxide as a passivation layer on germanium", J. Appl. Phys. 117, 214104 (2015)

6. I. Z. Mitrovic, M. Althobaiti, **A. D. Weerakkody**, V. R. Dhanak, W. M. Linhart, T. D. Veal, N. Sedghi, S. Hall, P. R. Chalker, D. Tsoutsou, and A. Dimoulas, "Ge interface engineering using ultra-thin La_2O_3 and Y_2O_3 films: A study into the effect of deposition temperature", J. Appl. Phys. 115, 114102 (2014)

7. R. E. Treharne, L. J. Phillips, K. Durose, **A. Weerakkody**, I. Z. Mitrovic, S. Hall, "Non-paeabolicity and band gap re-normalisation in Si doped ZnO", J. Appl. Phys., 115, 063505 (2014)

8. I. Z. Mitrovic, M. Althobaiti, **A. D. Weerakkody**, N. Sedghi, S. Hall, V. R. Dhanak, S. Mather, P. R. Chalker, D. Tsoutsou, A. Dimoulas, C. Henkel, E. Dentoni Litta, P.E. Hellstrom and M. Ostling, "Interface engineering routes for a future CMOS Ge-based technology", ECS Trans. 61, 73 (2014)

9. I. Z. Mitrovic, M. Althobaiti, **A. D. Weerakkody**, N. Sedghi, S. Hall, V. R. Dhanak, P. R. Chalker, C. Henkel, E. Dentoni Litta, P.E. Hellstrom and M. Ostling, "Interface engineering of Ge using thulium oxide: Band line-up study", Microelec. Eng. 109, 204 (2013)

Conference papers

1. **A. D. Weerakkody**, N. Sedghi, X. Zhan, I. Z. Mtrovic, S. Hall, "Conduction mechanisms in Al-Ta_2O_5-Al_2O_3-Al rectifiers", Proc. IEEE Prime, 133 (2015) (IEEE Prime, 29 June-2 July 2015, Glasgow, United Kingdom)

2. I.Z. Mitrovic, N. Sedghi, **A.D. Weerakkody**, J.F. Ralph, S. Hall, J.S. Wrench, P.R. Chalker, "Engineered Ta_2O_5/Al_2O_3 and Nb_2O_5/Al_2O_3 tunnel barriers for next-generation low turn-on voltage high-speed rectifiers" E-MRS spring meeting, Session M.P.-ref 57, Lille, France, 11 May – 15 May 2015 (Poster presentation)

3. **A.D. Weerakkody**, N. Sedghi, I.Z. Mitrovic, H. van Zalinge, S. Hall, J.S. Wrench, P.R. Chalker, L.J. Phillips, R. Treharne, K. Durose, "Metal-insulator-insulator-metal resonant tunnelling diode for THz rectification", IET Colloquium, University of Leeds, 25 March 2015 (Oral presentation).

4. **A.D. Weerakkody**, N. Sedghi, I.Z. Mitrovic, H. van Zalinge, I. Nemr Noureddine, S. Hall, J.S. Wrench, P.R. Chalker, L.J. Phillips, R. Treharne, K. Durose, "Enhanced low voltage nonlinearity in resonant tunnelling metal–insulator–insulator–metal nanostructures", INFOS conference, Udine, Italy, 30 June-2 July 2015 (oral presentation).

5. **A.D. Weerakkody**, N. Sedghi, I.Z. Mitrovic, S. Hall, J. Wrench, P. Chalker, J. Luo, S. Beeby, "Experimental tunnel-barrier rectifiers for IR energy harvesting" Nanoenergy conference, Liverpool, UK, 27 July-29 July 2016 (oral presentation).

6. R. Treharne, L. Phillips, **A. Weerakkody**, I. Z.Mitrovic, K. Durose, S. Hall, "Band gap non-parabolicity and renormalisation in Si doped ZnO", IEEE SISC conference, Arlington, VA, USA, 5 December-7 December 2013 (poster presentation).

Chapter 1

1. Introduction

1.1 Background of high-k materials

The semiconductor industry has evolved with the continuous improvement in performance of integrated circuits (IC). There were noticeable changes in the technology as the industry deviated from Si bipolar to p-channel metal oxide semiconductor (MOS), then from p-channel MOS to n-channel MOS and eventually to complementary metal oxide semiconductor (CMOS) technology. Moreover, the improvements of CMOS technology was achieved via continuous scaling down the dimensions of the metal oxide semiconductor field effect transistors (MOSFET) that are identified as the key components of ICs. The number of transistors integrated on a chip can be increased by reducing the device dimensions, leading to higher speeds at a reduced cost [1-4]. Over five decades the advancements of CMOS processing have resulted in reducing the minimum feature size of the transistor from 10 µm to ~14 nm [2, 5, 6]. The trend of the scaling down process of MOSFETs was proposed by Intel's co-founder Gordon Moore in 1965-1975, namely that the number of transistors on a chip would double in every two to three years (Moore's law) [7].

A MOSFET consists of a semiconductor, gate oxide material, gate electrode, source and drain (highly doped regions). The semiconductor industry has used SiO_2 as the gate dielectric in MOSFETs for more than four decades due to its superior interfacial properties with Si (low interface state density of ~10^{10} $eV^{-1}cm^{-2}$), low gate leakage current, large dielectric breakdown field of the order of 15 $MVcm^{-1}$ and good thermal stability at Si processing temperature (1000 ^oC) [2, 5, 6]. Moreover, amorphous SiO_2 can be thermally grown on Si with very good control over the thickness while maintaining excellent uniformity [8, 9]. The large band gap of ~9 eV of SiO_2 forms large conduction and valence band offsets with Si. The use of doped polycrystalline Si as the gate electrode in self-aligned CMOS technology was also a crucial parameter in scaling. However, as a result of the continuous scaling down process suggested by international technology roadmap for semiconductors (ITRS), ultra-thin (< 2 nm) SiO_2 gate oxide caused many issues such as large gate leakage current of 1 Acm^{-2} at 1 V [2], reduction in drive current, degradation of reliability and difficulties in growing ultra-thin uniform layers. It has been reported that quantum mechanical tunnelling becomes dominant when the thickness of SiO_2 decreased below 2 nm [2, 10]. Thus the main concern of scaling down the SiO_2 gate dielectric was the large leakage current which increases exponentially with the decrease in thickness. The exponential increase of current through SiO_2 with decrease in thickness has been proved by simulating the structure using Wentzel-Kramers-Brillouin (WKB) approximations [9]. Furthermore, the thickness uniformity across a 12 inch wafer

raised more problems as the difference of a mono-layer in actual thickness could cause a variation of the threshold voltage of the devices across the wafer. The leakage current through 1.2 nm thick SiO_2 in 90 nm node was significantly large, leading to increase in the circuit power dissipation [11]. Moreover, in the 65 nm node, the gate oxide was not scaled down due to the large leakage current. The source to drain current of a field effect transistor depends on the gate capacitance which can be calculated by:

$$C = \frac{\varepsilon_o \varepsilon_r A}{t_{ox}} \tag{1.1}$$

where ε_o is the dielectric constant of free space, ε_r is the relative dielectric constant of the gate dielectric, A is the device area and t_{ox} is the thickness of the gate dielectric. It is possible to replace the SiO_2 gate dielectric with a physically thicker material with a relatively large ε_r to maintain the same capacitance. The materials are known as 'high-k oxides'. The static dielectric constant of any material is the sum of the electronic and lattice contributions [2, 17, 18]. The electronic component is same as the optical dielectric constant which is refractive index (n) squared. The contribution from optical dielectric constant is smaller than the lattice contribution. The dielectric constant can be found by:

$$\varepsilon = n^2 + \frac{Nq^2 Z_{T^*}^2}{m\omega_{TO}^2} \tag{1.2}$$

where n is the refractive index, N is the number of ions per unit volume, q is the electron charge, Z_{T^*} is the transverse effective charge, m is the reduce ion mass and ω_{TO} is the frequency of the transverse optical phonon [2].

The high-k oxide primarily needs to meet a few key requirements in order to be identified as a potential candidate to replace SiO_2. The relative dielectric constant must be sufficiently large, so that the industry could rely on this material for further scaling in future years. It is also crucial to ensure that the chosen oxide is thermodynamically and kinetically stable as it is in direct contact with the semiconductor and also to be compatible with the processing temperature of 1000 ^oC for at least 5 seconds. Furthermore, the oxide needs to form sufficiently large band offsets (at least 1 eV) with the valence and conduction bands of the semiconductor to minimise the carrier injection into its bands [2]. The electrical interface with Si needs to be good with less pronounced defect states. With this approach, it is possible to use relatively thicker gate oxide layers which could potentially decrease the leakage current and also increase reliability of the gate oxide [2, 6].

The semiconductor industry has implemented high-k dielectrics and replaced SiO_2 in order to continue scaling beyond the 45 nm node [11, 12]. The high-k dielectric materials with a large relative dielectric constant (> 9) have been considered such as Al_2O_3, HfO_2, ZrO_2, $HfZrO_2$, TiO_2, Sc_2O_3, Y_2O_3, Lu_2O_3, Nb_2O_5, Ta_2O_5 [2, 6]. These materials enable to deposit relatively thicker gate dielectric layers compared to SiO_2 due to the large dielectric constant. This can be assessed by equivalent oxide thickness (EOT) which determines the effective thickness of the high-k dielectric in order to extract the same gate capacitance as SiO_2 for the relevant thickness of SiO_2. EOT can be found by:

$$EOT = \frac{t_{h-k}\varepsilon_{SiO_2}}{\varepsilon_{h-k}} \tag{1.3}$$

where $t_{h\text{-}k}$, ε_{SiO2} and $\varepsilon_{h\text{-}k}$ are the thickness of high-k dielectric, relative dielectric constant of SiO_2 (equal to 3.9) and relative dielectric constant of high-k dielectric respectively.

The deviation of the semiconductor industry towards high-k materials was to continue the scaling down the devices while maintaining a low leakage current. It is known that the band gap values of high-k dielectrics are smaller than that of SiO_2, therefore a large leakage can be expected unless the physical thickness of the dielectric films are increased [2]. However, due to the large dielectric constant values of high-k materials, the thickness can be increased sufficiently to obtain a low leakage current. After the implementation of HfO_2 high-k dielectrics to the 45 nm node by Intel, the continuous scaling of CMOS using high-k materials have drawn extensive attention [13-16]. A thin interfacial layer (0.6 - 1 nm) of SiO_2 was used under the high-k dielectric (1.5 - 2 nm) to obtain a large carrier mobility in the channel and also to maintain the reliability of the transistor. These two ultra-thin dielectric layers can be considered as two capacitors in series, thus Eqn. 1.3 can be modified as:

$$EOT = EOT_{IL} + EOT_{h-k} \tag{1.4}$$

The presence of ultra-thin interfacial layer with a smaller dielectric constant increases the EOT of the entire gate stack (Eqn 1.4). It has been reported that any silicide formed at the interface could be metallic leading to short out the field effect. Therefore it is crucial to achieve a good thermal stability with Si, inhibiting the formation of a thick interfacial layer at the Si/high-k oxide interface. As discussed in [2] the potentially less reactive high-k oxides such as SrO, CaO, BaO, Al_2O_3, ZrO_2, HfO_2, Y_2O_3, La_2O_3 and lanthanides were found in groups II, III in periodic table. However group II oxides such as SrO are reactive with water but they can be implemented as transition layers.

The high-k oxides must be compatible with the existing process technology. The properties of the high-k oxide must remain the same when the temperature increases to annealing temperature of 1000 ºC for 5 seconds to activate the poly-Si gate [2, 17]. However, most of the amorphous oxides crystallise at this temperature or below unlike SiO_2 and Al_2O_3. This issue can be eliminated by alloying the high-k oxide either with SiO_2 or Al_2O_3 or introducing nitrogen to the oxide. Nonetheless, it has been argued that the crystalline HfO_2 has a comparable leakage current to the amorphous HfO_2 [58].

The electrical quality of the oxide/semiconductor interface is extremely important. The interface must be ultra-smooth and contain minimum defect states. The extra defects are associated with the grain boundaries and this effect can be minimised by using an amorphous oxide or a crystalline oxide epitaxially grown on Si [2]. It has been argued that the use of amorphous oxides is more favourable over the crystalline oxides due to a number of reasons such as cost effectiveness, no grain boundaries and controllability over the defect states and the material composition without creating a new phase [2].

The chosen high-k dielectric must create a large band offsets with the semiconductor (> 1 eV) in order to restrict the conduction of electrons or holes by Schottky emission to the bands of the oxide. The conduction band offset is generally smaller than the valence band offset. Large band gap values (> 5 eV) are desirable in order to engineer the band structure to obtain sufficiently large barrier offsets. The high-k oxides, Al_2O_3, ZrO_2, HfO_2, Y_2O_3 and La_2O_3 can be recognised as potential candidates due to their large band gap values.

The use of high-k dielectrics is common in a wide range of emerging applications in addition to the gate oxide of MOSFETs [4]. These emerging applications are storage capacitor dielectric, resistive random access memory (RRAM), metal-insulator-metal (MIM) structures for operation at frequencies beyond the cut-off frequency of Schottky diodes, pinhole-free passivation layers for organic light emitting diodes (OLED), adhesion layers, bio micro-electro-mechanical systems (MEMS), electroluminescence, protective coating and others.

In this thesis, two emerging applications of high-k dielectrics are studied. The primary objective of this work is to perform a comprehensive study on metal-multi insulator-metal diode structures for infrared energy harvesting applications (rectenna), fabricated using high-k oxides such as Al_2O_3, Ta_2O_5 and Nb_2O_5. In addition to this, the interfaces of high-k oxide (Y_2O_3, Tm_2O_3, Al_2O_3) and Ge are assessed optically.

1.2 Background of Ge as a channel material

In recent years, extensive research has been conducted on high mobility non-silicon channel materials to replace the conventional silicon based channel material. This is because channel mobility is decreased as progressively higher channel doping is required to mitigate short channel effects. Furthermore, saturated drive current (on current) can be improved by increasing the carrier mobility which will enhance device performance or to maintain performance and reduce power consumption. The electron and hole mobility values of intrinsic Si are reported to be 1500 $cm^2V^{-1}s^{-1}$ and 450 $cm^2V^{-1}s^{-1}$ respectively, however for Ge, the electron and hole mobility values are 3900 $cm^2V^{-1}s^{-1}$ and 1900 $cm^2V^{-1}s^{-1}$ respectively [19]. It has been stated in the literature that Ge has the highest hole mobility implying this is a good candidate to be used as channel materials in future low power logic applications [20, 21]. Nevertheless, Ge is not a novel material to the semiconductor industry. Ge based electronic components such as Ge diode and the bipolar junction transistor were known before the development of SiO_2 and the Si MOSFET in the mid-1960s. The industry focused primarily on Si based MOSFETs without paying much attention to Ge due to the good interface quality with its native oxide, SiO_2 and the abundant nature of Si, which makes it lower cost. The band gap of a semiconductor is a key parameter when choosing the transistor channel material because it affects the supply voltage, off-state leakage current and scalability of the device. The band gap must not be too large as this may cause shifting of the turn on voltage of the transistor to higher voltages. Moreover, if the band gap is too small the off-state leakage current could increase as a result of thermionic emission and band to band tunnelling [20]. The expected turn-on voltage for the Ge based MOSFETs is around 0.5 V, therefore the band gap is 0.67 eV for Ge is sufficient to avoid band-to-band tunnelling and thermionic emission [20].

The Ge based technology must be compatible with the conventional CMOS fabrication process. Thin layers of Ge are grown epitaxially on Si substrates due to economic availability and this enables processing other silicon based components such as dynamic random access memory (DRAM) and non-volatile memory. The lattice constant of Ge is 4% larger than that of Si which results in a large build-up of strain energy in germanium deposited on silicon [20, 21]. This serves to generate lattice dislocations at the interface (misfit dislocations) which degrade the carrier mobility and increase the junction leakage. Nonetheless, this can be eliminated by growing a thick buffer layer between Si and Ge or growing a thicker layer of Ge on Si. The native oxide of Ge is not stable and decomposes into GeO_x sub-oxides at the interface [20, 21] unlike the interface between Si and its natural oxide SiO_2. The interface trap density at the interface of Ge and its natural oxide could be significantly larger than that of Si

which could result in degradation of the carrier mobility as a result of carrier scattering [20, 21]. This attracted many researchers' attention to overcome this challenge by introducing a gate oxide layer which would potentially match the superior interface of Si/SiO_2. The large carrier mobility values of Ge can only be utilized if a good gate oxide material is found. Among the initial studies, SiO_2 was used as the gate dielectric; however it resulted in a large concentration of interface trap states [20]. Then the focus was directed towards the natural oxide GeO_2 which led to interfaces with low trap density of $6\times10^{10}\ eV^{-1}cm^{-2}$ for thick GeO_2 grown on Ge (~20 nm GeO_2/Ge) [22-27]. It is worth mentioning that the dielectric constant of GeO_2 is ~6 and has high water solubility. Moreover, the electron mobility was degraded to 265 $cm^2V^{-1}s^{-1}$ when the thickness of the GeO_2 was reduced to 1.2 nm [24]. The gate oxide has to be as thin as possible to obtain a sub-nm EOT. This can be achieved by combining high-k oxide with a thin layer of GeO_2 at the interface. Interface quality has dramatically improved by introducing a small amount of rare-earth (RE) metal into the GeO_2 [28]. The high reactivity of high-k dielectrics such as La_2O_3, Y_2O_3, Dy_2O_3, $LaLuO_3$, Gd_2O_3 and CeO_2, with Ge substrate result in catalytic oxidation of Ge and formation of presumably GeO_x free stable interfacial layers. The Ge surface can also be passivated by introducing a robust ultra-thin high-k interfacial layer such as Al_2O_3 [29, 30] or Tm_2O_3 [31] that act as a barrier.

In this thesis, variable angle spectroscopic ellipsometry (VASE) is used to optically characterise the high-k dielectrics, Al_2O_3, Tm_2O_3, Y_2O_3 and GeO_2 deposited on Ge and to investigate the interfacial properties by analysing the sub-band gap absorption peaks present in the imaginary part of the dielectric constant.

1.3 Background of the rectenna

The current world energy consumption is around 10 terawatts (TW) per year and the projected energy consumption in 2050 will be around 30 TW based on the current calculations [32]. There must be a rapid growth in green energy generation of 20 terawatts out of the projected 30 terawatts by 2050 in order to stabilize CO_2 in the atmosphere [32]. This can be achieved by producing electricity with renewables such as solar and wind, transportation using hydrogen and fossil fuels for residential and industrial heating. The contribution of renewable energy to the global energy demand was 19.1% as of 2013 [33]. Solar power generation is the most powerful, sustainable and also scalable power that will play a key role in meeting the future energy demands, however the current contribution to the global power generation industry is around 0.1 - 0.2% [33]. It is known that light is an electromagnetic wave with a smooth energy distribution and also it exhibits the properties of particles. Photovoltaics (PV) rely on the particle behaviour of light where a free carrier will be created by the incident photon. The incident photons cause electrons to be excited from the valence to the conduction

band of a semiconductor. The excited electrons create holes in the valence band causing a potential drop across an external load. The energy transfer from photons to electrons is not to be 100% efficient due to, for example, the transmission losses of photons leading to energies smaller than the band gap and the electrons that are excited above the conduction band by energetic photons may relax to the conduction band edge resulting in an energy loss [32]. There are solutions available to overcome these limitations though these modifications increase the complexity of the solar cell device structures introducing more cost to the technology. The efficiency level of commercially available solar cells has increased from 12% to 16% in the last ten years. Furthermore, national renewable energy laboratory reported an efficiency of 46% for high concentration multi-junction solar cell modules [34]. Therefore, with the current technology, it can be said that more than half of the absorbed solar energy is wasted as heat and reflected back.

Alternatively, it is possible to exploit the wave nature of light and capture the associated energy using a concept known as the rectenna, instead of utilising the particle behaviour as in semiconductor solar cells. This concept primarily needs a rectifier with a wavelength smaller than that of the incident light for efficient energy conversion. The possibility of energy conversion from solar to DC current was proposed by Professor Robert Bialey in 1972 [35]. Nevertheless, the concept of the rectenna was initially demonstrated in 1964 as a microwave-powered helicopter by William. C. Brown [36]. The rectenna, which was used in 1964, was an array of 28 half-wave dipole antennas connected to a bridge rectifier using point-contact semiconductor diodes [36]. The rectenna is a two-stage device which is the combination of an antenna to receive the electromagnetic waves and to convert them to high frequency electric signals, and a rectifier to convert these high frequency signals to DC electricity (see Figure 1.1). The conversion through the rectifier occurs due to the different diode resistance in forward and reverse bias configurations, so that the oscillating current signal from the antenna could be rectified to DC electricity.

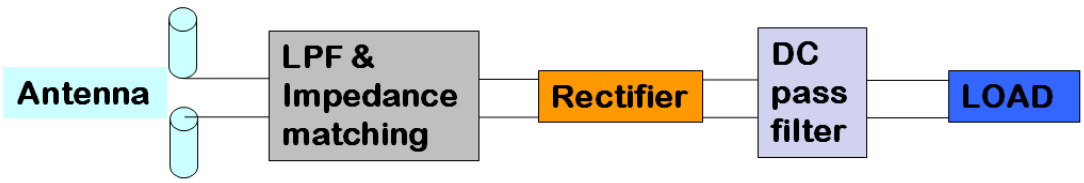

Figure 1.1: Rectenna block diagram.

The efficiency of a rectenna can be calculated by [37],

$$\eta = \eta_a \eta_s \eta_c \eta_j \tag{1.5}$$

where η_a is the coupling efficiency of incident electromagnetic radiation to the antenna, η_s is the efficiency of propagating the collected energy to the junction of the antenna and the diode, η_c is the coupling efficiency between antenna and the diode and η_j is the rectifying power received in the diode. The efficiency of the diode can be determined by the device responsivity. The unit of the overall rectenna efficiency is A/W, signifying the DC current generated per watt of incident radiation. Therefore a large responsivity is needed for efficient square law rectification [38].

If the input power is delivered to the diode in the form of AC power, the power coupling efficiency at the frequency ω can be obtained by [38],

$$\eta_c = \frac{P_{ac,R_D}}{P_A} = \frac{4\dfrac{R_A R_D}{(R_A + R_D)^2}}{1 + \left(\omega \dfrac{R_A R_D}{(R_A + R_D)} C_D\right)^2} \tag{1.6}$$

Where $P_A = \dfrac{V_A^{\,2}}{(8R_A)}$, R_A is the antenna resistance, R_D is the diode resistance and C_D is the capacitance of the diode. The numerator of Eqn. 1.6 implies the impedance match between the antenna and the diode whereas the denominator indicates the cut-off frequency of the rectenna. The cut-off frequency is based on the RC time constant which can be defined by the parallel combination of antenna and diode resistances and the diode capacitance. This has to be smaller than the time period $(2\pi/\omega)$ of radiation incident on antenna in order to make sure the signal from the antenna drops on the diode resistor and should not be short circuited by diode capacitance. Furthermore, for efficient coupling from the antenna requires a good impedance match between the antenna and the diode. Theoretically, a coupling efficiency of 1 can be obtained if $R_D = R_A$.

Solar radiation is concentrated in the visible and near infrared wavelength regions (0.1 μm – 1 μm), and radiated heat which is in the infrared regime of the spectrum (> 0.7 μm) can be exploited to extract energy as shown in Figure 1.2 [39]. Note that solar radiation is concentrated in the visible light wavelength regime during the day time; however the wasted energy due to radiated heat will be at its peak values even during the night time. The peak spectral intensity was obtained around 10 μm which corresponds to a frequency of 30 THz. However, to harness energy at the wavelengths corresponding to visible and near infrared regions of the electromagnetic spectrum is still beyond the capabilities of the current electronic and photonic technologies [40].

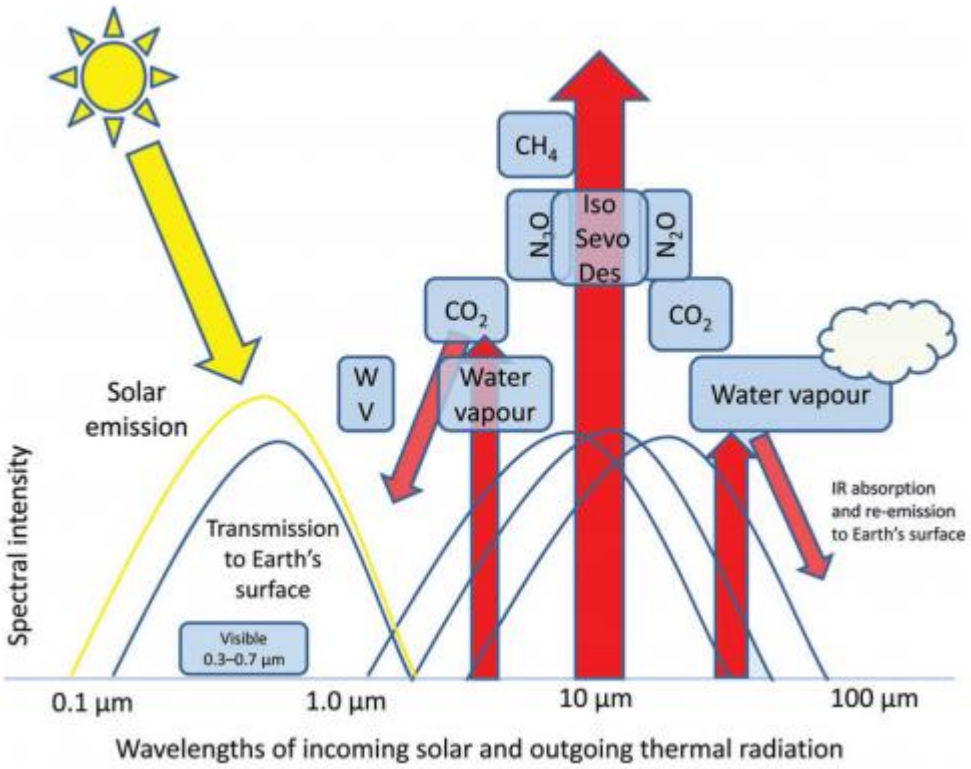

Figure 1.2: The spectra of incoming solar radiation and outgoing infrared radiation [39]

Brown *et al.* [41] reported conversion efficiencies beyond 90% using GaAs Schottky diodes and half-wave dipole antennas at microwave frequency regime which corresponds to a wavelength in the order of 10^{-2} m and have used them in many energy transmission and energy harvesting applications [42]. The great success achieved for rectennas in the low frequency regime (radio frequency and microwave) has inspired the research community to explore the possibilities of extending the frequency response to the upper THz regime. The first experimental results on rectification at optical frequencies with a parallel dipole antenna array were reported by Lin *et al.* in 1996 [43]. Further research was conducted by ITN energy systems; however the efficiencies they observed at 30 THz (10 µm) were very small 0.1% - 1% [44]. As stated before, it is crucial to choose a rectifier that could potentially operate at wavelengths smaller than those of incident light. Both PN junction and Schottky diodes are fabricated using semiconductor materials and exhibit an exponential dependence of current with voltage. The PN junction diode involves conduction under one polarity with drift and diffusion currents. Furthermore, this process is slow since the minority carriers must recombine with the majority carriers once transferred across the junction prior to switching the device to the other polarity. The frequency response of Schottky diodes are far superior compared to PN junction diodes as the conduction in Schottky diodes is dominated by majority carriers. As discussed in Hall *et al.* [40], the frequency response of Schottky diodes is limited by the junction capacitances and the dielectric relaxation response of the semiconductor which

is directly proportional to the conductivity of the semiconductor and inversely proportional to the dielectric constant.

It has been reported that for mixing and square law detection beyond ~12 THz, metal-insulator-metal (MIM) diode structures performed better compared to GaAs based Schottky diodes [45]. Fumeaux *et al.* [46-49], have reported that the Ni-NiO-Ni MIM structure coupled to thin film antennas can be used as an infrared detector and frequency mixer at the 10 μm (30 THz) band. Moreover, the same group demonstrated similar results at the wavelength of 3.39 μm and also in the visible light regime, but the sensitivity was very small [48, 49]. In addition to this, more promising results were reported for an Al/AlO_x/Pt (MIM) based rectenna at the frequency of 30 THz [50, 51]. Bean *et al.*, further stated that the controlled oxidation pressure led to devices exhibiting good current voltage (*IV*) characteristics with the necessary non-linearity [50]. ITN energy systems reported that the Au/Nb_2O_5/Nb based rectenna device could operate at 30 THz, but the efficiency was less than 1% [44]. Wang *et al.* reported an efficiency of 2.7% for an Au/Al_2O_3/Au based rectenna device at the wavelengths corresponding to visible light [52]. Krishnan *et al.* observed detection at 94 GHz, an asymmetry of 1.2 at 0.5 V and a responsivity of 2 A/W at 0.1 V for a Ni/NiO/Cr MIM device [53]. Furthermore, Periasamy *et al.* performed a brief study on the material selection for MIM structures and proposed Hf/TiO_2/Pt, Sm/ZrO_2/Pt, Y/ZrO_2/Pt, Cr/TiO_2/Pt and Cu/TiO_2/Pt as potential structures to obtain good *IV* characteristics [54]. Grover *et al.* reported experimental work on MIM structures (NbN/2 nm Nb_2O_5/Nb) with dissimilar metal electrodes at both electrodes and compared to theoretical results. A responsivity of 4 A/W at 0.4 V was obtained for this MIM device. Moreover, based on the simulations performed on a metal insulator insulator metal (MIIM) structure (W/4 nm Nb_2O_5/1 nm Ta_2O_5/W), they obtained a responsivity of 11 A/W at 0.02 V which was argued to be as a result of resonant tunnelling [55, 56].

The MIM rectifier coupled rectenna could operate at ambient temperature, similarly to conventional rectifiers and this can also be used in wide range of applications such as terahertz interconnects, terahertz imaging and energy harvesting [57]. In an MIM tunnel diode, the electrons flow by quantum-mechanical tunnelling through an insulator layer in the scale of a few nanometres thick. Electromagnetic radiation collected by the antenna is transformed into analogue signals, then the MIM diode rectifies the analogue signals efficiently due to its superior diode characteristics such as sharp turn on (high non-linearity). These characteristics are ideally achieved by quantum mechanical tunnelling which also has very low temperature dependence [57] and this results in high speed operation. Parasitic thermally activate processes need to be eliminated by optimisation of the material properties. The time constant of the diode can be calculated by the product of diode resistance and capacitance. Hence it is crucial to achieve rectifiers with small resistances and capacitances in order for rectennas to be used in

high frequency applications. A smaller resistance can be achieved by engineering the barrier height at the metal/oxide and the thickness of the dielectric layer. A coupling efficiency of 100% has been theoreticallly anticipated although experimental limitations are present with the fabrication process [58]. The main limitation of MIM diode structures was found to be the large reverse bias current [58]. The DC characteristics of MIM diodes can be enhanced only by applying a work fuction difference with the use of different metal electrodes. The DC characteristics can also be significantly improved by introducing another conduction mechanism to the structure in addition to the conventional quantum mechanical tunnelling process. This can be achieved via introducing more dielectric layers to the MIM diode structure and engineering the structure to obtain a quantum well in the conduction band of one of the oxides. The associated formation of bound states can be expected within the quantum well leading to enhanced conduction in one polarity through resonant tunnelling. An enhanced asymmetry can be achieved by electron transport aided by resonant tunnelling under forward bias whereas reverse bias is dominated by direct or Fowler-Nordheim tunnelling. Note that, this is a different approach to the resonant tunnelling diodes formed with semiconductors; here the semiconductors are replaced with high-k dielectrics.

In the work reported here, high-k oxides with thicknesses ranging from 1 nm to 5 nm, are chosen as the insulators in MIM diode structures. It is known that the band gap of high-k dielectrics decreases with the increase in static dielectric constant [59], therefore a large reverse current is expected through these thin oxides used in MIM structures. The two or three insulator layers must be chosen carefully while engineering the metal multi insulator metal structures in order to observe resonant tunnelling via the bound states created in the quantum well. A quantum well can be formed as a result of a large conduction band offset at the dielectric interface and a relatively smaller barrier height at the metal oxide interface. The aim of this thesis was to perform a comprehensive theoretical and experimental study to investigate the dominance of resonant tunnelling in metal multi insulator metal diode structures.

1.4 Thesis Outline

A detailed overview of the structure of this thesis is as follows:

- **Chapter 2:** The fabrication and characterisation techniques that were used to characterise the Ge-based MOS structures and MIM structures are discussed in chapter 2.
- **Chapter 3:** It has been argued that the interface at the oxide/Ge is not passivated due to the formation of Ge sub-oxides. Therefore a study has been carried out to investigate the optical properties of the gate dielectrics deposited on Ge. This was further extended to observe any unstable Ge sub-oxides present at the interface by analysing the sub-band gap absorption peaks. This will be discussed in detail in chapter 3 with the aid of results obtained by X-ray photoelectron spectroscopy (XPS), X-ray diffraction (XRD) and electrical analysis (capacitance voltage and current voltage).
- **Chapter 4:** The main objective in this chapter was to perform a comprehensive experimental study of MIM structures. The fabrication process of the MIM structures is discussed in detail. Electrical and physical characterisation results are presented for the materials that were used to process the diode structures. The electron affinity and band gap values of the high-k oxides as well as the work function values of the metals used in MIM structures were experimentally determined in this chapter.
- **Chapter 5:** The electrons must traverse across the oxide(s) via quantum mechanical tunnelling to achieve fast transit times and high frequency performance. Thus an in-depth analysis was conducted to verify if the dominant conduction is tunnelling, considering thermionic emission, Poole-Frenkel emission, direct tunnelling and Fowler-Nordheim tunnelling. In addition to this, the DC characteristics of the MIM diode structures are discussed in detail.
- **Chapter 6:** The metal-insulator-insulator-metal (MIIM) structures are studied with the aim of observing resonant tunnelling. The experimental structures were fabricated by choosing the oxide combination of either Ta_2O_5/Al_2O_3 or Nb_2O_5/Al_2O_3 with the metals such as Al, Nb, Ag, Ta, W and Cr, so that a triangular quantum well can be formed in the conduction band of the high-k oxide which has a relatively larger electron affinity value. The probability of observing resonant tunnelling was studied using a model and compared to the experimental results.
- **Chapter 7:** The metal-insulator-insulator-insulator-metal (MIIIM) structures are introduced with the possibility of observing resonant tunnelling at zero bias due to the formation of a bound state formed in the rectangular quantum well. This is a novel

structure in contrast to what has been reported in the literature and the DC characteristics of these structures are reported in detail in this chapter.

- **Chapter 8:** The experimental work is concluded with a full summary and the potential future work based on the conducted studies is discussed.

References

[1] M. Houssa, "High-k gate dielectrics", Institute of physics, 2004, Ch. 1, 3

[2] J. Robertson, "High dielectric constant materials", Eur. Phys. J. Appl. Phys. 28, 265 (2004)

[3] B. Nikolic, "Simpler, more efficient design", Proc. ESSCIRC, 20 (2015)

[4] R. D. Clark, "Emerging applications for high-k materials in VLSI technology" Materials, 7, 2913 (2014)

[5] M. L. Green, E. P. Gusev, R. Degraeve, E. L. Garfunkel, "Ultrathin (< 4 nm) SiO_2 and Si-O-N gate dielectric layers for silicon microelectronics: Understanding the processing, structure, and physical and electrical limits", J. Appl. Phys., 90 (5), 2057 (2001)

[6] G.D Wilk, R.M Wallace, J.M Anthony, "High-k gate dielectrics: current status and materials properties considerations", J. Appl. Phys., 89, 5243 (2001)

[7] G. E. Moore, "Cramming more components onto integrated circuits", Electronics, 38, 114 (1965)

[8] S. T. Cundiff, W. H. Knox, F. H. Baumann, K. W. Evans-Lutterodt, M.-T. Tang, M. L Green, H. M. van Driel, "Si/SiO_2 interface roughness: Comparison between surface second harmonic generation and X-ray scattering", Appl. Phys. Lett., 70, 1414 (1997)

[9] D. Z.-Y. Ting, E. S. Daniel, T. C. McGill, "Interface roughness in ultra-thin tunnelling oxides", VLSI Des., 8, 47 (1998)

[10] H. R. Huff, D. C. Gilmer, "High dielectric constant materials", Springer, 2005, Ch. 3, sec 3.3.3, 85

[11] R. Chau, S. Datta, M. Doczy, J. Kavalieros, M. Metz, "Gate dielectric scaling for high-performance CMOS: from SiO_2 to high-k", Int. Workshop on Gate Ins., 124 (2003)

[12] M. Heyns, W. Tsai, "Ultimate scaling of CMOS logic devices with Ge and III-V materials", MRS Bulletin, 34, 485 (2009)

[13] M. Bohr, "The evolution of scaling from the homogeneous era to the heterogeneous era", Proc. of IEEE IEDM Tech Digest, 11-1 (2011)

[14] K. J. Kuhn, U. Avci, A. Cappellani, M. D. Giles, M. Haverty, S. Kim, R. Kothyar, S. Maraipatruni, D. Nikomov, C. Pawashe, M. Radosavljevic, R. Rios, S. Shankar, R. Vedula, R. Chau, I. Young, "The ultimate CMOS device and beyond", Proc. of IEEE IEDM Tech Digest, 12-171 (2012)

[15] T. Ando, "Ultimate scaling of high-k gate dielectrics: Higher-k or interfacial layer scavenging?" Materials, 5, 478 (2012)

[16] J. H. Choi, Y. Mao, J. P. Chang, "Development of hafnium based high-k materials-A review", Mater. Sci. Eng. Rep., 72 (6), 97 (2011)

[17] S. Hall, O. Buiu, I. Z. Mitrovic, Y. Lu, W. M. Davey, “Review and perspective of high-k dielectrics on silicon”, J. Telecom. and Info. Tech., 21, 33 (2007)

[18] G.-M. Rignanese, “Dielectric properties of crystalline and amorphous transition metal oxides and silicates as potential high-k candidates: the contribution of density-functional theory”, J. Phys. Cond. Matt., 17 (7), R357 (2005)

[19] S. Takagi, T. Irisawa, T. Tezuka, T. Numata, S. Nakaharai, N. Hirashita, Y. Moriyama, K. Usuda, E. Toyoda, S. Dissanayake, M. Shichijo, R. Nakane, S. Sugahara, M. Takenaka, N. Sugiyama, “Carrier transport-enhanced channel CMOS for improved power consumption and performance”, IEEE Trans. Elec. Dev., 55, 21 (2008)

[20] R. Pillarisetty, “Academic and industry research progress in germanium nanodevices”, Nature, 479, 324 (2011)

[21] P. S. Goley, M. K. Hudait, “Germanium based Field-Effect Transistors: Challenges and opportunities”, Materials, 7, 2301 (2014)

[22] T. Nishimura, C. H. Lee, S. K. Wang, T. Tabata, K. Kita, K. Nagashio, A. Toriumi, “Electron mobility in high-k Ge-MISFETs goes up to higher”, Proc. IEEE Symp. on VLSI Tech., 209 (2010)

[23] C. H. Lee, T. Nishimura, T. Tabata, S. K. Wang, K. Nagashio, K. Kita, A. Toriumi, “Ge MOSFETs performance: Impact of Ge interface passivation”, Proc. of IEEE IEDM Tech Digest, 416 (2010)

[24] C. H. Lee, T. Nishimura, N. Saido, K. Nagashio, K. Kita, A. Toriumi, “Record-high electron mobility in Ge n-MOSFETs exceeding Si universality”, Proc. of IEEE IEDM Tech Digest, 457 (2009)

[25] C. H. Lee, T. Nishimura, K. Nagashio, K. Kita, A. Toriumi, “High-electron-mobility Ge/GeO_2 n MOSFETs with two-step oxidation”, IEEE Trans. Electron Devices 58(5), 1295 (2011)

[26] T. Takahashi, T. Nishimura, L. Chen, S. Sakata, K. Kita, A. Toriumi, “Proof of Ge-interfacing concepts for Metal/High-k/Ge CMOS - Ge-intimate material selection and interface conscious process flow-”, Proc. of IEEE IEDM Tech Digest, 697 (2007)

[27] C.H. Lee, T. Tabata, T. Nishimura, K. Nagashio, A. Toriumi, “Ge/GeO_2 interface control with high-pressure oxidation for improving electrical characteristics”, Appl. Phys. Express, 2, 071404 (2009)

[28] F. Bellenger, B. De Jaeger, C. Merckling, M. Houssa, J. Penaud, L. Nyns, E. Vrancken, M. Caymax, M. Meuris, T. Hoffmann, K. De Meyer, M. Heyns, “High FET performance for a future CMOS GeO_2-based technology”, IEEE Electron Device Lett., 31(5), 402 (2010)

[29] R. Zhang, P.C. Huang, J.C. Lin, M. Takenaka, S. Takagi, “Physical mechanism determining Ge p- and n-MOSFETs mobility in high Ns region and mobility improvement by atomically flat GeOx/Ge interfaces”, Proc. IEEE IEDM, 371. (2012)

[30] R. Zhang, T. Iwasaki, N. Taoka, M. Takenaka, S. Takagi, “High-Mobility Ge pMOSFET with 1-nm EOT Al_2O_3/GeO_x/Ge gate stack fabricated by plasma post oxidation”, IEEE Trans. Electron Dev., 59, 335 (2012)

[31] E. Dentoni Litta, P-E. Hellström, C. Henkel, M. Östling, “Thulium silicate interfacial layer for scalable high-k/metal gate stacks”, IEEE Trans. Electron Dev., 60(10), 3271 (2013)

[32] T. M. Razykov,C. S. Ferekides, D. Morel, E. Stefanakos, H. S. Ullal, H. M. Upadhyaya , “Solar photovoltaic electricity: Current status and future prospects, Solar Energy”, Solar Energy, 85 (8), 1580 (2011)

[33] Renewables 2015: Global Status Report. REN21 (2015)

[34] Photovoltaics report, Fraunhofer Institute for Solar Energy Systems, ISE (2016)

[35] R. L. Bailey, “A proposed new concept for a solar-energy converter”, J. Eng. Power, 94 (2), 73 (1972)

[36] W. C. Brown, “Experiments involving microwave beam to power and position a helicopter”, IEEE Trans. Aerospace Elec. Sys., AES 5 (5), 692 (1969)

[37] B. M. Kale, “Electron tunnelling devices in optics”, Opt. Eng., 24(2), 267 (1985)

[38] A. Sanchez, C. F. Davis Jr., K.C. Liu, A. Javan, “The MOM tunneling diode: theoretical estimate of its performance at microwave and infrared frequencies”, J. Appl. Phys., 49(10). 5270 (1978)

[39] M. Campbell, J. M. Pierce, “Atmospheric science, anaesthesia, and the environment”, BJA Education, 1 (2015)

[40] S. Hall, I. Z. Mitrovic, N. Sedghi, Y. C. Shen, Y. Huang, J . F. Ralph, “Energy harvesting using THz electronics”, in:A. Nazarov *et al.*, Functional nanomaterials and devices for electronics, Sensors and energy harvesting, Engineering materials, Springer, Switzerland, 241 (2014)

[41] W. C. Brown, “Optimization of the efficiency and other properties of the rectenna element”, Proc. IEEE-MTT-S Int. Microwave Symp., 142 (1976)

[42] S. Krishnan, E. Stefanakos, S. Bhansali, "Effects of dielectric thickness and contact area on current-voltage characteristics of thin film metal-insulator-metal diodes", Thin Solid Films, 516, 2244 (2008)

[43] G.H. Lin, R. Abdu, J. Bockris, “Investigation of resonance light absorption and rectification by subnanostructures”, J. Appl. Phys., 80(1), 565 (1996)

[44] B. Berland, “PV technologies beyond the horizon”, Final Report, NREL/SR-520-33263. ITN Energy System, 1 (2002)

[45] H. W. Hubers, G. W. Schwaab, H. Roser, “Video detection and mixing performance of GaAs Schottky-barrier diodes at 30 THz and comparison with metal-insulator-metal diodes”, J. Appl. Phys.,75, 4243 (1994)

[46] C. Fumeaux, W. Herrmann, F. K. Kneubuhl, H. Rothuizen, “Nanometer thin film Ni-NiO-Ni diodes for detection and mixing of 30 THz radiation”, Infra. Phys. And Tech., 39 (3), 123 (1998)

[47] C. Fumeaux, W. Herrmann, H. Rothuizen, P. De Natale, F. K. Kneubuhl, “Mixing of 30 THz laser radiation with nanometer thin-film Ni-NiO-Ni diodes and integrated bow-tie antennas ”, Appl. Phys., B 63, 135 (1996)

[48] C. Fumeaux, M. A. Gritz, I. Codreanu, W. L. Schaich, F. J. Gonzalez, G. D. Boreman, “Measurement of the resonant lengths of infrared dipole antennas”, Infra. Phys. And Tech., 41, 271 (2000)

[49] C. Fumeaux, J. Alda, G. Boreman, “Lithographic antennas at visible frequencies”, Optics Lett., 24 (22), 1629 (1999)

[50] J. A. Bean, B. Tiwari, G. H. Bernstein, P. Fay, W. Porod, “Thermal infrared detection using dipole antenna-coupled metal-oxide-metal diodes”, J. Vac. Sci. Tech., B 27(1), 11 (2009)

[51] J. A. Bean, A. Weeks, G. D. Boreman, “Performance optimization of antenna-coupled Al/AlOx/Pt tunnel diode infrared detectors”, IEEE J. Quantum Electon., 47 (1), 126 (2011)

[52] F. Wang, N. A. Melosh, “Plasmonic energy collection through hot carrier extraction”, Nano Lett., 11, 5426 (2011)

[53] S. Krishnan, H. La Rosa, E. Stefanakos, S. Bhansali and K. Buckle, "Design and development of batch fabricatable metal-insulator-metal diode and microstrip slot antenna as rectenna elements", Sens Actuators A Phys., 142, 40 (2008)

[54] P. Periasamy, H. L. Guthrey, A. I. Abdulagatov, P. F. Ndoone, J. J. Berry, D. S. Ginley, S. M. George, P. A. parilla, R. P. O’Hayre, “Metal-insulator-metal diodes: role of the insulator layer on the rectification performance”, Adv. Mater., 25, 1301 (2013)

[55] S. Grover, M. J. Estes, G. Moddel, ‘‘Traveling-Wave Metal/Insulator/Metal diodes for improved infrared bandwidth and efficiency of antenna-coupled rectifiers,’’ IEEE Trans. on Nanotech., 9, 716 (2010)

[56] S. Grover, G. Moddel, “Engineering the current-voltage characteristics of metal-insulator-metal diodes using double-insulator tunnel barriers” Solid State Electron, 67(1):94 (2012)

[57] S. Krishnan, E. Stefanakos, S. Bhansali, "Effects of dielectric thickness and contact area on current-voltage characteristics of thin film metal-insulator-metal diodes," Thin Solid Films, 516, 2244 (2008)

[58] T. K. Gustafson, “Coherent conversion of the sunlight spectrum final report”, NASA grant NAG 3-88, University of California, Berkley (1982)

[59] B.H. Lee, L. Kang, R. Nieh, W. Qi, J.C. Lee, “Thermal stability and electrical characteristics of ultrathin hafnium oxide gate dielectric reoxidized with rapid thermal annealing”, J. Appl. Phys., 76, 1926 (2000)

Chapter 2

2. Experimental techniques

The main experimental techniques involved in the fabrication and characterisation processes of oxide/Ge, metal insulator metal and metal multi insulator metal structures are explained in detail in this chapter. The material deposition techniques are discussed in section 2.1 whereas the physical and electrical characterisation techniques are addressed in sections 2.2 and 2.3 respectively.

2.1 Material deposition

2.1.1 Atomic layer deposition

Atomic layer deposition (ALD) is a chemical gas phase thin film deposition technique where the film is grown through sequential, self-limiting surface reactions. During the actual deposition process, two or more chemical vapours or gas precursors are pulsed sequentially into the growth chamber where the reaction occurs and the substrate is placed. These alternate precursor pulses are separated by inert gas (Ar) purging. The motivation of purging is to remove any by-products formed during the pulse process, hence a complete cycle needs two pulse and purge steps. The ALD technique offers superior large area uniformity and conformality, in addition to the good control over the desired thickness [1-3].

The precursor chemicals react with the surface groups of the substrate when they are released into the deposition chamber. The first precursor is introduced to the deposition chamber and forms a monolayer on the substrate followed by inert gas purging of 4-10 seconds. Then the second precursor is introduced, allowing the molecules from this precursor to react with the monolayer formed on the substrate from the first precursor. The same purging step was done for 4-10 seconds to remove all the by-products out of the reactor. This is known as one ALD cycle and this process will be continued until the desired thickness is obtained. In this work, an atomic layer of oxides was deposited by introducing a pulse of one metal organic precursor followed by pulsing water as the oxidant.

It is important to ensure self-limiting and saturated growth to achieve high quality films. Saturated growth occurs when all the available surface bonds after the exposure of each precursor react with the other precursor completely. This is a crtitical requirement for electronic application in order to minimise the amount of intrinsic defects, that is, pin holes and vacancies in the film [2, 4]. In flow type reactors such as ALD, 1 mTorr (pressure) of precursor is generally introduced into the chamber when pulsing [2]. Moreover, precursor flexibility is limited by the vapour pressure of the precursor material. A majority of metal-containing precurssors are either in liquid or solid form and the vapour pressure of these

precurssors is inadequate in room temperature. Therefore the precursors are heated (140 ^{o}C) to temperatures below the decomposition temperature of the precursor material to enhance the vapour pressure. It is recommended to obtain large vapour pressures to ensure the uniformity of the deposited layer. Furthermore, the deposition temperature must be smaller than the decomposition temperature of the precursor material, typically around 200 ^{o}C. If the deposition temperature is higher than the decomposition temperature, the precursor vapor may thermally decompose and chemisorbed species on the substrate can be desorbed from the surface. Thus, it is critical to perform the deposition in a precisely adjusted chamber temperature.

2.1.2 Sputter deposition

Sputtering is a widely used deposition method for the growth of thin metals, insulators and semiconductors onto a substrate. This is based on the theory whereby collisions between particles result in an elastic transfer of momentum that can be utilised to grow a thin film onto a substrate [5-7]. A target of the desired material is bombarded with energetic ions, generally inert gas ions such as Ar^{+} and the collisions will result in an ejection of atoms/molecules from the target into the free space. These ejected atoms will reach the substrate, forming a condensed film.

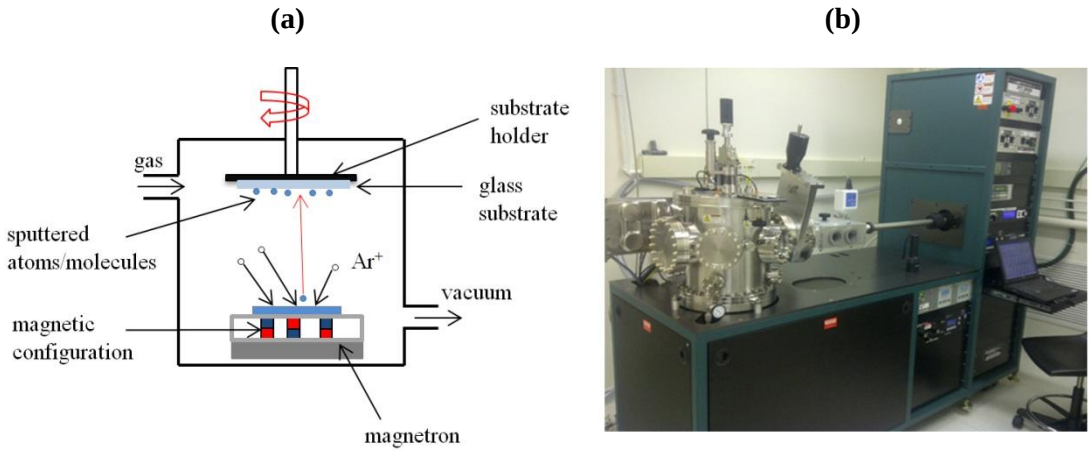

Figure 2.1: (a) Schematic of sputtering chamber and (b) AJA sputtering system.

The AJA International Orion – DV08 sputtering kit used (Figure 2.1 (b)) was a plasma-based system where the anode and cathode are placed opposite to each other in a vacuum chamber. The plasma is created when a potential is applied across the anode and cathode. As illustrated in Figure 2.1 (a), the energetic Ar^{+} ions will collide with the negatively biased cathode (sputtering target) and eject atoms/molecules from the target material. The ejected atoms/molecules will travel until they meet the substrate and grow a condensed film on it. A glow-discharge will be created between the anode and cathode. The Ar atoms that are inside

the glow-discharge are ionised and excited as a consequence of interaction with energetic electrons. These excited Ar atoms relax, emitting photons, causing the plasma to glow.

The sputtering kit used in this project consisted of both direct current (DC) and radio frequency (RF) sputter sources. When a DC source is used to bias the anode, the positively charged ions strike the target, capturing an electron. Moreover, if the target is conductive, the electron will be replaced by a transient electrical current [8]. On the other hand, if the target material is insulating, the captured electron cannot be replaced, leading to build up of positive charge on the target surface. This will result in a reduction in the potential difference between the anode and the cathode which is critical for the plasma. This explains why the DC sputtering technique is not suitable for insulators; however RF sputtering can be used to sputter insulating materials as the RF source reverses the surface polarity of the insulating target material, compensating the charge. In RF sputtering, an RF voltage with a frequency of 13.56 MHz is applied across the magnetron and the substrate holder [7]. As discussed before the Ar atoms that are in the target region are ionised by electrons, creating plasma. These Ar^+ ions are accelerated towards the target and collide on the target surface, ejecting the neutrally charged atoms/molecules. These ejected species will travel, within mean free paths until the substrate is met. It must be noted that the Ar^+ ions are not affected by the magnetic field due to their large mass in comparison to electrons.

It is also possible to apply a DC bias of 50 W (maximum) between the sample and the chamber. Therefore a plasma will be created between the sample stage and the chamber. In this scenario, the sample stage is used as the cathode, causing any impurities on the substrate surface to be etched away [7].

2.1.3 Thermal evaporation process

Thermal evaporation falls under the category of physical vapour deposition (PVD) which involves heating a solid material inside a high vacuum chamber to a temperature that produces vapour pressure. There will be heat generated in a resistive element when a large current passes through it. Metal that needs to be evaporated has to be inserted in to a W or Ta coil type filament. This is mainly due to the large melting points of metals such as W and Ta, therefore the metal (Al, Ag) inside the filament which has a relatively smaller melting point compared to W or Ta will reach its melting point and flow into the filament windings. The pressure inside the chamber was typically 210^{-6} mbar, creating a mean free path of vapour atoms created in the order of same dimensions as the vacuum chamber. Hence the particles follow a straight line when they travel from source to the substrate. Moreover, a small vapour pressure would be sufficient to raise a vapour cloud inside a vacuum chamber. The evaporated metal film forms a vapour stream which will travel across the chamber and hits the surface of

the substrate. This can be done either upwards (Moorfield minilab 060) or downwards (Edwards E306) evaporation. Film thickness and deposition rate were monitored by a quartz crystal in order to obtain a slow deposition rate of 0.4 nm/s, allowing the deposition of highly uniform metal films.

2.2 Physical characterisation techniques

2.2.1 Variable angle spectroscopic ellipsometry (VASE)

Light is an electromagnetic wave, represented by two vectors (*E* - the amplitude of the electric field strength and *B*- the amplitude of the magnetic field strength) that are perpendicular to each other at frequencies ranging from 310^{11} Hz to 310^{16} Hz. There are macroscopic electric currents generated as a result of light waves in a medium, which are linked to the induced motion of the electric charges of the electrons and atomic nuclei. It is possible to avoid the effect of induced magnetisation due to the considerably slower nature of motion in magnetic moments of electrons and nuclei. Hence the amplitude of the electric field strength is the most critical parameter when analysing the light wave, and can dictate that the polarisation state of light is dominated only by *E* [9]. The electromagnetic wave propagates in the *z* direction and can be described by the amplitude of the electric field (E_0), time (t), wave number (q) and the frequency (ω) in complex form [9].

$$E = E_0 e^{i(qz-\omega t)} \tag{2.1}$$

If the phase term δ is added to Eqn. 2.1, then

$$E = E_0 \cos(qz - \omega t + \delta)\,. \tag{2.2}$$

The vector *E* is composed by two individual components, E_x and E_y which are orthogonal to the propagation direction z where $E_z=0$ V/m [9]:

$$E_x = E_{01} \cos(qz - \omega t + \delta_x) \tag{2.3}$$

$$E_y = E_{02} \cos(qz - \omega t + \delta_y)\,. \tag{2.4}$$

δ_x and δ_y are phase constants whereas E_{01} and E_{02} are the amplitudes of E_x and E_y. The polarisation can be described as the change with time of the orientation of *E* along the wave propagation direction at any given point. Light is normally unpolarised as the *E* randomly propagates perpendicular to the propagation direction [9]. The light is linearly polarised if the E_x and E_y are in phase or out of phase by multiples of $\pm\pi$ (Figure 2.2 top) whereas light is circularly polarised if the amplitudes of E_x and E_y are equal and they are out phase by multiples

of $\pm\pi/2$ (Figure 2.2 bottom). However elliptically polarised light will be created if the waves are out of phase and the amplitudes are not equal.

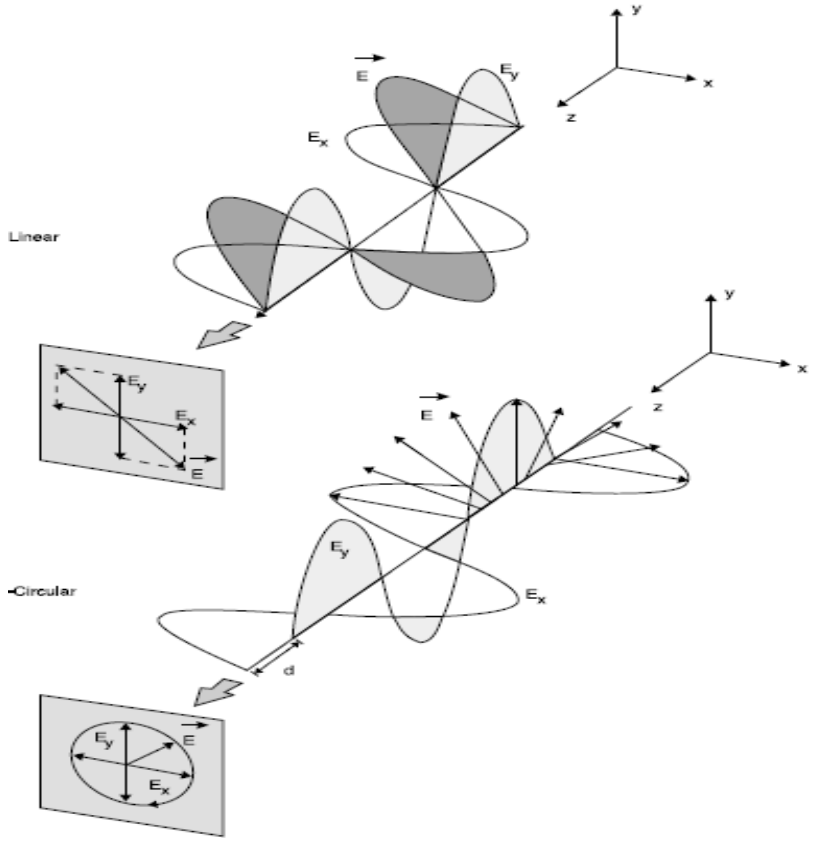

Figure 2.2: Linearly (top) and circularly (bottom) polarised light [9]

The experimental kit used in this work was a J. A. Woollam M2000UI variable angle spectroscopic ellipsometry (VASE) kit which uses a combination of deuterium & QTH lamps as the light source to achieve the wavelength region of 241-1700 nm. The polarisation state of the light wave can be defined by two components that are *s-plane* (perpendicular to the plane of incidence) and *p-plane* (parallel to the plane of incidence) where plane of incidence is the plane perpendicular to the sample surface. As per previous description, E_x refers to s-component and E_y to p-component [9]. The incident light wave is linearly polarised with the aid of a polariser, in other terms the *s* and *p* components of *E* are oscillating in same phase, resulting in the endpoint of *E* to move in a straight line in the *s-plane* and the *p-plane*. However, when the incident polarised light beam hits on the surface of the sample and reflects off the surface, the resultant light beam is elliptically polarised as can be seen in Figure 2.3.

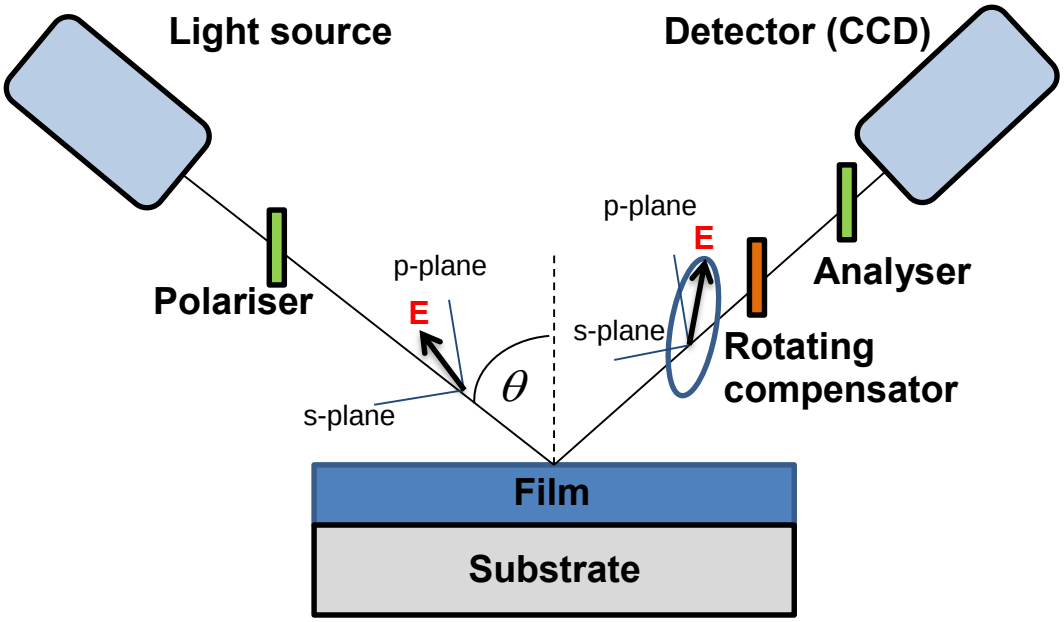

Figure 2.3: Schematic of ellipsometry measurements done on a thin-film sample

The polarisation state of the incident light beam is known, therefore the change in polarisation of the reflected beam from the surface can be measured by the detector. The mathematical background of the ellipsometry analysis is based on Fresnel reflection and transmission equations for polarised light reflected from the single or multi-layered sample surface [10]. These originate from Maxwell's equations [11]. Ellipsometry experimental results will be obtained in the form of two angles that are Δ and Ψ,

$$\tan\psi \cdot \exp(i\Delta) = \rho = \frac{r_p}{r_s} \tag{2.5}$$

where r_p and r_s are Fresnel reflection coefficients for the *p* and *s* components of the polarised light beam. Spectroscopic ellipsometry measures the complex ratio ρ as a function of wavelength. Ellipsometry is highly precise, reproducible and there is no need for a reference material due to the fact that it measures the ratio of two values. This technique is extremely precise even to characterise ultra-thin films as it measures the phase quantity (Δ) [12] and an amplitude ratio (ψ).

The complex refractive index ($\tilde{n}$) is represented as,

$$\tilde{n} = n + ik \tag{2.6}$$

where *n* and *k* are refractive index and the extinction coefficient whereby the refractive index describes a change in the phase velocity and the extinction coefficient determines the amplitude of electromagnetic wave propagating through a medium. Due to the effect of dispersion *n* and *k* vary with the wavelength. Alternatively, the optical constants can be represented as the complex dielectric function ($\tilde{\varepsilon}$) [12],

$$\tilde{\varepsilon} = \varepsilon_1 + i\varepsilon_2 \tag{2.7}$$

where ε_1 and ε_2 are the real and imaginary parts of the dielectric constant. Then it is possible to relate the complex dielectric function to the complex refractive index by,

$$\tilde{\varepsilon} = \tilde{n}^2 .$$

Light slows down when it enters a material which has larger refractive index than the vacuum as per the Eqn. 2.8,

$$v = \frac{c}{n} \tag{2.8}$$

where *c* is the speed of light in free space and *v* is velocity inside the corresponding medium. However the frequency of the light wave remains constant, resulting in a shortening of the wavelength. The amount of wave energy lost to the material can be estimated by the extinction coefficient (*k*). This is directly proportional to the absorption coefficient (α),

$$\alpha = \frac{4\pi k}{\lambda} . \tag{2.9}$$

Variable angle spectroscopic ellipsometry does the above stated measurements as a function of both wavelength and the angle of incidence. It is possible to achieve new information as a result of different optical path lengths traversed and also this optimises the sensitivity of the unknown parameters. The main advantage of having the option of changing the angle of incidence is to perform the measurements at or around the Brewster angle as the ellipsometric measurements are extremely precise at this angle [12]. When the angle of incidence is equal to the Brewster angle, the plane parallel to the plane of incidence cannot be reflected, instead refracted. The light reflected at this angle is s-polarized. Brewster angle is given by,

$$\tan\theta_B = \frac{n_2}{n_1} \tag{2.10}$$

The measurement is more accurate if it is performed by considering more than one angle in order to make sure that the measurement has performed at around the Brewster angle. When

characterising structures (semiconductors and dielectrics), the refractive index of the materials were used to calculate the Brewster angle and using three angles around it. VASE measurements and analysis are precise if the film thickness is between 5 nm and 1000 nm and also the roughness of the sample surface or at the interface is less than 10% of the wavelength of the source [12]. It may lead to non-specular scattering of the incident light beam and depolarisation of the reflected beam, if the roughness is large. Moreover, the thickness variation under the light spot on the sample must be less than 10% to validate the assumption of parallel interfaces in the thin films [12].

2.2.1.1 The modelling process

The general oscillator layer allows the user to utilise a large variety of oscillators to model the dielectric function of the desired film [13], that is, absorbance by characteristic defects in the film. This also enables the user to compare and fit the dielectric function directly to the optical constants of the desired reference material [13]. The general oscillator layer can effectively model the dielectric function of the film as a linear summation of real or complex terms (oscillators) as a function of wavelength or photon energy. For example, if three oscillator types are used, i.e., Gaussian, Lorentz and Tauc Lorentz, then the complex dielectric function consists of two e_1 offsets, Sellmeier terms (Pole 1 and Pole 2), Gaussian, Lorentz and Tauc Lorentz terms. The terms corresponding to Gaussian, Lorentz and Tauc Lorentz are complex functions of energy whereby the imaginary part of the dielectric function can be modelled. Then the real part is obtained from Kramers-Kronig relationships/transformation by fitting Sellmeier poles and e_1 offset [13].

The e_1 offset is a real constant added to ε_1 and usually represented by "ε_∞" [13]. Sellmeier and pole terms are Lorentz oscillators with zero-broadening [14], enabling them to only affect the real part of the dielectric function (ε_1). These can precisely determine the dispersion in zero absorption spectral regions. In most cases, Tauc Lorentz and Cody Lorentz oscillators were used in addition to Gaussian and Lorentz oscillators to model the imaginary part of the dielectric function [13]. The Tauc Lorentz oscillator can be used to accurately model the dielectric function of amorphous films, moreover, closer to the band edge, the absorption of Tauc Lorentz model follows a Tauc law formula which is $\varepsilon_2(E)\alpha(E\text{-}Eg)^2/E^2$ [15]. This approach also allows the user to multiple Tauc Lorentz oscillators with a common band gap value to achieve a good fit to the experimental data [13]. Nevertheless, the Cody Lorentz oscillator was also developed to model the amorphous films [16]. In comparison to the Tauc Lorentz model, the Cody Lorentz model behaves differently at the photon energies larger than the band gap energy [16]. In this region, Tauc Lorentz model anticipates the Tauc law formula whereas the Cody Lorentz model follows the $\varepsilon_2(E)\alpha(E\text{-}Eg)^2$ formula. Cody Lorentz model also

includes an Urbach absorption term and also it must be noted that although Cauchy model includes an Urbach absorption term, the Urbach term used in Cody Lorentz is completely Kramers-Kronig consistent [13].

The first step of analysis is to extract the thickness of the dielectric by using a Cauchy layer if the desired film is not included in the library. Then the extracted optical constants (*n*, *k*, and) from the Cauchy layer are saved and imported as the reference/starting material to the general oscillator. The imaginary part of the dielectric function is matched to the reference by using the oscillator models explained above. If a fit is not achieved, it is possible to add more of the same oscillator type or different oscillators and fit ε_2. Next step is to fit the pole 1 and pole 2, and e1 offset (if necessary) to match the reference ε_1. The mean standard error (MSE) determines the standard deviation between the experimental and model generated data (Δ and ψ). This can be extracted by,

$$MSE = \frac{1}{2N - M} \sum_{i=1}^{N} \left[\left(\frac{\psi_i^{\mathrm{mod}} - \psi_i^{\exp}}{\sigma_{\psi,i}^{\exp}} \right)^2 + \left(\frac{\Delta_i^{\mathrm{mod}} - \Delta_i^{\exp}}{\sigma_{\Delta,i}^{\exp}} \right)^2 \right].$$

Where N is number of measured Δ and ψ pairs, M is the total number of valued fit parameters, $\sigma_{\psi,i}^{\exp}$ and $\sigma_{\Delta,i}^{\exp}$ are the standard deviations of ψ and Δ. It is always best to achieve the smallest MSE, however a value below 10 signifies a good fit. Figure 2.4 illustrates the typical fitting process.

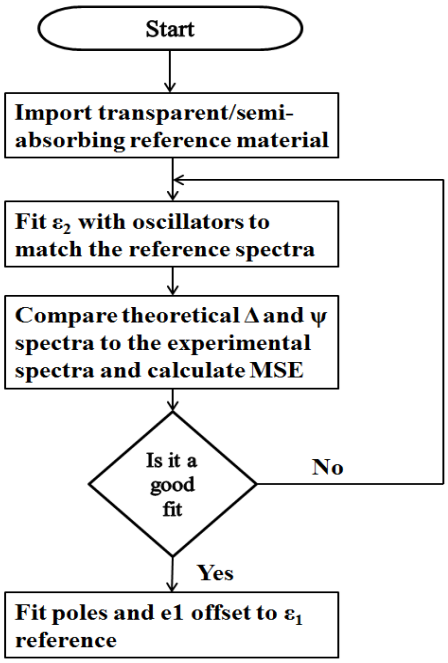

Figure 2.4: Flow chart of the modelling process using the general oscillator layer

2.2.2 X-Ray photoelectron spectroscopy (XPS)

The widely used surface analysis tool, X-ray photoelectron spectroscopy (XPS) was developed in 1960s by Siegbahn and colleagues [17, 18]. XPS is based on the principle of photoelectric effect. XPS utilises mono-energetic soft X-rays irradiating on a surface and analyses the energy distribution of the emitted electrons that are known as photoelectrons. It enables the user to study the electrons, from the core level to valence levels [18]. The spectrum is achieved as a plot of number of electrons per energy interval against the corresponding kinetic energy values. Therefore each element has its own unique spectrum. Moreover, the electrons which are suffering from energy losses while traversing the sample are visible in the spectral background. The kinetic energy (KE) of the measured electrons can be found by [17, 19],

$$KE = h\nu - BE - \phi_s \tag{2.11}$$

where $h\nu$ is the X-ray energy, BE is the binding energy and ϕ_s is spectrometer work function. The photon energy is known due to the use of twin Mg and Al anodes, in a conventional XPS kit. The photon energies of Mg source (Mg Kα) is 1253.6 eV whereas the photon energy of Al source is 1486.6 eV (Al Kα) [19]. The binding energy can be considered as the energy difference between the initial and final state after the photoelectron has left the atom. It is known that each element exists with a unique electron configuration; therefore the elemental composition of the desired sample can be determined by analysing the spectra [19].

Auger electrons may emit from the sample core levels as a consequence of the relaxation of excited ions remaining after photoemission. This occurs approximately 10^{-14} seconds after emitting the photoelectron [19]. In Auger electron emission process, an electron from an outer shell will jump to the inner orbital vacancy where the emitted photoelectron was, causing another electron from the outer shell to emit simultaneously [19]. Moreover, the Auger electron has a kinetic energy equivalent to the energy difference of the initial ion and the double charged final ion [19]. Hence photo-ionisation leads to two emitted electrons and the sum of their kinetic energy is equal to or less than the energy of ionising photons [19].

Although the penetration depth of the X-rays is in the order of micrometres, XPS measurements are limited to tens of angstroms [19]. This is because electrons interact with the matter; hence the electrons which are generated tens of angstroms below the surface can be emitted without suffering collisions [19]. The electrons emitted without any energy loss are detected by an electron spectrometer based on their kinetic energy values. The analyser operates as an energy window which is referred as pass energy (accepts electrons with energies

within the defined range of the analyser). Thus, the incoming electrons are adjusted to meet the pass energy prior to entering the analyser.

2.2.2.1 Element identification

The elements present in the sample with an atomic concentration larger than 0.1 - 1% can be identified by their strongest core-level features [20]. The BE values corresponding to a certain element may overlap with other elements, however this can be identified precisely by either prior knowledge of the expected elemental composition or utilising the secondary core level spectral features, for example the tantalum survey spectra contains sharp features due to the Ta 4p, Ta 4d, Ta 5s, Ta 5p core levels in addition to Ta 4f core level. However, elements that are present in the sample with low concentrations are difficult to identify as the intensities of the resultant signals are almost identical to the background noise. Nevertheless, with prior knowledge of minor contaminants that could occur, these elements can be identified by magnifying the expected region of the survey spectra [20]. The corresponding binding energy value and the spin-orbit splitting could verify the presence of that certain element. The spin-orbit splitting can be defined as the energy separation between two features generated by electrons from the same core level, however with different spin-orbit coupling [20]. The delta value (energy separation) varies from one element to another.

2.2.2.2 Chemical shift

XPS allows the user to distinguish the different chemical environments of the same element. The binding energy of an electron in an atom is sensitive to the variations in charge densities around the atom caused as a result of forming chemical bonds [19, 20]. The sensitivity of conventional XPS can identify the shifts greater than 0.1 eV. Formation of Al_2O_3 on Al is assessed by the Al 2p peak and this can be used as an example to describe this phenomenon. The binding energy of metallic Al is 72.7 eV whereas the binding energy of Al_2O_3 is 74.1 eV [19]. The binding energy corresponding to Al_2O_3 is larger than the metallic Al due to electronic structure differences. The Al-O bonds are ionic and the more electronegative oxygen will take more of the overall negative charge and create a dipole [20]. Therefore the electrons that undergo photoelectron effect from this atom have relatively small kinetic energies due to the positively charged nature of the atom in comparison to Al-Al covalent bonds where the valence electrons are shared equally (Al) [20].

2.2.2.3 Work function (Φ) estimation

The valence bands are occupied with electrons up to the Fermi energy level. The work function is defined as the minimum amount of energy which is needed to remove an electron from the metal and this can be estimated by calculating the difference between the vacuum level energy and the Fermi energy levels. In a metal, it can be stated that the ionisation energy and the work function are the same [21, 22]. The work function of a metal is extremely surface sensitive, for instance the work function value could be changed with the presence of small amounts of contamination even though it is less than a monolayer of atoms or molecules [21, 22]. The work function also significantly depends on surface reactions, for example, oxidation. The change of work function can be up to 1 eV for metals and semiconductors, depending on the surface condition. These changes are caused by the formation of electric dipoles at the surface, changing the minimum energy for an electron to leave the sample [21, 22]. Therefore it is possible to obtain information on the chemical changes on the surface due to the high sensitivity nature of the photoelectron spectroscopy (PES) measurements [21, 22].

A photoelectron spectrum is usually illustrated in binding energies with respect to the Fermi edge of the sample. The kinetic energies of the electrons photo-emitted from the sample are measured and photoemission can be described in three steps:

1) The energy of the incident photon is absorbed by an electron then it will excite to a higher energy state at the location of absorption.
2) The electron travels to the sample surface
3) The electron is transferred to the vacuum level from the surface of the sample.

The majority of generated electrons undergo inelastic collision while they travel to the surface of the sample from excited states. This results in a reduction of the kinetic energy values [19]. Therefore the spectrum consists of two main components that are [21, 22]:

1) Primary electrons which did not undergo inelastic collisions
2) Secondary electrons which are also primary electrons which went through inelastic collisions and lost a certain amount of kinetic energy depending on the energy loss due to the collision.

The primary electrons demonstrate well-defined spectral peaks that mirror (first order approximation) the density of states (DOS) of the sample. The secondary electrons may have a continuous energy spectrum down to zero kinetic energy that will be superimposed on the primary electron spectrum [21, 22]. The primary electrons can be used to determine the binding energies of electronic states in the sample whereas the secondary electrons can be

used for the extraction of work function value of the sample [21, 22]. The secondary electrons can be considered as being scattered into the conduction band levels beyond the vacuum level; hence they contain information on the density of states of the sample [21, 22].

The photoelectron effect involves the generation of free electrons with a certain kinetic energy depending on the exciting photon energy, work function of the sample, the binding energy of the excited electron and the inelastic scattering process in the sample [21, 22]. The fastest electrons of this spectrum are the primary ones emitted directly from the Fermi edge. The slowest electrons are the secondary ones barely escaping from the sample after losing energy due to scattering events (kinetic energy = 0 eV) [21, 22].

The kinetic energy of these electrons can be measured by sending them through a kinetic energy analyser in the detector where they can be counted. This type of a detector has a work function (analyser work function) too, a contact potential (difference between work function of the sample and work function of the analyser) exists, and therefore their Fermi levels are aligned [21, 22]. Normally, the work function of the analyser is smaller than the sample work function; hence the contact potential causes an acceleration of electrons as they travel through the analyser [21]. The kinetic energy will be increased by the difference in work function of sample and work function of analyser for the primary electrons. The secondary electrons are accelerated to an energy similar to the work function of the contact potential. Therefore the entire spectrum is now shifted by the difference between work function of substrate and that of the analyser. This is the spectrum measured in PES measurements [21, 22].

There is another aspect of the obtained spectrum, which is the effect of secondary electrons of the analyser itself [21]. These electrons are created as a result of photoelectrons from the sample that collide on the analyser surface. Yet again the kinetic energy of these electrons is 0 eV. They are not influenced by the contact potential as they are created in the analyser/detector. This results in a spectrum that is superimposed on the secondary edge of the sample spectrum, making it difficult to estimate the position of the secondary electrons edge of the sample. This can be compensated by applying an accelerating potential between the sample and the analyser, which is used to separate the secondary edges of the sample and the analyser. However the electrons emitting from the sample are accelerated as before due to the work function difference of the sample and the analyser. This phenomenon pushes the spectrum away from the analyser secondary electrons as these are not accelerated by the potential and remain closer to 0 eV [21, 22]. Therefore the sample and analyser secondary electrons are well separated for smoother analysis.

The work function of the analyser is an unknown variable; therefore it is possible to use the Fermi edge of a metal surface to calibrate the kinetic energy scale with respect to the Fermi

edge of the sample, i.e. internal kinetic energy. An internal kinetic energy scale can be defined by giving the energy of the electrons in their final state before they eject from the sample. The calibration step can be done easily as the work function of the sample does not affect the kinetic energy measurement of primary electrons. Moreover, the primary electrons are the fastest electrons of the spectrum have kinetic energy equivalent to photon energy and shift the entire spectrum accordingly. This process will shift the secondary cut-off edge to the appropriate kinetic energy that corresponds to the sample [21].

It is evident that there is a kinetic energy scale referenced to the Fermi level of the sample; hence the binding energy scale is defined as [21],

$$BE = h\nu - KE_{\mathrm{int}ernal} \tag{2.12}$$

where $KE_{internal}$ is the internal kinetic energy, and hν is the photon energy of the XPS source. This does put the binding energy of the Fermi edge to 0 eV. Moreover, the binding energy of secondary electrons cut-off can be obtained by [21],

$$\textit{Secondary cut-off}\ \ BE = h\nu - \phi_{sample} \tag{2.13}$$

where ϕ_{sample} is the work function of the sample. The analyser must be calibrated with a metal as explained before in order to extract the ionisation energy value. The ionization energy is the minimum energy required to remove an electron from the neutral atom.

2.2.2.4 Work function in semiconductors

In a semiconductor the valence and conduction bands are separated by the band gap of the material, hence the Fermi level is somewhere in between the two [22]. As a result of this, the work function and the ionisation energy are not the same; the ionisation energy is the energy difference between valence band maximum (VBM) and the vacuum level. It is also possible to state that the Fermi level is a theoretical approximation as there are not any electronic states within the band gap [21, 22]. Therefore the Fermi distribution function (statistical function which states the probability of finding an electron in any given energy state) has to be considered. The Fermi level is the state where the probability of finding an electron is 50%. The work function of a semiconductor can be found by PES regardless of having electrons in the Fermi energy level [22].

It must be noted that the majority of secondary cut-off electrons used to measure the work function are not created from the Fermi edge; instead they are created from all the primary electron emission combined. The process works regardless of having any electronic states at

the Fermi edge. This makes it possible to measure the work function of semiconductors [21, 22].

The information that can be obtained from the initial spectrum are the highest kinetic energy which is related to the VBM (unknown binding energy) and also a lowest kinetic energy (0 eV). It is however possible to calculate the ionisation energy (*IE*) by, [21, 22].

$$IE = h\nu - W \tag{2.14}$$

$$W = \sec ondary\ cut-off\ + applied\ \ bias - VBM$$

$$IE = E_{ion} = h\nu - (E_{secondary\ cut\text{-}off} + E_{app} - VBM)$$

where hν is the photon energy of the XPS source, $E_{secondary\ cut\text{-}off}$ is the energy referring to the secondary electrons spectrum edge, E_{app} is the added kinetic energy to the system by applying an accelerating potential between sample and analyser to separate the secondary electrons spectra cut-offs of sample and analyser, and VBM refers to the binding energy of valence band maximum of relevant material (semiconductor or oxide).

Therefore [21],

$$\phi = IE - E_g \tag{2.15}$$

where ϕ is the work function and E_g is the band gap of the material.

2.2.3 Atomic Force Microscopy (AFM)

AFM is a characterisation technique that could be utilised to analyse the surface of a material down to the atomic level. The technique overcomes the primary limitation of scanning tunnelling microscopy (STM) which has the capability of imaging only the surfaces of conducting or semiconducting films [23]. There is the possibility of obtaining a 3-D profile of the surface on the nanoscale by measuring forces between a sharp probe, below 10 nm and the surface at a short distance of typically 0.2 - 10 nm [23]. The probe is mounted on a flexible cantilever; thus the AFM tip can touch the sample surface and detects the small force between the probe and the sample surface. The force between the probe and the sample surface depends on the spring constant of the cantilever and also the distance between the sample and the cantilever [23]. This force can be determined by using Hooke's Law (Eqn. 2.16),

$$F = -kx \tag{2.16}$$

where F is the calculated force, k is the spring constant and x is the cantilever deflection. Typically, the cantilever spring constant is smaller than the stiffness of the surface, causing the cantilever to bend and this deflection can be monitored by an optical detection technique which consists of laser and position sensitive photodetector [8]. The laser beam is focused on the back of the AFM cantilever, so that the reflected beam can be detected by the position sensitive photodetector. The cantilever deflections are precisely monitored while a scan is performed on a non-uniform surface. The motion across the sample surface is controlled by a feedback loop and piezoelectric scanners [23].

The cantilever deflections are caused as a consequence of several forces generated between the AFM tip and the sample. Furthermore, the dominant interactions in AFM are Van der Waals interactions due to its short probe-sample distances. The main types of imaging modes in AFM are

1) Contact mode AFM (< 0.5 nm surface to probe separation) [23]

The force on the AFM tip is repulsive. It is possible to maintain a constant cantilever deflection with the aid of a feedback loop. Therefore the force between the probe and the sample surface remains constant leading to an image of the sample surface. Although the resolution is high, this mode may damage the tip and the sample surface due to high pressure. Moreover, soft samples such as polymers of biological materials cannot be imaged via contact mode.

2) Non-contact mode AFM (0.1 – 10 nm surface to probe separation) [23]

Unlike in the contact mode, the interatomic force between the cantilever and the sample is attractive due to long range Van der Waals interactions. The detection process is based on the shift of resonant frequency or amplitude of the cantilever as the AFM tip is not in contact with the sample. This is mainly used for surface analysis of soft samples as the non-contact mode has a weaker tip-sample interaction compared to the contact mode.

3) Intermittent mode (0.5 nm – 2 nm surface to probe separation) [23]

This resembles the contact mode features, but in this technique the cantilever oscillates at its resonant frequency. Moreover, the probe gently taps the sample surface while scanning. It is possible to obtain an image on the surface by maintaining constant oscillation amplitude and a tip-sample interaction. This technique overcomes most of the limitations caused by both contact mode and the non-contact mode such as, high resolution and less damage to the sample surface.

However, in this series of experimental work, contact mode was used to assess the surface roughness of the bottom metal electrode.

2.3 Electrical characterisation techniques

The current-voltage (*IV*) measurements were performed on completed metal insulator metal structures using the B1500A semiconductor parameter analyser connected to a screened probe station in the dark. The voltage sweeps were done using continuous (either from negative voltages to positive voltages or positive voltages to negative voltages) and discontinuous (either from zero to positive voltages or zero to negative voltages) measurements to investigate the charging effect in oxides. Voltage sweep and current sampling rates are also noted.

The aim of performing *IV* measurements is to investigate the rectification properties and the conduction process of the rectifier structures. The assessed rectification properties are explained in chapters 5, 6 and 7. Moreover, the room temperature measurements lead to the analysis of temperature independent quantum mechanical tunnelling mechanisms whereas the high temperature measurements were performed using a hot chuck connected to B1500A semiconductor parameter analyser and used to assess the temperature dependent conduction mechanisms such as Poole-Frenkel and Schottky emission. The temperature range considered was 20 - 100 ^{o}C with a step of 10 ^{o}C and the sample was left on the heated sample stage (under vacuum) for at least 15 minutes to ensure the devices that were fabricated on the corning glass substrates have reached the desired temperatures.

References

[1] R. W. Johnson, A. Hultqvist, S. F. Bent, "A brief review of atomic layer deposition: from fundamentals to applications", Materials Today, 17 (5), 236 (2014)

[2] S.M. George, "Atomic layer deposition: An overview", Chem. Rev., 110, 111 (2010)

[3] J. Hamalainen, M. Ritala, M. Leskela, "Atomic layer deposition of noble metals and their oxides", Chem. Mater., 26, 786 (2014)

[4] R. L. Puurunen, "Surface chemistry of atomic layer deposition: A case study for the trimethylaluminum/water process", J. Appl. Phys., 97, 121301 (2005).

[5] R. Kukla, "Magnetron sputtering on large scale substrates: an overview on the state of the art", Surf. Coat. Technol., 93, 1 (1997)

[6] P. J. Kelly, R.D. Arnell, "Magnetron sputtering: a review of recent developments and applications", Vacuum, 56, 159 (2000)

[7] R.E. Treharne, "RF magnetron sputtering of transparent conducting oxides and CdTe/CdS solar cells", PhD thesis, University of Durham at Durham (2011)

[8] J.D. Jin, "Metal-oxide-based electronic devices", PhD thesis, University of Manchester at Manchester (2013)

[9] D. Gonçalves, E.A. Irene, “Fundamentals and applications of spectroscopic ellipsometry”, Quim. Nova, 25(5), 794 (2002)

[10] J.A. Woollam, J.N. Hilfiker, T.E. Tiwald, C.L. Bungay, R.A. Synowicki, D.E. Meyer, C.M. Herzinger, G.L. Pgeiffer, G.T. Cooney, S.E. Green, “ Variable angle spectroscopic ellipsometry in the vacuum ultraviolet”, Proc: SPIE, 4099, 197 (2000)

[11] H.G. Thompkins, E.A. Irene, “Handbook of ellipsometry”, Norwich, USA, William Andrew Publishing, 2005, Ch 3, sec 3.2, 239

[12] J.M. Khoshman, “Spectroscopic ellipsometry characterisation of single and multilayer aluminium nitride/indium nitride thin fims”, PhD Thesis, Ohio University (2005)

[13] J.A. Woollam Co., “Guide to using WVASE”, User manual, Ch 8 (2012)

[14] W. Sellmeier, “Zur Erklärung der abnormen Farbenfolge im Spectrum einiger Substanzen”, Annalen der Physik, 219(6), 272 (1871)

[15] G.E. Jellison Jr., F.A. Modine, “Parameterization of the optical functions of amorphous materials in the interband region”, Appl. Phys. Lett., 69(3), 371 (1996)

[16] A.S. Ferlauto, G.M., Ferreira, J.M. Pearce, C.R. Wronski, R.W. Collins, X. Deng, G. Ganguly, “Analytical model for the optical functions of amorphous semiconductors from the near-infrared to ultraviolet: Applications in thin film photovoltaics”, J. Appl. Phys., 92(5), 2424 (2002)

[17] J.M. Hollander, W.L. Jolly, “X-Ray photoelectron spectroscopy”, Acc. Chem. Res., 3, 193 (1970)

[18] J.F. Watts, “X-ray photoelectron spectroscopy”, Vacuum, 45 (6), 653 (1994)

[19] J. F. Moulder, W.F. Stickle, P.E. Sobol, K.D. Bomben, “Handbook of X-ray photoelectron spectroscopy”, Physical Electronics, Inc., 1995

[20] S. McDonnell, “Spectroscopic characterisation of high dielectric constant materials on semiconducting surfaces”, PhD Thesis, Dublin City University (2009)

[21] R. Shalf, “Calibration of photoemission spectra and work function determination”, http://rsl.eng.usf.edu/Documents/Tutorials/PEScalibration.pdf (accessed Apr 7, 2016)

[22] R. Shalf, “Tutorial on work function”, http://rsl.eng.usf.edu/Documents/Tutorials/TutorialsWorkFunction.pdf (accessed Apr 7, 2016)

[23] R.A. Wilson, H.A. Bullen, “Introduction to scanning probe microscopy (SPM): Basic theory atomic force microscopy (AFM)”, see: http://asdlib.org/onlineArticles/ecourseware/Bullen/SPMModule_BasicTheoryAFM.pdf

Chapter 3

3. Optical properties of high-k oxides on germanium

The semiconductor technology was dominated by Si mainly due to the excellent quality of interface produced with its natural oxide, SiO_2. Si also benefited the semiconductor industry with a lower cost due to its abundant nature on the earth's surface. These factors led the industry to manufacture reliable MOSFETs at low cost. Moreover, the gate dielectric, SiO_2 can be simply form by oxidising the Si surface and also it is possible to use highly-doped poly-silicon as the gate electrode. Then the source and drain contacts of the MOSFET can be formed either by doping Si followed by annealing to form silicide to minimise contact resistance or depositing a metal. Therefore it is possible to state that a MOSFET can be fabricated by using Si as the semiconductor, gate electrode and oxide and source/drain contacts. Gordon Moore predicted the number of transistors that can be placed on a single chip doubles in every 2 years [1]. This was achieved by scaling down device dimensions such as oxide thickness, width, and channel length. However, it has been reported that the conduction mechanism in SiO_2 is dominated by quantum mechanical direct tunnelling when the oxide thickness is scaled below 2 nm [2, 4]. Thus, it was crucial to introduce new materials to this structure to allow continued scaling of devices.

The first transistor was built using Ge although Si became the most promising candidate mainly due to its good quality interface between SiO_2 and Si [3, 4]. It is known that Ge is not abundant as Si; therefore this could be expensive in contrast to the cost of Si. Moreover, it is distinctly challenging to obtain a good interface between Ge and its natural oxide GeO_2 due to the formation of an unstable GeO_x layer where $x < 2$ [5]. The melting temperature of Ge is 937 ^oC which is lower than the melting temperature of Si which is 1414 ^oC, leading to use a smaller thermal budget for CMOS processing [6]. Ge can be considered as a potential channel material with superior transport properties for future CMOS applications [7, 8]. Ge has high intrinsic mobilities for both electrons (3900 cm^2/Vs) and holes (1900 cm^2/Vs). The narrower band gap of 0.67 eV potentially implies the possibility of obtaining low contact resistances as the barrier height with the metals is smaller compared to metal/Si interfaces, hence is more suitable for voltage scaling and low power applications [9]. The other advantage is the compatibility with Si process technology, making it a suitable channel material for low power, high performance devices [10].

High performance Ge based MOSFET gate stacks can be fabricated by passivating the Ge surface in order to achieve a good interface between the gate oxide and Ge. It has been reported that GeO_2 can be recognised as a potential passivation layer due to its good interface control on Ge [11]. However, GeO_2 cannot be used for aggressive scaling of devices due to its small dielectric constant of 6. Therefore it is crucial to introduce a high-k rare earth material either

to combine with a thin layer of GeO_2 or to use individually in order to obtain an equivalent oxide thickness (EOT) below 1 nm. The latter is required for the 8 nm node where Ge channels are proposed to be introduced as specified in International technology roadmap for semiconductors (ITRS) roadmap. It has been reported that the thermodynamically robust interfacial layer engineering using Y_2O_3 doped GeO_2 can lead to an EOT of 0.94 nm on Ge with superior interface properties and mobilities on nMOSFETs [12]. A series of experiments were performed to study different Ge passivation techniques. Nonetheless, the main focus of this chapter is to study the optical properties of high-k dielectrics on Ge and its interface. The optical properties estimated were used to extract the band gap values for Y_2O_3, Tm_2O_3, Al_2O_3 and GeO_2 and also to analyse the sub-band gap absorption peaks in the dielectric and/or interfacial layer. These results were correlated with other analysis including X-ray photoelectron spectroscopy (XPS), X-ray diffraction (XRD), high resolution transmission electron microscopy (HRTEM) and electrical characterization. The original contribution reported in this chapter is the spectroscopic ellipsometry analysis and its subsequent correlation with results obtained by other characterisation techniques.

It has been reported that the rare earth oxides Y_2O_3, La_2O_3, $LaLuO_3$, Dy_2O_3, Gd_2O_3 and CeO_2 react well with the substrate resulting in catalytic oxidation of Ge and the spontaneous formation of a stable interface between the oxide and Ge [13-16]. This enables the realisation of an interface without the presence of GeO_x. In this scenario, Y_2O_3 was chosen as the gate dielectric as it is Ge-friendly and robust against water [17]. Amorphous Y_2O_3 is reported to have a wide band gap of ~5.5 - 5.7 eV [17], relatively high dielectric constant between 11 and 18 [18, 19], high crystallization temperature of 2325 ^oC and can effectively passivate the Ge surface by eliminating the formation of GeO_x [19, 20]. It is also possible to passivate the interface by introducing a robust, thin high-k interfacial layer barrier such as Al_2O_3 [7, 21–25] or Tm_2O_3 [26]. Ge surface passivation with Al_2O_3 results in a degradation of the speed of oxidisation without causing GeO_x diffusion or desorption. Hence all the Ge atoms near the interface are terminated with oxygen atoms or Ge atoms without any dangling bonds under the oxidation condition 4+, leading to low density of interface states values. An approach has been carried out to engineer the interface either by using Y_2O_3 as the gate dielectric, Tm_2O_3 or Al_2O_3 as a capping layer to passivate the Ge surface.

The optical constants related to the dielectric, interface and substrate were extracted in order to analyse the sub-band gap absorption peaks and also to extract the band gap values. This technique is extremely precise even for characterisation of ultra-thin films as it measures the phase quantity (Δ) and an amplitude ratio (ψ). The VASE measurements were performed considering a spectral range of 0.5 – 8.8 eV ($\lambda = 140 - 2500$ nm). As a result of wide spectral

range all the dielectric films became semi-absorbing making the modelling process more complex. The UV absorption can be determined by dispersion theory whereas many dispersion theories rely on oscillator theory. The oscillators such as Gaussian, Lorentz, Cody-Lorentz and Tauc-Lorentz can be used and it is also worth mentioning all these oscillators share mutual attributes such as amplitude, broadening, centre energy and band gap energy. Then Kramers-Konig (KK) consistency can be used to evaluate the shape of the real component of the complex dielectric function ($\tilde{\varepsilon}$) after the imaginary behaviour was modelled by an oscillator [27-29]. It is necessary to add an offset to the real component of the complex dielectric function in order to account for the extra absorption outside the measured spectral range.

There was a transparent region of spectra from 0.5 eV to 6 eV and this was modelled using a Cauchy layer if the dielectric is not included in the standard library. Then the energy spectra were extended up to 8.5 eV using a KK consistent B-spline layer [29]. This method was consistent with the point-by-point technique which was used in WVASE 32. Moreover, the B-spline layer was replaced with a general oscillator layer as this enabled the use of oscillators to model the imaginary part of the dielectric constant. Then the real part of the dielectric function outside the measured spectral range was modelled using two Sellmeier poles.

3.1 Y_2O_3/Ge, Al_2O_3/Ge and GeO_2/Ge band line-up study

The high-k oxide, Y_2O_3 was deposited on n-type Ge, by Molecular Beam Epitaxy (MBE) at two deposition temperatures which were 225 ^oC and 400 ^oC. It was mandatory to clean the surface of the Ge substrate with trichloroethylene, acetone and methanol for five minutes in each solvent to eliminate organics. Then the native oxide of Ge, GeO_x was thermally desorbed by annealing at 450 ^oC - 500 ^oC for the duration of 30 minutes. The reference samples, GeO_2/Ge with/without the Al_2O_3 capping layer, Al_2O_3/Ge and oxidized Y foil were prepared for VASE and XPS measurements. The Ge substrate was first measured in the spectral range of 0.5 to 8.8 eV and three angles, 65^o, 70^o and 75^o. Then the thickness of the native oxide layer was extracted to be 2.93 nm by using a KK consistent B-spline layer considering the entire spectral range. This model was used as the reference to model Al_2O_3, Y_2O_3 and thermally grown GeO_2 as all these layers were deposited on the same substrate. The modelling process of Al_2O_3, Y_2O_3 and GeO_2 was achieved by using a general oscillator layer and following the steps mentioned in chapter 2, section 2.2.1 (Figure 2.4). The extracted thickness and band gap values for 225 ^oC and 400 ^oC processed Y_2O_3/Ge samples, GeO_2/Ge (without the capping layer), Al_2O_3/GeO_2/Ge (with the capping layer) are summarised in Table 3.1. The refractive index (n) and extinction coefficient (k) were extracted after evaluating the real and imaginary parts of the dielectric function. Kramers-Kronig relationship was considered while evaluating

the real (ε_1) and imaginary (ε_2) parts of the dielectric function. The complex dielectric function ($\tilde{\varepsilon}$) can be written as,

$$\tilde{\varepsilon} = \varepsilon_1 \pm i\varepsilon_2 . \tag{3.1}$$

Then the complex dielectric function can be related to the complex refractive index ($\tilde{n}$) as,

$$\tilde{\varepsilon} = \tilde{n}^2 .$$

Eventually,

$$n = \sqrt{\frac{\varepsilon_1 + \sqrt{(\varepsilon_1^2 + \varepsilon_2^2)}}{2}} \text{ and } k = \sqrt{\frac{-\varepsilon_1 + \sqrt{(\varepsilon_1^2 + \varepsilon_2^2)}}{2}} \quad . \tag{3.2}$$

Moreover, the absorption coefficient (α) can be calculated using the extinction coefficient (k) as,

$$\alpha = \frac{4\pi k(E)E}{hc} \tag{3.3}$$

where *h* is the Planck's constant, *E* is the photon energy and *c* is the speed of light.

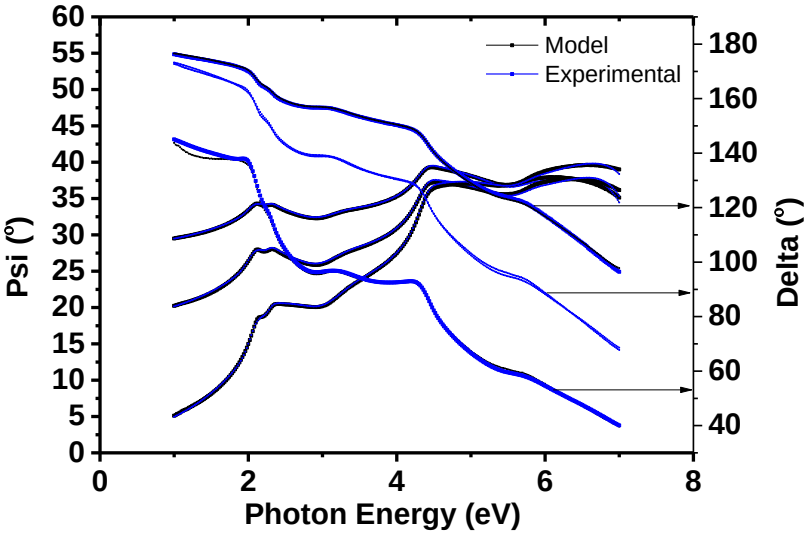

Figure 3.1: Experimental and modelled Δ and ψ ellipsometric angles against photon energy for Y_2O_3/Ge deposited at 225 °C.

The experimental and modelled Δ and ψ plots for the Y_2O_3/Ge sample deposited at 225 °C is shown in Figure 3.1. It can be seen that the modelled Δ and ψ curves (black curves) are almost identical to the experimental data (blue lines). The model was achieved using the general oscillator layer with a mean standard error (MSE) of 2.01. Furthermore, the modelling process was done by using both completeEASE and WVASE32 software programs to verify the

consistency of the modelling process. The error margin of the MSE was ± 0.02. The general oscillator was replaced with B-spline layer in order to verify the same results can be obtained. However, there was a slight variation of thicknesses extracted for Y_2O_3 of 6.3 ± 0.13 nm.

Table 3.1: Summary of thickness and band gap values extracted by VASE.

Sample	Thickness (nm)	Band gap (eV)		
		$(\alpha nE)^{1/2}$	$(\alpha E)^2$	α - method
Ge substrate	2.93 ± 0.002 (native oxide)			
Y_2O_3/Ge (deposited at 225 °C)	6.3 ± 0.04	5.77 ± 0.1	5.7 ± 0.1	5.99 ± 0.1
Y_2O_3/Ge (deposited at 400 °C)	7.9 ± 0.03	5.77 ± 0.1	5.77 ± 0.1	5.99 ± 0.1
GeO_2/Ge	4.4 ± 0.1	5.65 ± 0.1		5.95 ± 0.1
Al_2O_3/Ge	9.4 ± 0.002	6.12 ± 0.1	6.33 ± 0.1	6.43 ± 0.1
Al_2O_3/GeO_2/Ge	7.8/3.2 (±0.2) 8.8/7.2 (±0.2)			

The band gap of Y_2O_3 and Al_2O_3 were extracted by Tauc-Lorentz [30] and α methods. The band gap values were also assessed utilizing the plots of ε_2 and k, however the estimated values were almost identical to the value extracted by α as these parameters are directly proportional to each other. Both direct (αE^2) and indirect band gap ($\alpha E^{1/2}$) relationships were considered while analysing the Tauc plots. The absorption coefficient against photon energy plots are shown in Figures 3.3 (a) and (b) for Y_2O_3 and Al_2O_3 samples respectively. Moreover, the Tauc-Lorentz plots are illustrated in Figure 3.3 (c) and Figure 3.3 (d) for Y_2O_3 and Al_2O_3 samples respectively.

The real and imaginary parts of the complex dielectric constant were plotted against the photon energy (Figure 3.2) with the intention of observing if there are any absorption peaks below the band edge.

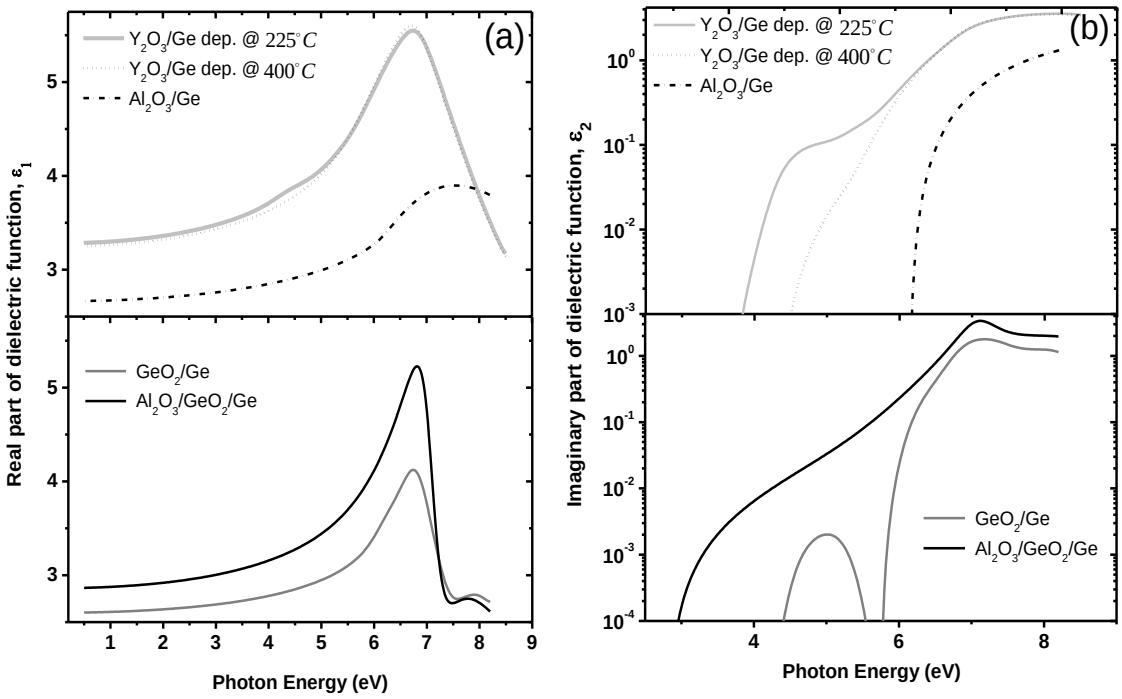

Figure 3.2: (a) Real part of the dielectric constant and (b) imaginary part of the dielectric constant for Y_2O_3/Ge structures deposited at 225 ^oC and 400 ^oC, and also GeO_2/Ge with and without the capping Al_2O_3 layer.

It was evident from Figure 3.2 (b) that there is absorption below the band edge of the Y_2O_3 stack deposited at 225 ^oC. This was observed consistently in both real and imaginary parts of the dielectric constant within the energy range of 4 to 5.5 eV (Figures 3.2 (a) and (b)). However, the absorption edge tailing was much less pronounced for the Y_2O_3/Ge stack deposited at 400 ^oC. The real and imaginary parts of dielectric function for the reference GeO_2/Ge were plotted with and without the Al_2O_3 capping layer (bottom graphs of Figures 3.2 (a) and (b)) in order to observe if there was any correlation with the absorption observed for the Y_2O_3/Ge structure deposited at 225 ^oC. Two absorption peaks have been identified due to Ge at 4.4 eV and 5.1 eV for the GeO_2/Ge structure analysed in Figure 3.12. In this analysis only one absorption peak can be seen at 5 eV. Toriumi *et al.* [31] have reported that the peak at 5.1 eV for the GeO_2/Ge structure can be ascribed to neutral O vacancies or Ge 2+ in O deficient GeO_2 [32]. *Ab initio* calculations [33, 34] have indicated that $–GeX_3$ [32] and X_3Ge-GeX_2 [32] defects may form a broad absorption band near 5 eV where X refers to –OH and $–OGeH_3$ simulating the: Ge< defect [34]. Hence the absorption observed below the band edge for Y_2O_3/Ge sample deposited at 225 ^oC could be associated with a defective non-stoichiometric GeO_x interfacial layer. Note that this was not visible for the Y_2O_3/Ge sample deposited at 400 ^oC.

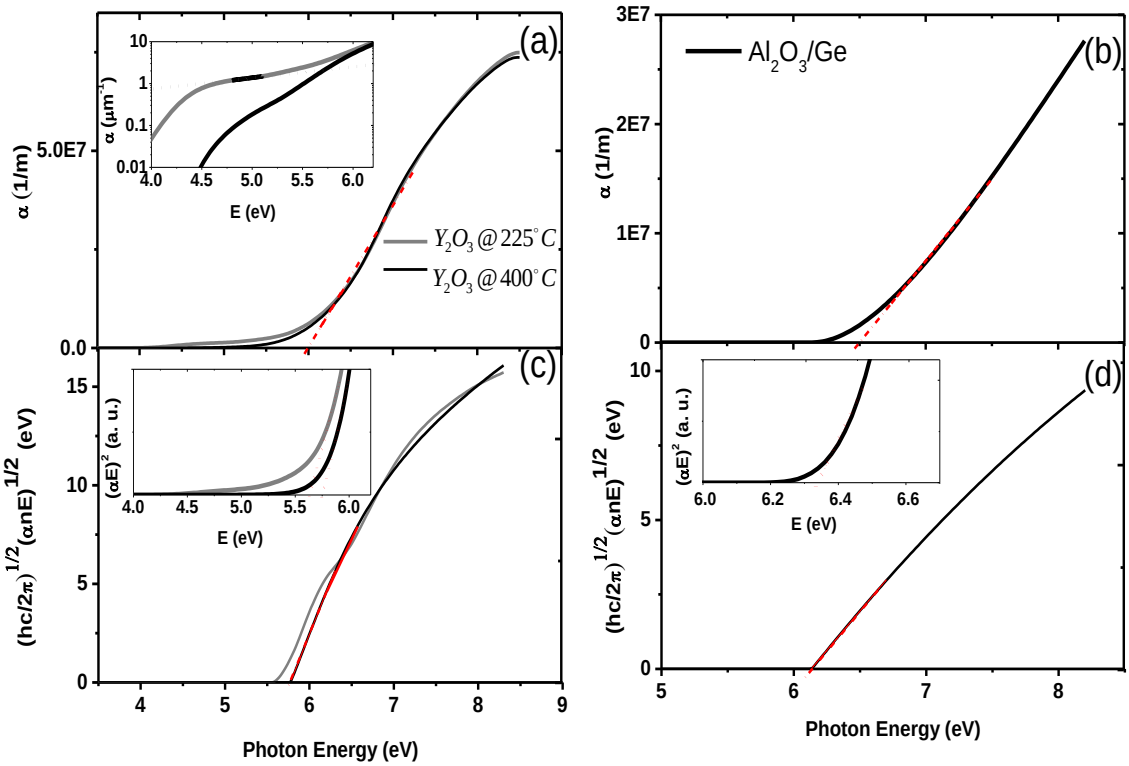

Figure 3.3: The absorption coefficient vs photon energy plots for (a) Y_2O_3 and (b) Al_2O_3. Tauc plots for (c) Y_2O_3 (225 °C and 400 °C) and (d) Al_2O_3 for indirect band gap approximation. The inset in (a) shows logarithmic absorption coefficient vs photon energy. The insets of (c) and (d) show Tauc plots for direct band gap approximation.

The band gap values were extracted by linearly extrapolating the segments on the curves in the non-absorbing regions. The band gaps assessed by absorption coefficient methods were 5.99 eV (Figure 3.3 (a)) and 6.43 eV (Figure 3.3 (b)) for Y_2O_3 and Al_2O_3 respectively. However, the corresponding band gap values extracted by Tauc-Lorentz method were ~0.3 eV smaller than the values extracted from absorption coefficient method. This is in agreement with the reported data in [35], where it has been deduced that the band gap extracted from Tauc- or Cody-Lorentz 0.69 eV smaller than from the absorption coefficient method. This is due to the tail of absorption coefficient/extinction coefficient method was largely neglected, resulting in large band gap values and the largest band gap can be expected from absorption coefficient method as the curve having a larger concavity. The Tauc- and Cody-Lorentz methods lead to extract smaller band gaps due to the functional forms for these methods reduce the upward concavity of the curves and enhance the tails [35]. The band gap values for Y_2O_3 and Al_2O_3 were also extracted by the indirect band gap approximation of Tauc-Lorentz method as shown in the insets of Figures 3.3 (c) and (d). The extracted band gap values are summarised in the Table 3.1.

The band gap values extracted for both Y_2O_3 layers deposited on Ge at 400 °C and 225 °C were identical (5.7 $\pm$ 0.1 eV). This band gap value is in agreement with the reported values

for radio frequency sputtered Y_2O_3 (from SE [17] and XPS [36]). Similarly, the band gap values extracted for Y_2O_3/Si was 5.6 eV from SE [17] whereas a band gap value of 6.0 eV was reported for Y_2O_3/SiO_2 by XPS [37], while for single crystal a value of 6.1 eV was reported by VASE [38]. On the other hand, the band gap values extracted for Al_2O_3 ranged from 6.1 eV to 6.4 eV as stated in Table 3.1. It has been reported that the ALD deposited Al_2O_3 has a smaller density (3.1 - 3.3 g/cm^3) compared to sapphire and also a narrower band gap of 6.2 eV and 6.5 eV determined by photoconductivity measurements [39, 40] and XPS respectively [41]. Note that the band gap of sapphire was reported to be 8.8 eV [42, 43].

The Tauc coefficient was found to be 1145.3 $eV^{-1/2}cm^{-1/2}$ from the slope of Tauc plots in Figure 3.3 (c) for both Y_2O_3 samples. In some cases, the slopes of Tauc plots have been related to the degree of order in the structures. It has been argued that disorder generates defects leading to removal of states from the bands and the creation of band tails of localised states [44]. These band states are described by the Urbach exponential law determined by Eqn. 3.4,

$$\alpha = \alpha_0 \exp\left(\frac{E}{E_u}\right) \tag{3.4}$$

where α_0 is the constant and E_u is the Urbach energy. This law evaluates the exponential tail in the absorption coefficient which generally corresponds to localised band-tail states [44]. Moreover, if the scale of Y-axis changes to logarithmic, Urbach tail appears as a linear region below the absorption edge (see inset of Figure 3.3 (a)). A linear region below the absorption edge was evident for the Y_2O_3 structure deposited at 225 ^oC. Presumably, this could be ascribed to the Urbach tail; moreover the Urbach energy was found by considering the inverse of the slope of the logarithmic plot of the absorption coefficient. The Urbach energy was calculated to be 1.1 eV for this structure. It has been previously reported an Urbach energy of 1.4 eV and a Tauc coefficient of 1344 $eV^{-1/2}cm^{-1/2}$ for polycrystalline HfO_2 [44]. Furthermore, a decrease in band tailing for HfO_2 samples that were annealed in high temperature has been reported and this was correlated with defect reduction and temperature induced crystallisation [45, 46]. In this study, the Y_2O_3 sample processed at 400 ^oC demonstrated negligible band tailing below the absorption edge. It was also evident that the band edges of both Y_2O_3 structures were overlapped (Figures 3.3 (a) and (c)) indicating similar structures. This argument was supported by the XRD result shown in Figure 3.4 (a).

Both films seem to be polycrystalline as the XRD pattern (Figure 3.4 (a)) demonstrates polycrystalline phases for both Ge (004) and Y_2O_3 (631) planes. There were no Ge peaks when the 2θ equals to 59^o, hence it was concluded that the peak observed at 59^o represents Y_2O_3 (631). Furthermore, there are two XRD peaks at 51.9^o and 54^o that could ascribed to Y_2O_3

(600) and Y_2O_3 (611) as can be seen Figure 3.4 (b) [47]. However, the signal intensities are comparable to the background noise. This can be related to the shorter duration (~1 hour) used to perform the measurement. Nevertheless, the resolution of the XRD spectra in Figure 3.4 can be further enhanced by performing an overnight measurement.

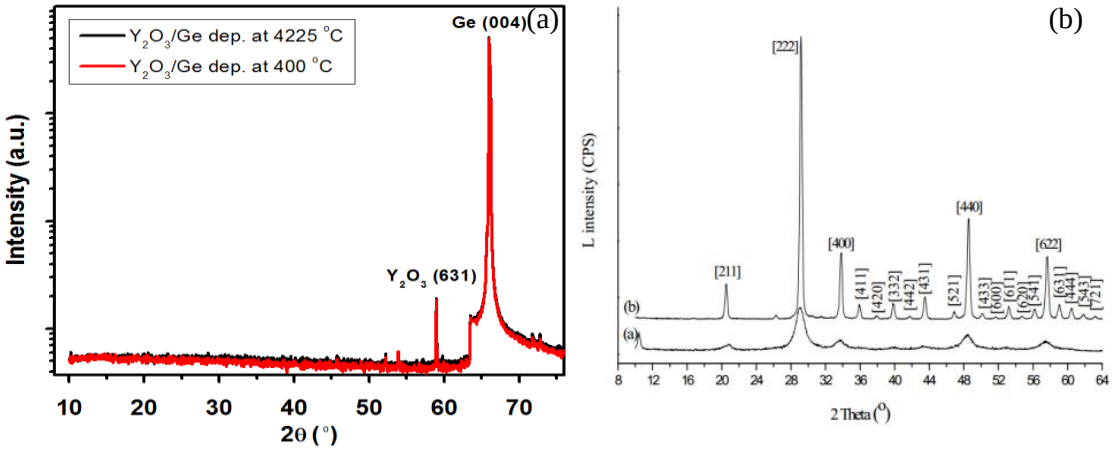

Figure 3.4: XRD spectra of (a) Y_2O_3/Ge deposited at two temperatures: 225 ºC and 400 ºC and (b) reference Y_2O_3 sample [47].

It was not possible to observe an Urbach tail for the Al_2O_3/Ge structure proving the sub-band gap absorption was negligible for Al_2O_3 (Figures 3.3 (b) and (d)). Al_2O_3 has been identified as a good O diffusion barrier that could potentially block the O vacancy diffusion [47]. This may lead to a sub-stoichiometric GeO_x free of interface states [47]. Li *et al.* have suggested a thin Al_2O_3 layer in the gate dielectric may result in a good passivation of the Ge surface [47, 48].

Further interfacial layer study was considered using XPS. The Ge 3d XPS core levels were identified as best to represent the chemistry at the interface due to their sufficient surface sensitivity and good resolution as a result of the narrow full width at half maximum (FWHM) [49]. The Ge 3d fittings were done using a doublet Voight functions for each peak as shown in Figures 3.5 (a) and (b). There was a high binding energy (BE) shoulder to the Ge 3d substrate peak for both Y_2O_3 samples but this was much more apparent for the Y_2O_3 sample deposited at 400 ºC (Figure 3.5 (a) bottom). It was also possible to note that the Ge 3d substrate intensity peak was smaller for the higher temperature deposited Y_2O_3 sample. This was due to the thicker Y_2O_3, 7.9 nm in comparison to 6.3 nm for sample deposited at 225 ºC (see Table 3.1). The interfacial layer formation can be assessed by analysing the chemical shifts of binding energy with respect to main Ge $3d_{3/2}$ and Ge $3d_{5/2}$ peaks. It was found in the literature that the Y-Ge-O bonding configuration results in a chemical shift between +2.2 eV to +2.5 eV due to a second nearest-neighbour effect [50]. Nonetheless the shift that was anticipated for

O-Ge-O bonding configuration was +3.4 eV with respect to the Ge 3d substrate peaks [51]. The Ge 3d spectra shown in Figure 3.5 (a) shows strong evidence of $YGeO_x$ bonding for both Y_2O_3 structures with a shift of 2.5 eV to 2.7 eV. Moreover, it was possible to observe GeO_x for the Y_2O_3 structure deposited at 225 ^oC (Figure 3.5 (a) top) with a shift of 1.1 eV (in line with ref. 52). There was evidence of GeO_2 instead of GeO_x for the Y_2O_3 structure deposited at 400 ^oC (Figure 3.5 (a) bottom).

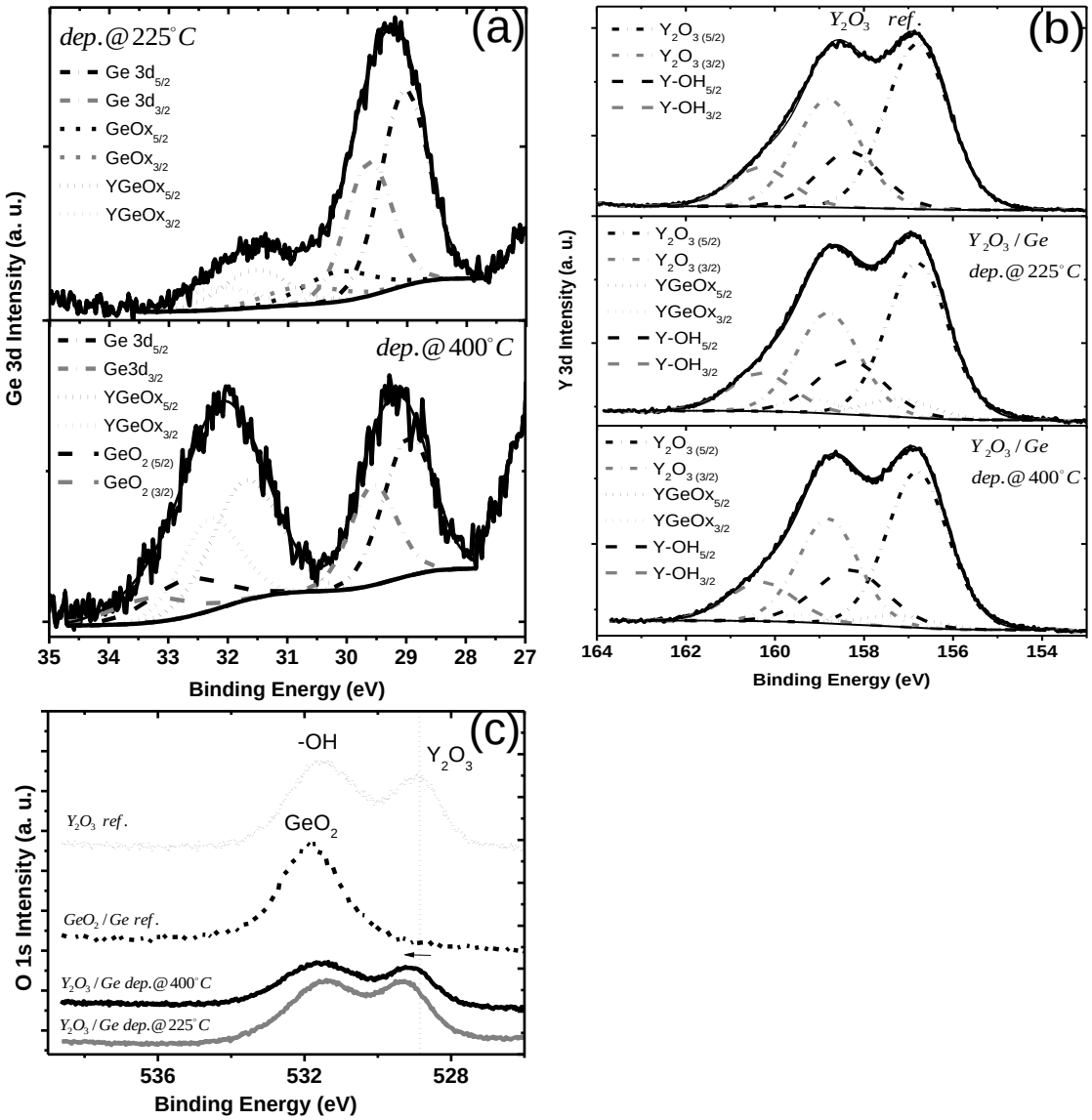

Figure 3.5 (a) Ge 3d, (b) Y 3d and (c) O 1s XPS core levels for Y_2O_3/Ge samples deposited at 225 ^oC and 400 ^oC with GeO_2/Ge and Y_2O_3 foil as reference samples.

The Y 3d spectra for the Y_2O_3 reference sample and Y_2O_3/Ge samples are shown in Figure 3.5 (b). The existence of Y_2O_3 was verified for Y_2O_3/Ge samples by referring to the top graph in Figure 3.5 (b) (oxidized Y foil). It was possible to find the corresponding binding energy values for $YGeO_x$ post analysing the known peaks which were Y-OH and Y_2O_3. The presence of $YGeO_x$ was evident in both Y_2O_3 structures as shown in Figure 3.5 (b) (middle and bottom

graphs). $YGeO_x$ was observed in Ge 3d for both 225 °C and 400 °C samples, hence the $YGeO_x$ sub-peaks were used while analysing the Y 3d spectra for both samples. Furthermore, the residual standard deviation was 0.88 ± 0.03 for the fittings shown in Figure 3.5 (b). However the residual standard deviation was increased to 2.23 if $YGeO_x$ peaks were disregarded. From Figure 3.5 (c), it can be seen that the O 1s spectra for Y_2O_3/Ge were shifted towards higher binding energy values compared to the binding energy values of Y_2O_3 reference, demonstrating strong evidence of charge transfer and formation of $YGeO_x$ at the interface of Y_2O_3/Ge.

Figure 3.6 shows the effect of temperature on the interfacial layer characteristics of Y_2O_3/Ge samples by performing *in situ* annealing considering the temperature range of 425 °C to 750 °C with a step of 25 °C. The formation of $YGeO_x$ was more pronounced with the increase in temperature for the Y_2O_3/Ge structure deposited at 400 °C. Moreover the absence of a GeO_2 interfacial layer for the temperatures above 525 °C was observed, indicating that $YGeO_x$ was the only interfacial layer for the structure deposited at 400 °C (Figure 3.7 (b)). In contrast, the Y_2O_3/Ge sample deposited at 225 °C demonstrated a less pronounced interfacial layer shoulder and the presence of GeO_x was evident at all temperatures (Figures 3.6 (a) and 3.7 (a)).

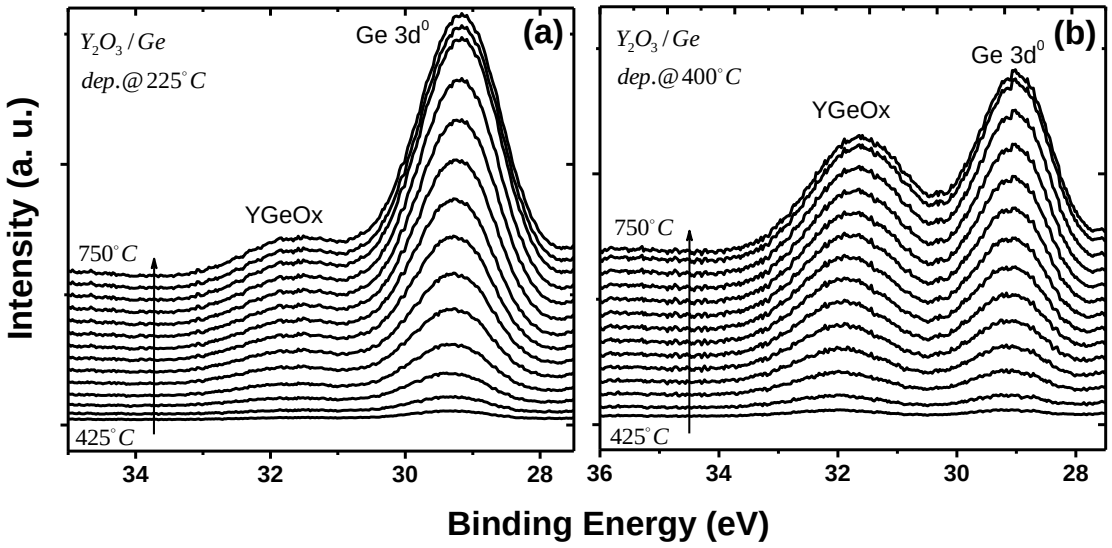

Figure 3.6: Ge 3d core levels for Y_2O_3/Ge samples deposited at (a) 225 °C and (b) 400 °C after *in situ* anneal from 450 °C to 750 °C, in steps of 25 °C

The valence band offset (VBO) was extracted by Kraut's method [53]. The corresponding binding energy values for the core levels and the valence band maxima for Ge substrate; bulk Y_2O_3 and interfacial Y_2O_3/Ge were found in order to estimate the VBO. The estimated VBO using this method was 2.68 $\pm$ 0.02 eV. Furthermore, it was possible to extract the conduction band offset (CBO) as 3.09 eV using,

$$CBO = E_g - VBO \tag{3.5}$$

where E_g is the band gap. In this scenario 5.77 eV was used as the band gap of Y_2O_3.

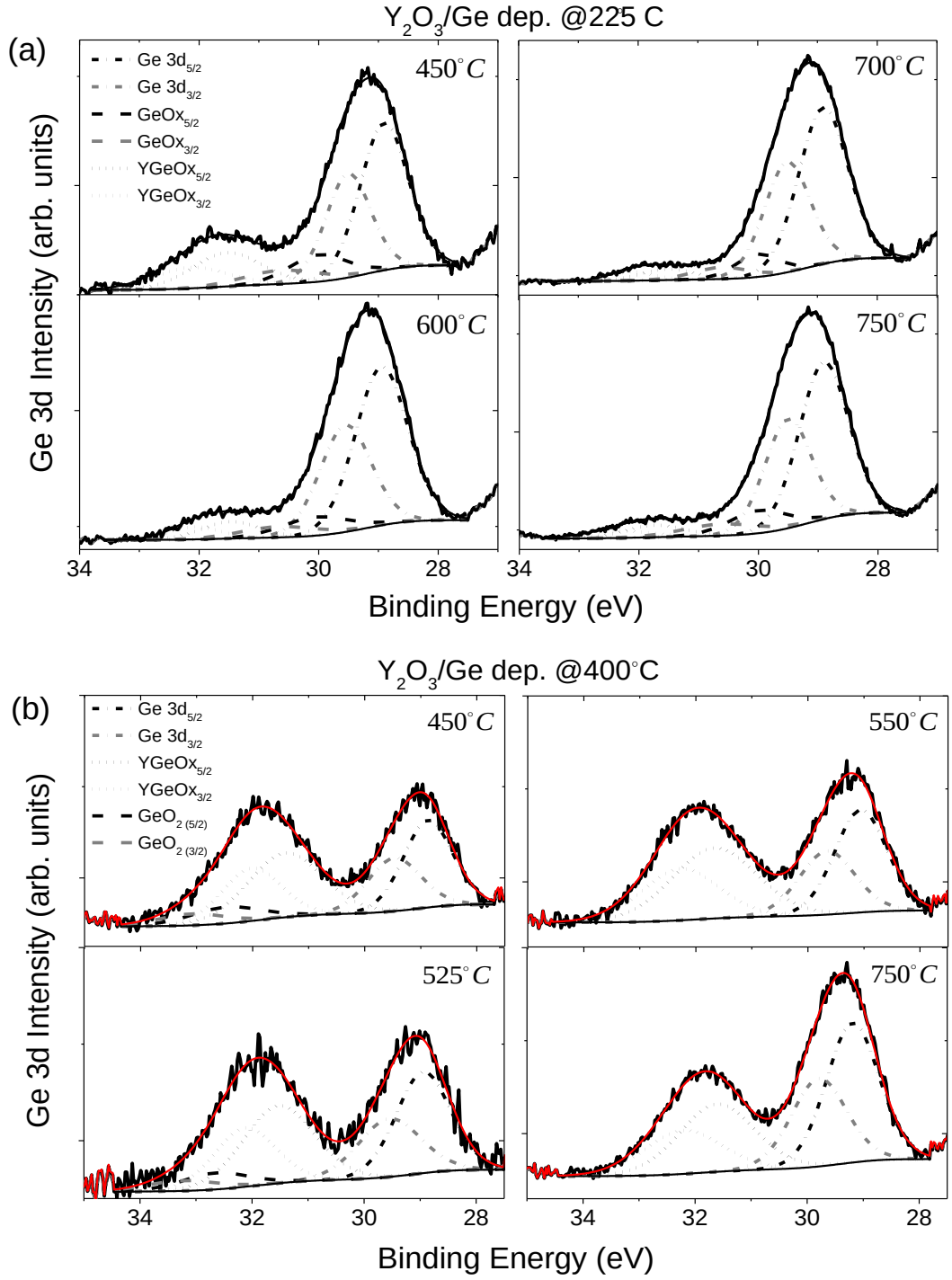

Figure 3.7: Ge 3d XPS core level fitting after in-situ anneal for two different Y_2O_3/Ge gate stacks deposited at: (a) 225°C, and (b) 400°C.

The GeO_2/Ge interface with and without the Al_2O_3 capping layer was investigated by performing XPS analysis. The Ge 3d peak was explored to study the effect of the Al_2O_3 capping layer and this was compared to the reference GeO_2/Ge structure. Figure 3.8 (a) shows the presence of Ge 4+ for the 4.4 nm GeO_2/Ge structure (without the capping layer). After the deposition of the Al_2O_3 capping layer on 3.2 nm GeO_2/Ge, it was observed that the peak related

to the interfacial layer has been shifted towards a lower binding energy (Figure 3.8 (b)). This could be ascribed to the formation of $AlGeO_x$ at the Al_2O_3/GeO_2 interface. The presence of GeO_x was also evident at the interface of this structure as shown in Figure 3.8 (b). However, for the thicker 7.2 nm GeO_2 layer with the Al_2O_3 capping layer, there was only a peak related to $AlGeO_x$ (Figure 3.8 (c)). Moreover, in the case of Al_2O_3/Ge structure, no evidence related to the interfacial layer was observed (Figure 3.8 (d)). The Al 2p core level peak corresponding to the Al_2O_3/Ge structure has not demonstrated a clear change, indicating that there is no noticeable chemical reaction in the Al_2O_3 capping layer. It can be inferred that Al_2O_3 acts as a barrier layer without causing any reaction with the Ge substrate. Nevertheless, the peaks of the core levels Al 2p and O 1s corresponding to Al_2O_3/GeO_2/Ge structures have shifted towards larger binding energies (Figures 3.9 (a) and (b)). This suggests the formation of $AlGeO_x$ at the Al_2O_3/GeO_2 interface.

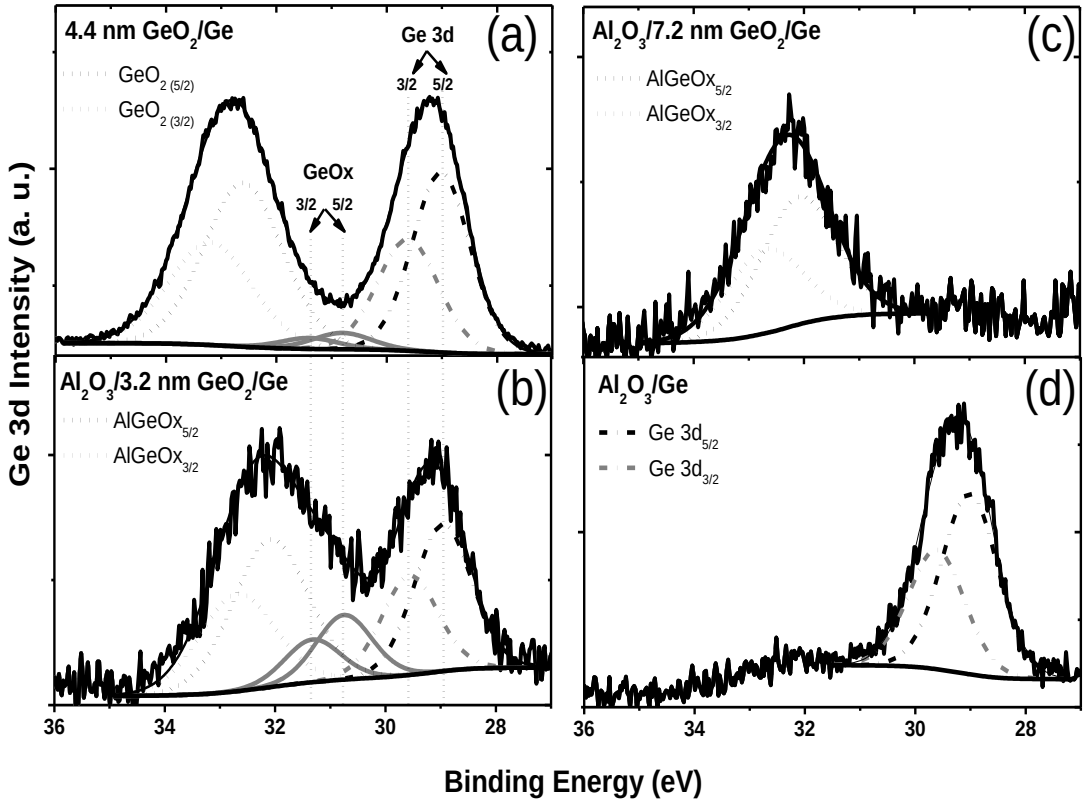

Figure 3.8: Ge 3d core level fitting for the (a) GeO_2/Ge, (b) Al_2O_3/3.2 nm GeO_2/Ge, (c) Al_2O_3/7.2 nm GeO_2/Ge and (d) Al_2O_3/Ge samples.

Based on the above observations $AlGeO_x$ at the interface of Al_2O_3/GeO_2 is present as a result of the Ge in-diffusion through the GeO_2 into Al_2O_3 [13]. The incorporation of Al into the GeO_2 matrix forms only Al-Ge-O bonds without creating any defect states at the interface [54], therefore the $AlGeO_x$ interlayer may not degrade the quality of the interface [55, 22, 23, 56].

The observations made by VASE and XPS were in agreement with the electrical characterisation performed on 225 ^oC and 400 ^oC deposited Y_2O_3/Ge structures. The high

frequency capacitance voltage measurements performed on these structures are shown in Figure 3.10. An equivalent oxide thickness of 3 nm was extracted using the Eqn. 1.1, 1.3 and 1.4. The relative dielectric constant of 15 was assumed for Y_2O_3 while performing the EOT calculation. As can be seen in Figure 3.10 (a), the CV curves of the 225 ^oC deposited Y_2O_3 structure demonstrated high frequency dispersion with large humps in the weak inversion regime. However, a significant improvement was noticed for the structure deposited at 400 ^oC as shown in Figure 3.10 (b). This could be ascribed to elimination of GeO_x interfacial layer in the 400 ^oC deposited Y_2O_3 sample and also to the formation of $YGeO_x$ interfacial layer.

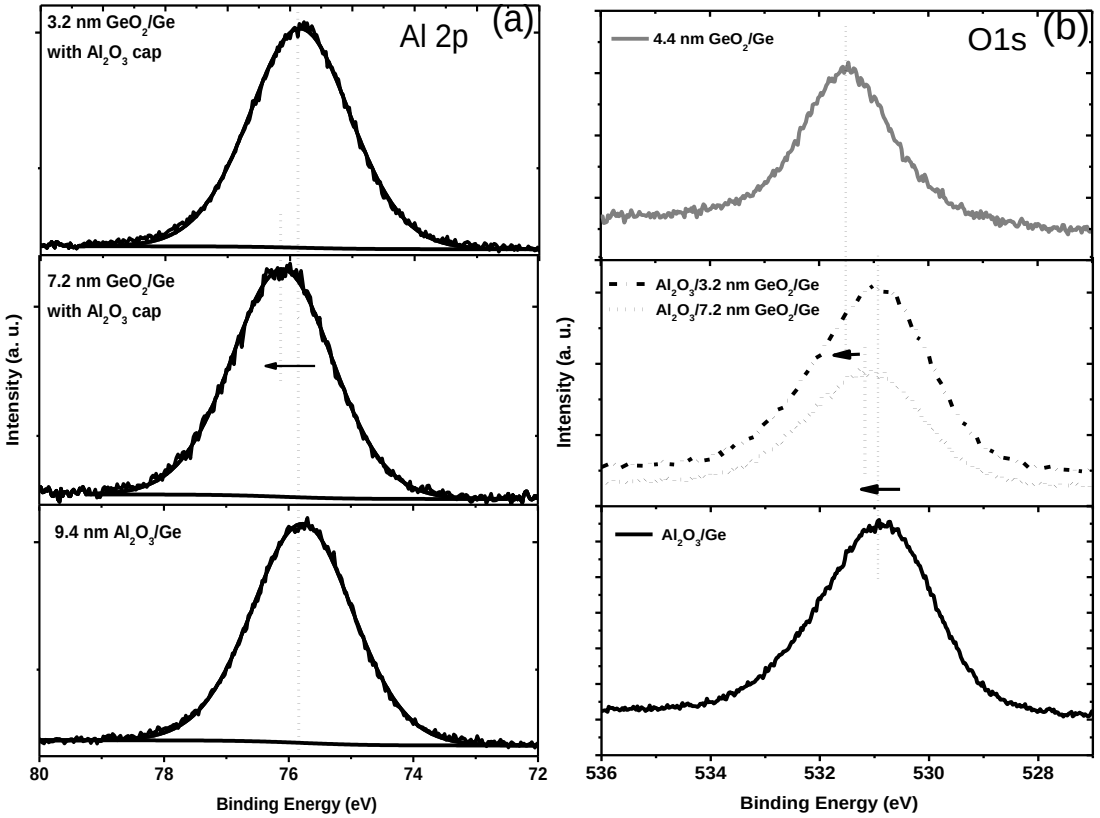

Figure 3.9: (a) Al 2p and (b) O 1s XPS core level spectra for GeO_2/Ge (with and without Al_2O_3 capping layer) and Al_2O_3/Ge samples.

It was also evident that a leakage current for the 400 ^oC deposited Y_2O_3 sample was significantly smaller in contrast to the 225 ^oC deposited Y_2O_3 sample as illustrated in Figure 3.11. The current density for the 225 ^oC deposited Y_2O_3 structure was in the order of 10^{-3} A/cm^2 at 1 V (Figure 3.11 (a)) whereas the current density of the 400 ^oC deposited Y_2O_3 structure was in the order of 10^{-6} A/cm^2 corresponds to a current in the order of 10^{-10} A at the same bias (Figure 3.11 (b)). The device area was $7.1x10^{-4}$ cm^2. The analysis carried out using VASE suggests that the Y_2O_3/Ge structure deposited at 400 ^oC has a defect free interface, in contrast to the 225 ^oC deposited structure. The pronounced sub-band gap absorption region which was evident for the 225 ^oC deposited Y_2O_3 structure can be attributed to a reported

neutral O vacancy coordinated with two Ge ions at 5.06 V and/or a Ge 2+ coordinated with O defects at 5.16 eV. The presence of GeO_x was confirmed after analysing the XPS Ge 3d core level peak for the 225 °C deposited Y_2O_3/Ge sample. Moreover, the sub-band gap absorption and GeO_x was not evident in the 400 °C deposited Y_2O_3 sample indicating a good interface by VASE and XPS, which was further supported by well-behaved CV characteristics and low leakage currents.

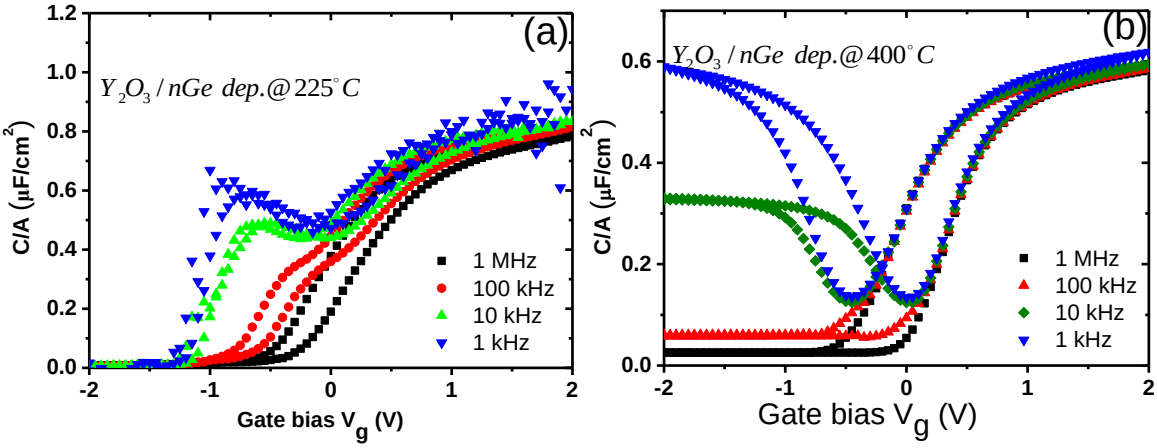

Figure 3.10: High frequency capacitance voltage characteristics for 10 nm (nominal) Y_2O_3/n-Ge gate stacks deposited at (a) 225 °C and (b) 400 °C.

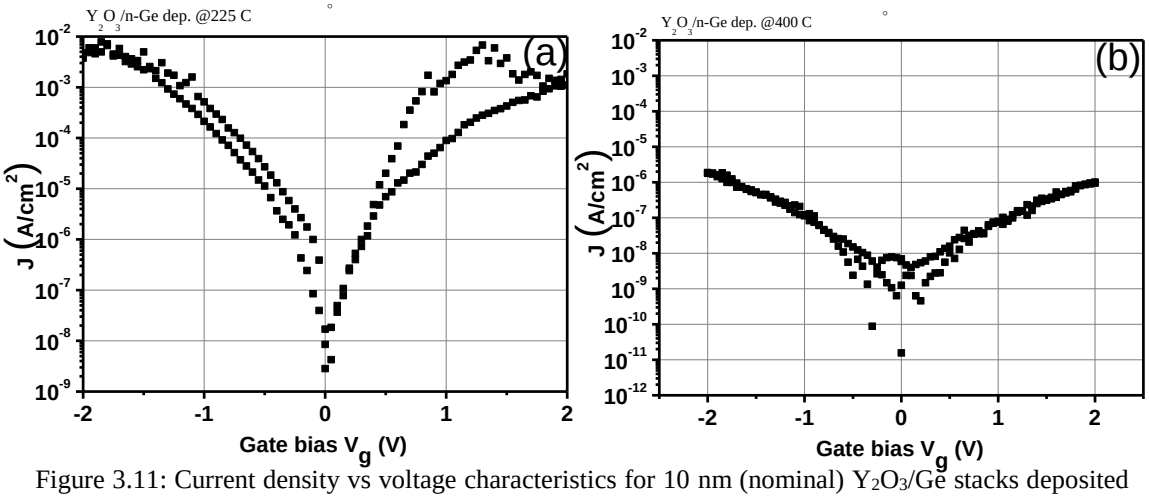

Figure 3.11: Current density vs voltage characteristics for 10 nm (nominal) Y_2O_3/Ge stacks deposited at (a) 225 °C and (b) 400 °C. The device area = 7.1×10^{-4} cm^2.

3.2 Tm_2O_3/Ge band line-up study

It has been reported that the rare-earth thulium oxide (Tm_2O_3) can be considered as the main gate dielectric [57] and also as a capping layer [58] on Si. It has also been observed that the reactivity between Tm_2O_3 and Si is minimal [59] even when the Tm_2O_3 is annealed in an ambient air that contains O [57, 60]. Nonetheless, not much has been reported on Tm_2O_3/Ge structures, in terms of either structural or electrical properties. Therefore a series of experiments were carried out to investigate the interfacial properties of Tm_2O_3/Ge structures in this work. The 5 nm and 10 nm (nominal) thick Tm_2O_3 structures were prepared by atomic layer deposition (ALD) on 35 nm p-Ge epitaxial layers. These stacks were deposited on Si

(100). Two more reference 5 nm and 10 nm GeO_2/Ge samples were prepared on the 35 nm n-Ge epitaxial layer/Si (100). This was done by a thermal oxidation process at 450 ^oC under 1 atm O_2. It was mandatory to clean the Ge surface in a solution containing 0.5% HF, 1% Isopropanol and H_2O to minimise the native Ge oxide layer. The Tm_2O_3 was deposited using the Tri(cyclopentadienyl)thulium, heated to 140 ^oC and water vapour as precursor gasses [61]. Moreover, after the oxide deposition a post deposition annealing treatment was used in order to investigate the post-processing temperatures of 350 ^oC to 450 ^oC and annealing atmosphere of O_2 and N_2/H_2 (10% H_2 in N_2) in comparison to the as-deposited samples.

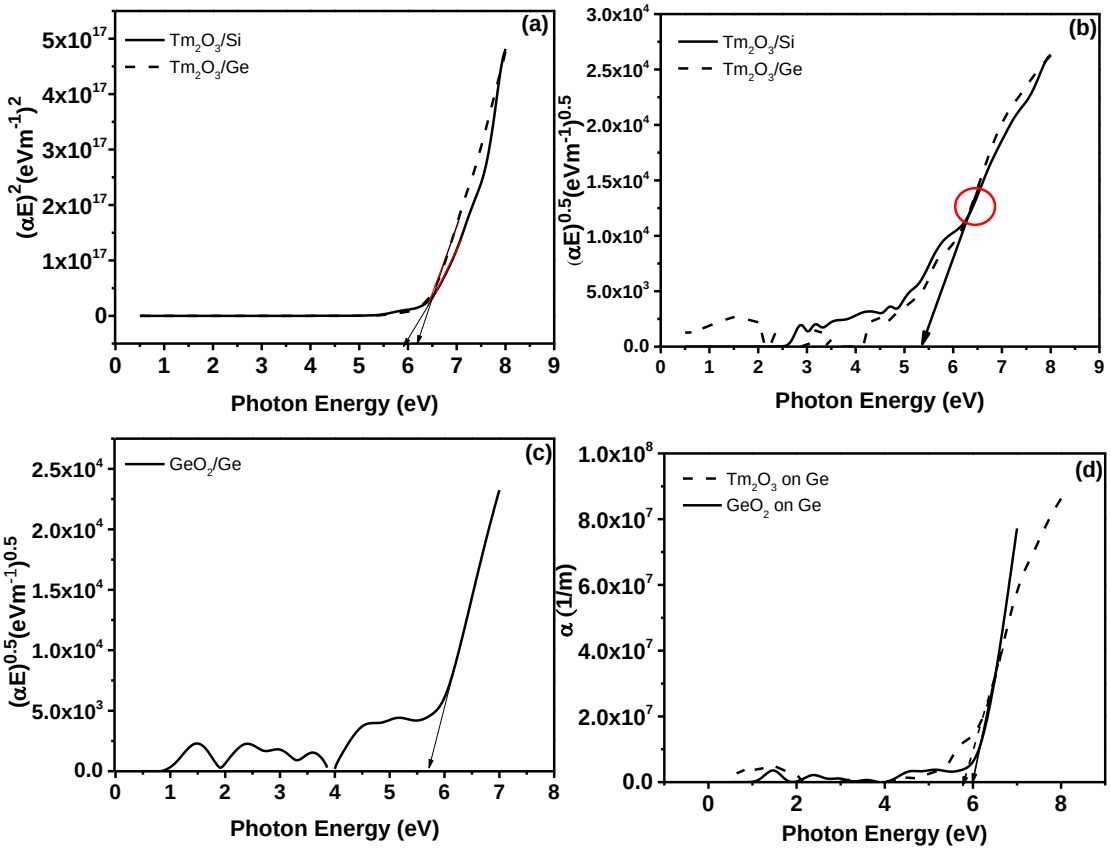

Figure 3.12: Tauc plots for Tm_2O_3/Si, Tm_2O_3/Ge and GeO_2/Ge samples assuming (a) direct (b)-(c) indirect band gap approximation and (d) absorption coefficient of Tm_2O_3/Ge and GeO_2/Ge samples.

The band gap of Tm_2O_3 was measured by performing VASE on the 10 nm Tm_2O_3/Ge sample. A spectral range from 0.5 eV to 8.8 eV and the angles of incidence of 55^0 to 75^0 were used. The modelling process was done following the same steps as explained before. The thicknesses of 10 nm (nominal) Tm_2O_3, 35 nm (nominal) Ge and native oxide were extracted to be 10.4 nm, 31.9 nm and 1.4 nm respectively. As can be seen in Figure 3.12, the absorption coefficient and Tauc plots for both direct and indirect band gap approximations were plotted against photon energy. The band gap values extracted on Tm_2O_3 deposited on both Ge and Si (Figure 3.12 (a)) were not identical if the direct band gap approximation of Tauc analysis was considered. However, the band gap values extracted considering the indirect band gap relationship of Tauc analysis were identical and as circled in Figure 3.12 (b), the absorption

edges overlapped for both Tm_2O_3/Si and Tm_2O_3/Ge. Therefore it was inferred the indirect band gap nature of Tm_2O_3, with value of 5.3 $\pm$ 0.1 eV. This extracted band gap value is in agreement with the theoretically predicted value of Iwai *et al* [62]; a value of 5.76 eV has been reported using optical absorbance [63] though the direct band gap relationship for Tauc analysis was considered. The band gap of 5.65 $\pm$ 0.1 eV for GeO_2 was extracted using Figure 3.12 (c). The band gap values assessed via absorption coefficient method for Tm_2O_3 and GeO_2 were ~5.77 eV and 5.95 eV respectively (Figure 3.12 (d)). This is in agreement with [35] since the band gap extracted from Tauc- or Cody-Lorentz methods could be 0.69 eV smaller compared to the value estimated using absorption coefficient method.

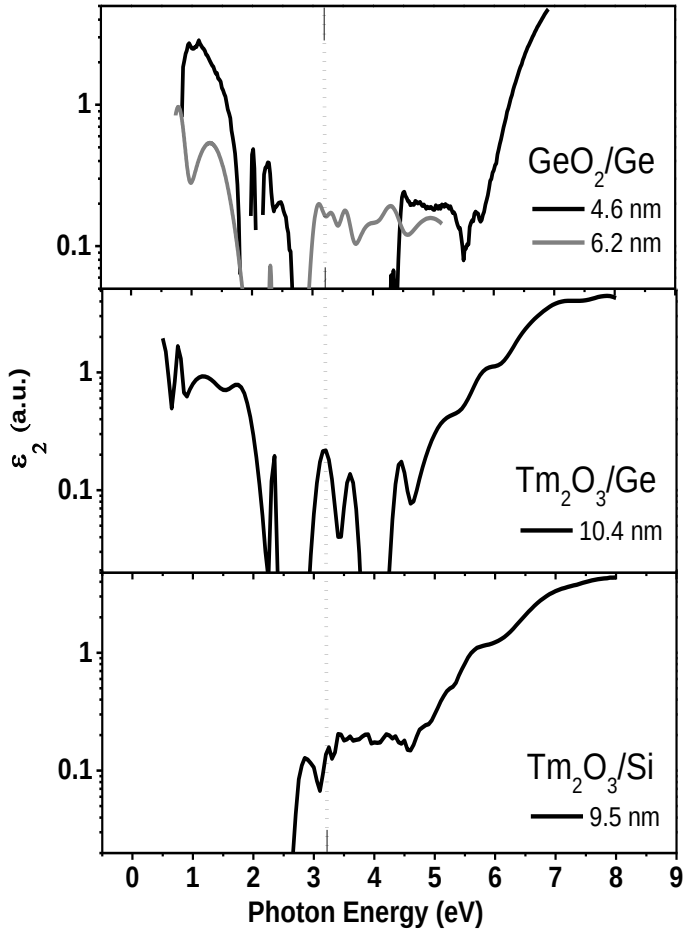

Figure 3.13: Logarithmic scale plots of ε_2 for Tm_2O_3 deposited on Si and Ge, with GeO_2/Ge as a reference spectrum.

The sub-band gap absorption was analysed considering the imaginary part of the dielectric constant for and GeO_2/Ge, Tm_2O_3/Ge and Tm_2O_3/Si as depicted in Figure 3.13. This graph was plotted on a log scale in order to observe the absorption peaks more clearly. The absorption peaks at the photon energies of 2.9 eV, 3.2 eV, 3.4 eV and 4.25 eV were noticed below the absorption edge for Tm_2O_3/Si structure. The peaks at 3.4 eV and 4.25 eV can be related to the critical points of Si, whereas a peak at 2.9 eV has been found as intrinsic to the

interface and related to the optical transitions associated with negatively charged O vacancies in SiO_2 [64, 65]. Referring to Figure 3.13, the peak at 3.2 eV could be related to the bulk Tm_2O_3 as this was observed in both Tm_2O_3/Si and Tm_2O_3/Ge. The mutual absorption peaks evident for both Tm_2O_3/Ge and GeO_2/Ge at 2.4 eV, 3.6 eV and 4.4 eV due to Ge. It was possible to observe band edge tailing for all the structures. The absorption peak at 5.1 eV for the GeO_2/Ge structure can be ascribed to neutral O vacancies or Ge 2+ in O deficient GeO_2.

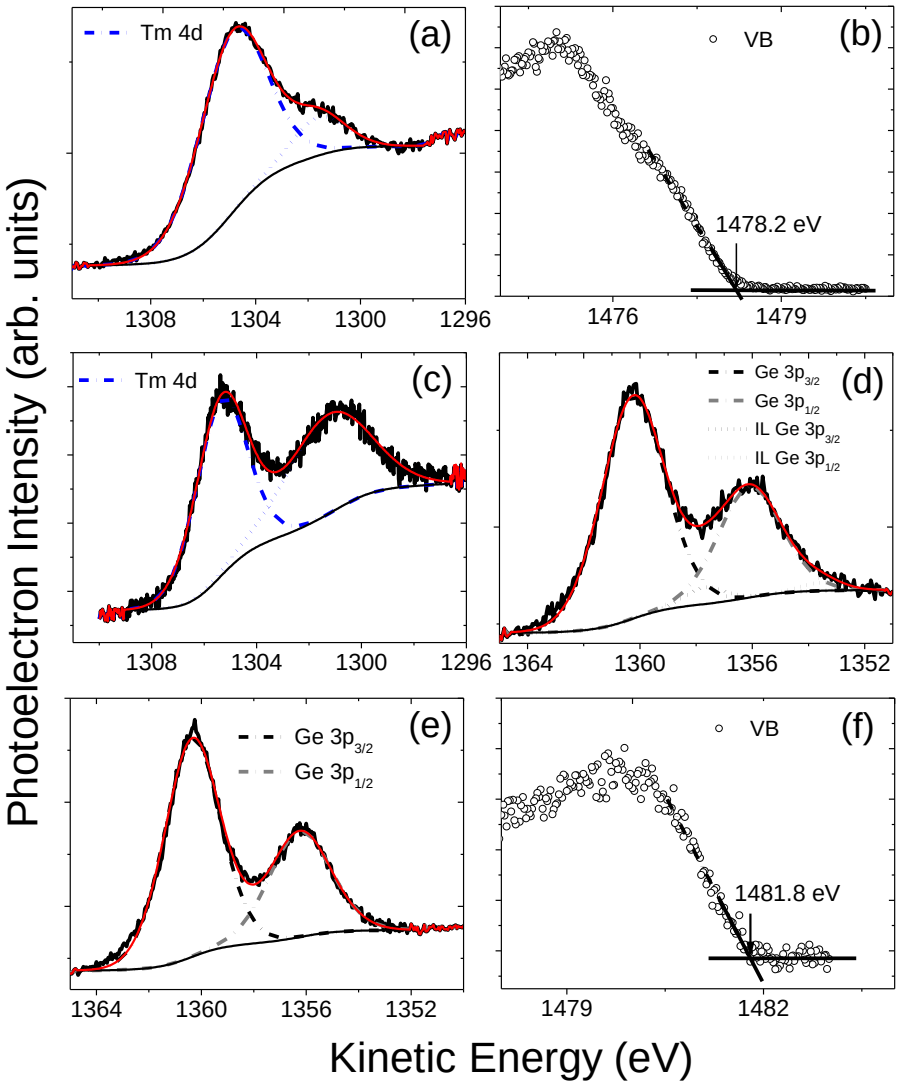

Figure 3.14: (a) Tm 4d core level fitting, (b) valence band spectra for bulk Tm_2O_3/Ge, (c) Tm 4d core level fitting, (d) Ge 3p core level fitting for interfacial Tm_2O_3/Ge and (e) Ge 3p core level fitting, (f) Valence band spectra for Ge substrate.

These observations can be further supported by performing XPS analysis. The XPS spectra of Ge 3p for bulk Tm_2O_3/Ge, interface Tm_2O_3/Ge and Ge substrate are illustrated in Figure 3.14. The Tm 4d core level for bulk Tm_2O_3/Ge is shown in Figure 3.14 (a). The extracted VBM for bulk Tm_2O_3 was 1472.2 eV (kinetic energy) from Figure 3.14 (b). The de-convolution of Ge 3d core level peaks were not straight forward due to the presence of neighbouring O 2s and Tm 5p. Therefore as can be seen in Figure 3.12 (d), Ge 3p core level was considered in order

to analyse the interface of Tm_2O_3/Ge. There was no evidence of GeO_x at the interface of Tm_2O_3/Ge as shown in Figure 3.14 (d), however there was evidence of a sub-nanometer level germanate (Tm-Ge-O).

The polycrystalline nature of Tm_2O_3 deposited on Si and Ge can be directly observed from high resolution transmission electron microscopy (HRTEM) in Figures 3.15 (a) and (b) respectively. In Figure 3.15 (b), it can be seen that a thin amorphous interfacial layer at the interface of Tm_2O_3/Si. However, for the Tm_2O_3/Ge sample a direct and a sharp interface between the Ge epitaxial layer and Tm_2O_3 can be observed from Figure 3.15 (a). This may represent a chemically modified interface (possibly germanate) with a thickness < 1 nm.

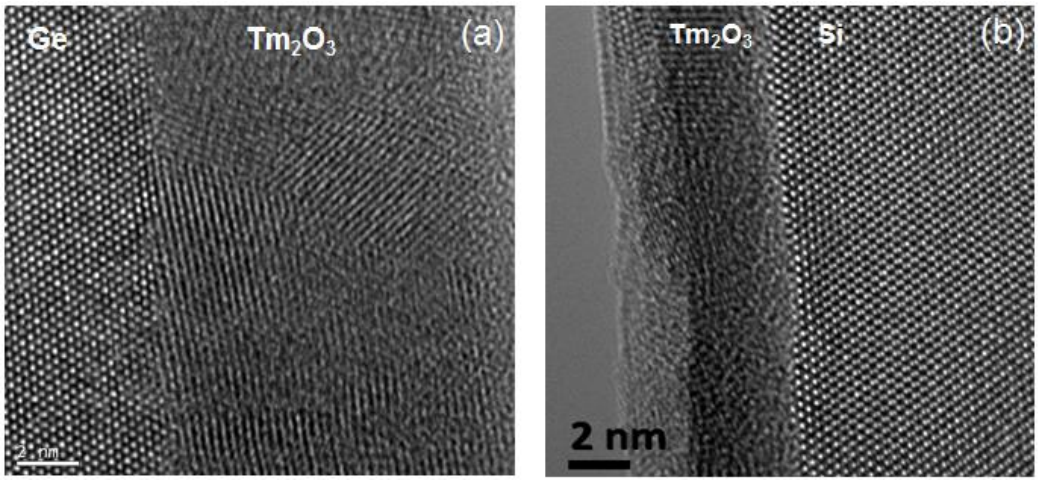

Figure 3.15: HRTEM images for (a) Tm_2O_3/Ge and (b) Tm_2O_3/Si.

The valence band offset at Tm_2O_3/Ge interface was found to be 3 ± 0.05 eV using Kraut's method. Then the conduction band offset was calculated after considering the band gap value of Tm_2O_3 and Ge. Moreover, the band gap of Tm_2O_3 was found to be ~5.3 eV and 5.77 eV by Tauc method and absorption coefficient method. A conduction band offset of ~1.7 eV was estimated if the smallest value of the extracted band gap considered. The valence band offset extracted for the GeO_2/Ge structure was 3.55 eV. This gives a conduction band offset of 1.73 eV if a band gap of ~ 6 eV from absorption coefficient method was used for GeO_2. However, the conduction band offset of 1.28 eV was estimated for the band gap values extracted by Tauc-Lorentz plots (5.65 eV). The presence of GeO_x at the GeO_2/Ge interface was evident from both VASE and XPS. However, the interface of Tm_2O_3/Ge was GeO_x free.

3.3 Discussion and conclusion

The primary motive of this chapter was to perform a comprehensive study on the interface of Ge and high-k dielectrics. This was achieved by performing variable angle spectroscopic ellipsometry on the structures: Y_2O_3/Ge (deposited at two different temperatures), Al_2O_3/Ge,

GeO_2/Ge and Tm_2O_3/Ge. The thicknesses and the real and imaginary parts of the complex dielectric function were extracted. The real and imaginary parts of the complex dielectric function were converted to refraction index and extinction coefficient in order to extract the absorption coefficient. Next, the Tauc analysis was performed for all the structures considering both direct and indirect band gap approximations. These graphs were used to extract the band gap and also to analyse sub-band gap absorption features of the above stated structures.

There was a pronounced sub-band gap absorption for the Y_2O_3/Ge structure deposited at 225 ^oC in the spectral range of ~4.5 eV – 5.5 eV. This was ascribed to a reported neutral O vacancy coordinated with two Ge ions and/or a Ge 2+ coordinated with two O defects suggesting the presence of GeO_x. However, such absorption below the absorption edge for the Y_2O_3/Ge structure deposited at 400 ^oC was not visible. These observations were in agreement with the XPS analysis performed on these structures. It has been found that the 400 ^oC deposited Y_2O_3/Ge sample shown no evidence of GeO_2 after annealing above 525 ^oC indicating that $YGeO_x$ was the only interfacial layer at the Y_2O_3/Ge interface. An Urbach tail was evident for the Y_2O_3/Ge structure deposited at 225 ^oC, but this was less apparent for the 400 ^oC deposited Y_2O_3/Ge structure. It was argued that a decrease in band tailing can be expected due to the defect reduction and temperature induced crystallization. Therefore it was assumed that Y_2O_3 has a polycrystalline structure; moreover this has been confirmed by XRD results. The band diagram of the Y_2O_3/Ge structure was derived using the VBO estimated by XPS and band gap estimated by VASE. The VBO and CBO were extracted to be 2.68 eV and 2.35 eV respectively and the band gap of Y_2O_3 was found to be 5.7 eV. It was evident that the Y_2O_3/Ge structure deposited at 400 ^oC demonstrated low leakage currents and also improved CV characteristics in contrast to the structure that was deposited at 225 ^oC.

The band gap value of Al_2O_3 was extracted to be in the range of 6.1 eV to 6.4 eV from the Tauc-Lorentz and absorption coefficient methods. It was not possible to observe an Urbach tail for the Al_2O_3/Ge structure, indicating negligible sub-band gap absorption. This was further proven from XPS analysis as there was no apparent interfacial layer for this structure. It is possible to conclude that Al_2O_3 could be used as a capping layer on Ge to passivate the surface.

Finally the optical properties of GeO_2/Ge and Tm_2O_3/Ge were investigated. The band gap values extracted for GeO_2 were 5.65 eV and 5.95 eV from Tauc-Lorentz and absorption coefficient methods respectively. The band gap values extracted for Tm_2O_3 were 5.3 eV and 5.77 eV for Tauc-Lorentz and absorption coefficient methods respectively. The presence of GeO_x was evident only in the interface of GeO_2/Ge. This was confirmed by both sub-band gap absorption peak analysis by VASE and from de-convolution of the XPS Ge 3d spectra. An

absorbance at 3.2 eV was ascribed to Tm_2O_3 as this was mutually observed for both Tm_2O_3/Si and Tm_2O_3/Ge structures. The Urbach tailing of Tm_2O_3 suggested the polycrystalline nature of the structure. Large conduction band offsets of 1.7 eV and 1.73 eV, and a large valence band offsets of 3 eV and 3.55 eV were evident for both Tm_2O_3/Ge and GeO_2/Ge structures creating a large barrier for electrons and holes. The presence of GeO_x was not evident at the interface of Tm_2O_3/Ge. Therefore Tm_2O_3 can be recognised as a potential alternative route to Al_2O_3 to passivate the Ge surface for future Ge-based scaled CMOS devices.

References

[1] G.E. Moore, "Cramming more components onto integrated circuits", Electronics, 38(8):4, 114 (1965)

[2] H.R. Huff, D.C. Gilmer, "High dielectric constant materials: VLSI MOSFET applications", Springer, 2005, Ch. 3, sec 3.3.3, 85

[3] H.R. Huff, D.C. Gilmer, "High dielectric constant materials: VLSI MOSFET applications", Springer, 2005, Ch. 3, sec 3.1.2, 45

[4] S. M. Sze, Kwok K. Ng., "Tunnel device in physics of semiconductor devices", 3rd edition. John Willey & Sons, 2007, Ch. 6, sec 6.5.2, 340

[5] H. Li, L. Lin, J. Robertson, "Identifying a suitable passivation route for Ge interfaces", Appl. Phys. Lett., 101, 052903 (2012)

[6] C. Castelerio, "Electrical and physical characterization of Ge devices", PhD thesis University of Warwick, (2014)

[7] S. Takagi, R. Zhang, M. Takenaka, "Ge gate stacks based on Ge oxide interfacial layers and the impact on MOS device properties", Microelec. Eng., 109, 389 (2013)

[8] A. Toriumi, C.H. Lee, S.K. Wang, T. Tabata, M. Yoshida, D.D. Zhao, T. Nishimura, K. Kita, K. Nagashio, "Material potential and scalability challenges of germanium CMOS", Proc. IEEE IEDM, 646 (2011)

[9] M. Caymax, G. Eneman, F. Bellenger, C. Merckling, A. Delabie, G. Wang, R. Loo, E. Simoen, J. Mitard, B. De Jaeger, G. Hellings, K. De Meyer, M. Meuris, M. Heyns, "Germanium for advanced CMOS anno 2009: a SWOT analysis", Proc. IEEE IEDM, 461 (2009)

[10] D. Reinking, M. Kammler, N. Hoffinann, M. Homvon Hoegen, K.R. Hofinann, "Ge p-MOSFETs compatible with Si CMOS-technology", Proc. Solid-state Dev. Res., 300 (1999)

[11] T. Takahashi, T. Nishimura, L. Chen, S. Sakata, K. Kita, A. Toriumi, "Proof of Ge-interfacing concepts for metal/high-k/Ge CMOS - Ge-intimate material selection and interface conscious process flow-", Proc. IEEE IEDM, 697 (2007)

[12] C. H. Lee, C. Lu, T. Tabata, W. F. Zhang, T. Nishimura, K. Nagashio, A. Toriumi, "Oxygen potential engineering of interfacial layer for deep sub-nm EOT high-k gate stacks on Ge", Proc. IEEE IEDM, 40 (2013)

[13] A. Dimoulas, D.P. Brunco, S. Ferrari, J.W. Seo, Y. Panayiotatos, A. Sotiropoulos, T. Conard, M. Caymax, S. Spiga, M. Fanciulli, Ch. Dieker, E.K. Evangelou, S. Galata, M. Houssa, M.M. Heyns, "Interface engineering for Ge metal-oxide–semiconductor devices", Thin Solid Films, 515, 6337 (2007)

[14] T. Tabata, C. H. Lee, K. Kita, A. Toriumi, "Impact of high pressure O_2 annealing on amorphous $LaLuO_3$/Ge MIS capacitors", ECS Trans., 16(5), 479 (2008)

[15] J.J. Gu, Y.Q. Liu, M. Xu, G.K. Celler, R.G. Gordon, P.D. Ye, '"High performance atomic-layer-deposited LaLuO3/Ge-on-insulator p-channel metal-oxide semiconductor field-effect transistor with thermally grown GeO2 as interfacial passivation layer", Appl. Phys. Lett. 97, 012106 (2010)

[16] K. Kita, K. Kyuno, A. Toriumi, "Growth mechanism difference of sputtered HfO_2 on Ge and on Si", Appl. Phys. Lett., 85, 52 (2004)

[17] Y. Zhao, K. Kita, K. Kyuno, A. Toriumi, "Band gap enhancement and electrical properties of La_2O_3 films doped with Y_2O_3 as high- k gate insulators", Appl. Phys. Lett., 94, 042901 (2009)

[18] T. Nishimura, C.H. Lee, S.K. Wang, T. Tabata, K. Kita, K. Nagashio, and A. Toriumi, "Electoron mobility in high-k Ge MISFETs goes up to higher", Proc. IEEE Symp. on VLSI Tech., 209 (2010)

[19] C. X. Li, P. T. Laia, "Wide-bandgap high-k Y_2O_3 as passivating interlayer for enhancing the electrical properties and high-field reliability of n-Ge metal-oxide semiconductor capacitors with high-k HfTiO gate dielectric", Appl. Phys. Lett., 95, 022910 (2009)

[20] Y-H. Wu, M.L. Wu, R.J. Lyu, J.R. Wu, L.L. Chen, C.C. Lin, "Crystalline ZrO_2-gated Ge metal-oxide-semiconductor capacitors fabricated on Si substrate with Y_2O_3 as passivation layer", Appl. Phys. Lett., 98, 203502 (2011)

[21] R. Zhang, T. Iwasaki, N. Taoka, M. Takenaka, S. Takagi, "High mobility Ge pMOSFETs with ~ 1nm thin EOT using Al_2O_3/GeO_x/Ge gate stacks fabricated by plasma post oxidation", Proc. IEEE Symp. VLSI Tech, 56 (2011)

[22] R. Zhang, P.C. Huang, J.C. Lin, M. Takenaka, S. Takagi, "Physical mechanism determining Ge p- and n-MOSFETs mobility in high Ns region and mobility improvement by atomically flat GeOx/Ge interfaces", Proc. IEEE IEDM, 371. (2012)

[23] R. Zhang, T. Iwasaki, N. Taoka, M. Takenaka, S. Takagi, "High-mobility Ge pMOSFET with 1-nm EOT Al_2O_3/GeO_x/Ge gate stack fabricated by plasma post oxidation", IEEE Trans. Electron Dev., 59, 335 (2012)

[24] R. Zhang, T. Iwasaki, N. Taoka, M. Takenaka, S. Takagi, "Al_2O_3 /GeO_x /Ge gate stacks with low interface trap density fabricated by electron cyclotron resonance plasma post oxidation", Appl. Phys. Lett., 98, 112902 (2011)

[25] R. Zhang, P. C. Huang, N. Taoka, M. Takenaka,S. Takagi, "High mobility Ge pMOSFETs with 0.7 nm ultrathin EOT using $HfO_2/Al_2O_3/GeO_x$/Ge gate stacks fabricated by plasma post oxidation", Proc. IEEE Symp. VLSI Tech., 161 (2012)

[26] E. Dentoni Litta, P-E. Hellström, C. Henkel, M. Östling, "Thulium silicate interfacial layer for scalable high-k/metal gate stacks", IEEE Trans. Electron Dev., 60(10), 3271 (2013)

[27] H. G. Thompkins, E. A. Irene, “Handbook of ellipsometry”, William Andrew Publishing, 2005, Ch. 2, sec 2.2.3, 125

[28] H. G. Thompkins, E. A. Irene, “Handbook of Ellipsometry”, William Andrew Publishing, 2005, Ch. 10, sec 10.4, 734

[29] B. Johs, J. S. Hale, “Dielectric function representation by b-splines”, Phys. Stat. Sol. (a), 205(4), 715 (2008)

[30] G.E. Jellison, Jr., F.A. Modine, “Parameterization of the optical functions of amorphous materials in the interband region”, Appl. Phys. Lett., 69, 371 (1996)

[31] A. Toriumi, S.K. Wang, C.H. Lee, M. Yoshida, K. Kita, T. Nishimura, K. Nagashio, “Oxidation, diffusion and desorption in a Ge/GeO_2 system”, ECS Trans., 28(2), 171 (2010)

[32] H. Hosono, Y. Abe, D.L. Kinser, R.A. Weeks, K. Muta, H. Kawazoe, “Nature and origin of the 5 eV band in Si on GeO_2 glasses” Phys. Rev. B, 46, 11445 (1992)

[33] A.S. Zyubin, A.M. Mebel, S.H. Lin, “Photoluminescence of oxygen-containing surface defects in germanium oxides: a theoretical study”, J. Chem. Phys., 123, 044701 (2005)

[34] A.S. Zyubin, A.M. Mebel, S.H. Lin, “Photoluminescence of oxygen-deficient defects in germanium oxides: A quantum chemical study”, J. Chem. Phys., 125, 064701 (2006)

[35] M. Di, E. Bersch, A.C. Diebold, S. Consiglio, R.D. Clark, G.J. Leusink, T. Kaack, “Comparison of methods to determine bandgaps of ultrathin HfO_2 films using spectroscopic ellipsometry”, J. Vac. Sci. Techn. A, 29(4), 041001 (2011)

[36] S.Y Chiam, W.K. Chim, C. Pi, A.C.H. Huan, S.J. Wang, J.S. Pan, S. Turner, J. Zhang, “Band alignment of yttrium oxide on various relaxed and strained semiconductor substrates”, J. Appl. Phys., 103, 083702 (2008)

[37] A. Ohta, M. Yamaoka, S. Miyazaki, “Photoelectron spectroscopy of ultrathin yttrium oxide films on Si (100)”, Microelec. Eng., 72, 154 (2004)

[38] T. Tomiki, J. Tamashiro, Y. Tanahara, A. Yamada, H. Fukutani, T. Miyahara, H. Kato, S. Shin, M. Ishigame, “Optical spectra of Y_2O_3 single crystals in VUV”, J. Phys. Soc. Japan, 55(12), 4543 (1986)

[39] V. V. Afanas’ev, M. Houssa, A. Stesmans, M. M. Heyns, “Band alignments in metal–oxide–silicon structures with atomic-layer deposited Al_2O_3 and ZrO_2”, J. Appl. Phys., 91, 3079 (2002)

[40] V. V. Afanas’ev, A. Stesmans, “Internal photoemission at interfaces of high- κ insulators with semiconductors and metals”, J. Appl. Phys., 102, 081301 (2007)

[41] H.Y. Yu, M.F. Li, B.J. Cho, C.C. Yeo, M.S. Joo, D.L. Kwong, “Energy gap and band alignment for $(HfO_2)_x$ $(Al_2O_3)_{1-x}$ on (100) Si”, Appl. Phys. Lett., 81, 376 (2002)

[42] J. Robertson, B. Falabretti, “Band offsets of high K gate oxides on III-V semiconductors”, J. Appl. Phys., 100, 014111 (2006)

[43] D. P. Norton, “Synthesis and properties of epitaxial electronic oxide thin-film materials”, Mater. Sci. Eng. R., 43, 139 (2004)

[44] F. L. Martinez, M. Toledano-Luque, J.J. Gandia, J. Carabe, W. Bohne, J. Rohrich, E. Strub, I. Martil, "Optical properties and structure of HfO_2 thin films grown by high pressure reactive sputtering", J. Phys. D: Appl. Phys., 40, 5256 (2007)

[45] Y. J. Cho, N. V. Nguyen, C. A. Richter, J. R. Ehrstein, B. H. Lee, J. C. Lee, "Spectroscopic ellipsometry characterization of high-k dielectric HfO_2 thin films and the high-temperature annealing effects on their optical properties", Appl. Phys. Lett., 80, 1249 (2002)

[46] H. Takeuchi, D. Han, T-J. King, "Observation of bulk HfO_2 defects by spectroscopic ellipsometry", J. Vac. Sci. Technol. A, 22, 1337 (2004)

[47] Z. M. Larimi, A. Amirabadizadeh, A. Zelati, "Synthesis Y_2O_3 nanoparticles by modified transient morphology method", Proc. IPCBEE, 10, 86 (2011)

[48] H. Li, L. Lin, J. Robertson, "Control of Schottky barrier heights by inserting thin dielectric layers", Appl. Phys. Lett., 101, 052903 (2012)

[49] H. Li, J. Robertson, "Defects at Ge:GeO_2 and Ge:MeO_x interfaces", Microelec. Eng., 109, 244 (2013)

[50] Z.Q. Liu, W.K. Chim, S.Y. Chiam, J.S. Pan, C.M. Ng, "Ambiguity in the magnitude and direction of the derived interface dipole in lanthanum aluminate heterostructures: Implications and proposed solution", J. Appl. Phys., 109, 093701 (2011)

[51] D. Schmeisser, R.D. Schnell, A. Bogen, F.J. Himpsel, D. Rieger, G. Landgren, J.F. Morar, "Surface oxidation states of germanium", Surf. Sci., 172, 455 (1986)

[52] R.L. Opila, G.D. Wilk, M.A. Alam, R.B. van Dover, B.W. Busch, "Photoemission study of Zr- and Hf-silicates for use as high-κ oxides: Role of second nearest neighbors and interface charge", Appl. Phys. Lett., 81, 1788 (2002)

[53] T. Sasada, Y. Nakakita, M. Takenaka, S. Takagi, "Surface orientation dependence of interface properties of GeO_2/Ge metal-oxide semiconductor structures fabricated by thermal oxidation", J. Appl. Phys., 106, 073716 (2009)

[54] E. Kraut, R. Grant, J. Waldrop, S. Kowalczyk, "Precise determination of the valence-band edge in X-Ray photoemission spectra: Application to measurement of semiconductor interface potentials", Phys. Rev. Lett., 44, 1620 (1980)

[55] M. Houssa, G. Pourtois, M. Caymax, M. Meuris, M. M. Heyns, "First-principles study of the structural and electronic properties of (100) Ge⁄Ge (M) O_2 interfaces (M = Al , La, or Hf)", Appl. Phys. Lett., 92(24), 242101 (2008)

[56] Q. Xie, S. Deng, M. Schaekers, D. Lin, M. Caymax, A. Delabie, X-P. Qu, Y-L. Jiang, D. Deduytsche, C. Detavernier, "Germanium surface passivation and atomic layer deposition of high-k dielectrics-a tutorial review on Ge-based MOS capacitors", Semicond. Sci. Techn., 27, 074012 (2012)

[57] C.H. Lee, T. Tabata, T. Nishimura, K. Nagashio, A. Toriumi, "Ge/GeO_2 interface control with high-pressure oxidation for improving electrical characteristics", Appl. Phys. Express, 2, 071404 (2009)

[58] M. Kouda, T. Kawanago, P. Ahmet, K. Natori, T. Hattori, H. Iwai, K. Kakushima, A. Nishiyama, N. Sugii, K. Tsutsui, "Interface and electrical properties of Tm_2O_3 gate dielectrics for gate oxide scaling in MOS devices", J. Vac. Sci. Technol. B, Microelectron. Nanometer Struct., 29(6), 062202 (2011)

[59] M. Kouda, K. Kakushima, P. Ahmet, K. Tsutsui, A. Nishiyama, N. Sugii, K. Natori, T. Hattori, H. Iwai, "Rare earth oxide capping effect on La_2O_3 gate dielectrics for equivalent oxide thickness scaling toward 0.5 nm", Jpn. J. Appl. Phys., 50(10), 10PA04 (2011)

[60] T. Ji, J. Cui, Z.B. Fang, T.X. Nie, Y.L. Fan, X.L. Li, Q. He, Z.M. Jiang, "Single crystalline Tm_2O_3 films grown on Si (001) by atomic oxygen assisted molecular beam epitaxy", J. Cryst. Growth, 321, 171 (2011)

[61] S. Sioncke, H.C. Lin, A. Delabie, T. Conard, H. Struyf, S. De Gendt, M. Caymax, "Scaling the Ge gate stack: Toward sub 1 nm EOT", ECS J. of Solid State Sci. and Techn., 1(3), 127 (2012)

[62] E. Dentoni Litta, P.-E. Hellstrom, C. Henkel, S. Valerio, A. Hallen, M. Ostling, "High-Deposition-Rate atomic layer deposition of thulium oxide from $TmCp_3$ and H_2O", J. Electrochem. Soc., 160(11), D538 (2013)

[63] H. Iwai, S. Ohmi, S. Akama, C. Ohshima, A. Kikuchi, I. Kashiwagi, J. Taguchi, H. Yamamoto, J. Tonotani, Y. Kim, I. Ueda, A. Kuriyama, Y. Yoshihara, "Advanced gate dielectric materials for sub100 nm CMOS", Proc. IEEE IEDM, 625 (2002)

[64] J. Wang, T. Ji, Y. Zhu, Z. Fang, W. Ren, "Band gap and structure characterization of Tm_2O_3 films", J. Rare Earths, 30, 233 (2012)

[65] J. Price, G. Bersuker, P.S. Lysaght, "Identification of interfacial defects in high- k gate stack films by spectroscopic ellipsometry", J. Vac. Sci. Technol. B, 27, 310 (2009)

[66] X-J. Zhang, G. Xue, Z. Agarwal, R. Tsu, M-A. Hassan, J.E. Greene, A. Rockett, "Thermal desorption of ultraviolet–ozone oxidized Ge(001) for substrate cleaning", J. Vac. Sci. Technol. A, 11, 2553 (1993)

Chapter 4

4. Experimental methods for metal-insulator-metal and metal-multi insulator-metal devices

The metal-insulator-metal (MIM) diode concept has been identified as a potential candidate to operate beyond 12 THz [1-6]. However, it is crucial to obtain a time constant, that is, the product of diode resistance (R) and capacitance (C), below 10^{-15} seconds for the operation in infrared and visible light wavelengths. Note that the diode resistance is the combination of differential resistance and the series resistance of metal electrodes. However, the series resistance is ~100 Ω whereas the differential resistance in the order of 10^{3}-10^{6} Ω. Therefore in this thesis, the primary concern is to minimise the differential resistance of the diode. The device area is inversely proportional to the dynamic resistance but on the other hand it is directly proportional to the device capacitance. This constitutes a design trade-off. The MIM diode needs an oxide layer with a relatively small electron affinity compared to the work functions of the metals. A small device dynamic resistance can be achieved by engineering the barrier heights at the metal/oxide interface to be small as possible. Moreover it was reported that the Ni-NiO-Ni MIM structure demonstrated a small resistance of 1 $\Omega(\mu m)^2$ (product of resistance and area) due to the low barrier height of ~0.2 eV while maintaining a small device area [6]. Hence a time constant in the order of 10^{-15} seconds can be expected if the device structure is engineered with a small barrier height of 0.2 eV and by achieving nanoscale device dimensions. The other crucial factor is to obtain extremely good diode characteristics for efficient rectification of the analogue signal. This can be achieved by engineering the device structures with either one insulator or more than one insulator stacked in-between the metal electrodes.

The material properties including the oxide band gap and electron affinity values, metal work function values must be determined experimentally as there is wide variation in reported values (see Table 4.4). Therefore the experimental techniques atomic force microscopy (AFM), variable angle spectroscopic ellipsometry (VASE), X-ray photoelectron spectroscopy (XPS) and electrical current-voltage (*IV*) measurements, were used to characterise the materials in the diode structures and also to assist in the engineering design of the band structures prior to fabricating the diode structures that are presented in chapters 5, 6 and 7. In this chapter the material deposition, device patterning, physical and electrical characterisation techniques are addressed. The material deposition and patterning techniques are explained in section 4.1 whereas the physical characterisation techniques are discussed in section 4.2 and electrical characterisation in section 4.3.

4.1 Device fabrication

4.1.1 Sample preparation

The devices were fabricated on cleaned Corning glass substrates due to the ultra-smooth surface. The measured root mean square (RMS) roughness was 0.32 nm. The first step of cleaning was to blow away particulates using a nitrogen gun. Next, the slide was dipped in a solution of dionized water (DI) water and Decon 90 and thoroughly washed with running DI water for a long duration of approximately 10 minutes depending on the concentration of Decon 90. It was necessary to blow with nitrogen the sample surface in order to remove water/moisture. Then the sample was cleaned with isopropanol and acetone. Finally, the glass substrates were cleaned by the ultraviolet (UV) ozone cleaner for a time period of two minutes to remove the remaining residues from the cleaning solvents. The metal wires for thermal evaporation were cleaned with the aid of isopropanol and acetone.

4.1.2 Material deposition

The diode structures were fabricated with approximately 60 - 100 nm of a metal layer on Corning glass slides. The metals were deposited by either thermal evaporation or direct current (DC) sputtering technique. Furthermore, the metals Al, Cr and Ag were deposited by thermal evaporation process using the Moorefields Minilab 060 evaporator. It was mandatory to optimise the deposition conditions in order to obtain an ultra-smooth surface due to the sensitive nature of the structure, as will be discussed in section 4.2.1. The metals Nb, Ta and W were deposited by DC sputtering technique using an AJA International Orion – DV08 sputter system. The deposition rate was 0.3 nm/s. It was important to condition the metal targets by low power sputtering for a longer duration prior to the actual deposition. The uniformity of the sputtered materials was examined and this is discussed in section 4.2.2.

The thin oxide layers were deposited by either the atomic layer deposition (ALD) or radio frequency (RF) sputtering techniques. It is crucial to extract the deposition rates precisely due to the small thicknesses (1-5 nm) used. Hence the dielectrics were deposited on a Si wafer for a known period of time and the thickness evaluated by VASE at least three times in order to ensure the same growth rate has been achieved. ALD films were deposited by conventional thermal ALD using a Cambridge/Nanotech Savannah reactor with water and relevant precursors such as try-methyl-aluminium (TMA), tantalum ethoxide and niobium ethoxide for Al_2O_3, Ta_2O_5 and Nb_2O_5 respectively. The precursor was heated to 140 ^oC in order to obtain transport into the reactor, pulse and purge times were selected to ensure a self-limiting ALD reaction occurred, and the substrate temperature was 200 °C. Then the precursor was pulsed for 0.2 seconds followed by a purge time of 4-10 seconds. Next, H_2O was pulsed for 0.04

seconds followed by a purge time of 4-10 seconds. This cycle was continued until the desired thicknesses were obtained. RF sputtered oxides were deposited by an AJA International Orion – DV08 sputter system. The deposition was done by post-conditioning the targets. The Ar flow rate and deposition pressure were 10 sccm and 5 mTorr respectively. The dielectric Al_2O_3 deposition rate was 0.006 nm/s at 140 W. The deposition rates for Ta_2O_5 and Nb_2O_5 were determined to be 0.045 nm/s at 100 W and 0.03 nm/s at 70 W respectively.

4.1.3 Device patterning techniques

The device structures were patterned either by shadow mask or a conventional photolithography process. The first step was to design the photo and shadow masks with the aid of advanced design system (ADS). The mask designs and the patterning techniques are discussed below.

4.1.3.1 Photolithography process

The designed masks to pattern the bottom metal electrodes are shown in Figure 4.1. The photo mask was designed based on the aligner specifications and the substrate dimensions. The Corning glass slides with the dimensions of 4×4 cm^2 were chosen as substrates and therefore the mask was designed considering the dimensions of 2.73×2.73 cm^2. There were two mask designs considered for the bottom metal electrodes since to probe the bottom contact the oxide had to be etched. Therefore one mask was designed to dry-etch the oxide and the other was designed to use a wet etch.

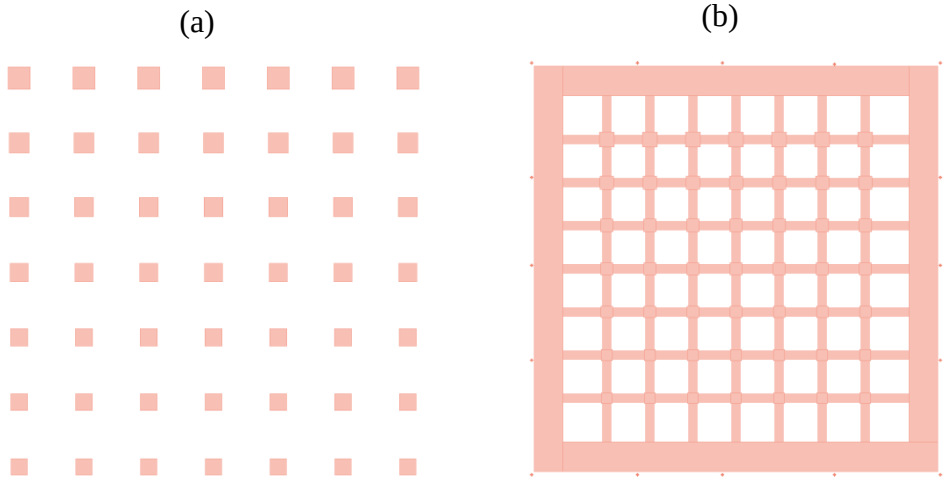

Figure 4.1: A schematic of bottom contact masks designed for (a) wet etching and (b) dry etching.

The areas of the contact pads were varied (730×730 µm^2- 1000×1000 µm^2) in order to fabricate devices with different device areas (15×15µm^2- 150×150 µm^2) as shown in Figure 4.1. However, after fabricating several devices using the mask designed for wet etching, it was found that the probe needle could penetrate through the thin dielectric(s) and reach the bottom

metal electrode easily. Therefore it was not necessary to etch the oxide by using any wet etchants or dry etching techniques to expose the bottom electrodes. The dielectric films were deposited by ALD or RF sputtering as explained in section 4.1.2. A mask was designed to pattern the top metal electrodes with a contact pad area of $600 \times 600\,\mu m^2$ (Figure 4.2). As shown in Figure 4.2 (b), there were four equally spaced (700µm) contact pads and the aim was to have the bottom metal electrode in the middle, resulting in four devices at the four corners of the bottom metal electrode.

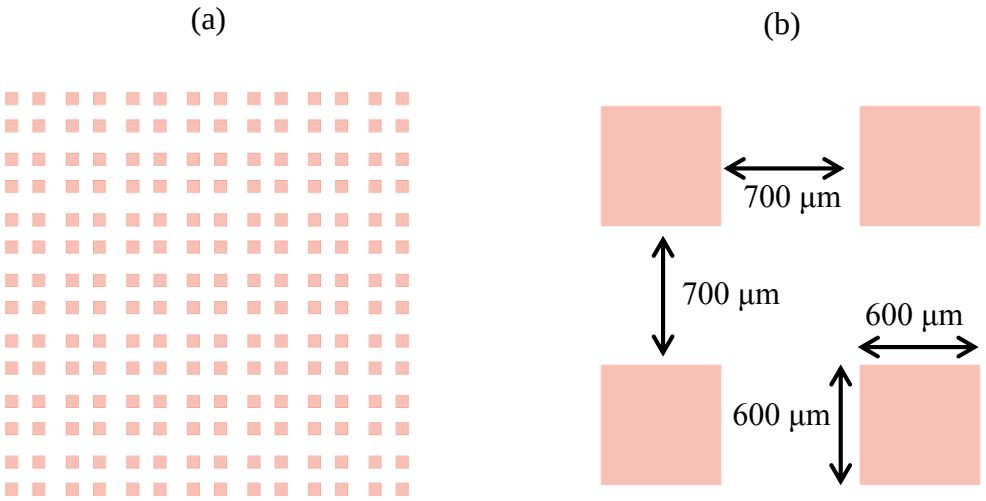

Figure 4.2: Schematic of top contact mask (a) full mask and (b) magnified view.

The final device structure is shown in Figure 4.3.

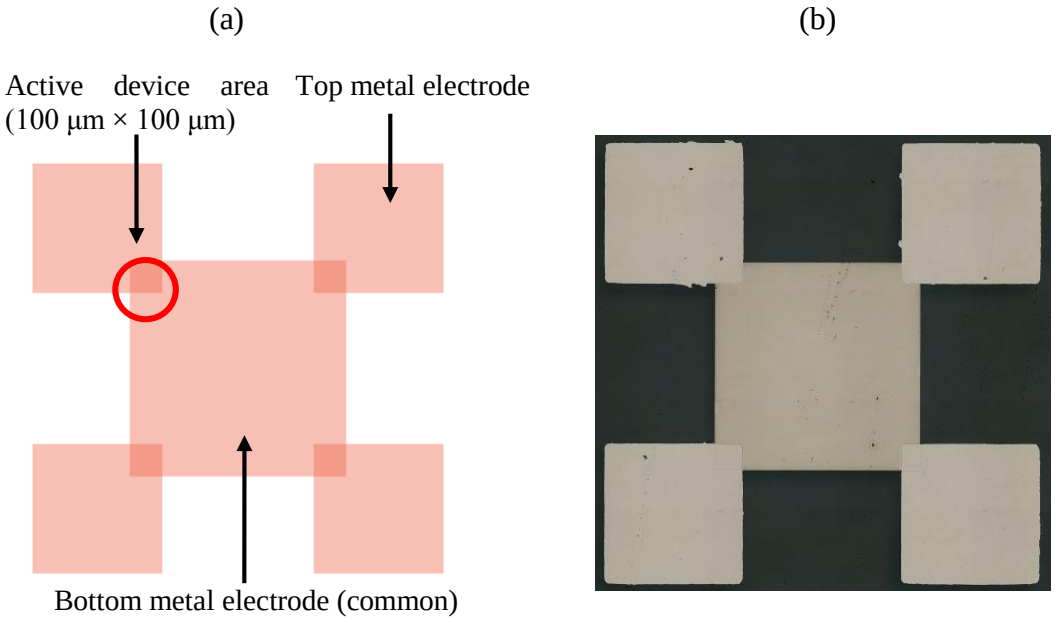

Figure 4.3: Final device structure: (a) mask design and (b) fabricated device.

The *IV* results extracted on these structures were comparable to the results extracted on devices that were patterned by shadow masks. The total number of devices per substrate was 196 and 9 for photolithography and shadow mask processes.

4.1.3.2 Shadow mask process

A set of shadow masks was designed to pattern the top and bottom metal electrodes of the device structures. This process was relatively easy and consumed only a short period of time compared to the photolithography process. The device structures were fabricated on a 2.5× 2.5 cm^2 Corning glass slide however the total number of devices was reduced from 196 to 9 in shadow mask process. The line width was chosen to be 100 µm meanwhile the area of the contact pad was selected to be 1.2×1.2 mm^2. The mask design is shown in Figure 4.4.

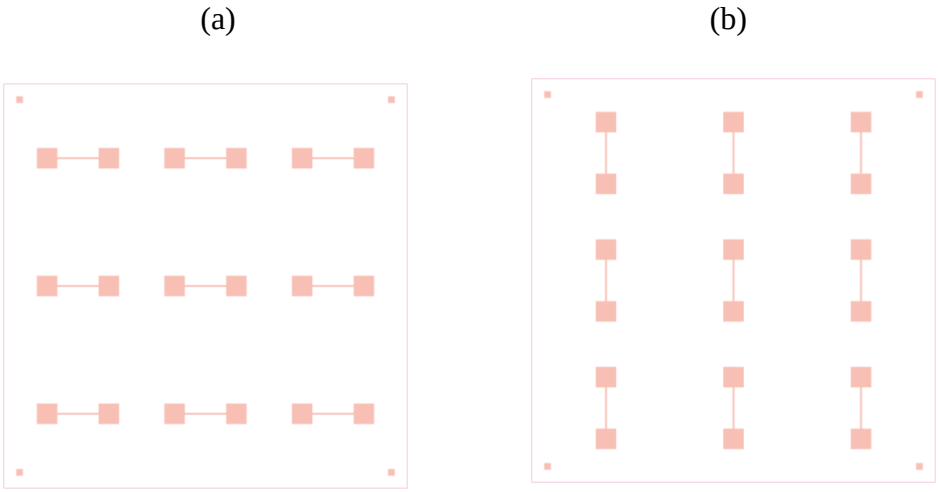

Figure 4.4: Shadow mask design: (a) bottom contacts and (b) top contacts.

The mask was placed on the substrate and held tightly with the aid of magnets. Initially the bottom metal electrodes were defined using the mask shown in Figure 4.4 (a). However, after the deposition of oxides, the mask was rotated by 90^0 as shown in Figure 4.4 (b), to define the top metal electrodes.

4.2 Physical characterisation

4.2.1 Surface roughness estimation of bottom metal electrode

The conduction process of MIM/MIIM/MIIIM structures is based on quantum mechanical tunnelling. Moreover, the tunnelling probability exponentially depends on the thickness of the dielectric layer(s) and is electrode limited; therefore the performance of the diode structure is dependent upon the surface roughness at the metal oxide interface [7-10]. In a worst case, the diode could be short-circuited due to the ultra-thin (1-5 nm) oxide layers if the roughness is

large. The first batch of devices were all short circuited and possibly this could be due to the large surface roughness of the bottom metal electrode. Initially the surface roughness of the Corning glass slide was measured by AFM to be 0.32 ± 0.01 nm RMS and the deposited Al, 3.4 ± 0.01 nm RMS as shown in Figure 4.5 (a). These values were much improved by optimising the evaporation conditions and cleaning process of metals and glass slides.

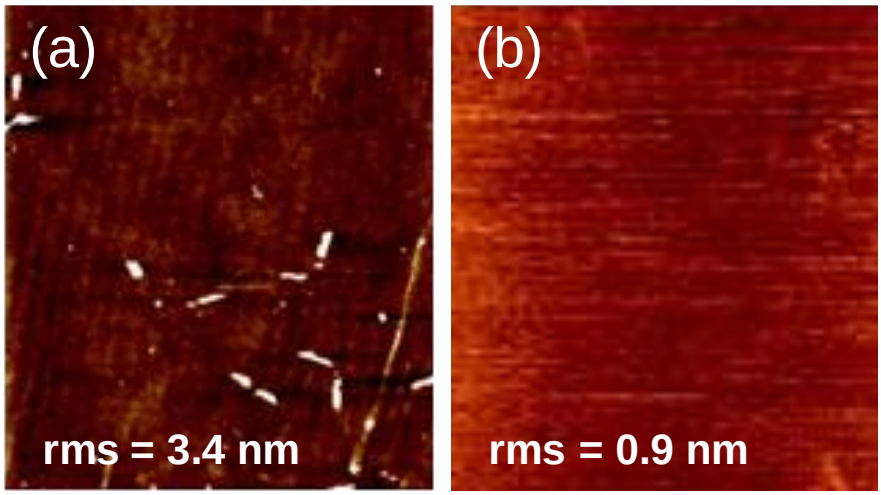

Figure 4.5: AFM images of the Al blanket films (a) before, and (b) after optimizing the thermal evaporation and cleaning processes. The scanned area is 40 $\mu m \times$ 40 μm.

The roughness was minimised substantially from 3.4 nm to 0.9 nm after following a slow deposition rate of 0.3 nm/s for thermal evaporation. It is expected that the ALD and RF sputtering processes are extremely uniform across the surface, as further indicated in Figure 4.9. Moreover, the chosen substrate, Corning glass has an ultra-smooth surface; therefore the main focus was to improve the roughness of the bottom metal electrode. The metals were deposited by DC sputtering and did not lead to any issues such as short circuits due to the high uniformity of the deposition. The uniformity of sputtered layers is discussed further in section 4.2.2.

4.2.2 Uniformity, thickness and band gap estimation by VASE

The VASE measurements were performed and analysed as elaborated in chapter 2, to find the thickness and optical constants of the dielectrics. The measurements were performed with a wavelength range of 241.1 nm – 1686.7 nm which corresponds to an energy range of 0.7 eV – 5.2 eV. There were three angles chosen around the Brewster angle in order to increase the resolution of the measurements. The experimental data extracted in the form of two angles (ψ, Δ) vs. photon energy (E) were analysed using both completeEASE and WVASE 32 software programs by developing a theoretical model to match the experimental results. The initial attempt was to model the Si substrate using the predefined Si model available in the software database as all the oxides were deposited on Si. Then as seen in Figure 4.6, the relevant

predefined oxide layers were superimposed to the Si reference model and extracted the thicknesses. This was achieved by placing a Si substrate in the chamber while depositing oxides for the MIM/MIIM/MIIIM structures in order to verify the thickness by VASE. It has been observed that the thickness of the nominal 5 nm Ta_2O_5 structures was 4.58 ± 0.004 nm whereas the measured thickness values of the double insulator structure was 3.35 nm (4 nm nominal) for Ta_2O_5 and 1.15 ± 0.007 nm (1 nm nominal) for Al_2O_3 as can be seen in Figures 4.6 (a) and (c) respectively. Moreover it was evident that the actual thickness extracted on 5 nm (nominal) Nb_2O_5 was found to be 5.54 ± 0.004 nm as shown in Figure 4.6 (b).

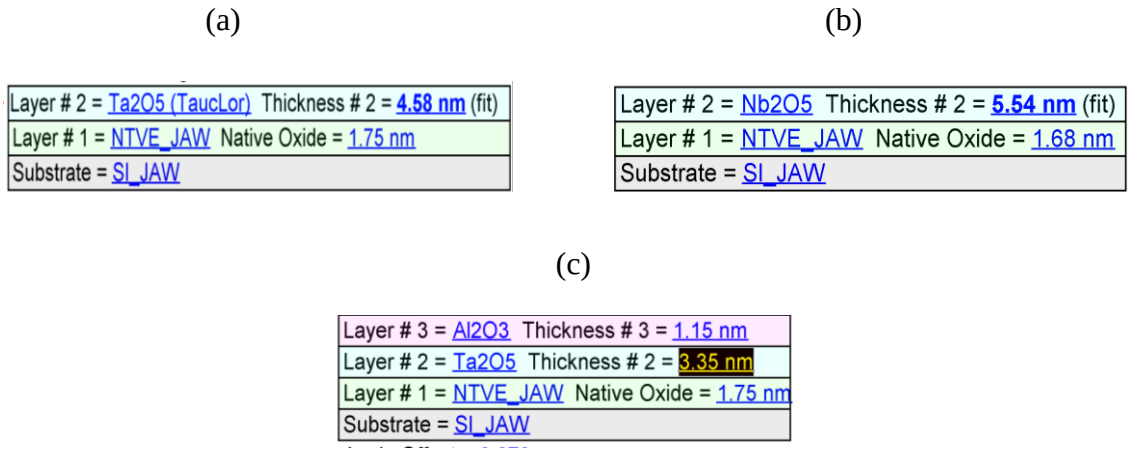

Figure 4.6: Thicknesses measured by VASE (a) 5 nm (nominal) Ta_2O_5, (b) 5 nm (nominal) Nb_2O_5, (c) 1 nm (nominal) Al_2O_3 and 4 nm (nominal) Ta_2O_5. The mean squared error (MSE) for the fitting of thickness was <5.

The optical constants of the dielectrics that are used to fabricate the MIM/MIIM/MIIIM structures were extracted by performing VASE measurements on thick oxides deposited on Si. There were three samples fabricated by depositing thick oxides of Ta_2O_5, Nb_2O_5 and Al_2O_3. The extracted optical constants, refractive index, extinction coefficient are shown in Figure 4.7. The band gap values were extracted using three different techniques, namely extinction coefficient (k), absorption coefficient (α) and Tauc plots (αE^2 for direct band gap and $\alpha E^{1/2}$ for indirect band gap approximations). The extracted thicknesses and band gap values are summarised in Table 4.1.

The precision of the modelling process explained before is increased by superimposing a general oscillator with either Tauc-Lorentz or Cody-Lorentz oscillator to the reference Si model to model Ta_2O_5, Nb_2O_5 and Al_2O_3 layers. The imaginary part of the dielectric constant was fitted followed by fitting the real part of the complex dielectric function while maintaining Kramers-Kronig (KK) consistency. Then the refractive index and extinction coefficient were extracted as discussed in chapter 2. The band gap of Ta_2O_5 was extracted to be 4.40 eV whereas the thickness of the bulk sample was 17.21 ± 0.001 nm (Table 4.1). The dynamic

permittivity was extracted by, n^2 at 580 nm [11] which was 4.55 for Ta_2O_5. Then the optical constants of Nb_2O_5 were investigated and a band gap of 3.76 eV extracted by both extinction coefficient and absorption coefficient methods (Figure 4.7 (b) & 4.7 (c)). The thickness was estimated to be 11.15 ± 0.05 nm for the bulk sample (Table 4.1). The dynamic permittivity of Nb_2O_5 was estimated as 5.49 at 580 nm.

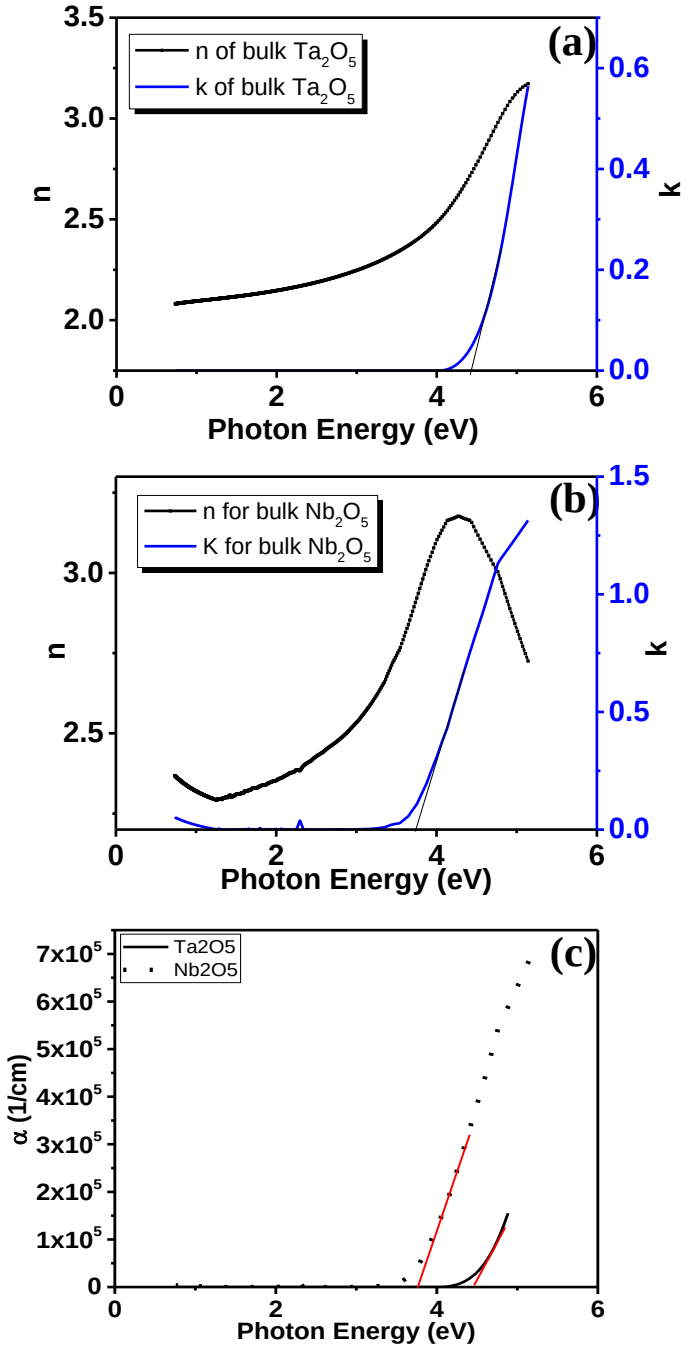

Figure 4.7: Optical constants (n, k) vs photon energy extracted from VASE modelling for: (a) Ta_2O_5, (b) Nb_2O_5, and (c) absorption coefficient vs photon energy for both Nb_2O_5 and Ta_2O_5. The nominal thicknesses of Ta_2O_5 and Nb_2O_5 samples were 20 nm.

The band gap of Al_2O_3 could not be estimated due to the limitation of the spectral range (0.7 to 5.2 eV), however this was measured and analysed in chapter 3 with an instrument in the spectral energy range of 0.5 eV and 8.8 eV. The band gap values of 6.31 ± 0.1 eV and 6.43 ± 0.1 eV for the extinction and absorption coefficient methods respectively.

Table 4.1: Summary of thickness and band gap values extracted from VASE measurements.

Sample	Nominal thickness (nm)	Measured thickness (nm)	Band gap (eV)-extinction coefficient (k)	Band gap (eV)-Absorption coefficient (α)	Band gap (eV)-Tauc plots $(\alpha E)^n$
Al_2O_3	10	9.40 ± 0.01	6.33 ± 0.1	6.43 ± 0.1	6.12 ± 0.1 (Indirect, n=0.5)
Ta_2O_5	20	17.21 ± 0.01	4.40 ± 0.1	4.40 ± 0.1	4.19 ± 0.1 (Indirect, n=0.5)
Nb_2O_5	20	11.15 ± 0.05	3.76 ± 0.1	3.76 ± 0.1	3.6 ± 0.1 (Indirect, n= 0.5)

A further experiment was carried out to investigate the temperature dependence of the band gap of Ta_2O_5 layer deposited on Si. The motivation was to observe any correlation to the temperature dependent *IV* characteristics discussed in chapter 5. Temperatures in the range 25 ^oC to 75 ^oC were used. The temperature dependence of the extinction coefficient is shown in Figure 4.8 (a) whereas that of the absorption coefficient is shown in Figure 4.8 (b).

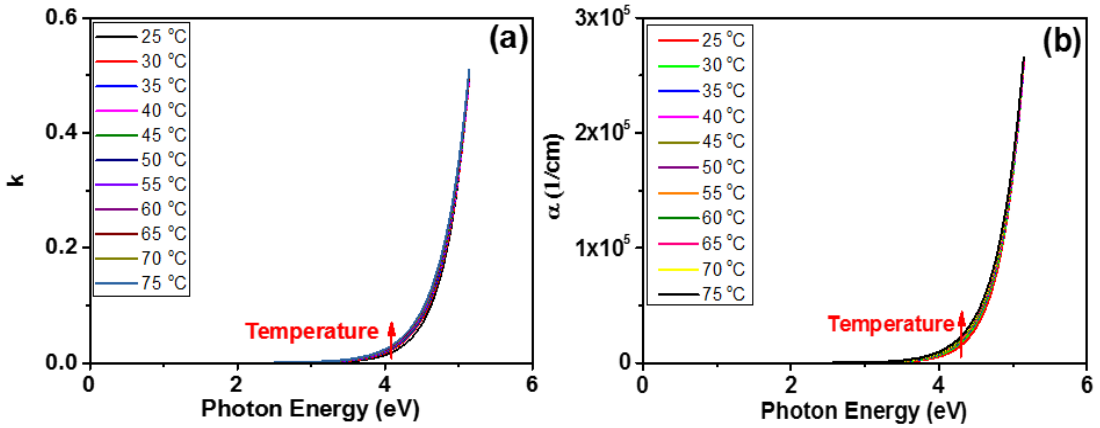

Figure 4.8: Temperature dependence of (a) extinction coefficient and (b) absorption coefficient for Ta_2O_5/Si sample.

The band gap values were extracted by linearly extrapolating the absorption edge of the extinction coefficient and the absorption coefficient and it was possible to observe a small

decrease in band gap by ~0.08 ± 0.002 eV with the increase in temperature from 25 °C (293 K) to 75 °C (348 K). The change in band gap values is smaller than the resolution of the kit (~0.1 eV), but it is clearly evident that the absorption edge varies with the change in temperature, resulting in a variation in band gap values.

The thickness profile of the RF sputtered and ALD Al_2O_3 was extracted in order to check the uniformity of the deposited oxide across the surface. The thickness profile was investigated (Figure 4.9) by defining a mapping recipe in completeEASE software.

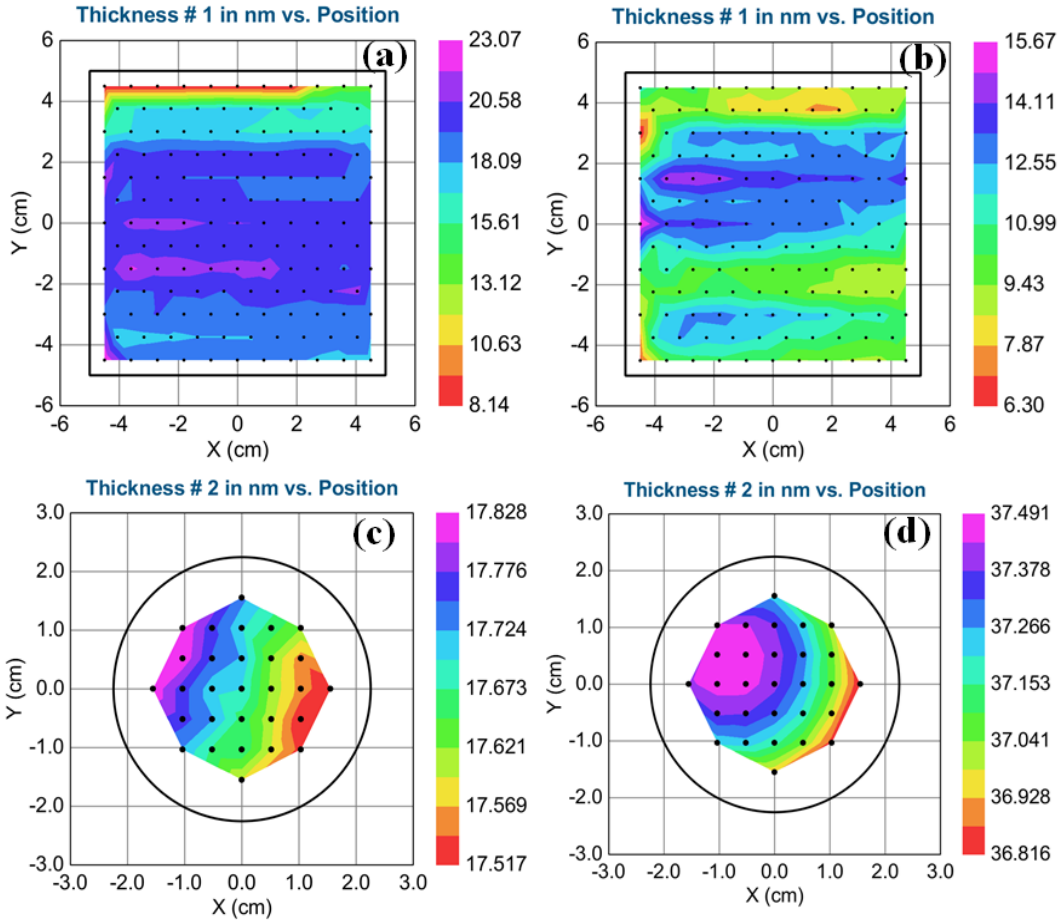

Figure 4.9: The thickness profile of (a) and (b) 20 nm (nominal) RF sputtered Al_2O_3 on glass as deposited and etched respectively (c) RF sputtered 20 nm (nominal) Al_2O_3 on Si and (d) ALD deposited 40 nm (nominal) Nb_2O_5 on Si. The colour scheme on the right of figures relates to thickness values in nanometre (nm).

The dielectric, Al_2O_3 (RF sputtered) was deposited on a 10×10 cm^2 glass slide with the intended nominal thickness of 20 nm. However, it was noticed that the signal intensity for glass was 4.26 in contrast to the large intensity value of ~14 observed for Si or Ge. This could be due to the small refractive index of glass (~1.5) in contrast to the refractive index of Si (~3.4) and the backside reflections of glass. Therefore the experimental ψ and Δ values obtained for layers on glass were not smooth as the signals from layers deposited on Si. The thickness profile extracted for the 20 nm (nominal) Al_2O_3 on glass structure is shown in Figure

4.9 (a). It was evident that the dielectric layer deposited on glass was fairly uniform (18 ± 5 nm) across the area 10 × 10 cm^2 as illustrated in Figure 4.9 (a). Moreover, it was found that if the deposition and the measurement were performed using deposited layer on a Si substrate the uniformity is better, due to the larger signal intensity that leads to less noisy signals, as shown in Figure 4.9 (c). The thickness profile for Al_2O_3 on Si sample was 17.6 ± 0.1 nm across the mapped area. Note that the two Al_2O_3 layers were deposited simultaneously on glass and on Si substrate in the same chamber. It was attempted to dry-etch the Al_2O_3 layer for 10 minutes with an applied power of 50 W. As explained in chapter 6, the Al bottom contacts were dry etched in order to eliminate the native AlO_x layer. The results shown in Figure 4.9 (b) indicate that approximately 10 nm of Al_2O_3 was etched away with the uniformity of thickness ± 1.56 nm. The ALD deposited 40 nm (nominal) Nb_2O_5 shows good uniformity across the mapped area, as illustrated in Figure 4.9 (d). The measured thickness was 37.1 ± 0.3 nm.

4.2.3 X-Ray photoelectron spectroscopy (XPS)

XPS measurements were performed with the aim of deriving the energy band diagrams for the MIM/MIIM/MIIIM structures. This technique can be used to extract the valence band offset by Kraut's method [12] and also to determine the electron affinity [13] of the materials used in diode structures. The first step was to prepare the samples that were needed to perform XPS measurements in order to extract the above stated parameters. The oxide layers were deposited on a 50 nm SiO_2/Si wafer (4''). Then 20 nm nominal (17.28 nm measured by VASE) Al_2O_3 () was deposited by ALD on the wafer. The objective was to use Al_2O_3 as the substrate and to extract the valence band offset at the interface of Nb_2O_5 (or Ta_2O_5) and Al_2O_3. Then the wafer was cut into 4 pieces to deposit top Nb_2O_5 (or Ta_2O_5) films of thickness > 10 nm as bulk samples and < 5 nm as interface samples. The latter was done in order to be able to perform Kraut's method for extracting valence band offset (VBO). The following samples were prepared:

1) 17.28 nm Al_2O_3/50 nm SiO_2/Si (bulk Al_2O_3)
2) 17.21 nm of Ta_2O_5/17.28 nm Al_2O_3/50 nm SiO_2/Si (bulk Ta_2O_5)
3) 2.70 nm of Ta_2O_5/17.28 nm Al_2O_3/50 nm SiO_2/Si (interface 1 Ta_2O_5)
4) 4.58 nm of Ta_2O_5/17.28 nm Al_2O_3/50 nm SiO_2/Si (interface 2 Ta_2O_5)
5) 11.15 nm of Nb_2O_5/17.28 nm Al_2O_3/50 nm SiO_2/Si (bulk Nb_2O_5)
6) 3.80 nm of Nb_2O_5/17.28 nm Al_2O_3/50 nm SiO_2/Si (interface Nb_2O_5)

The thicknesses stated above are extracted by VASE. The core level (CL) fittings were performed after understanding the stoichiometric ratios of elements present in the films. Carbon 1s correction was performed as the carbon scans were shifted above 284.60 eV and

used this value as a reference to calibrate the other CL peaks [14]. Core level fittings were carried out with a combination of Gaussian and Lorentzian line shapes using the Shirley-type background.

4.2.3.1 XPS CL fittings for Bulk Al_2O_3 sample

The CL fittings were done considering the stoichiometry for the Al 2p and O 1s peaks as shown in Figure 4.10. The Al 2p CL was fitted using a doublet of Voigt functions corresponding to Al $2p_{3/2}$ and Al $2p_{1/2}$. The spin-orbit splitting and area ratio of 0.44 eV and 1:2 were used while de-convoluting the Al 2p spectra.

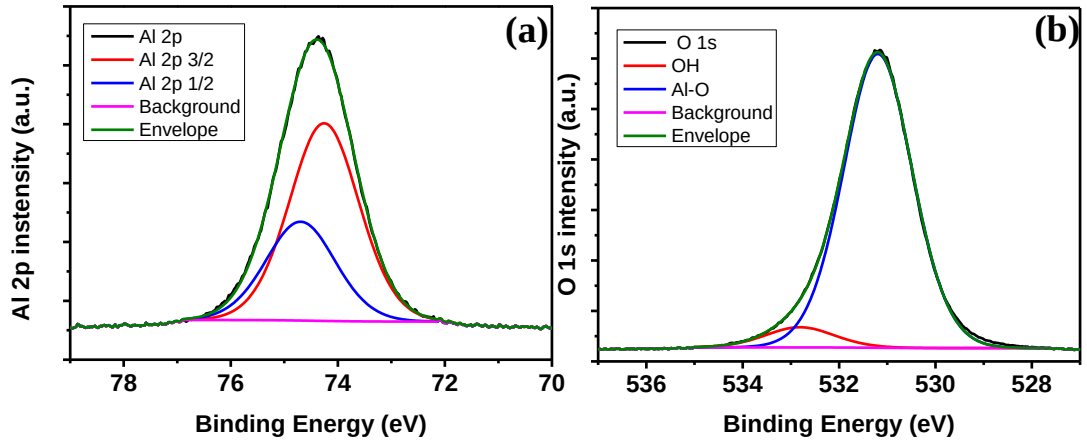

Figure 4.10: Core level fittings (a) Al 2p core level of bulk Al_2O_3, (b) O 1s core level of bulk Al_2O_3.

The binding energy value of Al $2p_{3/2}$ in Al_2O_3 has to be 74.1-74.6 eV [15] whereas its binding energy in pure Al metal is 72.70 eV [15]. As can be seen in Figure 4.10 (a), the fitting was done considering two sub-peaks, Al $2p_{3/2}$ and Al $2p_{1/2}$ at 74.27 eV and 74.71 eV respectively, indicating the presence of Al_2O_3. The O 1s core level was fitted using two oscillators that are, Al_2O_3 (Al-O) at 531.17 eV and OH at 532.76 eV. The sub-peak fitting for Al_2O_3 is in agreement with the reported 531.1 eV and 531.2 eV [15, 16].

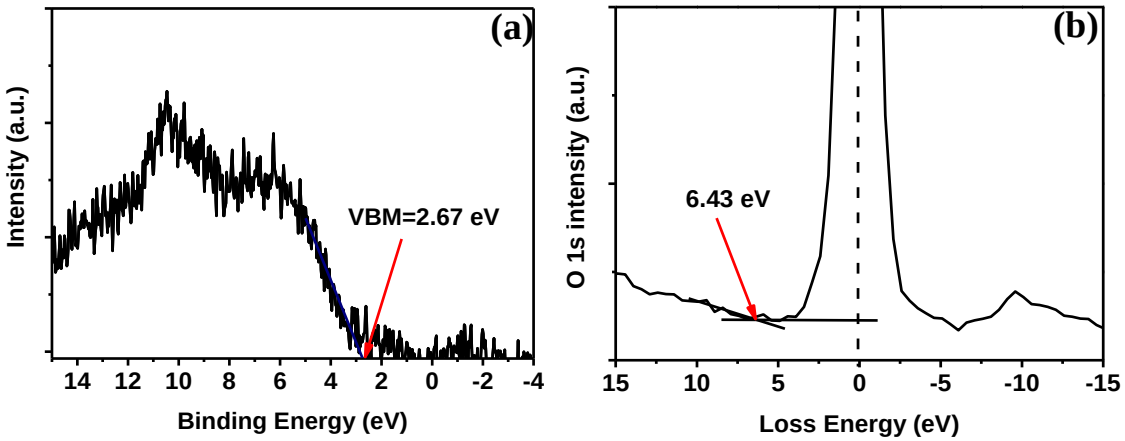

Figure 4.11: (a) VBM extraction and (b) electron energy loss spectrum of Al_2O_3/Si sample.

The valence band maximum (VBM) was extracted to be 2.67 ± 0.2 eV using Figure 4.11 (a).

The estimated VBM is in agreement with 2.4 eV that has been reported in the literature [17]. The band gap was extracted using the O 1s XPS energy loss spectrum (Figure 4.11 (b)) in addition to the VASE. It can be seen in Figure 4.11 (b), there is an edge at larger binding energy values compared to the main O 1s peak. This is as consequence of inelastic losses of photoelectrons due to band edge excitations. Therefore the extracted band gap was 6.43 eV by considering the energy difference between the centroid of the O 1s peak and the edge.

4.2.3.2 XPS CL fittings for Bulk Ta_2O_5 sample

The core level fittings were carried out for Ta 4f, Ta 4d and O 1s peaks.

The difference between Ta $4f_{7/2}$ and Ta $4f_{5/2}$ sub-peaks is 1.80 eV [15] and has a branching ratio of 4:3. Hence these peaks were fitted with two oscillators at 26.10 eV and 27.85 eV for Ta $4f_{7/2}$ and Ta $4f_{5/2}$ respectively as shown in Figure 4.12 (a). The binding energy value of the Ta $4f_{7/2}$ has been reported to be 26.50 eV [15, 18].

The difference between Ta $4d_{5/2}$ and Ta $4d_{3/2}$ sub-peaks is reported to be 11.2 eV [19], 11.40 eV [20] and 12 eV [15] and has a branching ratio of 3:2 (Figure 4.12 (b)). Finally, as shown in Figure 4.12 (c), the O 1s is fitted with two sub-peaks and the corresponding energy of Ta_2O_5 is 530.40 eV which is in line with reported 530.3 eV [15].

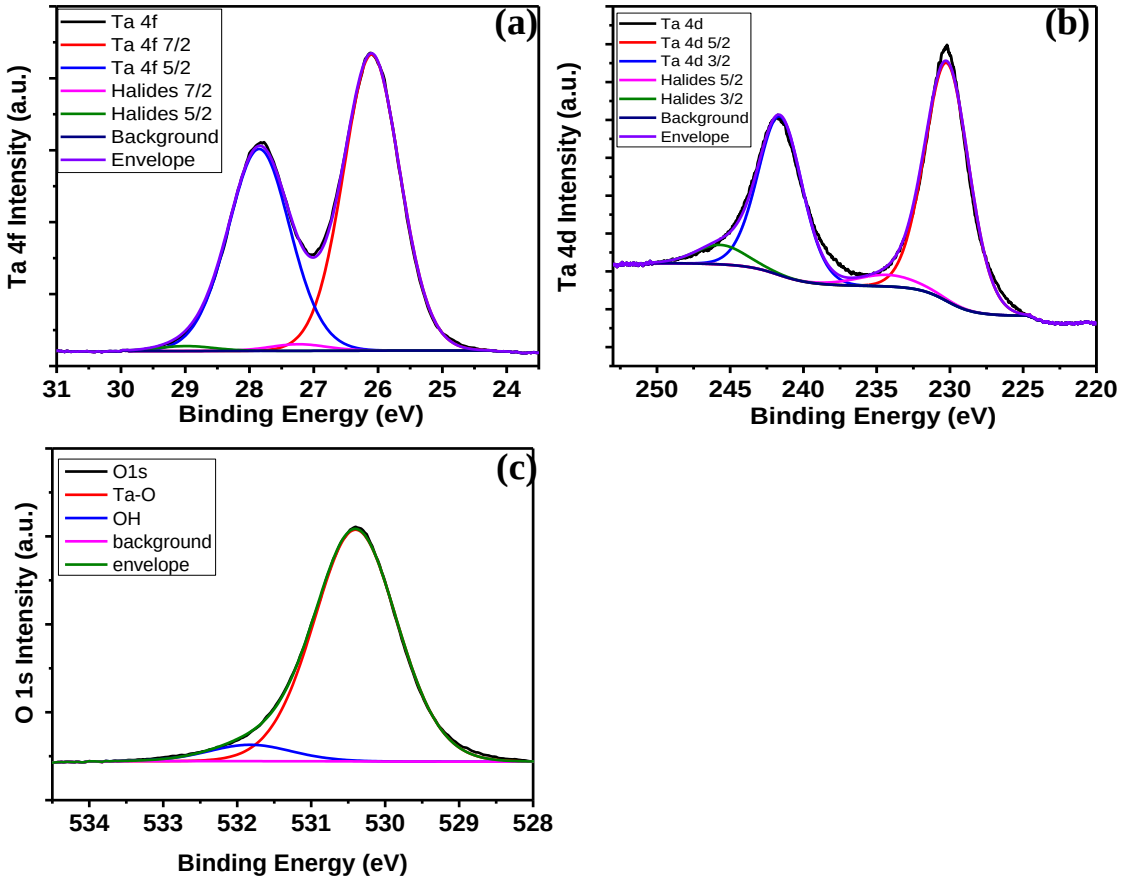

Figure 4.12: XPS core level fittings for (a) Ta 4f , (b) Ta 4d l and (c) O 1s of bulk Ta_2O_5 sample.

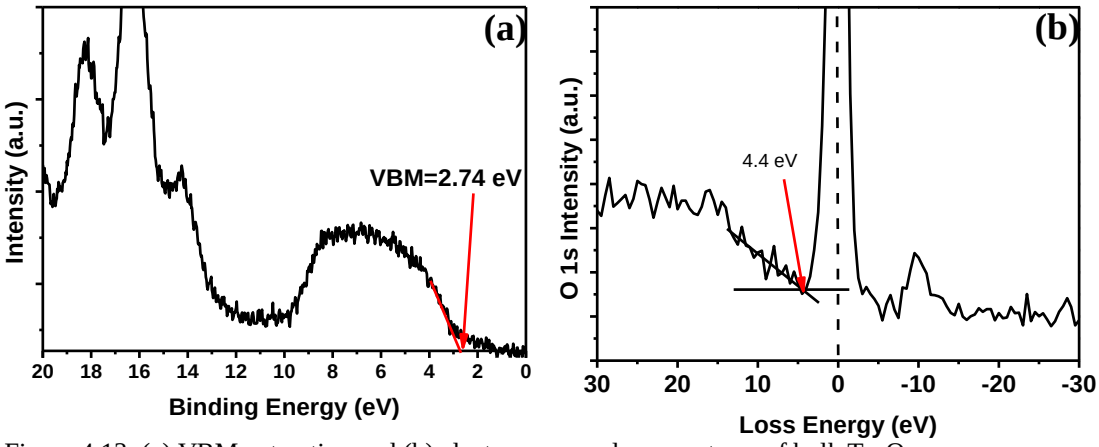

Figure 4.13: (a) VBM extraction and (b) electron energy loss spectrum of bulk Ta_2O_5

The extracted valence band maximum for bulk Ta_2O_5 sample was 2.74 ± 0.2 eV.

Finally, the band gap was extracted to be 4.4 eV using the same O 1s XPS loss energy spectrum as can be seen in Figure 4.13 (b). This was comparable to the band gap of 4.40 eV extracted by VASE.

4.2.3.3 XPS CL fittings for interface Ta_2O_5/Al_2O_3 samples

Two samples with a thin layer of Ta_2O_5 were measured and analysed in order to characterise the Ta_2O_5/Al_2O_3 interface. The CL fittings were performed considering Ta 4f, Ta 4d, O 1s and Al 2p peaks. Al 2p core level peak corresponding to bottom Al_2O_3 film was observed due to the thin (< 5 nm) nature of Ta_2O_5. The core level fittings related to 2.70 nm Ta_2O_5/Al_2O_3 sample are shown in Figure 4.14. Another thin 4.58 nm Ta_2O_5/Al_2O_3 sample was prepared in order to observe whether there is a shift in CL peaks in comparison to the 2.70 nm Ta_2O_5/Al_2O_3 interface sample. All the extracted binding energy values corresponding to the core levels are summarised in table 4.2.

The motivation of having two interface samples was to check the reliability of the VBO extraction due to the differential charging effects. Charging may occur in an XPS experiment when the holes created as a result of ejection of photoelectrons accumulate in a sample. This could result in an increase in binding energy of spectral features [21]. The valence band offset was calculated by considering both 4.58 nm Ta_2O_5 and 2.70 nm Ta_2O_5 deposited on 17.28 nm Al_2O_3 in order to ensure the consistency and precision of performed analysis. Furthermore, the valence band offset between Al_2O_3 and Ta_2O_5 was estimated using the method initially proposed by Kraut *et al* [12].

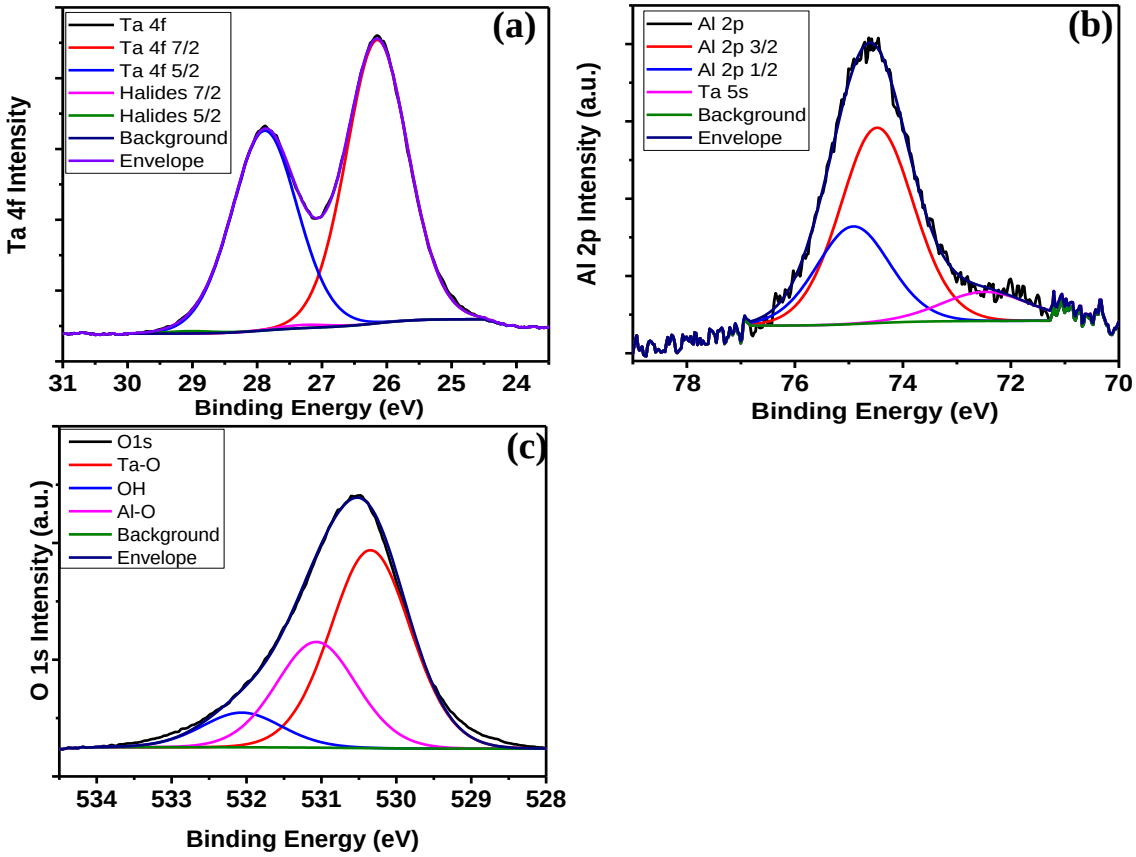

Figure 4.14: Core level fittings of (a) Ta 4f, (b) Al 2p and (c) O 1s for 2.7 nm Ta_2O_5/17.28 nm Al_2O_3.

4.2.3.4 Valence band offset estimation for Ta_2O_5/Al_2O_3 samples

The VBO was estimated using Kraut's equation and based on CL positions used in Table 4.2.

Table 4.2: A summary of CL binding energy values for bulk Al_2O_3, bulk Ta_2O_5 and Ta_2O_5/Al_2O_3 interfacial samples.

Core Level	Bulk Al_2O_3 (eV)	Bulk Ta_2O_5 (eV)	Thin Ta_2O_5/ Al_2O_3 (eV)	Thick Ta_2O_5/ Al_2O_3 (eV)
Ta $4d_{5/2}$		230.20 ± 0.1	230.28 ± 0.1	230.52 ± 0.1
Ta $4d_{3/2}$		241.60 ± 0.1	241.68 ± 0.1	241.92 ± 0.1
Ta $4f_{7/2}$		26.10 ± 0.1	26.15 ± 0.1	26.39 ± 0.1
Ta $4f_{5/2}$		27.85 ± 0.1	27.90 ± 0.1	28.14 ± 0.1
Al $2p_{3/2}$	74.27 ± 0.1		74.48 ± 0.1	74.76 ± 0.1
Al $2p_{1/2}$	74.71 ± 0.1		74.92 ± 0.1	75.20 ± 0.1
VBM	2.67 ± 0.2	2.74 ± 0.2		
O 1s	531.17	530.40	Ta-O 530.34 Al-O 531.07	Ta-O 530.91 Al-O 531.43

The Eqn. used from the data on 2.7 nm Ta_2O_5/17.28 nm Al_2O_3 sample is:

$$VBO = (E_{Al\,2p} - E_V)^{Al_2O_3} + (E_{Ta4d} - E_{Al\,2p})^{Interface} - (E_{Ta4d} - E_V)^{Ta_2O_5} \quad (4.1)$$

$$VBO = (74.27 - 2.67) + (230.28 - 74.48) - (230.20 - 2.74)$$
$$VBO = -0.06eV$$

In this case Ta 4d peak was used to estimate the valence band offset. If Ta 4f CL peak is used, then the Eqn. 4.1 changes into 4.2:

$$VBO = (E_{Al\,2p} - E_V)^{Al_2O_3} + (E_{Ta4f} - E_{Al\,2p})^{Interface} - (E_{Ta4f} - E_V)^{Ta_2O_5} \quad (4.2)$$

which gives,

$$VBO = (74.27 - 2.67) + (26.15 - 74.48) - (26.10 - 2.74)$$
$$VBO = -0.09eV$$

Using data from another interfacial 4.58 nm Ta_2O_5/Al_2O_3 sample VBO can be calculated. The Eqn. becomes,

$$VBO = (E_{Al\,2p} - E_V)^{Al_2O_3} + (E_{Ta4f} - E_{Al\,2p})^{Interface} - (E_{Ta4f} - E_V)^{Ta_2O_5} \quad (4.3)$$

$$VBO = (74.27 - 2.67) + (26.39 - 74.76) - (26.10 - 2.74)$$
$$VBO = -0.13eV$$

It is evident that the valence band offsets values using core level positions from both interface samples are within ± 0.03 eV error. In summary, the VBO for Ta_2O_5/Al_2O_3 is estimated to be 0.09 ± 0.03 eV.

4.2.3.5 XPS CL fittings for bulk Nb_2O_5 sample

The core level fittings were performed for the Nb 3d and O 1s levels. The binding energy difference and branching ratio between Nb $3d_{5/2}$ and Nb $3d_{3/2}$ were 2.72 eV and 3:2 respectively [15]. The Nb 3d and O 1s core level fittings are shown in Figures 4.15 (a) and (b) respectively.

The binding energy value of the Nb $3d_{5/2}$ and Nb $3d_{3/2}$ were observed at 207.12 eV and 209.84 eV respectively (Figure 4.15 (a)) that were in line with reported 207.4 eV and 207.6 eV for Nb $3d_{5/2}$ [18, 22]. The corresponding binding energy value of Nb-O was extracted at 530.25 eV (Figure 4.15 (b)) which was comparable to reported 530.4 eV [22]. The valence band maximum of 2.61 ± 0.02 eV was calculated as illustrated in Figure 4.15 (c).

The band gap was extracted using the electron energy loss spectrum shown in Figure 4.15 (d) and estimated to be 3.96 eV although the band gap value extracted from VASE was 3.76 eV.

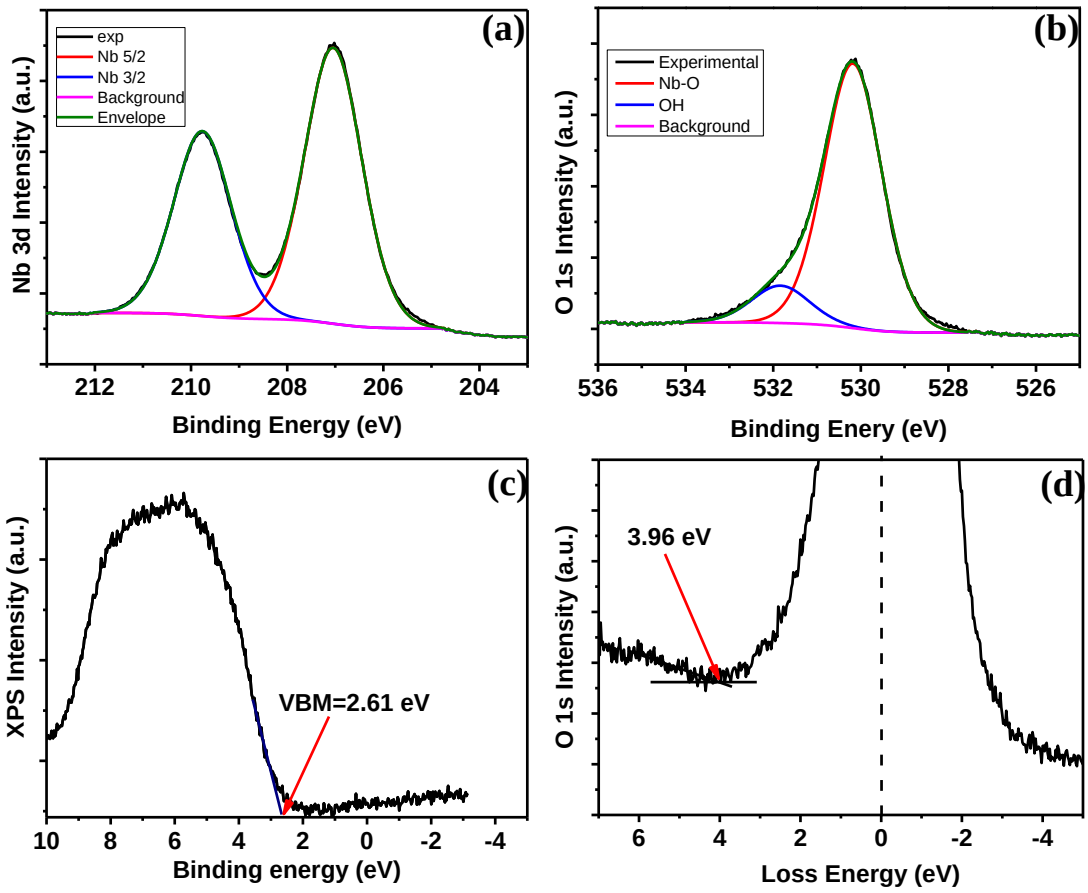

Figure 4.15 (a) Nb 3d CL fitting, (b) O 1s CL fitting, (c) VBM and (d) electron energy loss spectrum of bulk Nb_2O_5 sample.

4.2.3.6 XPS CL fittings for interface Nb_2O_5/Al_2O_3 sample

A sample with a thin layer (3.8 nm) of Nb_2O_5 was measured and analysed in order to characterise the Nb_2O_5/Al_2O_3 interface. The core level fittings were performed for Nb 3d, Al 2p and O 1s as shown in Figure 4.16.

The core level fittings were carried using the same analytical approach as before. The corresponding binding energy values for Nb $3d_{3/2}$ and Nb $3d_{5/2}$ were recorded at 209.93 eV and 207.21 eV respectively (Figure 4.16 (a)). Then the Al 2p CL fitting was performed with two sub-peaks representing Al $2p_{3/2}$ and Al $2p_{1/2}$ and the corresponding binding energy values were 74.75 eV and 75.19 eV (Figure 4.16 (b)).

The O 1s CL was fitted with three sub-peaks referring to Al-O, Nb-O and -OH peaks as shown in Figure 4.16 (c). A summary of binding energy values of the key CLs for bulk Al_2O_3, bulk Nb_2O_5 and thin Nb_2O_5/Al_2O_3 sample are summarised in Table 4.3. It was sufficient to perform the measurement on one interface sample for Nb_2O_5/Al_2O_3 after considering the consistent VBO values extracted for Ta_2O_5/Al_2O_3 using both interface samples.

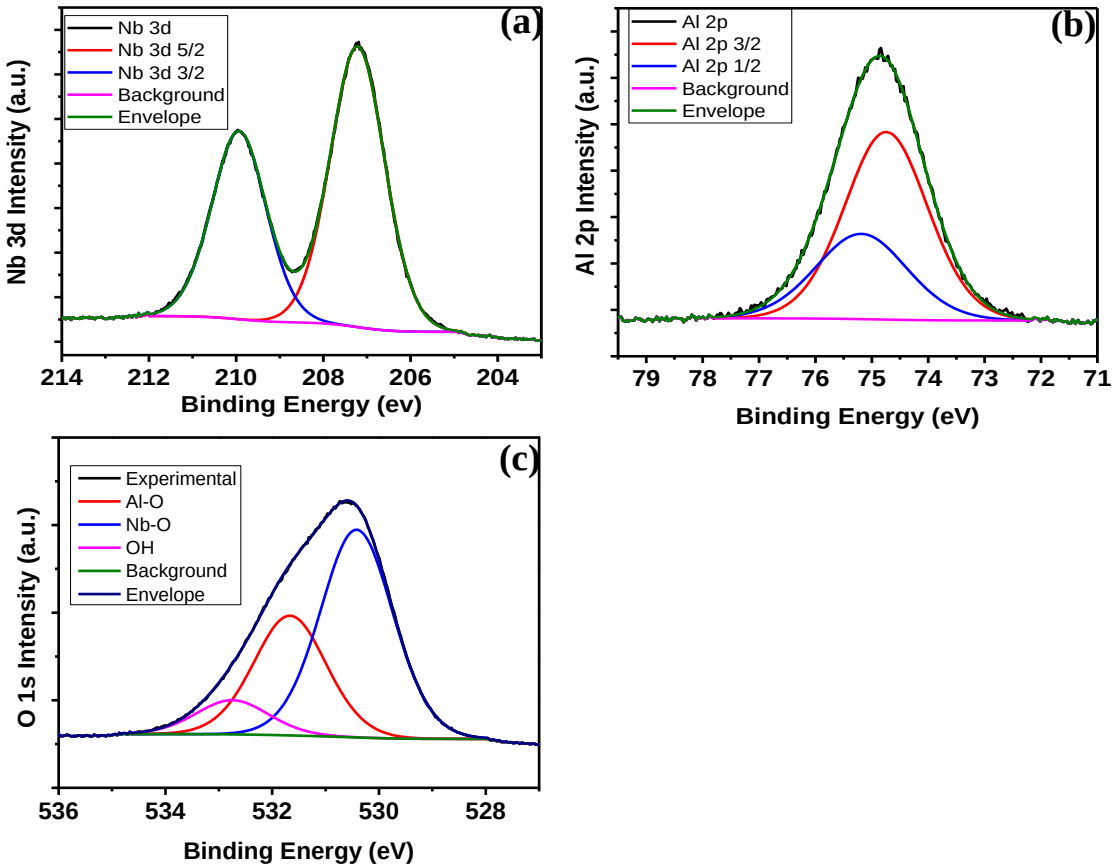

Figure 4.16: XPS CL fittings for (a) Nb 3d, (b) Al 2p and (c) O 1s for interface 3.8 nm Nb_2O_5/17.28 nm Al_2O_3 sample.

Table 4.3: A summary of CL binding energy values for bulk Al_2O_3, bulk Nb_2O_5 and interfacial Nb_2O_5/Al_2O_3 samples.

Core Level	Bulk Al_2O_3 (eV)	Bulk Nb_2O_5 (eV)	3.8 nm Nb_2O_5/17.28 nm Al_2O_3 (eV)
Nb $3d_{5/2}$		207.12 ± 0.1	207.21 ± 0.1
Nb $3d_{3/2}$		209.84 ± 0.1	209.93 ± 0.1
O 1s	531.17 ± 0.1	530.25 ± 0.1	Nb-O 530.57 ± 0.1 Al-O 531.67 ± 0.1
Al $2p_{3/2}$	74.27 ± 0.1		74.75 ± 0.1
Al $2p_{1/2}$	74.71 ± 0.1		75.19 ± 0.1
VBM	2.67 ± 0.2	2.61 ± 0.2	

4.2.3.7 VBO estimation of Nb_2O_5/Al_2O_3 sample

The valence band offset at the interface of Nb_2O_5/Al_2O_3 was calculated using the Kraut's method, using the equation:

$$VBO = (E_{Al\,2p} - E_V)^{Al_2O_3} + (E_{Nb3d} - E_{Al\,2p})^{Interface} - (E_{Nb3d} - E_V)^{Nb_2O_5} \quad (4.4)$$

which gives,

$$VBO = (74.27 - 2.67) + (207.21 - 74.75) - (207.12 - 2.61) = -0.45eV$$

It can be seen that the valence band offset at the interface Nb_2O_5/Al_2O_3 was larger compared to Ta_2O_5/Al_2O_3 interface. The conduction band offsets for Ta_2O_5/Al_2O_3 and Nb_2O_5/Al_2O_3 were estimated to be 1.94 eV and 2.22 eV respectively. The relatively larger conduction band offset at the Nb_2O_5/Al_2O_3 interface will result in deeper potential well in MIIM structure compared to the Ta_2O_5/Al_2O_3 structure.

4.2.3.8 Electron affinity estimation for Al_2O_3, Nb_2O_5 and Ta_2O_5

The electron affinity of the oxides that were used in the diode structures was calculated by using the equation [13]:

$$\chi = IE - E_g \quad (4.5)$$

where *IE* is the ionisation energy given as [13]:

$$IE = XPS\ source\ energy - (E_{secondary\ cut\ off} + E_{bias} - VBM) \quad (4.6)$$

In this series of XPS experiments, a bias of 10 V (equivalent to energy of E_{bias} = 10 eV) was applied to the bulk oxide samples in order to distinguish the secondary cut off signal from the analyser (see Chapter 2, section 2.3.2.4). The objective of this was to separate the energy of analyser and sample secondary electrons cut-offs [13]. The XPS source energy (Mg Kα) was 1253.6 eV. The *IE* was found by extracting the energy of secondary electrons cut-off and valence band maxima from the XPS spectra shown in Figure 4.17.

The secondary cut-off and VBM for Al_2O_3 sample were extracted to be 1240.24 ± 0.2 eV as shown in Figure 4.17 (a) and 4.67 ± 0.2 eV Figure 4.17 (b) respectively. Moreover, the secondary cut-off and VBM for Nb_2O_5 were 1239.74 ± 0.2 eV (Figure 4.17 (c)) and 3.62 ± 0.2 eV (Figure 4.17 (d)) respectively. The secondary cut off and VBM for Ta_2O_5 were 1240.48 ± 0.2 eV (Figure 4.17 (e)) and 4.11 ± 0.2 eV (Figure 4.17 (f)) respectively. These values led to

IE values of 8.03 ± 0.3 eV, 7.48 ± 0.3 eV and 7.23 ± 0.3 eV for Al_2O_3, Nb_2O_5 and Ta_2O_5 respectively.

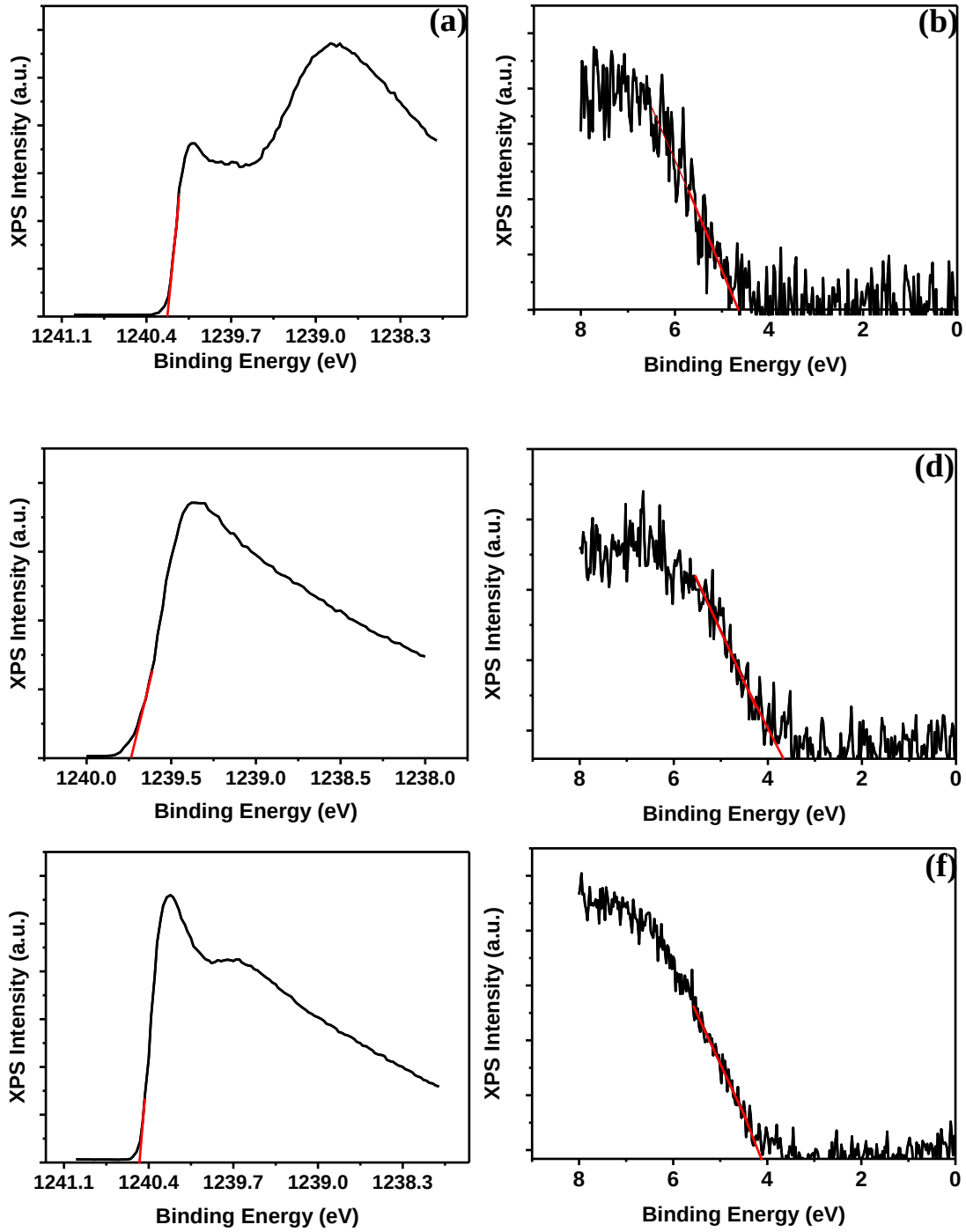

Figure 4.17: XPS spectra of (a, c, e) secondary cut-off and (b, d, f) valence band maximum of bulk Al_2O_3, Nb_2O_5 and Ta_2O_5.

The C 1s correction was not necessary for spectra in Figure 4.17 as the difference between binding energies of secondary electrons cut off and valence band maximum was considered. Then the electron affinity can be extracted by considering the difference between the *IE* and the band gap (Eqn. 4.6). The band gaps of Al_2O_3, Nb_2O_5 and Ta_2O_5 were found to be 6.43 ± 0.1 eV, 3.76 ± 0.1 eV and 4.4 ± 0.1 eV respectively by XPS and VASE. Hence the extracted

electron affinity of Al_2O_3, Nb_2O_5 and Ta_2O_5 were 1.60 ± 0.2 eV, 3.72 ± 0.2 eV and 2.83 ± 0.2 eV respectively.

The extracted electron affinity of Al_2O_3 and Nb_2O_5 resulted in a CBO of 2.12 ± 0.3 eV which is in agreement with the CBO of 2.22 ± 0.2 eV, found from VBO and the band gap of the oxides. The CBO at the interface of Ta_2O_5/Al_2O_3 was 1.23 ± 0.3 eV if the calculated electron affinity of Ta_2O_5 (2.83± 0.2 eV) was used. However, the CBO found after considering the VBO and band gap of oxides was 1.94 ± 0.2 eV. Therefore further analysis was performed to ensure the electron affinity of Ta_2O_5 considering the electron affinity values of Nb_2O_5 and Al_2O_3 as reference values. This was achieved using Fowler-Nordheim plots based on *IV* characteristics extracted on MIM structures as discussed in section 4.3.

4.3 Work function estimation of Al, Nb, Ta, W and Ag

Fowler-Nordheim tunnelling analysis was carried out in order to extract the barrier height at the metal/oxide interface. The barrier height at the metal/oxide interface can be found by extracting the slope of Fowler-Nordheim tunnelling plot (Eqn. 4.7):

$$Slope = \left(\frac{-1.33\sqrt{2m_{ox}}(q\phi_b)^{\frac{3}{2}}}{\hbar q} \right) \tag{4.7}$$

where q - electron charge, $\hbar$ - plank's constant, ϕ_b - barrier height, m_{ox}- effective mass of electrons in the oxide, considered to be $0.5 \times m_0$ [23] where $m_0 = 9.1 \times 10^{-31}$ kg.

It is possible to correlate the extracted electron affinity (χ) values to the barrier heights (ϕ_b) calculated and extract the work function of metals that were used in MIM/MIIM/MIIIM structures.

$$WF = \chi + \phi_b \tag{4.8}$$

The barrier height (in eV) at the interfaces of metal/Nb_2O_5 structures were extracted prior to extracting the barrier heights at the interfaces of metal/Ta_2O_5 due to the inconsistent electron affinity extracted for Ta_2O_5.

4.3.1 Barrier height at the interface of Al/Nb_2O_5

The *IV* measurements were done on Al/1.6 nm AlO_x/5 nm Nb_2O_5/Al to perform Fowler-Nordheim analysis. The aim was to fabricate an MIM structure; however the inevitable growth of the Al native oxide (AlO_x) resulted in obtaining two oxides between the Al electrodes.

Therefore it was crucial to calculate the potential applied on Nb_2O_5 layer to perform Fowler-Nordheim analysis.

The barrier height was extracted by evaluating the slope of the Fowler-Nordheim plot as shown in Figure 4.18 (a). The linear region from the Fowler-Nordheim plot shown in Figure 4.18 (b) was selected in order to extract the slope precisely.

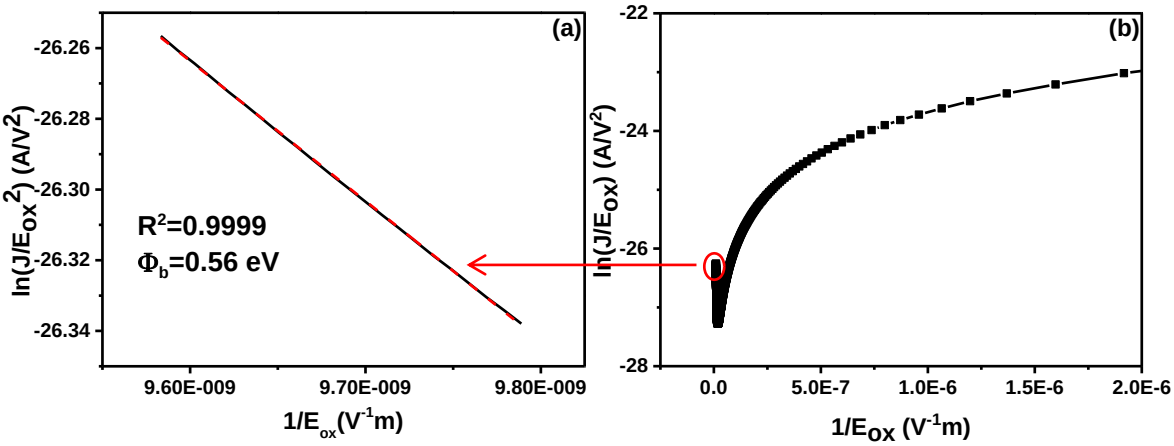

Figure 4.18: Fowler-Nordheim plots for (a) limited range (b) full range of Al/1.6 nm AlO_x/5 nm Nb_2O_5/Al.

The barrier height was calculated to be 0.56 eV at the Al/Nb_2O_5 interface. Then using the Eqn. 4.8, the estimated work function of Al was 4.28 eV. The Al work function extracted was in agreement with the reported 4.26 eV [24] and 4.28 [25] eV in the literature.

4.3.2 Barrier height at the interface of Nb/5 nm Nb_2O_5

The *IV* measurements were done on Nb/5 nm Nb_2O_5/Nb in order to perform Fowler-Nordheim analysis and extract the barrier height at the interface of Nb/Nb_2O_5. Moreover, it was possible to eliminate the effect of AlO_x layer by replacing Al with Nb. The Fowler-Nordheim plot is shown in Figure 4.19:

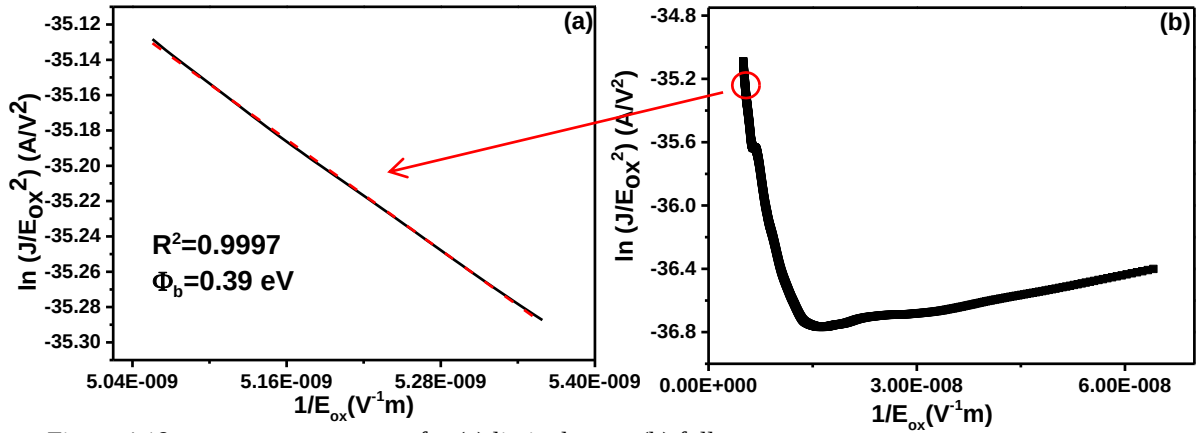

Figure 4.19: Fowler-Nordheim plots for (a) limited range (b) full range of Nb/5 nm Nb_2O_5/Nb.

The barrier height at the Nb/Nb_2O_5 interface was calculated to be 0.39 eV which led to a work function of 4.11 eV (Eqn. 4.8).

4.3.3 Barrier height at the interface of Al/Ta_2O_5

The work function of Al extracted after analysing the Al/1.6 nm AlO_x/5 nm Nb_2O_5/Al was used as a reference value to calculate the electron affinity of Ta_2O_5. It was mandatory to evaluate and use the potential applied on Ta_2O_5 layer while performing Fowler-Nordheim analysis due to the formation of AlO_x. A barrier height of 0.74 eV at the interface of Al/Ta_2O_5 was evaluated by extracting the slope of the Fowler-Nordheim plot shown in Figure 4.20.

$$\chi = WF - \phi_b \tag{4.9}$$

The electron affinity extracted for Ta_2O_5 was 3.54 eV after considering the Eqn. 4.9.

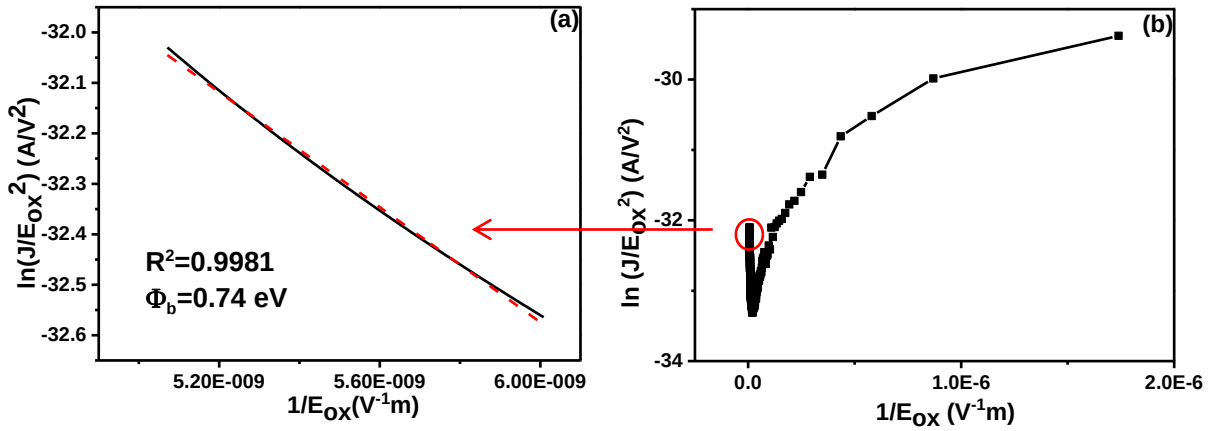

Figure 4.20: Fowler-Nordheim plots for (a) limited range (b) full range of Al/1.6 nm AlO_x/5 nm Ta_2O_5/Al.

4.3.4 Barrier height at the interface of Ta/Ta_2O_5

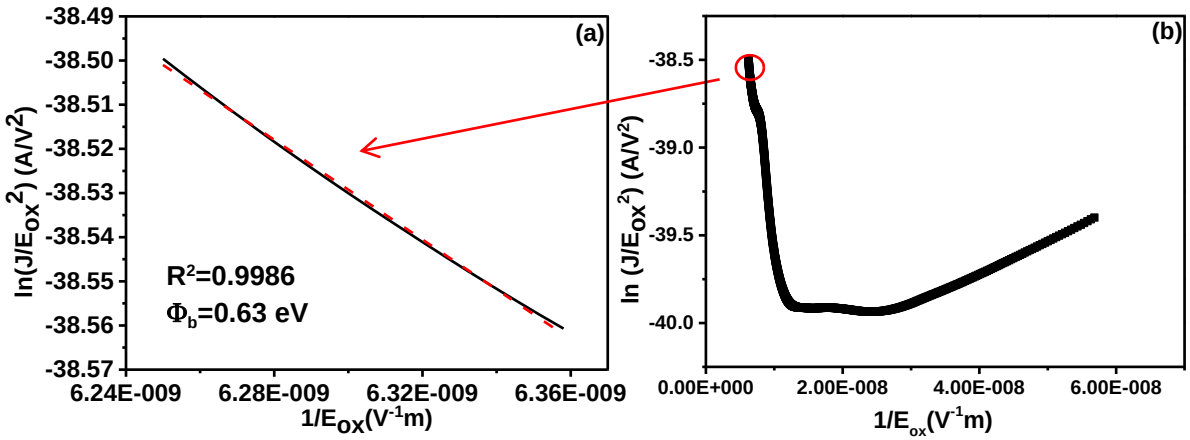

Figure 4.21: Fowler-Nordheim plots for (a) limited range (b) full range of Ta/5 nm Ta_2O_5/Ta.

The *IV* measurements on Ta/5 nm Ta_2O_5/Ta were done to perform Fowler-Nordheim analysis. Moreover, the electron affinity of Ta_2O_5 was extracted before as 3.54 eV. Therefore it was possible to estimate the work function of Ta by extracting the barrier height at the Ta/Ta_2O_5

interface. The barrier height was estimated by extracting the slope of Fowler-Nordheim plot shown in Figure 4.21

The barrier height at the Ta/Ta_2O_5 interface was extracted to be 0.63 eV which led to a work function of 4.17 eV for Ta.

4.3.5 Barrier height at the interface of W/Nb_2O_5 and W/Ta_2O_5

The barrier height at the interfaces of W/Nb_2O_5 and W/Ta_2O_5 were found to be 0.96 eV and 1.1 eV respectively after extracting the slopes from the Fowler-Nordheim plots shown in Figure 4.22.

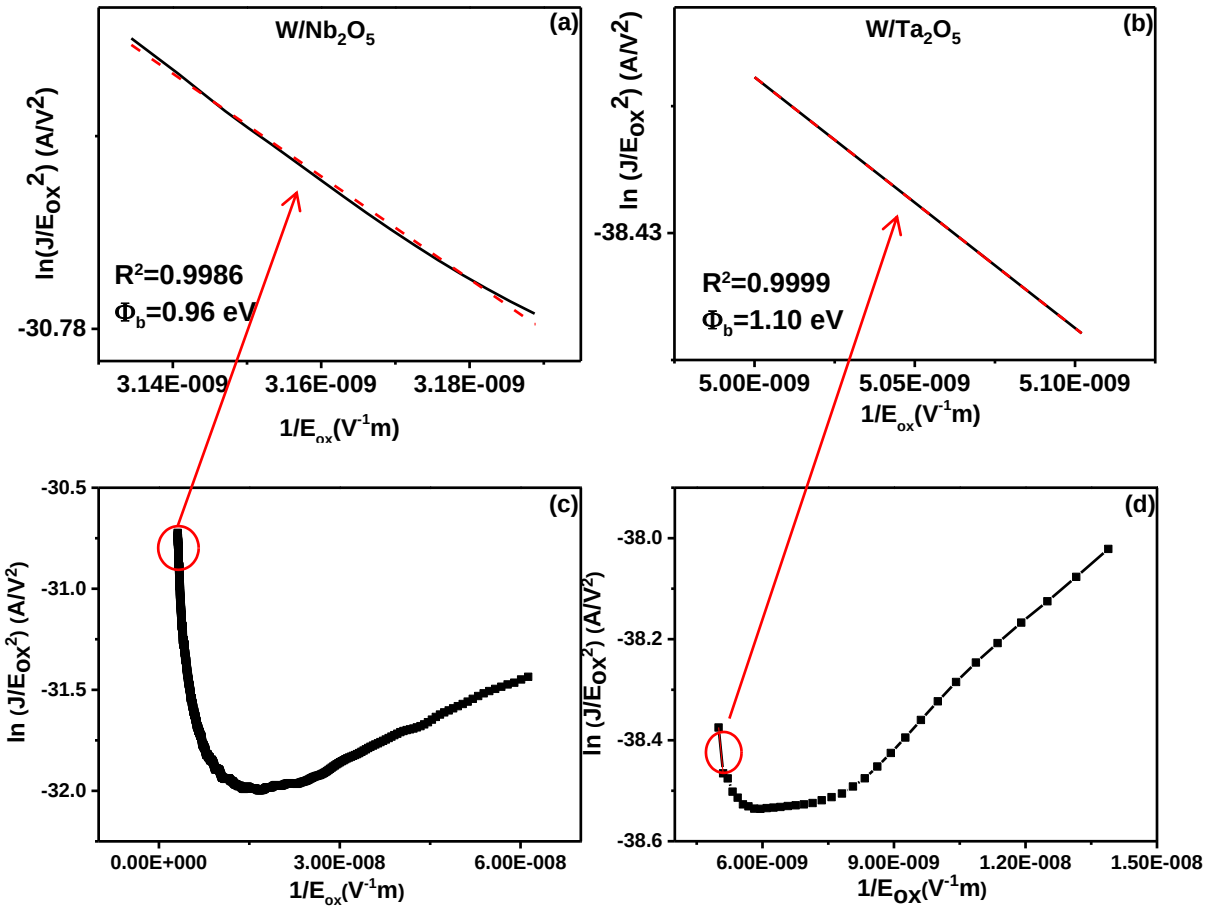

Figure 4.22: Fowler-Nordheim plot of (a) W/5 nm Nb_2O_5/W and (b) W/5 nm Ta_2O_5/W for a limited range, (c) W/ 5 nm Nb_2O_5/W and (d) W/5 nm Ta_2O_5/W for full range.

A work function of 4.68 eV was estimated for W considering the electron affinity of Nb_2O_5 (3.72 eV). Moreover, this work function value resulted in an electron affinity of 3.58 eV for Ta_2O_5. This is in close agreement with the electron affinity of 3.54 eV extracted from Al/1.6 nm AlO_x/5 nm Ta_2O_5/Al structure. Similar values of 4.55 eV [24, 26] and 4.63 eV [24] were reported as the work function of W.

4.3.6 Barrier height at the interface of Ag/Ta_2O_5

The barrier height at the Ag/Ta_2O_5 was assessed by extracting the slope in Figure 4.23.

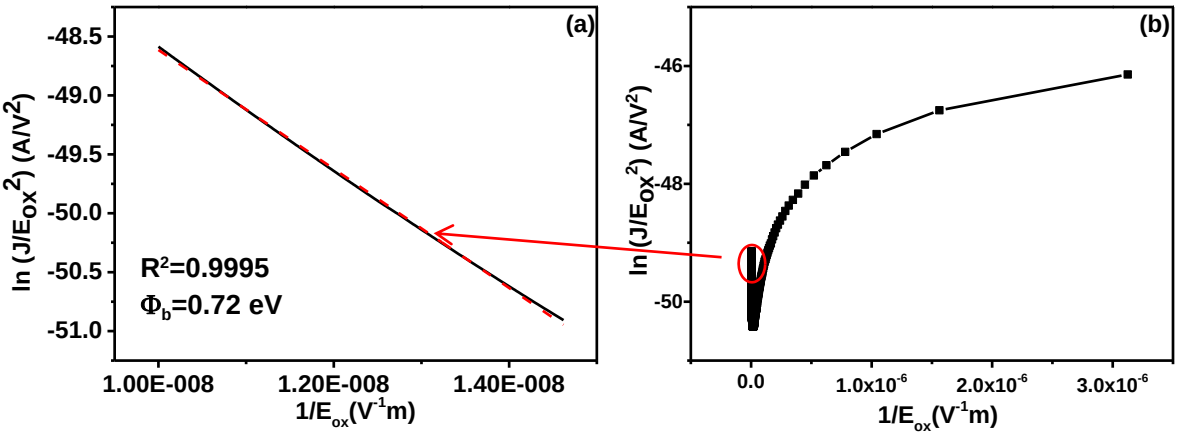

Figure 4.23: Fowler-Nordheim plots for (a) limited range (b) full range of Ag/5 nm Ta_2O_5/Ag.

The estimated barrier height was 0.72 eV. Moreover, the work function of Ag is reported to be 4.30 eV [27] resulting an electron affinity of 3.58 eV for Ta_2O_5.

As proven from Fowler-Nordheim analysis the electron affinity of Ta_2O_5 (3.54 $\pm$ 0.04 eV) was extracted precisely with the aid of many devices. It is possible to extract a CBO of 1.94 eV using the electron affinity values of Ta_2O_5 and Al_2O_3 extracted by Fowler-Nordheim analysis and electron affinity measurements.

4.3 Discussion and summary

The device fabrication process and the physical and electrical characterisation of the materials used in the diode structures were explained in detail in this chapter. The metals were deposited either by thermal evaporation or DC sputtering whereas the oxides were deposited either by ALD or RF sputtering. The devices were patterned either by photolithography or shadow mask process. The materials that are used in MIM/MIIM/MIIIM structures were physically characterised by AFM, XPS and VASE. The uniformity and the thicknesses of the deposited oxides were assessed by VASE. The surface roughness of the bottom metal electrode had to be evaluated and improved to values < 1 nm due to its effect on the thin oxide layers electrical performance in the diode structures. Moreover, the VASE and XPS measurements were performed in order to extract the band gap, valence band offset, conduction band offset and electron affinity values of the oxides used. Nonetheless, the main objective was to derive band diagrams by combining XPS and VASE analysis.

Table 4.4: Comparison between experimentally obtained and reported work function and electron affinity values.

Material	Experimental work function/electron affinity (eV)	Reported work function/electron affinity (eV)
Al	4.28 ± 0.2 (FNT and XPS)	4.26 [20], 4.28 [21]
Ta	4.17 ± 0.2 (FNT)	4.25 [21], 4.35 [28]
Nb	4.11 ± 0.2 (FNT)	4.30 [29]
W	4.64 ± 0.3 (FNT)	4.55 [20, 22], 4.63 [20]
Ag	4.26 ± 0.1 (FNT)	4.30 [23]
Cr		4.50 [24]
Al_2O_3	1.60 ± 0.2 (XPS)	1.40 [30]
Ta_2O_5	3.54 ± 0.2 (XPS)	4.68 [31], 4.05 [32], 3.20 [28], 3.83 [26], 4.40 [33]
Nb_2O_5	3.72 ± 0.2 (XPS and FNT)	4.23 [26], 4 [30]

The conduction band offset was determined using the extracted VBO and band gap values, and also by considering the difference in electron affinity values extracted for Nb_2O_5 or Ta_2O_5 and Al_2O_3. There was a discrepancy in CBO values of 0.61 eV; however the CBO extracted considering both methods for Nb_2O_5 and Al_2O_3 interface varied only by 0.11 eV. Therefore electrical analysis was performed to extract the work function of metals and also the electron affinity of Ta_2O_5 while the electron affinity values for Nb_2O_5 and Al_2O_3 were precisely calculated.

Finally, the extracted electron affinity and work function values of oxides and metals are compared to the values reported in the literature as illustrated in Table 4.4.

References

[1] H.-W. Hübers, G. W. Schwaab, H. P. Röser, "Video detection and mixing performance of GaAsSchottky-barrier diodes at 30 THz and comparison with metal-insulator-metal diodes", J. Appl. Phys., 75, 4243 (1994)

[2] A New Technology for Terahertz Electronics, Phiar Corporation, Np 1.0(2013)

[3] A. Sanchez, C. F. Davis Jr., K. C. Liu, A. Javan, "The MOM tunneling diode: Theoretical estimate of its performance at microwave and infrared frequencies", J. Appl. Phys., 49, 5270 (1978)

[4] L. O. Hocker, D. R. Sokoloff, V. Daneu, A. Szoke, A. Javan, "Frequency mixing in the infrared and far-infrared using a metal-to-metal point contact diode", Appl. Phys. Lett., 12, 401 (1968)

[5] R. Stratton, "Volt-Current characteristics for tunnelling through insulator films", J. Phys. Chem. Solids, 23(9), 1177 (1962)

[6] P. C. D. Hobbs, R. B. Laibowitz, F. R. Libsch, “Ni-Nio-Ni tunnel junctions for terahertz and infrared detection”, Appl. Opt., 44 (32), 6813 (2005)

[7] J. G. Simmons, “Generalized formula for the electric tunnel effect between similar electrodes separated by a thin insulating film”, J. Appl. Phys., 34, 1793 (1963)

[8] J. G. Simmons, “Conduction in thin dielectric films”, J. Phys. D: Appl. Phys., 4, 613 (1971)

[9] J. G. Simmons, “Electric tunnel effect between dissimilar electrodes separated by a thin insulating film”, J. Appl. Phys., 34, 2581 (1963)

[10] N. Alimardani, E. W. Cowell III, J. F. Wager, J. F. Conley Jr., D. R. Evans, M. Chin, S. J. Kilpatrick, M. Dubey, “Impact of electrode roughness on metal-insulator-metal tunnel diodes with atomic layer deposited Al_2O_3 tunnel barriers”, J. Vac. Sci. Technol. A, 30, 01A113 (2012)

[11] N. Alimardani, J. McGlone, J.F. Wager, J.F. Conley Jr., “Conduction process in metal-insulator-metal diodes with Ta_2O_5 and Nb_2O_5 insulators deposited by Atomic Layer Deposition”, J. Vac. Sci. and Tech. A, 32, 01A122-1 (2014)

[12] E. A. Kraut, R. W. Grant, J. R. Waldrop, S. P. Kowalczyk, “Precise determination of the valence-band edge in X-Ray photoemission spectra: Application to measurement of semiconductor interface potentials”, Phys. Rev. Lett., 44, 1620 (1980)

[13] R. Schlaf , H. Murata , Z.H. Kafaf, “Work function measurements on indium tin oxide films”, J. Electron Spectroscopy and Related Phenomena, 120, 149 (2001)

[14] M. C. Burrell, J. J. Chera, “Charge correction of the binding energy scale in XPS analysis of polymers using surface deposition of PDMS”, Surf. Interface Anal., 27, 811 (1999)

[15] J.F. Moulder, W.F. Stickle, P.E. Sobol, K.D. Bomben, “Handbook of X-ray photoelectron spectroscopy”, Perkin-Elmer Corp, Eden Prairie, 1992

[16] J. Haeberle, K. Henkel, H. Gargouri, F. Naumann, B. Gruska, M. Arens, M. Tallarida, D. Schmeiber, “Ellipsometry and XPS comparative studies of thermal and plasma enhanced atomic layer deposited Al_2O_3-films”, J. Nanotechnol., 4, 732 (2013)

[17] I. Geppert, M. Eizenberg, A. Ali, S. Datta, “Band offsets determination and interfacial chemical properties of the Al_2O_3/GaSbAl_2O_3/GaSb system”, Appl. Phys. Lett., 97, 162109 (2010)

[18] D. D. Sarma, C. N. R. Rao, “XPES Studies of oxides of second- and third row transition metals including rare earths”, J. Electron Spectroscopy and Related Phenomena, 20, 25-45 (1980)

[19] S. Husain, S. Akansel, A. Kumar, P. Svedlindh, S. Chaudhary, “Growth of Co2FeAl Heusler alloy thin films on Si(100) having very small Gilbert damping by Ion beam sputtering”, Sci. Rep. 6, 28692 (2016)

[20] R. Shi, J. Lin, Y. Wang, J. Xu, Y. Zhu, “Visible-Light photocatalytic degradation of BiTaO4 photocatalyst and mechanism of photocorrosion suppression”, J. Phys. Chem. C, 114, 6472 (2010)

[21] M. Perego, G. Seguini, “Charging phenomena in dielectric/semiconductor heterostructures during x-ray photoelectron spectroscopy measurements”, J. Appl. Phys., 110, 053711 (2011)

[22] N. Ozer, M. D. Rubin, C. M. Lampert, "Optical and electrochemical characteristics of niobium oxide films prepared by sol-gel process and magnetron sputtering A comparison", Solar Energy Mate. And solar cells, 40, 285 (1996)

[23] B. C. Lai, N. Kung, J. Y. Lee, "A study on the capacitance-voltage characteristics of metl-Ta_2O_5-silicon capacitors for very large scale integration metal-oxide-semiconductor gate oxide applications", J. Appl. Phys., 85, 4087 (1999)

[24] C. Wyon, "Future technology for advanced MOS devices", Nuc. Instru. and Meth. in Phys. Res., B 186: 380-391 (2002)

[25] Y. Yeo, T. King, C. Hu, "Metal-dielectric band alignment and its implications for metal gate complementary metal-oxide-semiconductor technology", J. Appl. Phys., 92, 7266 (2002)

[26] S. Grover, G. Moddel, "Engineering the current-voltage characteristics of metal-insulator-metal diodes using double-insulator tunnel barriers", Solid State Electron., 67(1), 94 (2012)

[27] A. J. Moulson, J. M. Herbert, "Electromechanics: materials, properties and applications", 2nd Edition, Wiley, 2003

[28] J. Han, W. K. Kim, S. J. Hong, S. K. Park, "Effects of post annealing on current-voltage characteristics of metal-insulator (Ta_2O_5)-metal type thin-film diodes", J. the Korean Phys. Soc., 39, 686 (2001)

[29] R.J.P. Bain, G.B. Donaldson, "Sputtered all-niobium Josephson tunnel junctions with barrier oxide protected by gold", J. Phys. C: Solid State Phys., 18, 2539 (1985)

[30] N. Alimardani, S. King, Be. French, C. Tan, B. Lampert, J. Conley Jr., ''Investigation of the impact of insulator material on the performance of dissimilar electrode metal-insulator-metal diodes'' J. Appl. Phys., 116 , 024508-1 (2014)

[31] A. Teverovsky, "Effect of post-HALT annealing on leakage currents in solid tantalum capacitors", Capacitors and Resistors Technology Symposium, USA, 43 (2010)

[32] S. Ezhilvalavan, Tseung-Yuen Tseng, "Electrical properties of Ta_2O_5 thin films deposited on Cu", Thin Solid Films, 360, 268 (2000)

[33] K.L. Wang, B. Lai, M. Lu, X. Zhou, L.S. Liao, X.M. Ding, X.Y. Hou, S.T. Lee, "Electronic structure and energy level alignment of $Alq_3/Al_2O_3/Al$ and Alq_3/Al interfaces studied by ultraviolet photoemission spectroscopy", Thin Solid Films, 363, 178 (2000)

Chapter 5

5. Metal-insulator-metal (MIM) devices

Metal-insulator-metal (MIM) diodes have been identified as potential candidates to replace conventional diodes, to overcome the limitations of semiconductor technology in the high frequency regime [1-5]. The MIM rectifier coupled rectenna could operate at ambient temperature, same as conventional rectifiers in a wide range of applications such as detectors of terahertz and infrared radiation [6], terahertz interconnects, terahertz imaging and energy harvesting [7-9]. The non-linear characteristics of the MIM diode are achieved by the transport mechanisms of thermionic emission and quantum mechanical tunnelling however for less temperature dependent high speed operation [10], the dominant conduction should be quantum tunnelling.

The conduction mechanisms are explained using the Figure 5.1.

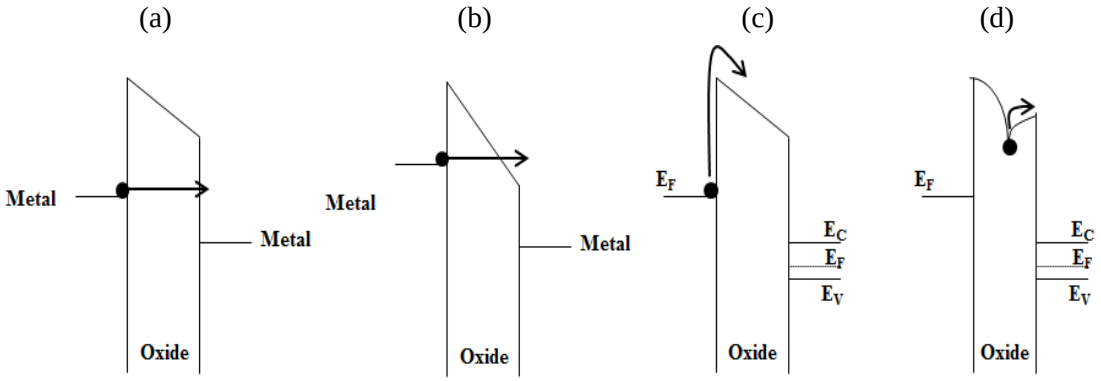

Figure 5.1: Energy band diagrams for (a) direct tunnelling, (b) Fowler-Nordheim tunnelling, (c) Schottky emission and (d) Poole-Frenkel emission.

Direct Tunnelling

As can be seen in Figure 5.1 (a), electrons from the first metal electrode (left) travel through the forbidden energy barrier formed by the ultra-thin dielectric layer (< 5 nm) to the right metal electrode [11]. An approximate equation for direct tunnelling (DT) is:

$$J_{DT} = \frac{q^2}{8\pi^2 \hbar (t_{ox})} E_{ox}^2 (\phi_b - \frac{V_{app}}{2}) \exp\left(\frac{-1.33\sqrt{2m_{ox}q}(\phi_b - (\phi_b^{\frac{3}{2}} - V_{app})^{\frac{3}{2}}}{\hbar E_{ox}} \right), \quad (5.1)$$

where q is electron charge, t_{ox} is oxide thickness, E_{ox} is electric field in the oxide, $\hbar$ is Planck's constant, V_{app} is applied gate voltage, ϕ_b is barrier height at the injecting electrode, m_{ox} is electron effective mass.

Fowler Nordheim Tunnelling

Fowler Nordheim tunnelling (FNT) refers to the scenario when electrons travel through a triangular potential barrier where the thickness of the barrier has a strong dependence upon the applied voltage between the two metal electrode plates as shown in Figure 5.1 (b) [12]. When the barrier is bent, the electrons tunnel through only a partial width of the barrier. The barrier height can be defined as the energy level difference between the Fermi level of the metal and the lowest energy level of the conduction band of the oxide. The equation for FN can be written as [12]

$$J_{FN} = \frac{q^3}{16\pi^2 \hbar(q\phi_b)} E_{ox}^2 \exp\left(\frac{-1.33\sqrt{2m_{ox}}(q\phi_b)^{\frac{3}{2}}}{\hbar q E_{ox}} \right). \tag{5.2}$$

Schottky emission

The electrons in the metal electrode can overcome the energy barrier formed at the metal/insulator interface if they can obtain enough energy provided by thermal activation [13]. This phenomenon is illustrated in Figure 5.1 (c). The energy barrier at the metal/oxide interface may become smaller due to image force lowering. The expression of Schottky Emission (SE) is,

$$J_{SE} = A^* T^2 \exp\left[-q\left(\Phi_B - \sqrt{\frac{qE_{ox}}{4\pi\varepsilon_i \varepsilon_o}} \right) \right] \tag{5.3}$$

$$A^* = \frac{4\pi q k^2 m^*}{h^3} = \frac{120 m^*}{m_0},$$

where A^* is the Richardson constant and Φ_B is the Schottky barrier height, ε_i is the optical dielectric constant, T is the absolute temperature, ε_o is the dielectric constant in vacuum, m^* is the effective electron mass in dielectric and m_0 is the free electron mass. The effective electron mass of Ta_2O_5 was reported to be $0.5 \times m_0$ [14].

Image-force lowering

The energy barrier will be lowered for charge emission in the presence of an electric field due to the induced image-force as can be seen in Figure 5.2 [15]. This phenomenon is known as the image-force lowering/Schottky effect or Schottky barrier lowering. When a metal oxide interface is assumed, the minimum energy required by an electron to eject itself from the Fermi

level of the metal to the vacuum level is the work function. When an electron has travelled a distance x, from the metal, a positive image charge will be induced on the surface of the metal. The force of attraction, F between the electron and its image charge is equivalent to the force that will create between the electron and an equal positive charge at the distance, – x [15].

Integration of force results in the work done to an electron travelling from infinity to x. Therefore,

$$E(x) = \frac{-q^2}{16\pi\varepsilon_0\varepsilon_{ox}x}. \tag{5.4}$$

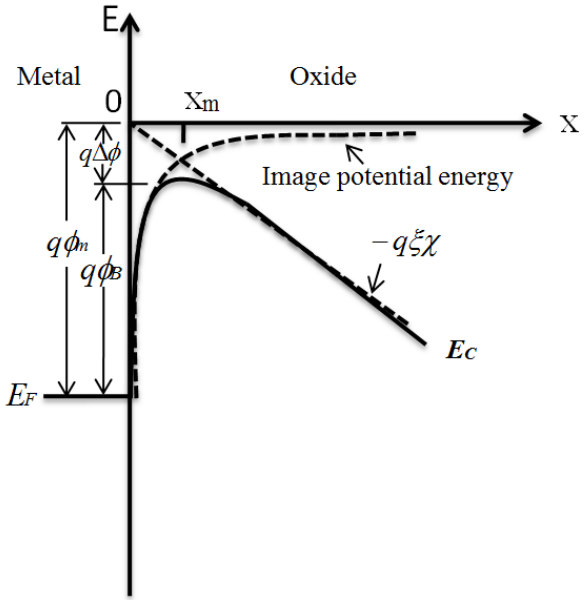

Figure 5.2: Image force barrier lowering.

The potential energy of the electron sitting at distance x is shown in Figure 5.2 and therefore the total potential energy *PE* when an external field is applied,

$$PE(\chi) = \frac{-q^2}{16\pi\varepsilon_0\varepsilon_{ox}x} - q|\xi|x.$$

This equation has a maximum value. The image-force lowering $(\Delta\phi)$ is given by,

$$\frac{d(PE)}{dx} = 0$$

$$x_m = \sqrt{\frac{q}{16\pi\varepsilon_{ox}\varepsilon_0|\xi|}}$$

$$\Delta\phi = \sqrt{\frac{q|\xi|}{4\pi\varepsilon_{ox}}}\,. \tag{5.5}$$

However due to the large values of ε_{ox}, barrier lowering is negligible in this work. For example if ε_{ox} =12, then the barrier lowering is only 0.036 V for $\xi = 10^5$ V/cm [15].

Poole-Frenkel emission

Poole-Frenkel (PF) emission is one of the bulk-limited conduction mechanisms which arises from defect energy states in the dielectric. The trap energy level in the dielectric film is a critical parameter in bulk-limited conduction mechanisms. The Coulomb potential energy of the electron can be reduced by an applied electric field when an electron is in a trapping centre. This reduction in barrier height enhances the thermal emission rate for an electron excited from the trap level to the conduction band of the dielectric as illustrated in Figure 5.1 (d) [13]. The current density for PF can be obtained by,

$$J_{PF} = \sigma E_{ox} \exp(\beta_{PF}\sqrt{E_{ox}})\exp(-(q\phi_t)/kT) \tag{5.6}$$

$$\sigma = qn_o\mu$$

$$\beta_{PF} = (q/kT)\sqrt{(q/(\pi\varepsilon_o\varepsilon_i))}$$

where μ is the electron drift mobility, n_o is the carrier density, $q\phi_t$ is the trap energy level.

Background of MIM structures

The MIM diodes comprise an ultra-thin dielectric film sandwiched in between two metal electrodes. The work function of the metal electrodes must be large compared to the electron affinity of the dielectric in order to create a barrier at the metal/dielectric interface. When two electrodes are separated by a thin dielectric, the carriers will tunnel through the film depending on the thickness of the film [16]. Quantum mechanical electron tunnelling through the high-k oxide layer has to be the dominant conduction mechanism leading to a time constant in the order of 10^{-15} seconds [17]; therefore the diode will operate at optical frequencies. The time constant of the diode can be calculated by the product of diode resistance (R) which is the combination of dynamic resistance and series resistance and capacitance (C). Thus it is crucial to achieve low-resistance and low-capacitance rectifiers to use in high frequency (> 12 THz) applications. A smaller resistance can be achieved by engineering the barrier height at the metal/oxide and the thickness of the dielectric layer as small as possible. Moreover, the

capacitance can be significantly reduced with the choice of dielectrics with smaller relative dielectric constants (ideally 1) and reducing the device area.

The transmission probability can be ascribed to the chance of an electron tunnelling through the forbidden region of the insulator band gap. Furthermore this probability has a nonlinear dependence on the dielectric thickness and the metal/oxide barrier height [5]. This leads to the nonlinear dependence of tunnel current on the applied voltage as shown in Eqn. 5.1 and 5.2.

The current-voltage (*IV*) characteristics of MIM structures that are fabricated with small barrier heights are not purely exponential. The MIM structures are characterised by their dynamic resistance, device asymmetry, device non-linearity, rectification reversal and responsivity. Device conductance (inverse of resistance) can be calculated from differentiation of the *IV* curve. It is important to note that a small resistance is favourable for efficient power coupling to the antenna. Another important figure of merit is the responsivity which defines how efficiently the diode could rectify the analogue input signal [18]. This can be extracted by considering the ratio of curvature and slope of any point of interest in the *IV* curve. In the case of an exponential *IV* curve, the device responsivity is equal to the bias-independent ideality factor. The device responsivity, *Resp* is defined as $I^{''}/2I^{'}$ and has the units A/W. It can be thought as the DC current generated per unit AC power incident on the diode. A large responsivity can be extracted by having a large curvature and/or a small slope in the *IV* curve. However, a small slope gives a large dynamic resistance. It is important to obtain a high responsivity for an efficient rectification process. Next, the device asymmetry can be evaluated by considering either the forward to reverse bias or reverse to forward bias current ratio (depending on the current levels). For potential ultraviolet/infrared energy harvesting applications, diodes with a large asymmetry are required. The next figure of merit that needs to be analysed is the device non-linearity (F_{NL}) and this can be evaluated by considering the ratio of dynamic conductance to static conductance [19].

$$F_{NL} = \frac{V}{I}\left(\frac{dI}{dV}\right) \tag{5.7}$$

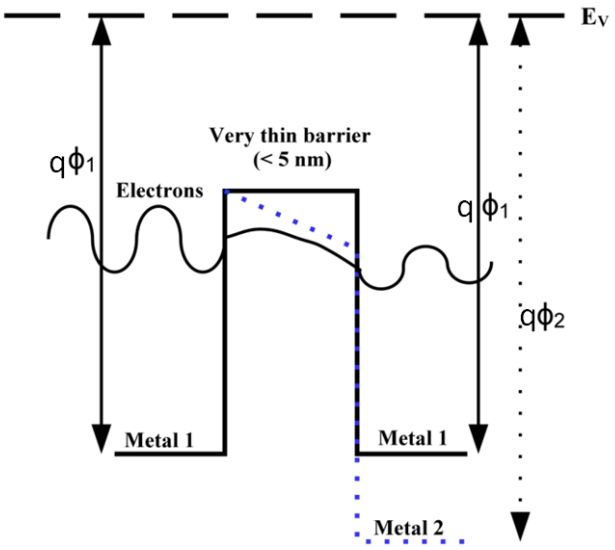

Figure 5.3: Band diagram for MIMs with same metals and different metals.

Ideally an MIM diode should have a high asymmetry of the current for an efficient rectification of signals [19, 20]. This can be achieved by varying the work function offset between two metal electrodes. As shown in Figure 5.3, the band offset can be changed by using metals with significantly different work function values since this increases the tunnelling probability of electrons in one direction compared to the other [19, 20]. Metals must be chosen carefully to observe FNT at lower biasing voltages. This can be achieved by obtaining a smaller barrier height at one side with respect to the other side.

In this chapter, an extensive study is presented to investigate the pronounced conduction mechanism(s) in dielectrics that are used to fabricate the MIM devices. The dielectcrics, Ta_2O_5 and Nb_2O_5, and metals, Al, Ta and Nb were chosen to achieve small barrier heights at the metal/oxide interface in order to facilitate the dominance of quantum mechanical tunnelling at low bias. Values for the electron affinity, band gap and work function were shown in chapter 4. The dominant conduction mechanisms in Nb_2O_5 and Ta_2O_5 are investigated in section 5.1, whereas the rectification properties of the fabricated MIM structures are discussed in section 5.2. The list of samples assessed are stated in Table 5.1 and as can be seen in the table the high temperature measurements were done on 4 nm Ta_2O_5 and Nb_2O_5 samples whereas the rectification properties were investigated for 5 nm Ta_2O_5 and Nb_2O_5 samples. The motivation was to compare the single dielectric MIM structures with the MIIM structures with the oxide combination of either 4 nm Ta_2O_5 or 4 nm Nb_2O_5 and 1 nm Al_2O_3 (total thickness is 5 nm) investigated in chapter 6.

Table 5.1: Sample specifications.

Sample	Bottom electrode	First oxide	Second oxide	Top electrode	Measurements performed
Al/Ta_2O_5/Al (MIIM-1)	~60 nm Al (thermally evaporated)	1.6 nm AlO_x (Native oxide)	4 nm Ta_2O_5 (ALD)	~60 nm Al (thermally evaporated)	Room/high temperature *IV* measurements
Al/Al_2O_3/ Ta_2O_5/Al (MIIM-2)	~60 nm Al (thermally evaporated)	1.6 nm AlO_x+1 nm Al_2O_3 (ALD)	4 nm Ta_2O_5 (ALD)	~60 nm Al (thermally evaporated)	Room/high temperature *IV* measurements
Al/Al_2O_3/ Nb_2O_5/Al	~60 nm Al (thermally evaporated)	1.6 nm AlO_x+1 nm Al_2O_3 (ALD)	4 nm Nb_2O_5 (ALD)	~60 nm Al (thermally evaporated)	Room/high temperature *IV* measurements
Al/Al_2O_3/ Ta_2O_5/Al	~60 nm Al (thermally evaporated)	1.6 nm AlO_x (Native oxide)	5 nm Ta_2O_5 (ALD)	~60 nm Al (thermally evaporated)	Room/high temperature *IV* measurements
Al/Al_2O_3/ Nb_2O_5/Al	~60 nm Al (thermally evaporated)	1.6 nm AlO_x (Native oxide)	5 nm Nb_2O_5 (ALD)	~60 nm Al (thermally evaporated)	Room temperature *IV* measurements
Ta/Ta_2O_5/Ta	Ta (DC sputtered)	5 nm Ta_2O_5 (RF sputtered)	-	Ta (DC sputtered)	Room temperature *IV* measurements
Nb/Nb_2O_5/Nb	Nb (DC sputtered)	5 nm Nb_2O_5 (RF sputtered)	-	Nb (DC sputtered)	Room temperature *IV* measurements

5.1 Dominant conduction in dielectrics

5.1.1 Dominant conduction mechanism(s) in Ta_2O_5

Tantalum oxide (Ta_2O_5) with large electron affinity $\chi = 3.54$ eV [21-23] is now considered, as a dielectric for rectenna applications. It has been reported recently that conduction in thick (10 nm) and thin (5 nm) Ta_2O_5-based MIM diodes is by electrode-limited SE in the low bias regime and bulk-limited PF at larger biases [21], limiting their ultra-high frequency

applications. Therefore it is necessary to study the dominant conduction mechanism(s). The metal, Al was used as both top and bottom metal electrodes; however the effect of Al-native oxide was inevitable. Nonetheless the effect of AlO_x layer can be taken into account by considering two capacitors in series and estimating the voltage across the Ta_2O_5 layer.

Two types of structures were fabricated: $Al/Ta_2O_5/Al$ with unintentional AlO_x (MIIM-1) and $Al/Al_2O_3/Ta_2O_5/Al$ with 1 nm intentional Al_2O_3 layer (MIIM-2) as shown in Figure 5.5 (a) and (b) respectively. The aim was to understand the effect of native AlO_x on device performance.

The dielectric Ta_2O_5 was deposited by either ALD or RF sputtering and Al was deposited by thermal evaporation. The Ta_2O_5 ALD films were deposited by conventional thermal ALD using a Cambridge/Nanotech Savannah reactor with water and tantalum ethoxide $Ta(OEt)_5$ precursors. The $Ta(OEt)_5$ was heated in order to obtain transport into the reactor, pulse and purge times were selected to ensure a self-limiting ALD reaction occurred, and the substrate temperature was 200 °C. When the above results were obtained, $Ta(OEt)_5$ was pulsed for 0.2 seconds followed by a purge time of 4 seconds. Secondly, H_2O was pulsed for 0.04 seconds followed by a purge time of 4 seconds then begin the cycle again. The thicknesses and the optical properties of the dielectric layers were examined using VASE analysis whereas the roughness of the metal, Al was measured by both AFM and VASE as discussed in chapter 4. It has been shown that tunnelling is a dominant mechanism in Al_2O_3 [22]; hence conduction in Ta_2O_5 was considered as the main objective of this work. The portion of potential applied on each layer was found by considering the two oxide layers as two capacitors connected in series as illustrated in Figure 5.4.

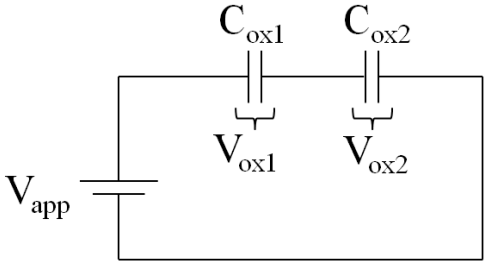

Figure 5.4: Two oxides are considered as two capacitors connected in series

The equivalent capacitance is given by:

$$C_{eq} = \frac{C_{ox1}C_{ox2}}{C_{ox1} + C_{ox2}} \tag{5.8}$$

The voltage across C_{ox1} can be estimated by,

$$V_{ox1} = V_{app} \frac{C_{ox2}}{C_{ox1} + C_{ox2}} \tag{5.9}$$

where V_{ox1} is the voltage applied on the first oxide and V_{app} is the applied voltage on the entire MIIM structure. The dielectric constants values used were 20 for Ta_2O_5 [24, 25], 25 for Nb_2O_5 [24] and 10 for Al_2O_3 [25, 26].

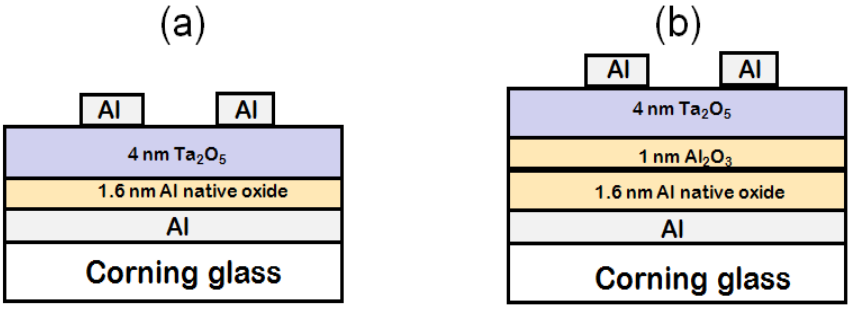

Figure 5.5: The cross-sections of Al-Al_2O_3-Ta_2O_5-Al devices without (a) and with (b) intentionally deposited 1 nm Al_2O_3 layer.

High temperature *IV* measurements were done to study the nature of conduction in the dielectrics. These measurements were performed using a hot chuck connected to the Agilent B1500A semiconductor parameter analyser to perform DC sweeps at each temperature. As seen in Figure 5.5, the devices were fabricated on Corning glass substrates. The sample was left for 15 minutes to ensure that the temperature had stabilised. The *IV* measurements were performed by varying the temperature from 20 ^{o}C to 100 ^{o}C (ascending) and again from 100 ^{o}C to 20 ^{o}C (descending). Each measurement was repeated three times to ensure repeatability. The *JV* characteristics for both MIIM-1 and MIIM-2 device structures are shown in Figure 5.6 (a) and (b) respectively. In Figure 5.6 (c), the *JV* characteristics of MIIM-1 two different device area such as 1×10^{-8} m^2 and 1.69×10^{-8} m^2 are illustrated to verify the homogeneity of the current. The current density was calculated by dividing the experimentally obtained current (*I*) by the device area (1×10^{-8} m^2).

As seen in Figure 5.6, the *IV* characteristics were strongly temperature dependent; therefore PF and SE analysis was carried out. Eqn. 5.6 is re-written as:

$$\ln\left(\frac{J_{PF}}{E_{ox}}\right) = \ln\sigma + \frac{q}{kT}\left(\sqrt{\left(\frac{qE_{ox}}{\pi\varepsilon_o\varepsilon_i}\right)} - \phi_t\right) \tag{5.10}$$

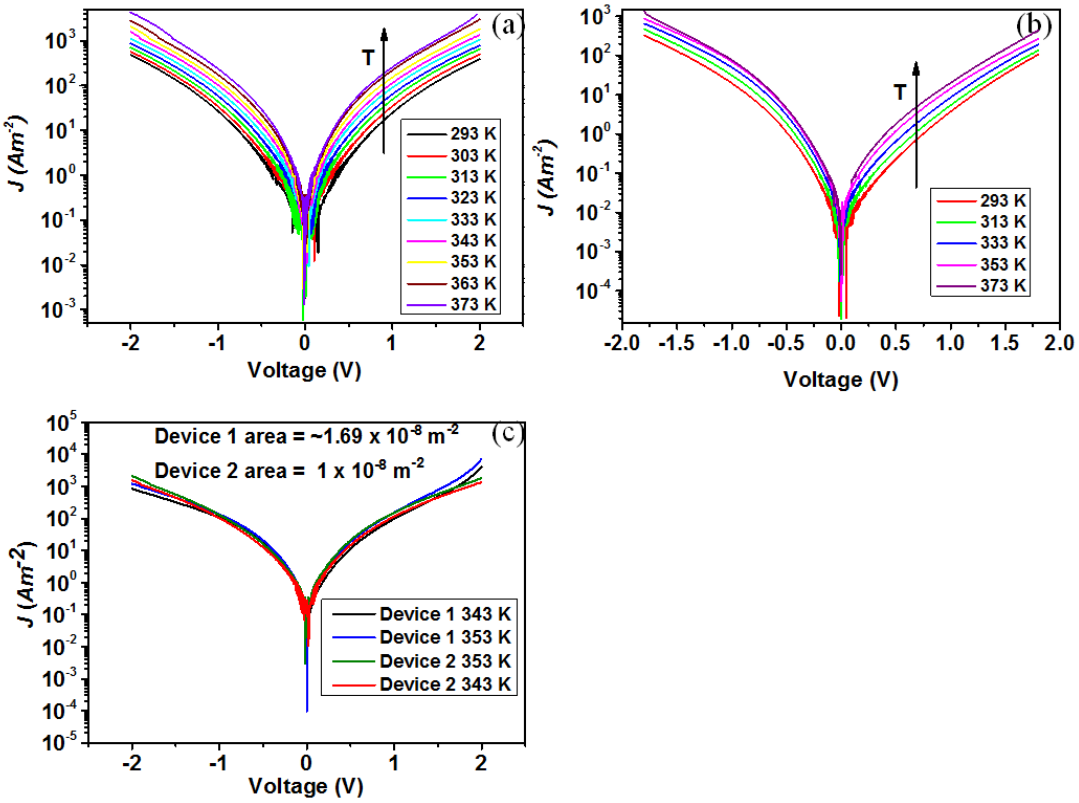

Figure 5.6: Temperature dependent *JV* plots of (a) MIIM-1, (b) MIIM-2 devices and (c) MIIM-1 with different device area.

The term $\ln(J_{PF}/E_{ox})$ is plotted against $\sqrt{E_{ox}}$ as the X-axis to yield a slope of $\beta_{PF} = (q/kT)\sqrt{(q/(\pi\varepsilon_o\varepsilon_i))}$. The PF plots for the MIIM-1 and MIIM-2 structures are shown in Figure 5.7 (a) and (b).

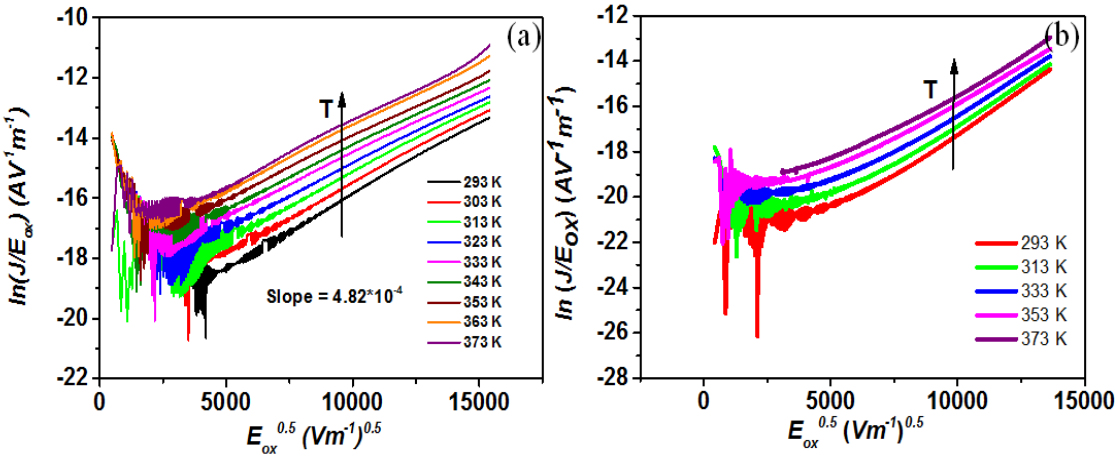

Figure 5.7: Temperature dependent PF plots of (a) MIIM-1, and (b) MIIM-2 devices.

The optical/dynamic dielectric constant, ε_i is thus found from the slope. The extracted slope from the PF plot (MIIM-1) at 293 K was 4.82×10^{-4} which gave a ε_i value of 25.6. The dielectric constant associated with PF conduction is expected to have the high frequency value

as emission of electrons from the traps should occur at times corresponding to optical frequencies. Since the optical permittivity (n^2) was estimated to be ~4.5 at the wavelength of 580 nm from VASE (chapter 4, Figure 4.8), PF can be excluded as a conduction mechanism for this device (MIIM-1). Alimardani *et al.* have reported a relative dynamic permittivity of 4.6 + 0.1 by similar analysis [21]. Relative dynamic permittivity value of 14.5 at 293 K was extracted for the Ta_2O_5 layer from the PF plots shown in Figure 5.7 (b). Since the dynamic permittivity extracted from PF plots does not agree with that from VASE (chapter 4, Figure 4.8), PF conduction can be disregarded as a pronounced conduction mechanism for this device also.

The temperature dependent nature of *IV* characteristics extracted from both diode structures were further analysed for SE according to the Eqn. 5.3.

The equation 5.3 can be rearranged as,

$$\ln\left(\frac{J_{SE}}{T^2}\right) = \ln A^* + \frac{q}{kT}\left(\sqrt{\left(\frac{qE_{ox}}{4\pi\varepsilon_o\varepsilon_i}\right)} - \Phi_B\right). \qquad (5.11)$$

The SE plot was generated by plotting $\ln(J_{SE}/T^2)$ versus $\sqrt{E_{ox}}$ giving a slope of $(q/kT)\sqrt{(q/(4\pi\varepsilon_o\varepsilon_i))}$. The SE plots for the diode structures are shown in Figure 5.8.

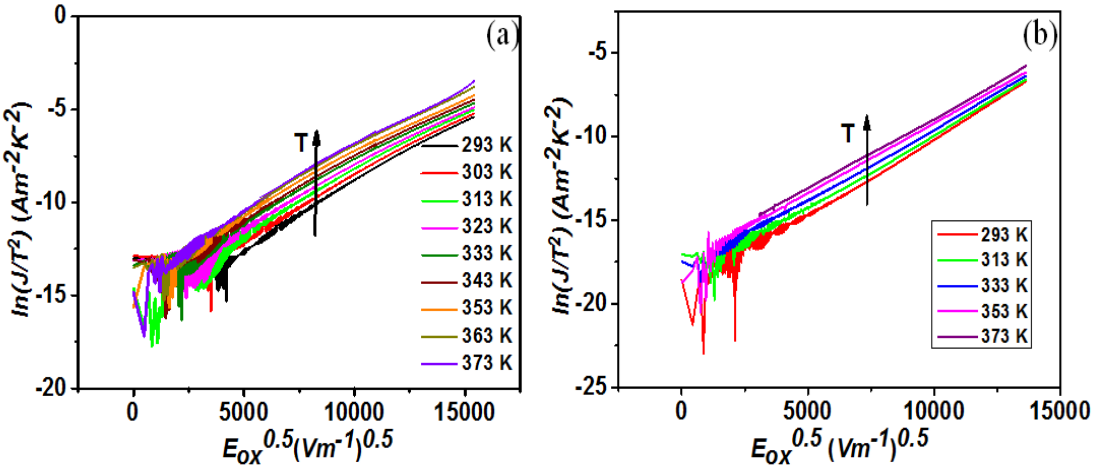

Figure 5.8: Temperature dependent Schottky plots of (a) MIIM-1 and (b) MIIM-2 devices

The dynamic dielectric constant, ε_i was evaluated from the slopes of the SE plots in Figure 5.8. The dynamic dielectric constant of Ta_2O_5 layer of MIIM-1 structure (Figure 5. 8 (a)) varied from 5.1 to 2.6 with the increase in temperature from 293 K to 373 K. The room temperature dynamic permittivity value was comparable to the optical dynamic permittivity extracted from VASE, which was ~4.5 however the dynamic permittivity extracted on the MIIM-2 (Figure 5.8 (b)) structure ranged from 2.5 to 1.7 over the same temperature range. Since the dynamic

permittivity values extracted from both SE plots and VASE were comparable to each other, further analysis were carried out to calculate the Schottky barrier heights from Arrhenius plots.

Arrhenius plots were generated by plotting ln (J_{SE}/T^2) versus ($1/T$) to give slope of $(q/k)\sqrt{(qE_{ox}/(4\pi\varepsilon_o\varepsilon_i))} - \Phi_B$. Arrhenius plots for the MIIM-1 and MIIM-2 are shown in Figure 5.9 (a) and (b).

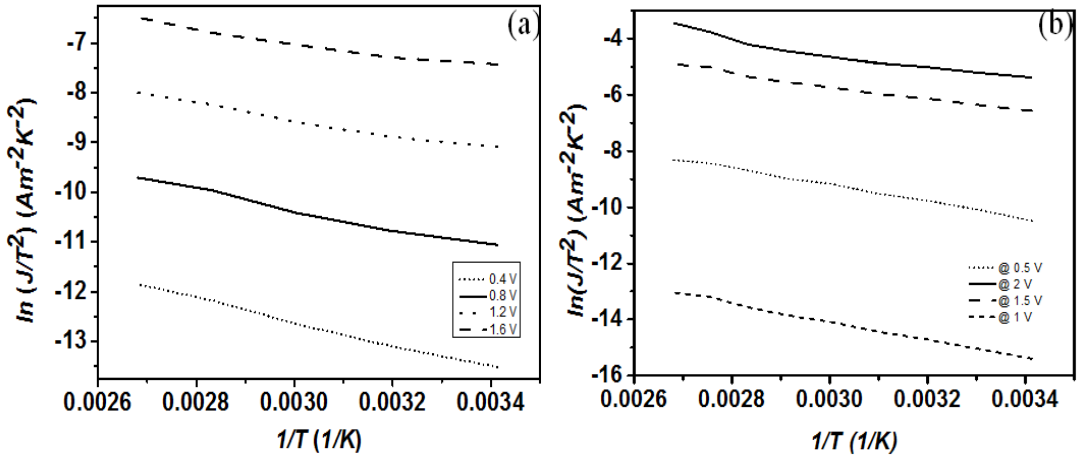

Figure 5.9: Arrhenius plots for Schottky emission conduction for (a) MIIM-1 and (b) MIIM-2 devices

The Schottky barrier height was evaluated from the slopes of Arrhenius plots in Figure 5.9. The extracted values for the MIIM-1 device (Figure 5.9 (a)) ranged from 0.66 eV to 1.08 eV with the increase in electric field from 1.25 $MVcm^{-1}$ to 5 $MVcm^{-1}$ respectively. This could be due to the presence of both tunnelling and SE at low electric fields (< 2.5 $MVcm^{-1}$). The Schottky barrier height increased with the increase in electric field suggesting the increase of electric field, tunnelling becomes more dominant. Figure 5.9 (b) shows the plots for MIIM-2 where the extracted values range between 0.44 eV to 0.35 eV with the increase in electric field from 1 $MVcm^{-1}$ to 4 $MVcm^{-1}$ respectively. These values were used in the theoretical equations for the mechanisms to check for consistency.

The dynamic permittivity and the Schottky barrier height extracted from the experimental results were used in Eqn. 5.3 and the theoretical values are shown for different barrier heights at the Al/Ta_2O_5 interface, in Figure 5.10.

The experimentally obtained currents for the MIIM-1 structure are one to two orders of magnitude smaller than the theoretically estimated current using the SE equation with barrier height of 0.66 eV (Figure 5.10 (a)). As shown in Figure 5.6 (c), the same temperature dependent trend of *IV* characteristics was observed for another Al/Ta_2O_5 based MIIM structure with a device area of 1.69×10^{-8} m^2. From previous analysis it was evident that the Schottky barrier height changes with the change in electric field (1.25 $MVcm^{-1}$ - 5 $MVcm^{-1}$).

Nevertheless, DT with a barrier height of 0.7 eV at the Al/Ta_2O_5 was comparable at lower electric fields (0 – 2.5 $MVcm^{-1}$).

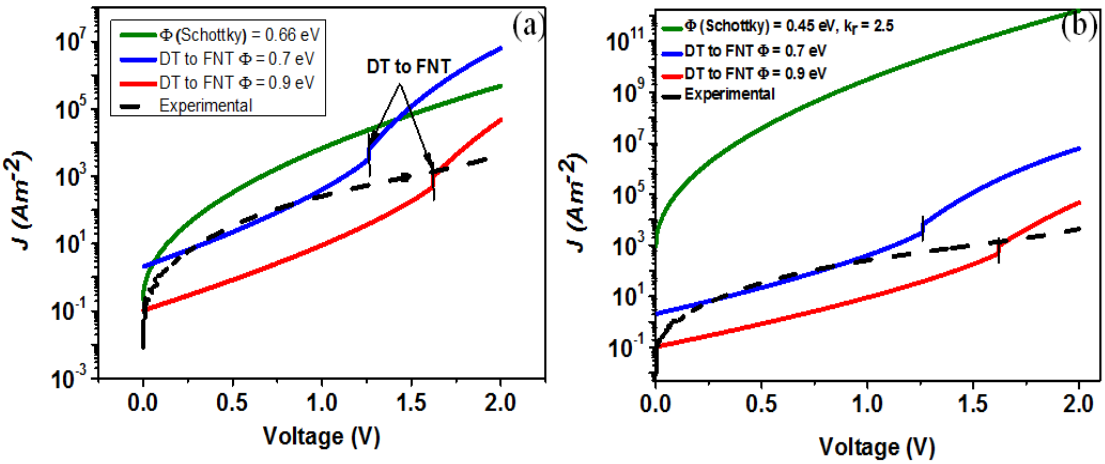

Figure 5.10: Experimental and calculated *JV* plots (DT, FNT and SE) for (a) MIIM-1 and (b) MIIM-2 structures.

The dominant conduction mechanism in MIIM-2 could be quantum mechanical tunnelling, since SE theoretical current density obtained if the dynamic permittivity of 2.5 and barrier height of 0.45 eV were used, gave a very high current level in comparison to the experimental curve (Figure 5.10 (b)). However, the temperature dependent nature of the *IV* characteristics obtained is arguable to the previous assumption, thus the conduction in MIIM-2 could be a combination of SE and DT. A larger difference between the theoretically approximated SE current and the experimental current may be observed as a consequence of Al_2O_3 becoming the current limiting layer at smaller voltages in comparison to the MIIM-1. For a bi-layered device it is not straight forward to determine the conduction mechanism, but it is assumed here that the conduction in thin Al_2O_3 (< 3 nm) in this range of electric field (0 – 5 $MVcm^{-1}$) is always DT [5]. This is supported experimentally by the temperature independence of current in Al_2O_3 (ZCAN/Al_2O_3/Al) [7]. Ta_2O_5 is therefore the current limiting layer at low fields (< 2.5 $MVcm^{-1}$), so presumably the conduction in Ta_2O_5 layer at electric fields < 2.5 $MVcm^{-1}$ could be a combination of SE and DT and changing to FN at fields > 3.5 $MVcm^{-1}$. The presence of PF can be excluded due to the large values extracted for the dynamic permittivity after performing PF analysis. At electric fields > 2.5 $MVcm^{-1}$, the Al_2O_3 is limiting the current by DT in both polarities. A possible reason for the change in current at high fields with the increase in temperature could be due to increased current levels at lower fields as a result of SE; hence it follows the same trend.

Figure 5.11 (b) shows temperature independent *IV* characteristics for Al/1.6 nm AlO_x/5 nm Ta_2O_5/Al when the ALD purge times were increased to 10 seconds after pulsing both precursors. The growth rate was 0.043 nm/cycle.

As illustrated in Figure 5.11 (b), the *JV* characteristics of the structure was temperature independent, indicating the domination of quantum mechanical tunnelling. Moreover, the FN analysis performed on this structure as shown in the inset of Figure 5.11 (b), gives a barrier height of 0.74 eV. This is in agreement with the value of 0.70 eV which was assumed in theoretical approximations in Figure 5.10.

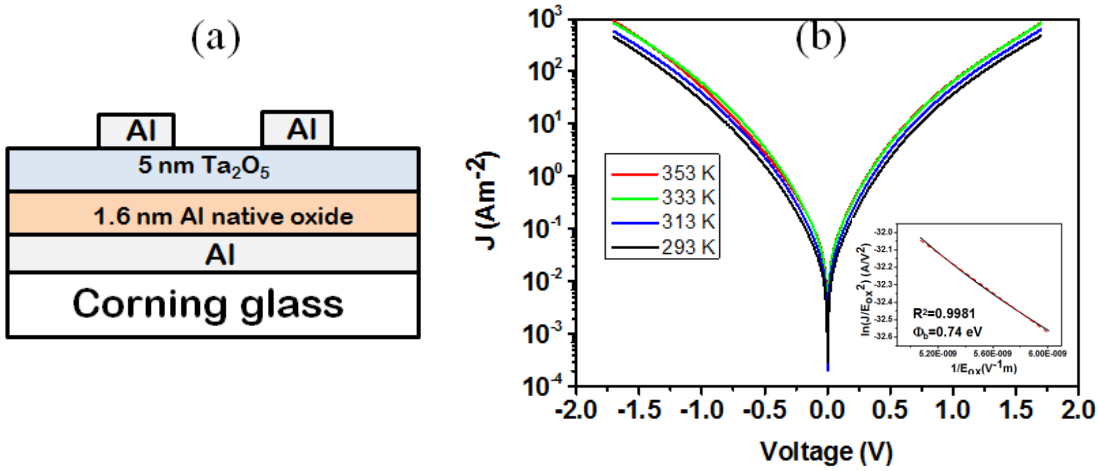

Figure 5.11: Al/1.6 nm AlO_x/5 nm Ta_2O_5/Al (a) Device cross-section (b) High temperature *JV* characteristics, inset of (b) is FN plot of Al/Ta_2O_5/Al (A = 10^{-8} m^2).

5.1.2 Dominant conduction mechanism(s) in Nb_2O_5

The conduction process of Nb_2O_5 was investigated in detail by analysing the room and high temperature *IV* characteristics. Thermally evaporated Al was used as the top and bottom metal electrodes and Nb_2O_5 and Al_2O_3 were deposited by either RF sputtering or ALD. This device structure was patterned by conventional photolithography process as explained in chapter 4. The device cross-section is shown in Figure 5.12 (a).

A temperature range of 299 K to 347 K was considered with an increment of 5 K. It is worth mentioning that the measurements have repeated several times in order to ensure the consistency of measurements and also the repeatability. The *JV* characteristics at each temperature are shown in Figure 5.12.

The results of Figure 5.12 show that the *IV* characteristics are temperature independent. Therefore it can be concluded that the conduction in Nb_2O_5 is dominated by quantum mechanical tunnelling. Based on the analysis performed in chapter 4, the barrier height at the interface of Al/Nb_2O_5 was found to be 0.56 eV (Figure 4.18).

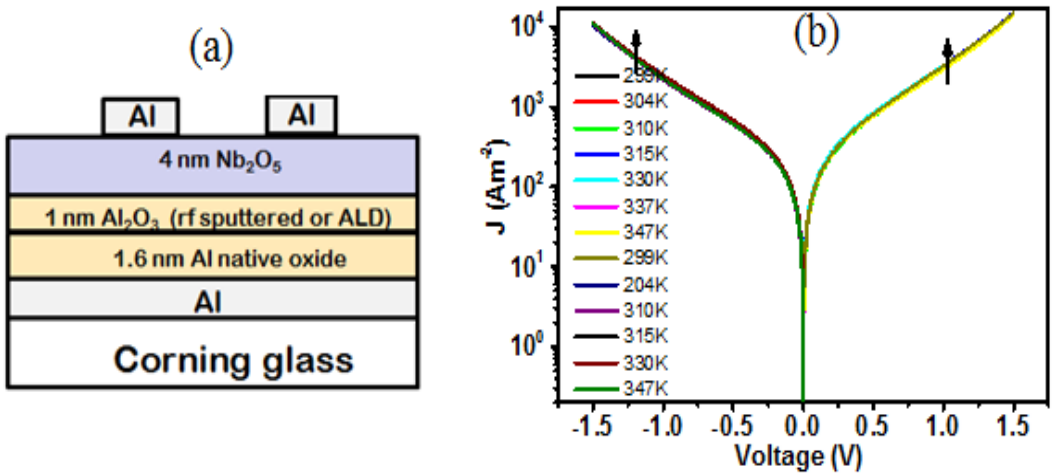

Figure 5.12: Device (a) cross-section and (b) *JV* characteristics for Al/1.6 nm AlO_x/1 nm Al_2O_3/4 nm Nb_2O_5/Al (A = 10^{-8} m^2)

In summary, the conduction in Ta_2O_5, Nb_2O_5 and Al_2O_3 was dominated by femto-second fast quantum mechanical tunnelling, indicating strongly that these are promising candidates to be used in high frequency rectifier applications.

5.2 Rectification properties of MIM structures

After determining the dominant conduction in dielectric layers (section 5.1), several MIM structures were fabricated in order to investigate their rectification properties. The voltage or the field when the oxide reaches FNT regime varies on the barrier height at the metal/dielectric interfaces. The rectification properties extracted by performing room temperature *IV* measurements in a dark probe station and using the Agilent B1500 semiconductor analyser. These measurements were done considering a step voltage of 1-3 mV depending on the voltage range.

The MIM devices were fabricated by involving the deposition techniques, RF sputtering, DC sputtering, ALD and thermal evaporation. The top and bottom electrodes were patterned by either photolithography or shadow mask process. The rectification properties of these fabricated MIM structures are discussed in detail below.

5.2.1 Al/1.6 nm AlO_x/5 nm Ta_2O_5/Al device rectification properties

The rectification properties of 5 nm Ta_2O_5 MIM devices are given in Figure 5.13. Note that the measured dielectric thickness by VASE was 4.48 nm.

The electric field when 5 nm Ta_2O_5 reached FNT was 1.6 $MVcm^{-1}$ which is equivalent to 0.8 V (chapter 4, Figure 4.20). Alternatively, a voltage bias of 1.2 V must be applied on the structure to reach the Ta_2O_5 FNT regime as a result of the formation of native AlO_x.

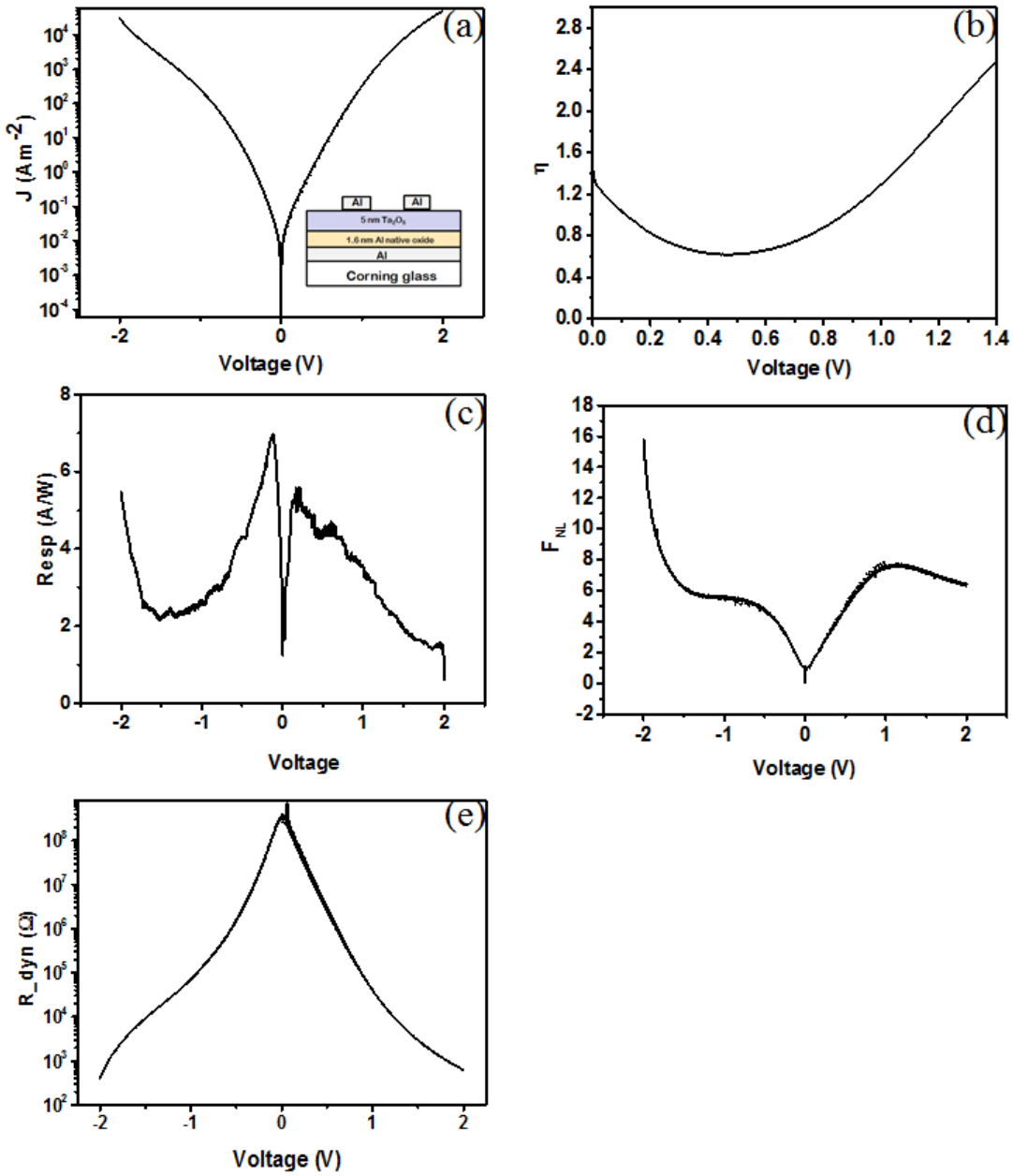

Figure 5.13: Device (a) JV characteristics (inset-device cross-section), (b) asymmetry, (c) responsivity, (d) non-linearity and (e) dynamic resistance for Al/1.6 nm AlO_x/5 nm Ta_2O_5/Al. The device area = 1×10^{-8} m^2.

Referring to Figure 5.13 (a), the voltage sweep was done from -2 V to 2 V with a step of 2 mV, however the origin of the *JV* characteristics did not shift, proving the effect of charging was negligible. This device was not purely symmetric due to the formation of a native AlO_x layer; therefore an asymmetry of 2.4 was extracted at 1.4 V (Figure 5.13 (b)). A peak device responsivity of 5 A/W was recorded at 0.2 V (Figure 5.13 (c)). The peak device non-linearity was 7 at 1 V with rate of change of non-linearity 7 V^{-1} as shown in Figure 5.13 (d). The extracted dynamic resistance values were 335 MΩ at zero bias and 0.63 kΩ at 2 V (Figure 5.13 (e)).

The asymmetric nature of the *IV* curve can be ascribed to the formation of native AlO_x layer.

5.2.2 Al/1.6 nm AlO_x/5 nm Nb_2O_5/Al device rectification properties

The conduction in Nb_2O_5 was dominated by DT at small voltages (< 0.53 V) and FNT at relatively larger voltages (> 0.53 V). The electric field of Nb_2O_5 reaches the FNT regime at 1.05 $MVcm^{-1}$ (see Figure 4.18). Nonetheless, a voltage of 0.53 V must be applied to the 5 nm Nb_2O_5 sample in order to reach the FNT regime, however due to the formation of a layer of native AlO_x, the applied potential was divided across the two layers. Hence a potential of 1 V had to be applied Nb_2O_5 to reach FNT regime. It is evident that the Nb_2O_5-based device structure reaches FNT regime at 0.2 V earlier than the Ta_2O_5-based device (see section 5.2.1).

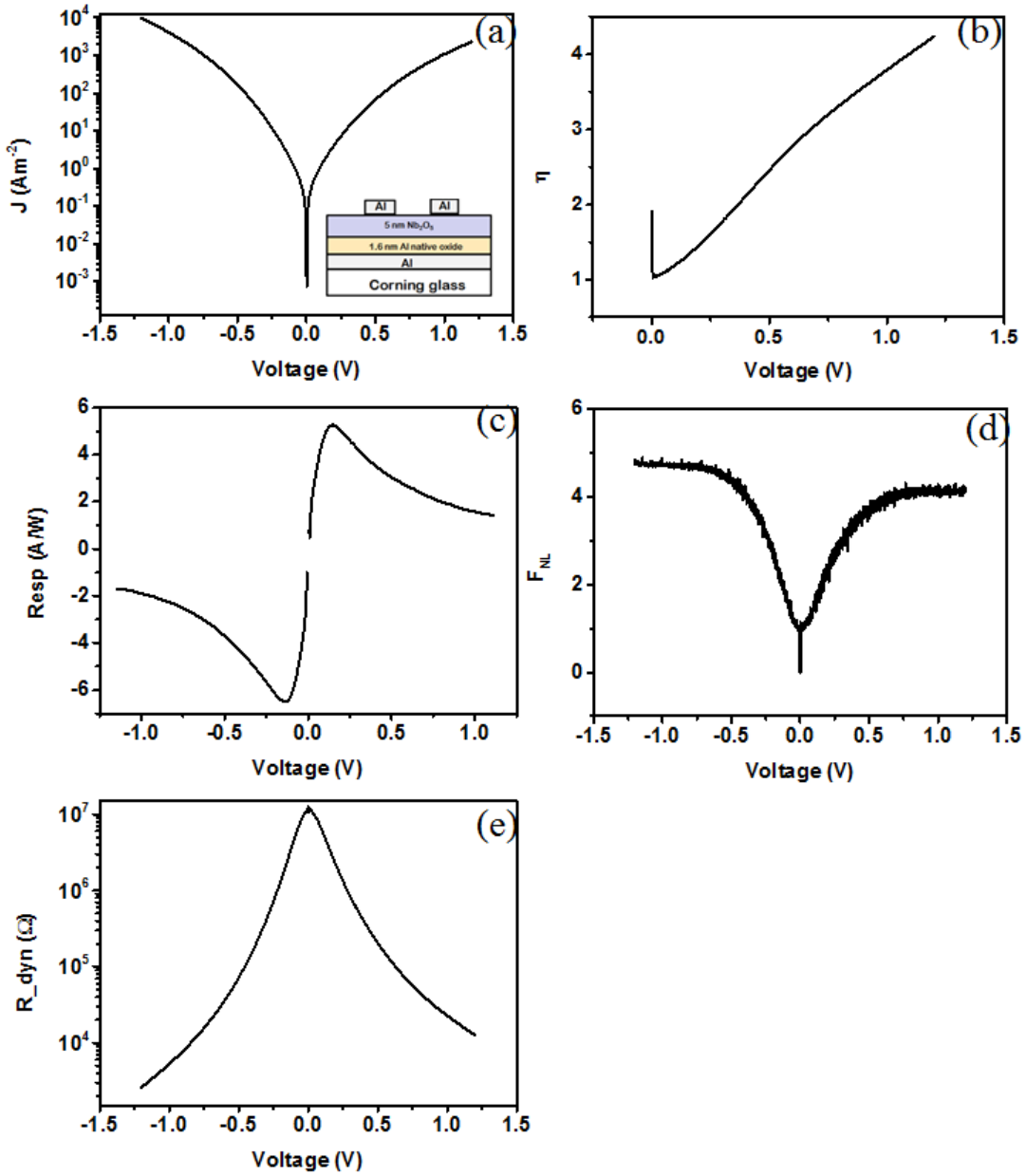

Figure 5.14: Device (a) JV characteristics (Inset-Device corss-section), (b) asymmetry, (c) responsivity, (d) non-linearity and (e) dynamic resistance for Al/1.6 nm AlO_x/5 nm Nb_2O_5/Al. The device area = 1×10^{-8} m^2.

The rectification properties of MIM based on 5 nm Nb_2O_5 (5.40 nm measured) are shown in Figure 5.14. As seen in Figure 5.14 (a), the reverse bias current was relatively large in contrast to forward bias as a result of the formation of AlO_x. A peak device asymmetry of 4.2 was found at 1.2 V. A peak device responsivity of 5.2 A/W was extracted at 0.14 V (Figure 5.14 (c)). A peak non-linearity of 4.13 at 0.75 V and a rate of change of non-linearity of 5.37 V^{-1} were extracted from Figure 5.14 (d). The dynamic resistance at zero bias was 11 MΩ whereas the resistance at 1.2 V was 2.6 kΩ as can be seen in Figure 5.14 (e).

It is evident that larger currents by a factor of 3 have been obtained on this structure in contrast to the Ta_2O_5 MIM structure. Therefore a reduction of resistance from 335 MΩ to 11 MΩ at 0 V was observed in Nb_2O_5 based MIM structure. This is attributed to the reduction in metal/oxide barrier height from 0.74 eV to 0.56 eV. Note it was not possible to obtain symmetric *IV* characteristics as a result of formation of native AlO_x layer on the bottom electrode.

5.2.3 Ta/5 nm Ta_2O_5/Ta device rectification properties

An approach has been carried out to replace Al with other metals to eliminate the issue of the AlO_x layer. Since Ta_2O_5 was used as the dielectric layer, Ta was used as the top and bottom metal electrodes. It is possible to fabricate a symmetric MIM structure with this approach.

The shadow mask patterned Ta metal electrodes were deposited by DC sputtering technique at Southampton University. Then 5 nm (nominal) Ta_2O_5 was deposited by RF sputtering and the thickness of this layer was measured to be 4.58 nm by VASE (Figure 4.9).

The Ta_2O_5 layer reaches the FNT regime when the applied electric field is 1.47 $MVcm^{-1}$ (see chapter 4, Figure 4.21), which refers to a voltage of 0.73 V. The barrier height between Ta/Ta_2O_5 extracted from FN plots, was found to be 0.63 eV. It is evident that the structure reaches the FNT regime at a smaller voltage of 0.73 V compared to the 1.2 V of Al/Ta_2O_5/Al structure (see section 5.2.1). This is likely to be due to the smaller barrier height at the Ta/Ta_2O_5 interface and also the absence of the bottom electrode native oxide layer.

The *IV* measurements were performed from -1 V to 1 V with a step voltage of 1 mV in order to observe any charging effect of the oxide. As can be seen in Figure 5.15 (a), the origin of the *JV* characteristics was not shifted showing the effect of activated ions in the oxide was minimal. The *JV* characteristics of the structure were symmetric as anticipated (Figure 5.15 (a)). As illustrated in Figure 5.15 (b), a peak device asymmetry of 1.06 was recorded at 0.27 V. A peak device responsivity of 4.4 A/W was extracted at 0.6 V as shown in Figure 5.15 (c). A peak device non-linearity of 6.8 at 0.7 V and a rate of change of non-linearity of 9 V^{-1} were

extracted from the Figure 5.15 (d). A zero bias resistance of 24 GΩ and also a relatively smaller resistance of 11 MΩ was recorded at 0.97 V (Figure 5.15 (e)).

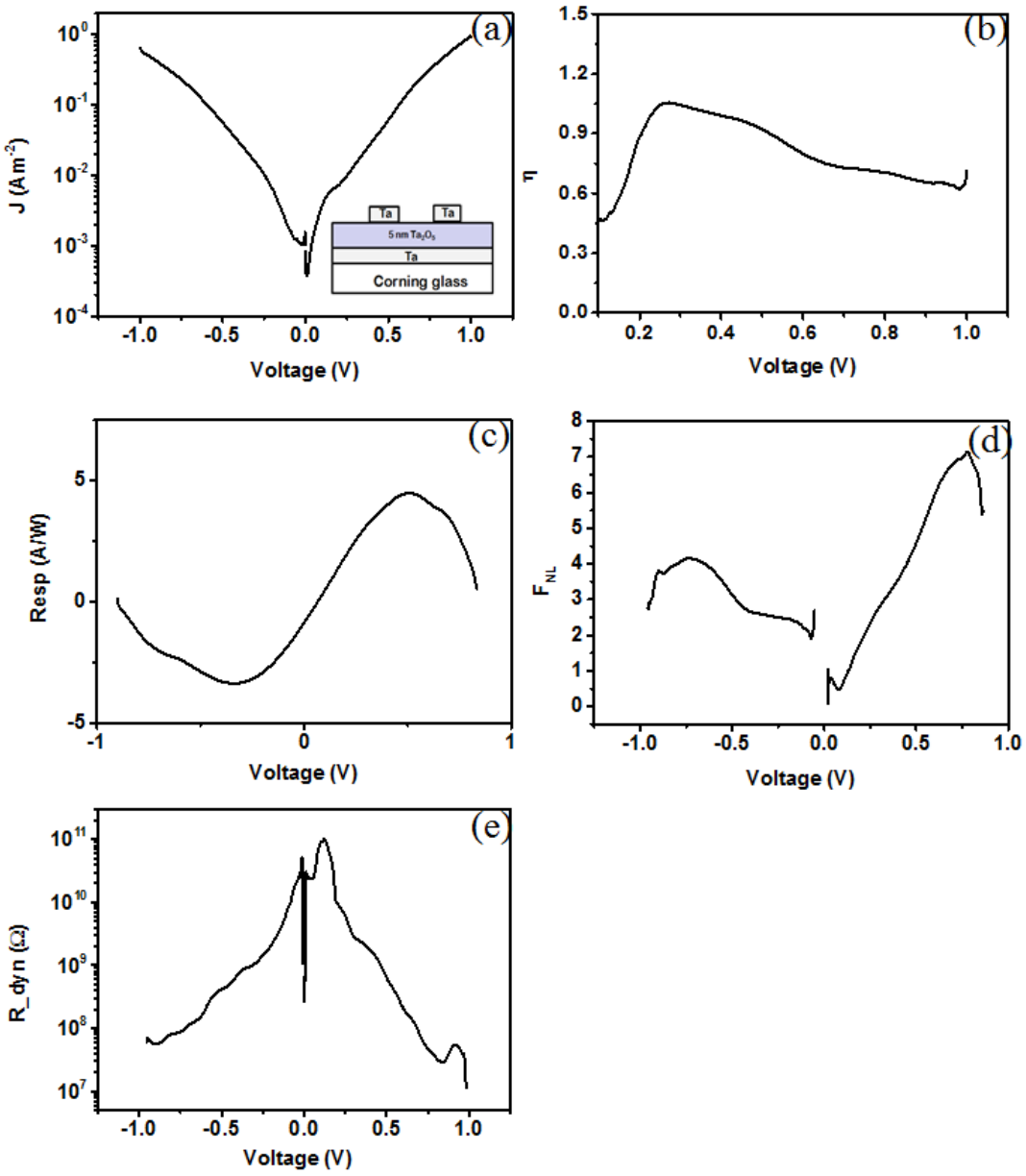

Figure 5.15: Device (a) JV characteristics (Inset - Device cross-section), (b) asymmetry, (c) responsivity, (d) non-linearity and (e) dynamic resistance for Ta/5 nm Ta_2O_5/Ta. The device area = 1×10^{-8} m^2.

In summary, a symmetric Ta_2O_5-based MIM structure was fabricated by replacing the Al electrodes with Ta. The barrier height at the Ta/Ta_2O_5 interface was 0.11 eV smaller than that of Al/Ta_2O_5; therefore a smaller dynamic resistance should have been evident from this structure in comparison to the structure that was fabricated with Al. This was not evident from the analysis performed. This could be due to the relatively large series resistance of Ta,

resulting in a reduction of the voltage applied across the oxide. This issue can be eliminated by optimising the deposition conditions of Ta.

5.2.4 Nb/5 nm Nb_2O_5/Nb device rectification properties

The barrier height at the metal/oxide interface is now reduced by replacing Ta_2O_5 with Nb_2O_5 and also using Nb as the metal electrodes. This is due to the larger electron affinity of Nb_2O_5 (3.72 eV) in contrast to Ta_2O_5 (3.54 eV) and the smaller work function of Nb (4.11 eV) compared to Al (4.28 eV) and Ta (4.17 eV). This approach also allows for a symmetric MIM structure. The material deposition was done by a combination of DC and RF sputtering. The metal, Nb was deposited and patterned by DC sputtering and shadow mask process respectively. The dielectric 5 nm (nominal) Nb_2O_5 was deposited by RF sputtering and the thickness of this layer was measured to be 5.54 nm by VASE.

This MIM structure reaches FNT regime at the lower field of 0.8 $MVcm^{-1}$, which corresponds to a voltage of 0.40 V as a result of the small barrier height of 0.39 eV.

The *IV* measurements were performed from -1 V to 1 V with a step voltage of 1 mV. The effect of charging was negligible as the origin of the *JV* curve was not shifted (see Figure 5.16 (a)). As shown in Figure 5.16 (a), the *JV* characteristics were symmetric around the origin due to the zero work function difference between both metal electrodes. A peak asymmetry of 1.18 at 0.98 V can be seen in Figure 5.16 (b). The peak device responsivity is 2.9 A/W at 0.5 V (Figure 5.16 (c)). A peak device non-linearity of 3.9 at 0.87 V and a rate of change in non-linearity of 5.36 V^{-1} were extracted from the Figure 5.16 (d)). A reduction in resistance values in contrast to the Ta/Ta_2O_5/Ta structure was observed. A zero bias resistance is 0.24 GΩ, reducing to 0.8 MΩ at 1 V (Figure 5.16 (e)).

In summary, a symmetric MIM structure with a smaller barrier height of 0.39 eV was fabricated by replacing the Al electrodes with Nb, and Ta_2O_5 with Nb_2O_5. Higher currents were obtained due to the smaller metal/oxide barrier. A smaller dynamic resistance is expected from this structure in comparison to the MIM diodes fabricated with Al and Ta. This is clearly seen when compared to Ta/Ta_2O_5/Ta diodes. However, the MIM diodes with Al electrodes show smaller dynamic resistances although the metal/oxide barriers are higher. This is likely to be due to the different deposition techniques and conditions.

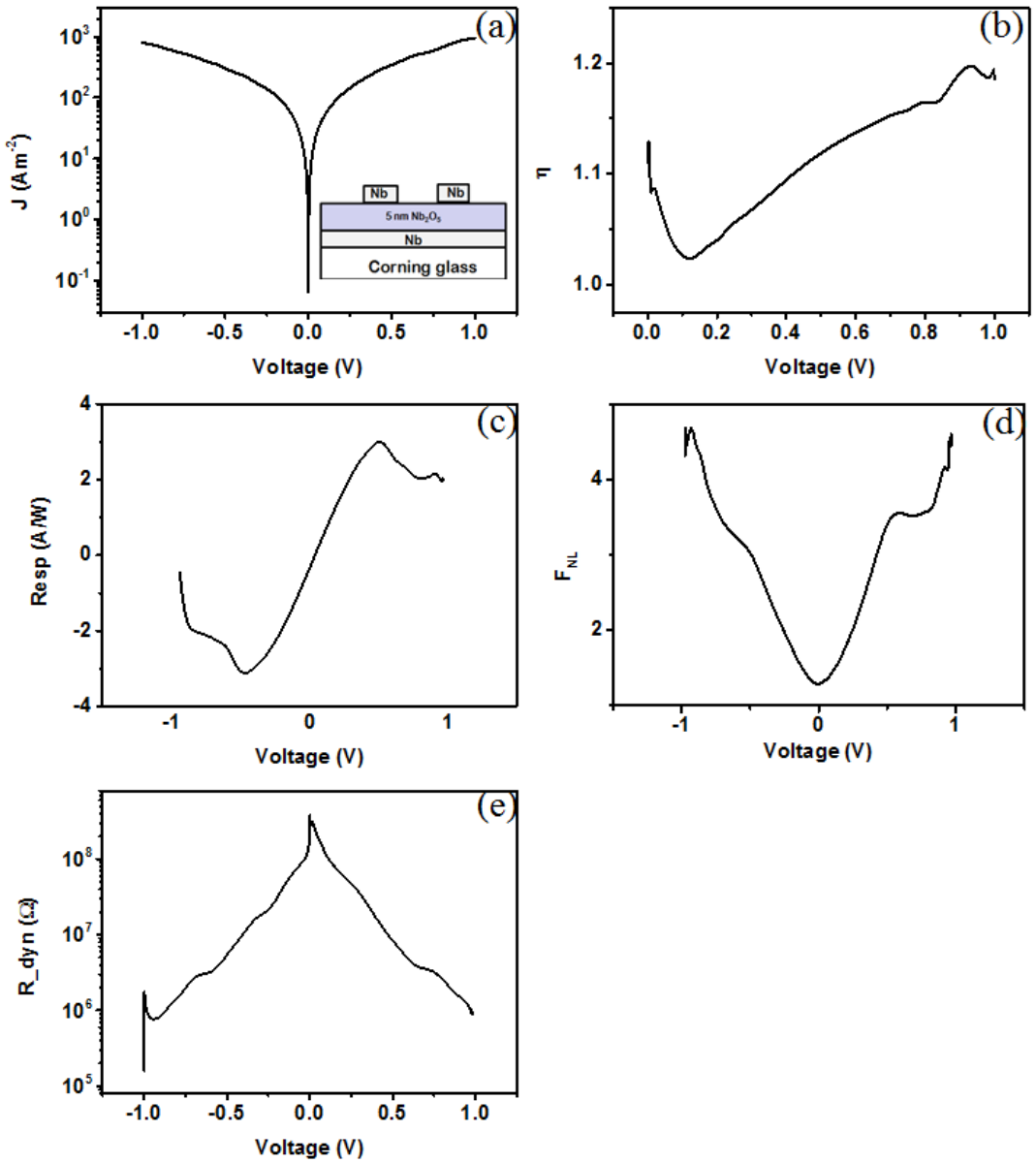

Figure 5.16: Device (a) JV characteristics (inset - device cross-section), (b) asymmetry, (c) responsivity, (d) non-linearity and (e) dynamic resistance for Nb/5 nm Nb_2O_5/Nb. The device area = 1×10^{-8} m^2.

5.3 Discussion and conclusion

The conduction processes of the dielectrics that were used to fabricate the MIM diodes were studied in this chapter. High temperature *IV* measurements were performed to ascertain the presence of the thermally activated processes: of PF and SE. The *IV* characteristics obtained for the Ta_2O_5-based MIM structure were temperature dependent. It was found that the conduction could be dominated by a combination of Schottky emission at low voltage levels and quantum mechanical tunnelling at higher applied voltages. The PF is excluded due to unrealistic large dynamic permittivity values obtained from electrical measurements. The theoretically estimated currents for SE, using the experimentally extracted Schottky barrier height and the dynamic permittivity were significantly larger than the experimental currents.

As discussed in chapter 1 (Eqn. 1.2), static dielectric constant is related to the dynamic/optical dielectric constant. Moreover, if the dielectric constant decreases with the increase in temperature, the tunnel resistivity will be reduced, leading to temperature dependent *IV* characteristics [27]. However, the current values were changed by an order of magnitude when the temperature was increased from 20 ^{o}C to 100 ^{o}C. Therefore the dominant conduction may not be just quantum mechanical tunnelling but a combination of SE and DT. It must be noted that investigating the conduction process of a bi-layer MIM structure is not straight forward, therefore the performed series of experiments must be repeated for a precisely fabricated single insulator MIM structure in order to determine the conduction process. Nevertheless, temperature independent *IV* characteristics for Ta_2O_5 based MIM were obtained after increasing the ALD purge times of both precursors ($Ta(OEt)_5$) and (H_2O) from 4 seconds to 10 seconds. The optimised ALD purge times were used while fabricating the Ta_2O_5 based metal-multi insulator-metal structures to assess the rectification properties. For Nb_2O_5 based MIM, the conduction was dominated by quantum mechanical tunnelling.

A small dynamic resistance at or near zero bias and a small diode capacitance are crucial to achieve a time constant of 10^{-15} seconds for ultraviolet/infrared energy harvesting. The small resistance value is also crucial for efficient coupling to the antenna. If the diode resistance is large there is a possibility of increasing the antenna resistance for efficient coupling. This will create opportunities to fabricate diode structures with smaller device areas in order to obtain small diode capacitances. However, it is known that the total resistance of the rectenna circuit is given by the parallel combination of antenna resistance (R_A) and diode resistance (R_D). Therefore if R_A and R_D are increased, the total resistance ($R_A||R_D$) of the rectenna circuit increases, resulting in the product of ($R_A||R_D)C_D$ (time constant) to increase. In conclusion, it is extremely important to obtain a smaller resistance (~100 Ω) for the diode while maintaining a small diode capacitance. This can be possibly achieved by engineering barrier height at the metal/oxide interface and keep the thickness of the dielectric as small as possible. The results in the chapter are now discussed in the above context.

It was found that Ni/NiO/Ni and Cr/NiO/Ni could be considered as good candidates for use in fast detectors of terahertz and infrared radiation [28]. The barrier height at the Ni/NiO interface has been found to be 0.2 eV, leading to a small resistance-area product of 1 Ωμm^2. The RC time constant for this device has been found to be 3×10^{-14} seconds [6]. Fumeaux *et al.* reported that Ni/NiO/Ni MIM coupled antennas could be used as detectors in 10 μm band [29]. However, this does not satisfy the requirement for near-IR frequencies ($\lambda = 0.88\,\mu$m), where RC time constant is 9.4×10^{-16} seconds which is smaller than 3×10^{-14} seconds [6, 30]. Krishnan *et al.* observed detection at 94 GHz, an asymmetry of 1.2 at 0.5 V and a responsivity of 2 A/W

at 0.1 V for a Ni/NiO/Cr MIM device [31]. Moreover experimental work on MIM structures by Grover *et al.* with dissimilar electrodes ($NbN/Nb_2O_5/Nb$) and compared well with theoretical results. They obtained a responsivity of 4 A/W at 0.4 V for an asymmetric MIM device [24]. In advance to the state-of-the-art, $Ta/Ta_2O_5/Ta$ symmetric MIM structure demonstrated a responsivity of 4.4 A/W at 0.6 V. Alimardani *et al.* reported an asymmetry in the order of 10^3 and a non-linearity of ~20 at 4.1 V with a $ZrCuAlNi/Al_2O_3/Al$ MIM structure [21, 22, 32] however the current density was lower than 10^{-3} Am^{-2} even at 2.2 V [32], demonstrating a high dynamic resistance due to use of 10 nm Al_2O_3 as the dielectric and the large barrier heights of 3.4 eV and 2.8 eV at the interfaces of $ZrCuAlNi/Al_2O_3$ and Al/Al_2O_3 respectively. Alimardani *et al.* further reported peak asymmetries of 1.4 and 2.4 at 0.8 V, and peak non-linearities of 5.7 and 6.1 at ~1 V for $ZrCuAlNi/Nb_2O_5/Al$ and $ZrCuAlNi/Ta_2O_5/Al$ structures respectively [21]. Maraghechi *et al.* reported an asymmetry of 0.8, rate of change of non-linearity of 2.8 V^{-1} and a responsivity of 1.6 A/W for $Cr/HfO_2/Cr$ and $Cr/Al_2O_3/Cr$ MIM devices [19]. Periasamy *et al.* reported large device asymmetries of 130 and 80 with peak non-linearity values of 3.8 and 3.5 for $Nb/Nb_2O_5/Pt$ and $Nb/TiO_2/Pt$ respectively [33]. The same group further reported asymmetries > 10^3 for $Nb/Nb_2O_5/Pt$ structures [34].

The rectification properties extracted on the MIM devices are summarised in Table 5.2. The zero bias resistance values extracted are too large for efficient coupling to the antenna. This is mainly due to the large barrier height at the metal/oxide interface and also thick dielectric layers of 5 nm or more. The resistance can be significantly reduced to ~100 Ω by lowering the barrier height to 0.2 eV and reducing the thickness of the dielectric as much as possible. Also the responsivity values were considerably larger near 0 V. The device asymmetry evaluated on Al based MIM diodes was higher, likely to be due to the formation of a native AlO_x layer. The bottom two MIM structures in Table 5.2 show the same asymmetry as expected.

The values of responsivity and non-linearity from MIM devices in this work are comparable to those reported in the literature though larger asymmetry values have been recorded for $ZrCuAlNi/Al_2O_3/Al$, $Nb/Nb_2O_5/Pt$ and $Nb/TiO_2/Pt$ MIM structures as noted in Table 5.2. The rectification properties of the MIM structure can be enhanced by obtaining a metal work function difference and varying the thickness of the insulator layer. In the next chapter, an approach has been carried out to improve the rectification properties at/near 0 V by introducing another dielectric layer to the MIM structure.

Table 5.2: Summarised rectification properties.

Device	Peak device symmetry	Responsivity (A/W)	Non-linearity	Dynamic Resistance
$Al/Ta_2O_5/Al$	2.40 at 1.4 V	5 at 0.2 V	7 at 1 V 7 V^{-1}	0.34 GΩ at 0 V 0.63 kΩ at 2 V
$Al/Nb_2O_5/Al$	4.2 at 1.2 V	5.2 at 0.14 V	4.13 at 0.75 V 5.37 V^{1}	11 MΩ at 0 V 2.6 kΩ at 1.2 V
$Ta/Ta_2O_5/Ta$	1.06 at 0.27 V	4.40 at 0.6 V	6.80 at 0.7 V 9 V^{-1}	24 GΩ at 0 V 11 MΩ at 0.97 V
$Nb/Nb_2O_5/Nb$	1.18 at 0.98 V	2.90 at 0.5 V	3.90 at 0.87 V 5.36 V^{-1}	0.24 GΩ at 0 V 0.8 MΩ at 1 V
Ni/NiO/Ni [6]	-	-	-	1 Ω(μm^2).
Ni/NiO/Cr [31]	1.2 at 0.5 V	2 at 0.1 V	-	-
$NbN/Nb_2O_5/Nb$ [24]	-	4 at 0.4 V	-	~0.6 MΩ at 0.4 V
$ZrCuAlNi/Al_2O_3/Al$ [21, 22]	$>10^3$ at voltages > 3 V	-	~20 at ~4.1 V	-
$ZrCuAlNi/Nb_2O_5/Al$ [21]	1.4 at 0.8 V		5.7 at ~1 V	
$ZrCuAlNi/Ta_2O_5/Al$ [21]	2.4 at 0.8 V		6.1 at ~1 V	
$Cr/HfO_2/Cr$ [19] $Cr/Al_2O_3/Cr$ [19]	0.8 at ~0.5 V	1.6 at ~0.5 V	7 at ~ 3 V 2.8 V^{-1}	-
$Nb/Nb_2O_5/Pt$ [33, 34]	130 and $> 10^3$ at 0.5 V	-	3.8 at 0.5 V	-
$Nb/TiO_2/Pt$ [33]	80 at 0.5 V	-	3.5 at 0.5 V	-

References

[1] H.-W. Hübers, G. W. Schwaab, H. P. Röser, "Video detection and mixing performance of GaAs Schottky-barrier diodes at 30 THz and comparison with metal-insulator-metal diodes", J. Appl. Phys.,75, 4243 (1994)

[2] A New Technology for Terahertz Electronics, Phiar Corporation, Np 1.0 (2013)

[3] A. Sanchez, C. F. Davis Jr., K. C. Liu, A. Javan, “The MOM tunneling diode: Theoretical estimate of its performance at microwave and infrared frequencies”, J. Appl. Phys., 49, 5270 (1978)

[4] L. O. Hocker, D. R. Sokoloff, V. Daneu, A. Szoke, A. Javan “Frequency mixing in the infrared and far-infrared using a metal-to-metal point contact diode”, Appl. Phys. Lett., 12, 401 (1968)

[5] R. Stratton, “Volt-Current characteristics for tunnelling through insulator films”, J. Phys. Chem. Solids, 23, 1177 (1962)

[6] P. C. D. Hobbs, R. B. Laibowitz, F. R. Libsch, “Ni-NiO-Ni tunnel junctions for terahertz and infrared detection” IBM Research Report, 2005

[7] M. Chin, S. Kilpatrick, R. Osgood, “Metal-Insulator-Metal diode process development for energy harvesting applications” Progress Report, Army Research Laboratory, (2010)

[8] B. Berland, “Photovoltaic technologies beyond the horizon: Optical rectenna solar cell”, ITN Energy Systems, Inc, National Renewable Energy Laboratory (U.S.) (2003)

[9] B. J. Eliasson, “Metal-Insulator-Metal diodes for solar energy conversion”, PhD Thesis, University of Colorado, Boulder (2001)

[10] S. Krishnan, E. Stefanakos, S. Bhansali, "Effects of dielectric thickness and contact area on current-voltage characteristics of thin film metal-insulator-metal diodes", Thin Solid Films, 516, 2244 (2008)

[11] S. M. Sze, Kwok K. Ng., “Tunnel device in physics of semiconductor devices”, 3rd edition. John Willey & Sons, 2007, Ch. 8, sec 8.3.2, 438

[12] S. M. Sze, Kwok K. Ng., “Tunnel device in physics of semiconductor devices”, 3rd edition. John Willey & Sons, 2007, Ch. 8, sec 8.3.2, 437

[13] S. M. Sze, Kwok K. Ng., “Tunnel device in physics of semiconductor devices”, 3rd edition. John Willey & Sons, 2007, Ch. 4, sec 4.3.4, 228

[14] B. C. Lai, N. Kung, J. Y. Lee, “A study on the capacitance-voltage characteristics of metal-Ta_2O_5-silicon capacitors for very large scale integration metal-oxide-semiconductor gate oxide applications”, J. Appl. Phys., 85, 4087 (1999)

[15] S. M. Sze, Kwok K. Ng., “Tunnel device in physics of semiconductor devices”, 3rd edition. John Willey & Sons, 2007, Ch. 3, sec 3.2.4, 146

[16] S. M. Sze, Kwok K. Ng., “Tunnel device in physics of semiconductor devices”, 3rd edition. John Willey & Sons, 2007, Ch. 8, sec 8.3.4, 448

[17] M. Nagae, “Response time of metal-insulator-metal tunnel junctions” Jpn. J. Appl. Phys., 11(11), 1611-21 (1972)

[18] T. C. L. G. Sollner, W. D. Goodhue, P. E. Tannenwald, C. D. Parker, D. D. Peck, “Resonant tunnelling through quantum wells at frequencies up to 2.5 THz”, Appl. Phys. Lett.. 43, 588 (1983)

[19] P. Maraghechi, A. Foroughi-Abari, K. Cadien, A. Y. Elezzabi, "Enhanced rectifying response from metal-insulator-insulator-metal junctions,” Appl. Phys. Lett., 99, 253503 (2011)

[20] P. Maraghechi, A. Foroughi-Abari, K. Cadien, A. Y. Elezzabi, “Observation of resonant tunnelling phenomenon in metal-insulator-insulator-insulator metal electron tunnel devices”, Appl. Phys. Lett.. 100, 092103 (2012)

[21] N. Alimardani, J. McGlone, J.F. Wager, J.F. Conley Jr., “Conduction process in metal-insulator-metal diodes with Ta_2O_5 and Nb_2O_5 insulators deposited by Atomic Layer Deposition”, J. Vac. Sci. and Tech. A, 32, 01A122-1 (2014)

[22] N. Alimardani, S. W. King, B. L. French, C. Tan, B. P. Lampert, J. F. Conley Jr., “Investigation of the impact of insulator material on the performance of dissimilar electrode metal-insulator-metal diodes”, J. Appl. Phys., 116, 024508-1 (2014)

[23] B.C. Lai, J Y. Lee, “Leakage current mechanism of metal-Ta_2O_5-metal capacitors for memory device applications”, J. Electrochem.l Soc., 146, 1, 266 (1999)

[24] S. Grover, G. Moddel, “Engineering the current-voltage characteristics of metal-insulator-metal diodes using double-insulator tunnel barriers”, Solid State Elec., 67(1), 94 (2012)

[25] J. Robertson, “High dielectric constant gate oxides for metal oxide Si transistors”, Rep. Prog. Phys.. 69, 328 (2006)

[26] P. D. Ye, B. Yang, K. K. Ng, J. Bude., “GaN metal-oxide-semiconductor high-electron-mobility-transistor with atomic layer deposited Al_2O_3 as gate dielectric”, Appl. Phys. Lett., 86, 063501 (2005)

[27] J. G. Simmons, “Generalized formula for the electric tunnel effect between similar electrodes separated by a thin insulating film”, J. Appl. Phys.. 34, 1793 (1963)

[28] J. G. Small, G. M. Elchinger, A. Javan, A. Sanchez, F. J. Bachner, D. L. Smythe, "ac electron tunneling at infrared frequencies: Thin-film M-O-M diode structure with broad-band characteristics," Appl. Phys. Lett.. 24, 275 (1974)

[29] C. Fumeaux, M. Gritz, I. Codreanu, W. Schaich, F. Gonzalez, G. Boreman, “Measurement of the resonant lengths of infrared dipole antennas”, Infrared Phys. and Tech., 41, 271 (2000)

[30] S. Grover, “Diodes for optical rectennas”, PhD thesis University of Colorado, Boulder, 53 (2011)

[31] S. Krishnan, H. La Rosa, E. Stefanakos, S. Bhansali, K. Buckle, "Design and development of batch fabricatable metal-insulator-metal diode and microstrip slot antenna as rectenna elements", Sens Actuators A Phys., 142, 40 (2008)

[32] N. Alimardani, J. Conley Jr., ‘‘Enhancing metal-insulator-insulator-metal tunnel diodes via defect enhanced direct tunnelling,’’ J. Appl. Phys., 105, 082902 (2014)

[33] P. Periasamy, H. L. Guthrey, A. I. Abdulagatov, P. F. Ndione, J. J. Berry, D. S. Ginley, S. M. George, P. A. Parilla, R. P. O’Hayre, “ Metal-insulator-metal diodes: role of the insulator layer on the rectification performance”, Adv. Mat., 25, 1301 (2013)

[34] P. Periasamy, J. J. Berry, A. A. Dameron, J. D. Bergeson, D. S. Ginley, R. P. O’Hayre, P. A. Parilla, “Fabrication and characterisation of MIM diodes based on Nb/Nb_2O_5 via a rapid screening technique”, Adv. Mat., 23, 3080 (2011)

Chapter 6

6. Resonant tunnelling in Metal-Insulator-Insulator-Metal (MIIM) structures

The main drawback of MIM structures is the poor rectification properties. The device asymmetry and non-linearity can only be enhanced up to a certain extent by applying a work function difference between the two metal electrodes [1-5]. A diode with a sufficiently large non-linearity is crucial for rectification [1, 2]. It is also important to obtain a large current magnitude, low dynamic and series resistance, and low turn-on voltages in order to achieve high conversion efficiencies [6, page 49]. Therefore it is necessary to introduce an alternative approach with the aim of achieving a large device asymmetry and non-linearity near zero bias. There is a possibility of achieving this through changing the conduction mechanism in forward and/or reverse bias; however it is crucial to maintain the dominant conduction mechanism as tunnelling for the femto-second fast transit times. In addition to conventional direct tunnelling (DT) and Fowler-Nordheim tunnelling (FNT) in forward bias, it is possible to introduce another conduction mechanism known as resonant tunnelling [7]. An increased asymmetry can be achieved if electron transport is aided by resonant tunnelling under forward bias whereas reverse bias is dominated by DT and FNT [2, 6, 7]. This phenomenon can be achieved by engineering the structure by introducing another ultra-thin dielectric layer to the MIM structure. This is a different approach in contrast to the resonant tunnelling diode/double-barrier diode concept [8] because the semiconductors used in the resonant tunnelling diodes are replaced with high-k dielectrics with a conduction band offset at the oxide interface to form a triangular quantum well with the applied bias in MIIM [9, 10].

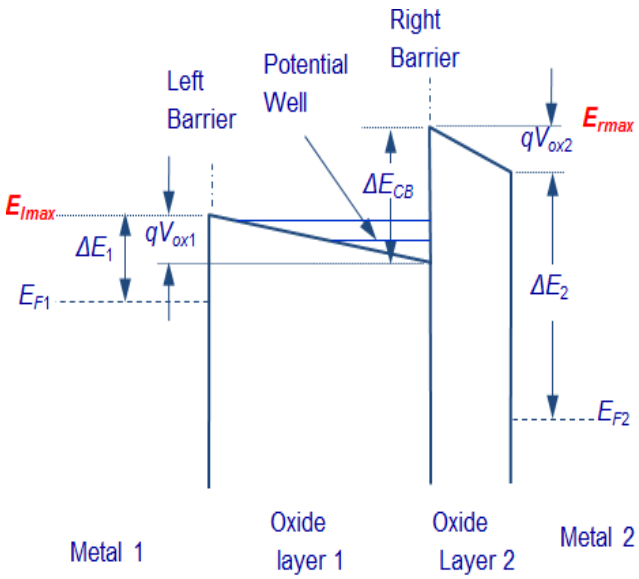

Figure 6.1: The energy band diagram when a positive bias is applied to the metal 2 [9, 10]

The two insulator layers must be chosen carefully to engineer the structure in order to observe resonant tunnelling through a triangular quantum well [1] as shown in Figure 6.1. The band gap and the electron affinity values of the high-k dielectrics play a key role in oxide selection process and these are summarised in Table 6.1.

Table 6.1: Band gap and electron affinity values of Al_2O_3, Ta_2O_5 and Nb_2O_5 extracted in chapter 4.

High-k oxide	Band gap (eV)	Electron affinity (eV)
Al_2O_3	6.43 ± 0.1	1.60 ±0.2
Ta_2O_5	4.40 ± 0.1	3.54 ± 0.2
Nb_2O_5	3.76 ± 0.1	3.72 ± 0.2

In this work, a wide band gap dielectric such as Al_2O_3 (oxide 2) and a narrow band gap dielectric such as Ta_2O_5 or Nb_2O_5 (oxide 1) were chosen to engineer the MIIM structure. The electron affinity of Al_2O_3 is significantly smaller in contrast to Ta_2O_5 or Nb_2O_5, resulting in a large conduction band offset (ΔE_{CB}) between Al_2O_3 and Ta_2O_5 or Al_2O_3 and Nb_2O_5 as shown in Figure 6.1. The quantum well will be formed as a result of the large conduction band offset at the dielectric interface and the relatively smaller barrier height at the metal/oxide interface. There are discrete energy levels created in the quantum well, whereby the electrons could transmit through these states to the other side of the structure.

A quantum well is a potential well with discrete energy levels which spatially confine the electron. Initially the electrons are free to move in three dimensions; then confined to two dimensions by forcing the electrons to occupy a planar region [11]. The quantum confinement occurs when the de Broglie wavelength of electrons is comparable to the thickness of the quantum well [12], thus the carriers exist with only discrete energy levels. A solution for the quantum mechanical problem was proposed by Erwin Schrödinger. An approach was carried initially from a classical description of the total energy, E that is the sum of kinetic energy, *K.E.* and potential energy, V [12],

$$E = K.E. + V = \frac{p^2}{2m} + V(x). \tag{6.1}$$

Then by multiplying both sides of the equation by the wave function, ψ it is possible to transform the Eqn. 6.1 into a wave equation,

$$E\psi = \frac{p^2}{2m}\psi + V(x)\psi \,. \tag{6.2}$$

The square law of momentum, p^2 can be replaced by the operator $\frac{-\hbar^2\partial^2}{\partial x^2}$ by correlating the de Broglie wavelength of the particle when applied to a plane wave. Therefore,

$$-\hbar^2 \frac{\partial^2\psi}{\partial x^2} = \hbar^2 k^2\psi = p^2\psi \text{, for } \psi = e^{i(kx-\omega t)} \tag{6.3}$$

where *k* is the wave number defined as,

$$k = \frac{2\pi}{\lambda}$$

where λ is the wavelength. The time-independent Schrodinger equation is

$$-\frac{\hbar^2}{2m}\frac{\partial^2\psi(x)}{\partial x^2} + V(x)\psi(x) = E\psi(x)\,. \tag{6.4}$$

The Hamiltonian matrix can be defined by rewriting the equation 6.4 as [10],

$$\hat{H}\psi = E\psi \tag{6.5}$$

where $\hat{H}$ is the Hamiltonian operator [11] defined as $\hat{H} = -\frac{\hbar^2}{2m}\frac{\partial^2}{\partial x^2} + V$.

The single dimensional infinite quantum well can be used to demonstrate certain important properties of a quantum mechanical system. The potential between the boundaries $x = 0$ and $x = L_x$ is zero and is infinite at the boundaries [11, 12]. Since the potential in the quantum well is zero, *V(x)* term in original Schrodinger equation can be avoided while calculating the energy states inside the well,

$$-\frac{\hbar^2}{2m}\frac{\partial^2\psi(x)}{\partial x^2} = E\psi(x)\,. \tag{6.6}$$

The general solution to this equation is,

$$\psi(x) = A\sin(kx) + B\cos(kx) \tag{6.7}$$

where coefficients *A* and *B* can be determined by applying the boundary conditions and $k = \frac{\sqrt{2mE}}{\hbar}$. The probability of finding an electron outside the quantum well and at the boundary is zero due to potential is infinite on both sides of the boundaries. Hence the wave function should be zero at both boundaries [11, 12], i.e.

$\psi(0) = 0$ and $\psi(L_x) = 0$.

These boundary conditions lead to the coefficient *B* being zero and the sine function must be multiples of π at the edge of the quantum well; i.e.

$$k_n = \frac{n\pi}{L_x}.$$

Energy corresponding to a specific value of n is given by,

$$E_n = \frac{\hbar^2}{2m}\left(\frac{n\pi}{L_x}\right)^2.$$

The electrons can exist only in discrete energy levels in such a quantum well. The coefficient *A* can be evaluated by assuming that the probability of finding an electron in the quantum well is unity, i.e.

$$\int_0^{L_x} \psi_n(x)\psi_n^*(x) = 1. \tag{6.8}$$

The asterisk corresponds to the complex conjugate of $\psi_n(x)$. Then,

$$\int_0^{L_x} |A|^2 \sin^2(k_n x)\partial x = |A|^2 \frac{L_x}{2} = 1 \tag{6.9}$$

Therefore

$$\psi_n(x) = \sqrt{\frac{2}{L_x}} \sin\left(\frac{n\pi}{L_x} x\right). \tag{6.10}$$

6.1 Theoretical considerations

When the conduction band offset between the metal/oxide interfaces (barrier height) is smaller than the conduction band offset between two dielectrics, with the applied electric field there will be a potential well created between the left and right barriers (Figure 6.1). The Eigen states that are localised in the quantum well between the left barrier and the right barrier of the two dielectrics can be considered as bound states (Figure 6.1). Resonant tunnelling occurs when the electron wave propagates through these bound states. The Fermi energy level of the metal 1 should be aligned with the energy level of one of the bound states in order to obtain a large current by resonant tunnelling. This is because the transmittance is the product of Fermi-Dirac-like distribution of particles over energy states of the metal electrode and tunnelling probability; moreover, these parameters are at peak values when the Fermi energy level of the metal is aligned with the energy level of a bound state. Therefore in order to achieve resonant tunnelling at small voltages it is crucial to have a small barrier height at the metal/oxide interface (metal/Ta_2O_5 or metal/Nb_2O_5).

A theoretical model has been built to calculate the number of bound states that can be obtained in the quantum well by numerically solving the time-independent Schrödinger equation in the dielectric layers [7, 9, 10]. The number of bound states in a one dimensional (1-D) well was extracted by diagonalizing the Hamiltonian matrix which was constructed using a set of localised Eigen states in the stack. The energy levels of the Eigen states were estimated by taking a general superposition state, formed by sinusoidal basis [7, 9, 10]. It was necessary to evaluate the energy position of these Eigen states. The Eigen states created above E_{rmax} (right barrier) and E_{lmax} (left barrier) may leak to left or right depending on the energy level. Then the modified multi-barrier Tsu-Esaki model was used to evaluate the current by dividing the dielectric layer into multiple slices and each slice has different barrier heights due to barrier bending [9]. The resultant current depends on the available density of states at each energy level and also on the occupancy of electrons at each energy state which can be determined by Fermi-Dirac distribution. The transmission amplitude was calculated by solving the time-independent Schrödinger equation using the transmission matrix method. The model was based on the Wentzel-Kramers-Brillouin (WKB) approximation for wave function at each slice through a potential barrier by constructing a piecewise constant transfer matrix for each slice [7, 9, 10]. Many MIIM structures have been simulated using this model to identify the best structure that may lead to resonant tunnelling effect below 1 V to obtain good rectification properties.

The metals were chosen to form a small barrier height < 0.74 eV at the metal/oxide interface. The optimal structure was found to be with the first oxide thickness of 4 nm and the second

oxide (which has the larger band gap and the smaller electron affinity) of 1 nm. It was apparent that the resonant tunnelling occurred when the oxide 1 to oxide 2 thickness ratios was 1:3 [9]. Initially when simulating these structures, the electron affinity and work function values were chosen from the literature. However, it is worth noting that there is a broad range of reported values of electron affinity and work function for metals and oxides (see chapter 4, Table 4.4). Therefore as discussed in chapter 4, physical characterisation experiments were performed to estimate these parameters directly from our fabricated structures and input them in our theoretical model (Table 6.1). The prime objective of MIIM work was to observe resonant tunnelling experimentally and then to investigate its effect on rectification properties.

Next, it is possible to demonstrate the difference between the reverse bias current and the forward bias current in presence of resonant tunnelling. This can be done with the aid of simulated results on one MIIM structure (Nb/4 nm Nb_2O_5/1 nm Al_2O_3/Nb) using the technique explained in [7, 9, 10]. The theoretical model gives the transmittance which is the product of tunnelling probability and Fermi-Dirac-like distribution [9].

The Nb/4 nm Nb_2O_5/1 nm Al_2O_3/Nb structure is in flat band condition at zero bias due to the zero work function difference (Figure 6.2 (a)). It is known that the electron is a free running sinusoidal wave in the metal electrode, but the wave function changes accordingly when it transmits across the oxide barrier from left metal electrode to the right metal electrode in Figure 6.2 (a). The energy level of the electron (left metal) is important to determine the changes in wave function. The conduction in both dielectric layers are limited by DT if the energy level of the electron resides below the conduction band of Nb_2O_5, resulting in the amplitude of the wave function to decay exponentially when travelling through the forbidden energy gap of two dielectrics. If a small positive bias is applied to the right metal electrode, the wavelength of the electrons at the right metal in Figure 6.2 (a) is identical to the left metal electrode although the amplitude of the sinusoidal wave in right metal is significantly smaller with respect to the amplitude of the left side metal (small magnitudes of transmittance) as the conduction is limited by DT. If the energy of the electron is above the conduction band of Nb_2O_5, the wave function of electrons exists with a free-running sinusoidal shape in Nb_2O_5. This wavelength is increased compared to the wavelength in the metal depending on the energy difference between the conduction band and the state where the electron exists. Moreover, the amplitude will decay exponentially when the electron tunnels through the thin Al_2O_3 layer as the conduction in Al_2O_3 is limited by DT. The tunnelling probability in this scenario is relatively larger comparing to the previous case where the energy level of the electron is below the conduction band of Nb_2O_5, however the number of electrons at higher energy states is not significant according to the Fermi-Dirac statistics (Figure 6.3 (a)). At zero

bias, the bands are flat so the tunnelling probability from left to right and right to left is the same, resulting in a net current of zero.

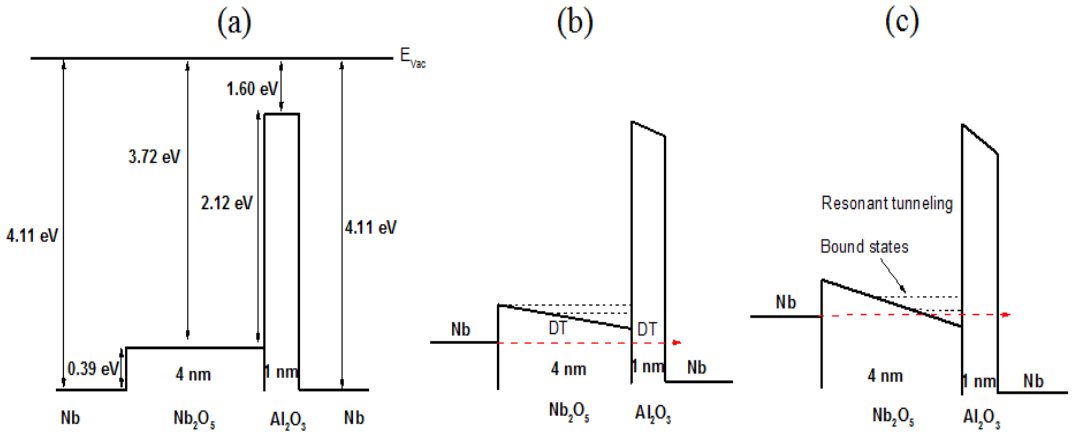

Figure 6.2: The energy band diagrams at (a) zero bias, (b) 0.5 V and (c) 1 V for Nb/4 nm Nb_2O_5/1 nm Al_2O_3/Nb device.

The band diagrams with applied positive biases to the right electrode are illustrated in Figures 6.2 (b) and (c). As can be seen in Figures 6.2 (b) and 6.3 (b), if a potential of 0.5 V is applied to the right electrode, a quantum well is built and two bound states exist at 0.22 eV and 0.39 eV above the Fermi level of the metal electrode. However, as shown in Figure 6.3 (b), when a potential of 0.5 V was applied, the tunnelling probability is in the order of 10^{-2}, but the transmittance was in the order of 10^{-6} after considering the Fermi-Dirac-like distribution which is 1.3×10^{-4}. This suggests the number of electrons at the energy level of the bound state is small.

Nevertheless, if the applied potential was -0.5 V, the tunnelling probability was in the order of 10^{-6} (shown in black line of Figure 6.3 (b)) and the transmittance was 10^{-7} after considering the Fermi-Dirac-like distribution (~10^{-1}). It is known that the area under the transmittance curve is directly proportional to the resultant current levels as illustrated in Eqn. 6.11.

$$J = \frac{m^* qkT}{2\pi^2\hbar^3}\int_0^\infty T_{coeff}(E_x)\ln\left\{\frac{1+\exp\left[\left(E_x - E_{FL}\right)/kT\right]}{1+\exp\left[\left(E_x - E_{FR} - qV_{app}\right)/kT\right]}\right\}dE_x \qquad (6.11)$$

where m^* is electron effective mass, q is electronic charge, k is Boltzmann constant, T is absolute temperature, $\hbar$ is reduced Planck constant, T_{coeff} is transmission coefficient, E_x is energy of electron in tunneling direction, and E_{FL} and E_{FR} are the Fermi levels of left and right electrode.

The area under the transmittance curves (Figure 6.3 (b)) when the applied bias was 0.5 V and -0.5 V were found to be 2.4×10^{-9} and 5.4×10^{-9} respectively. Therefore it is possible to state that the reverse bias current at this bias was larger in contrast to the forward bias.

Moreover, as can be seen in Figures 6.2 (c) and 6.3 (c), if a bias of 1 V is applied to the right contact, the dominance of resonant tunnelling can be observed as the energy levels of the bound states (0.01 eV and 0.22 eV) are much closer to the Fermi-level of the metal electrode, leading to large magnitudes of Fermi-Dirac-like distribution. The area under the transmittance curve at 1 V is larger by a factor of 1.5 in contrast to the transmittance corresponding to -1 V. The rectification reversal point when the forward bias current starts to dominate the reverse bias current occurs at 0.88 V.

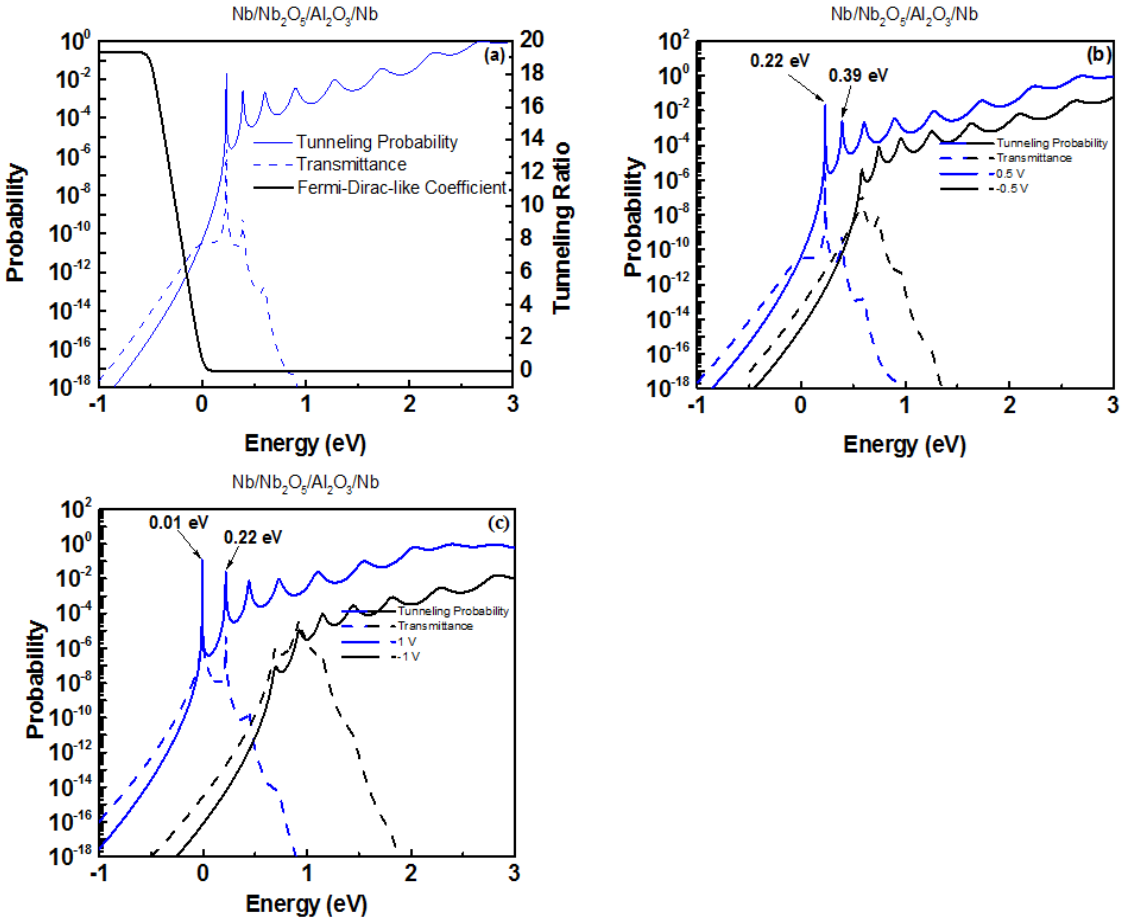

Figure 6.3: Tunnelling probability and transmittance for bias voltages: (a) 0.5 V with the Fermi-Dirac-like distribution (black line), (b) 0.5 V and -0.5 V, and (c) 1 V and -1 V for Nb/4 nm Nb_2O_5/1 nm Al_2O_3/Nb [7, 9].

This phenomenon has been investigated experimentally by fabricating these MIIM devices. The onset of resonant tunnelling towards smaller/larger voltages can also be changed by varying the work function difference between metal electrodes.

As illustrated in Figure 6.4, if the work function of the right metal (M) is reduced by 0.5 eV, there is a higher probability of obtaining a deep quantum well even at zero bias. Then the effect of resonance can be observed by applying a small positive bias to the right metal (M). The effect of resonance can be shifted to higher voltages by using metal electrodes with larger work function values with respect to Nb.

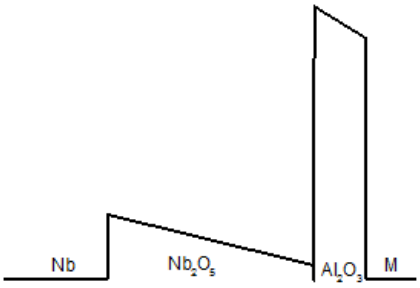

Figure 6.4: The band diagram of Nb/4 nm Nb_2O_5/1 nm Al_2O_3/M where M is a different metal.

The electron transport in reverse bias occurs by a combination of DT and FNT through both oxide layers in the low voltage regime (Figure 6.2 (b) and see chapter 5). However, when the metal Fermi level aligns with the conduction band edge of either Nb_2O_5 or Ta_2O_5, the MIIM structure reaches the step tunnelling regime [2, 6, 13-15]. It is expected to have a step change in overall tunnel distance as the electrons tunnel through the forbidden gap of Al_2O_3 and inject into the conduction band of either Ta_2O_5 or Nb_2O_5. The electrons may quickly relax to the Fermi level of the other metal electrode; typically of the order of femto-seconds [14]. Electrons injected from Al_2O_3 with energy greater than kT, will quickly thermalise to the conduction band of the thicker dielectric (Ta_2O_5 or Nb_2O_5) and then drift to the contact. A fraction of the electrons will fall into oxide traps. However, it is experimentally observed that a large reverse bias current can be expected with the increase in applied voltage. Moreover, it has been experimentally shown in chapter 5 that the presence of Poole-Frenkel (PF) mechanism is unlikely due to the large dynamic permittivity value of ~26 extracted from PF plots compared to the optical permittivity of ~4.5. Trap assisted tunnelling (TAT) is also considered. Figure 6.5 shows *J* against *1/T* for the structures presented in chapter 4. The Arrhenius plot for Al/native AlO_x/4 nm Ta_2O_5/Al (temperature dependent) is shown in Figure 6.5 (a) whereas plots for Al/ native AlO_x/1 nm Al_2O_3/4 nm Nb_2O_5/Al (temperature independent) and Al/ native AlO_x/5 nm Ta_2O_5/Al (temperature independent) are shown in Figures 6.5 (b) and (c) respectively.

The activation energy was found by,

$$J \approx \exp\left(\frac{-E_a}{kT}\right) \tag{6.12}$$

where E_a is the activation energy of the trap level.

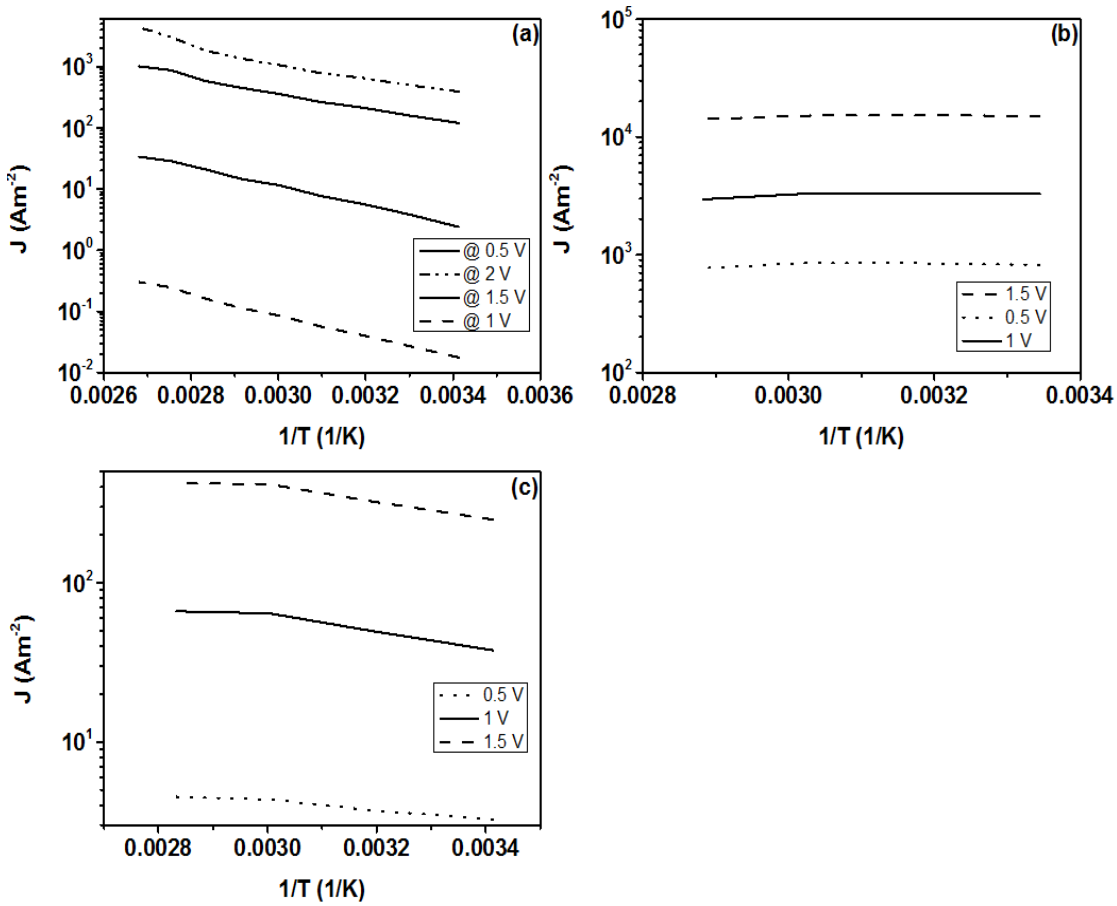

Figure 6.5: Arrhenius plots for (a) Al/ native AlO_x/4 nm Ta_2O_5/Al, (b) Al/ native AlO_x/1 nm Al_2O_3/4 nm Nb_2O_5/Al and (c) Al/ native AlO_x/5 nm Ta_2O_5/Al. ALD purge time in (a) was 4 seconds whereas the purge time was 10 seconds for (c) while depositing Ta_2O_5.

An activation energy of ~0.3 eV was extracted for the temperature dependent Al/4 nm Ta_2O_5/Al structure but the trap level activation energy value remained constant with the increase in voltage from 0.5 V to 2 V. Moreover, the E_a values extracted for temperature independent Nb_2O_5 and Ta_2O_5 structures were 0.00063 eV and 0.0121 eV respectively and remained constant over the applied voltage range from 0 V to 1.5 V. For dominant TAT mechanism, it is expected to observe a reduction in trap level activation energy with the increase in voltage [16], this was not observed in this work. The constant E_a values extracted for the structures suggest that TAT is unlikely to occur. Thus the large reverse bias currents observed in our experimental MIIM structures cannot be ascribed to a dominant PF or TAT mechanism.

The fabricated devices that demonstrated state-of-the-art rectification properties were chosen and are discussed in detail in this chapter. In each case the fabrication process, conduction and rectification parameters are explained and finally the structures are compared with the reported values.

The rectification properties are investigated considering several parameters. Firstly, the device asymmetry is calculated by considering the forward to reverse bias current ratio or vice versa:

$$\eta = \left| I_+ / I_- \right| \text{ or } \left| I_- / I_+ \right|. \tag{6.13}$$

Then the device responsivity is calculated at the operating voltage of interest by [17],

$$Resp = \frac{I_{dc}}{P_{in}} = \frac{1}{2}\frac{I''}{I'}\bigg|_{V_p} = \frac{1}{2}\frac{dg_d/dV}{g_d}, \tag{6.14}$$

where g_d is the conductance. This is a measure of the diode non-linearity. This also signifies the DC current generated in the diode per unit of alternating current (AC) power incident, in other terms the efficiency of the diode. There is a necessity of large responsivity values for efficient square law rectification [17].

Next, the device non-linearity was calculated by considering the ratio of dynamic conductance to static conductance:

$$F_{NL} = \frac{dI/dV}{I/V}. \tag{6.15}$$

Finally the device dynamic resistance is calculated by differentiating the current voltage curve, i.e.

$$R_{dyn} = \frac{dV}{dI}. \tag{6.16}$$

In this chapter the following sequence is followed when discussing the experimental results. Initially, the MIIM structures fabricated with the same metal electrodes are discussed followed by tuning the effect of resonance by applying dissimilar metal electrodes. Finally, the experimental results are correlated to the simulations [7, 9, 10] in order to explore the validity of theoretical predictions.

6.2 Experimental

The MIIM device structures were fabricated on either 4 cm× 4 cm or 2 cm×2 cm Corning glass substrates due to its root mean squared (RMS) surface roughness of 0.32 nm, as confirmed by AFM measurement. As discussed in chapter 4, section 4.2.1, the roughness of the bottom metal electrode is an important parameter which will affect the device performance. It has been experimentally observed that the devices will be short-circuited if the roughness of the bottom electrode (Al) is large (3.4 nm) due to the ultra-thin (1-5 nm) oxides used in these MIM/MIIM structures. Therefore the metals were sputtered or evaporated on the smooth corning glass substrates, following optimised deposition conditions to minimise the roughness. The bottom metal electrode was patterned either by photolithography or shadow mask process followed by the oxide deposition. The oxides, Al_2O_3, Ta_2O_5 and Nb_2O_5 were deposited either by atomic layer deposition (ALD) or radio frequency (RF) sputtering technique. It was not necessary to pattern the high-k dielectric layers as the thicknesses of these layers are sufficiently thin for the needle to penetrate through the oxides and probe the bottom contact while performing current voltage (*IV*) measurements. Finally the top metal electrode was deposited by the same technique as that used to deposit the bottom electrode and patterned by either photolithography or shadow mask technique.

The DC electrical measurements were performed in a dark screened probe station using the Agilent B1500 semiconductor analyser to assess the rectification properties and the conduction process of each MIIM structure. The step voltage considered was ranged between 1 mV and 3 mV depending on the voltage sweep performed. It was crucial to perform the *IV* sweeps from zero to positive voltages and zero to negative voltages in order to minimise any charging effect [18, page 42]. Note that the charging effect was found to be negligible in MIIM structures presented in this chapter.

The voltage applied on each oxide layer was calculated in order to perform in-depth analysis of the conduction at different biasing levels. The portion of potential applied on each layer was found by considering the two oxide layers as two capacitors connected in series as illustrated in Figure 6.6.

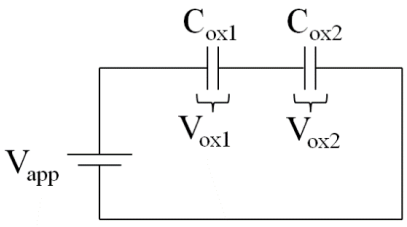

Figure 6.6: Two oxides are considered as two capacitors connected in series

The equivalent capacitance can be found by Eqn. 6.17, i.e.

$$C_{eq} = \frac{C_{ox1}C_{ox2}}{C_{ox1} + C_{ox2}}. \tag{6.17}$$

The voltage dropped across C_{ox1} is given as,

$$V_{ox1} = V_{app}\frac{C_{ox2}}{C_{ox1} + C_{ox2}}. \tag{6.18}$$

where V_{ox1} is the voltage dropped across the first oxide and V_{app} is that across the entire MIIM structure. The voltage dropped across each oxide is approximated using Eqn. 6.18. The dielectric constants used when calculating the oxide capacitances were 20 for Ta_2O_5 [2, 19], 25 for Nb_2O_5 [2] and 10 for Al_2O_3 [19, 20].

6.2.1 Al-based MIIM structures with the same metal electrodes

6.2.1.1 Al/1 .6 nm AlO_x/1 nm Al_2O_3/4 nm Ta_2O_5/Al device

The thermally evaporated top and bottom metal electrodes of this MIIM structure were patterned by the shadow mask process. There was an unintentional growth of native AlO_x on the Al metal electrodes which was found to be 1.6 nm by VASE. This native AlO_x on the bottom electrode could have a significant effect on the device performance as this will result in an increase of the overall thickness of the oxide layers sandwiched between the top and bottom metal electrodes as shown in Figure 6.7 (a). The oxides Al_2O_3 and Ta_2O_5 were deposited by ALD and the thicknesses of the 4 nm (nominal) Ta_2O_5 and 1 nm (nominal) Al_2O_3 were measured by VASE. The measured thicknesses were 3.48 nm for Ta_2O_5 and 1.15 nm for Al_2O_3 (see chapter 4).

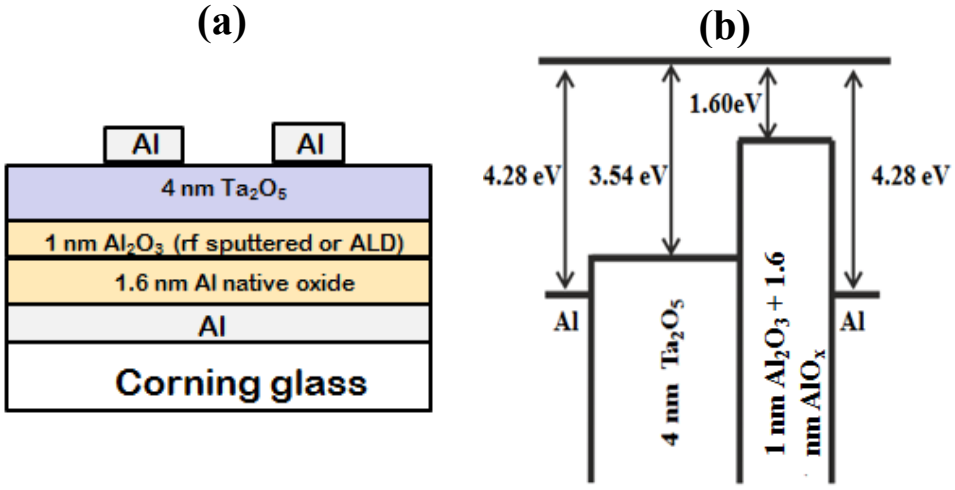

Figure 6.7: Device (a) cross-section and (b) energy band diagram for Al/1.6 nm AlO_x/1 nm Al_2O_3/4 nm Ta_2O_5/Al.

The energy band diagram of this structure is illustrated in Figure 6.7 (b). The work function of Al was previously calculated to be 4.28 eV and the electron affinities of Ta_2O_5 and Al_2O_3

were 3.54 eV and 1.6 eV respectively (see chapter 4). These values resulted in a barrier height at the interface of Al/Ta_2O_5 of 0.74 eV and the conduction band offset between Ta_2O_5 and Al_2O_3 of 1.94 eV as can be seen in Figure 6.7 (b). Moreover, at least eight devices were tested and each measurement has been repeated three times in order to verify the consistency and the repeatability of the results obtained.

The voltage across each dielectric layer was calculated using Eqn. 6.18 in order to analyse the conduction process of this MIIM structure. The fraction of voltage across the oxide layers Ta_2O_5:Al_2O_3 was found to be 0.44:0.56.

It can be observed that a large fraction of applied voltage falls across Al_2O_3 as a result of the native AlO_x layer. Therefore a larger voltage must be applied to the MIIM structure for the Ta_2O_5 conduction band (CB) edge to slope sufficiently to allow the formation of the quantum well. The influence of the native alumina later was evident in experimental results as explained later in this section; hence dry etching of the native AlO_x layer was employed. Then the portion of applied voltage across the 4 nm Ta_2O_5 and 1 nm Al_2O_3 layers was found to be 0.6:0.4, assuming the native AlO_x layer is completely etched.

The voltage across the Ta_2O_5 is larger than that across the Al_2O_3 as consequence of the reduction in Al_2O_3 thickness. The effect will be further illustrated clearly with the aid of band diagrams in Figure 6.8.

The device was in the flat band condition at zero bias as a result of the zero work function difference between the metal electrodes. Figure 6.8 shows calculations for 4 nm Ta_2O_5 and 1 nm Al_2O_3 + 1.6 nm AlO_x. A voltage of 1.5 V must be applied on Ta_2O_5 to reach the FNT regime when the native oxide was present, however 1 V is sufficient after dry etching of the native oxide layer. Moreover, as can be seen in Figure 6.8 (a), the dominant conduction mechanism is DT in etched and un-etched structures when the applied bias is smaller than 1 V and 1.5 V respectively as a consequence of the large energy difference of 0.33 eV between the metal Fermi level and the bound state created in the quantum well. The effect of resonant tunnelling was observed at about 2 V in experimental structures when the native AlO_x was not etched however it was evident that the onset of resonant tunnelling was shifted to 1.5 V after dry etching the native AlO_x as shown in Figures 6.8 (c) and 6.9 (a). This was mainly due to the small energy difference of 0.09 eV and 0.39 eV between the metal Fermi level and the two bound states created.

In the case of reverse bias there was no evidence of the formation of a quantum well. When the applied bias on the un-etched structure was smaller than ~ -1.5 V, the electron transport occurs through both oxides as can be seen in Figure 6.8 (d). However, if the applied voltage

is further increased (> -1.5 V), the structure reaches the step tunnelling regime. The MIIM structure with the etched native AlO_x entered the step tunnelling regime at -1.2 V as the electric field applied on Ta_2O_5 is larger compared to the previous case (Figure 6.8 (e)).

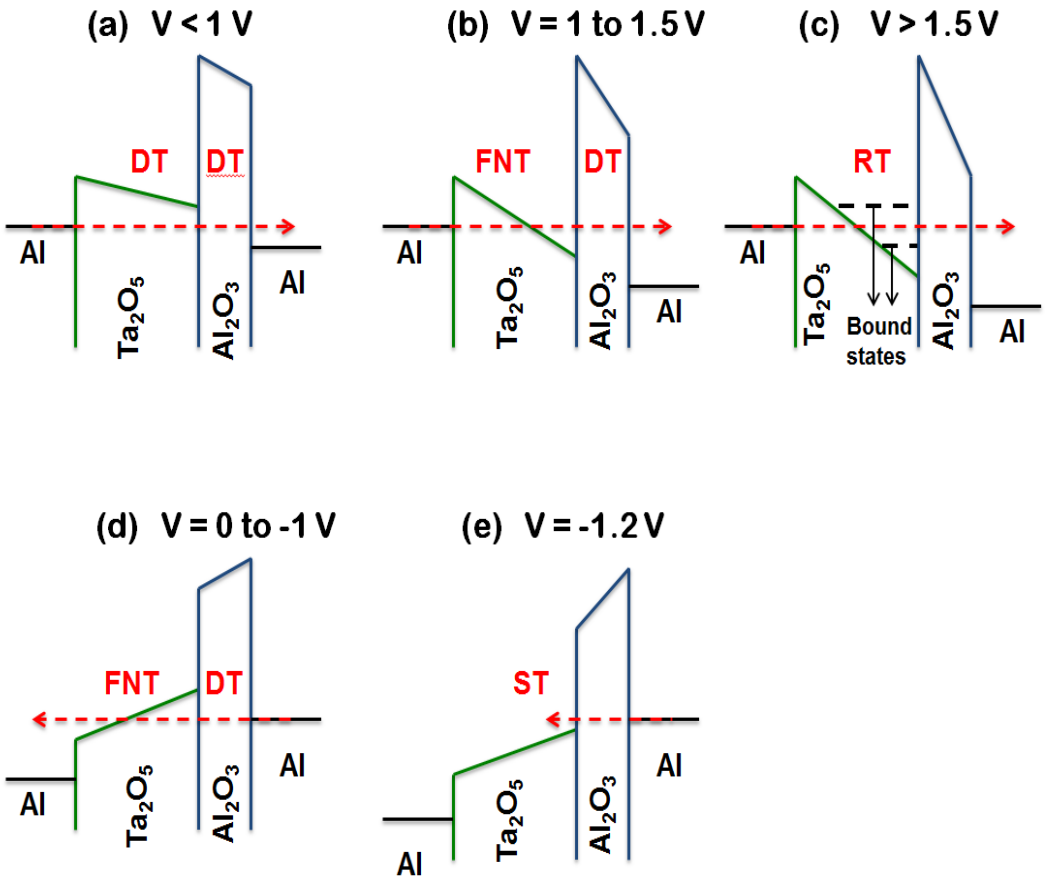

Figure 6.8: Calculated energy band diagrams of Al/1.6 nm AlO_x + 1 nm Al_2O_3/4 nm Ta_2O_5/Al MIIM tunnel rectifier depicting various conduction scenarios being dependent on external bias: (a)-(c) positive voltages; (d)-(e) negative voltages. DT, FN, ST, and RT refer to direct, Fowler-Nordheim, step and resonant tunneling, respectively.

The *IV* characteristics and referring rectification properties of these MIIM structures are shown in Figures 6.9 (a)-(f).

The *IV* measurements were performed by sweeping from negative to positive voltages and compared with the discontinuous sweeps that were done considering zero to positive and zero to negative voltages. As can be seen in Figure 6.9 (a), the origin of the *IV* curve was not shifted, suggesting the effect of charging was negligible. It was observed that the current level of the etched MIIM structure has significantly increased in contrast to the un-etched MIIM structure. This is in agreement with reduced thickness of the oxide stack after etching. Furthermore, the change in curvature of the *JV* curve of the etched device was observed at a smaller bias compared to the un-etched structure as can be seen in Figure 6.9 (a). The change in curvature can be ascribed to increased current due to resonance. The device asymmetry was calculated

by considering both forward to reverse current and reverse to forward bias current ratios. When the forward to reverse current ratio was considered, a peak device asymmetry of 6 was recorded at 1.75 V for the etched MIIM structure as a result of resonant tunnelling (Figure 6.9 (b)). However, when the reverse to forward current ratio was considered a large device asymmetry of 18 was observed at 0.3 V for the same MIIM structure (the inset of Figure 6.9 (b)).

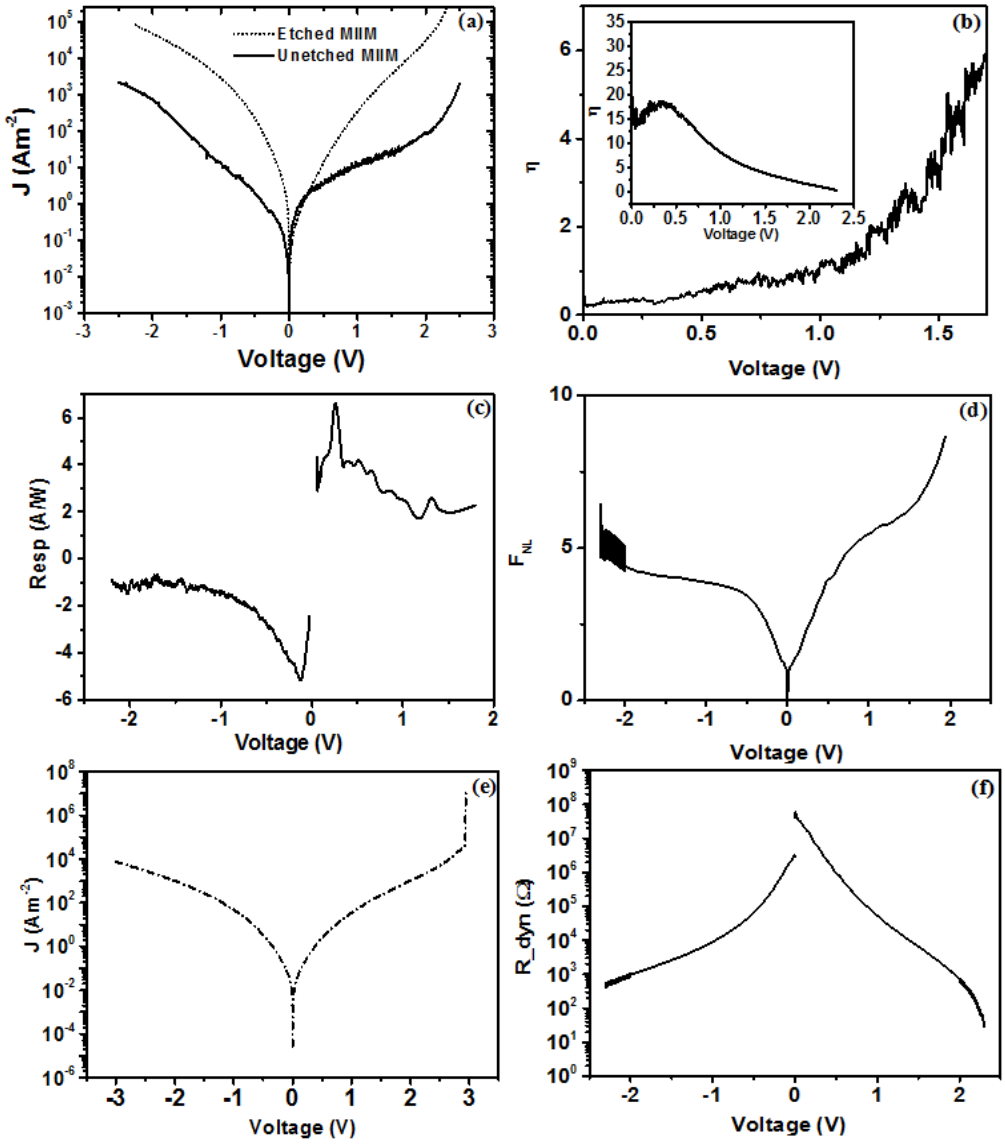

Figure 6.9: Device (a) JV characteristics (logarithmic scale), (b) asymmetry, (c) responsivity, (d) non-linearity, (e) JV characteristics with breakdown region, (f) dynamic resistance for Al/1 nm Al_2O_3/4 nm Ta_2O_5/Al. The device area $=1\times10^{-8}$ m^2.

A peak device responsivity of 6.7 A/W was found at 0.27 V as illustrated in Figure 6.9 (c). As seen in Figure 6.9 (d), a peak device non-linearity of 6.2 at 1.5 V and a rate of change of non-linearity of 5.8 V^{-1} were extracted. It can be seen clearly in Figure 6.9 (e) that the device broke down at ~3 V; thereby the change in curvature around 1.5 V cannot be ascribed to a soft

breakdown. The dynamic resistance at zero bias was 15.6 MΩ reducing to 24 Ω at 2.3 V as illustrated in Figure 6.9 (f).

The effect of resonant tunnelling was observed at larger voltages (> 1.5 V) due to large barrier height of 0.74 eV at the Al/Ta_2O_5 interface. Although there are bound states in the potential well leading to a large tunnelling probability, the transmittance is significantly smaller due to magnitudes of the Fermi-Dirac-like function being small. This caused the effect of resonant tunnelling to be observed at larger voltages in the experimental Al/Al_2O_3/Ta_2O_5/Al MIIM structure. Moreover, the measured thickness of 4 nm (nominal) Ta_2O_5 was 3.48 nm, making the onset of resonant tunnelling to shift towards larger voltages as the electric field applied on this layer reduced.

6.2.1.2 Al/1.6 nm AlO_x/1 nm Al_2O_3/4 nm Nb_2O_5/Al device

The Ta_2O_5 layer has been replaced with Nb_2O_5 with the aim of observing the effect of resonance (rectification reversal) at smaller bias voltages. The electron affinity of Nb_2O_5 was found to be 3.72 eV (see chapter 4). Therefore as can be seen in Figure 6.10 (b), the barrier height at the interface of Al/Nb_2O_5 is 0.56 eV, which is 0.18 eV smaller than that of Al/Ta_2O_5. Moreover, Nb_2O_5 created a larger conduction band offset of 2.12 eV to Al_2O_3, indicating the depth of the quantum well is larger than that of Ta_2O_5/Al_2O_3 interface.

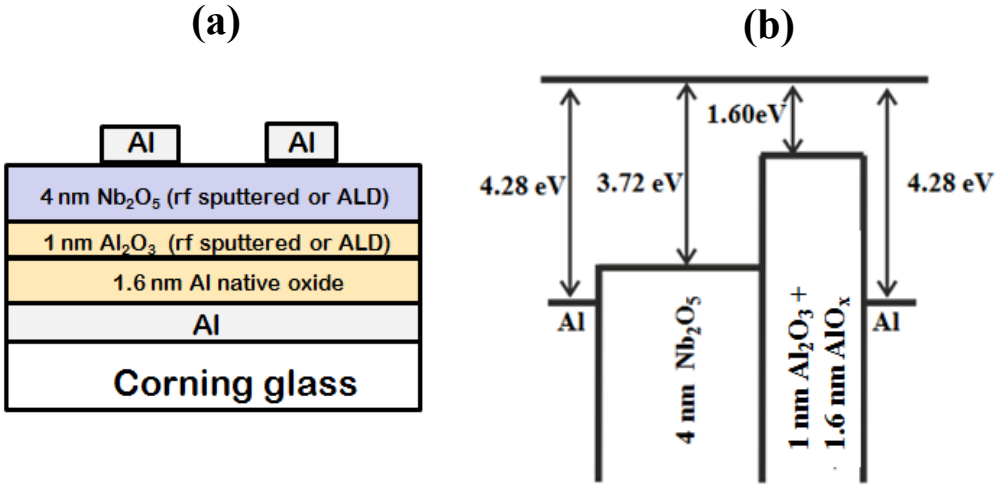

Figure 6.10: Device (a) cross-section and (b) energy band diagram for Al/1.6 nm AlO_x/1 nm Al_2O_3/4 nm Nb_2O_5/Al.

As can be seen in Figure 6.10 (a), Al was used as both top and bottom metal electrodes and Nb_2O_5 and Al_2O_3 were used as the oxides. The metal, Al was thermally evaporated and the electrodes were patterned by photolithography technique. The oxides were deposited by ALD technique. The inevitable growth of native AlO_x increases the total thickness of the oxide stack sandwiched between the Al electrodes. The voltages across the Nb_2O_5 and Al_2O_3 layers were found using Eqn. 6.18; the fraction of potential across Nb_2O_5 and Al_2O_3 was found to be

0.4:0.6. An electric field of 0.8 MV/cm is required for the 4 nm Nb_2O_5 to reach the FNT regime (see chapter 4, Figure 4.18). The measurements were repeated at least ten times and also about fifteen devices were tested in order to check the consistency and repeatability of results.

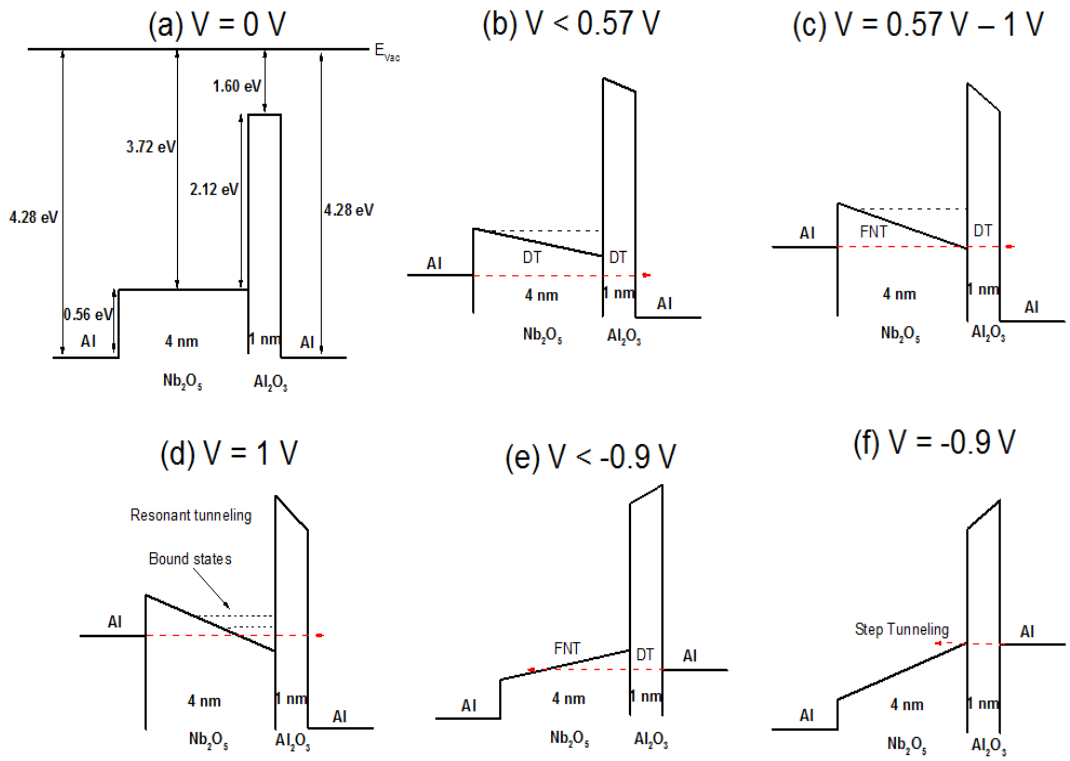

Figure 6.11: Energy band diagrams for A/1.6 nm AlO_x/1 nm Al_2O_3/4 nm Nb_2O_5/Al (a) flat band condition, (b), (c) and (d) conduction in forward bias (e), (f) conduction in reverse bias.

As can be seen in Figure 6.11 (a), the device is in flat band condition at zero bias due to the zero metal work function difference. It is possible to obtain a bound state in the conduction band of Nb_2O_5 when the applied voltage is 0.45 V; however the conduction in this structure dominates by DT until 0.57 V (Figure 6.11 (b)) due to the large energy difference of 0.31 eV between the metal Fermi level and the energy level of the bound state. The effect of resonance was more pronounced at 0.6 V according to Figures 6.11 (c) and 6.12 (a). It must be noted that Nb_2O_5 reaches the FNT regime when the applied voltage is 0.9 V, and strong evidence of resonance can be expected at voltages larger than this due to the small energy difference of 0.11 eV and 0.25 eV between the metal Fermi level and the bound states. Note that the second bound state is formed at an applied voltage of ~0.9 V. However, the rectification reversal in this experimental MIIM structure can be observed at ~0.6 V (see Figure 6.12 (d)), 0.4 V before the theoretically anticipated reversal of 1 V. This could be a consequence of the larger thickness of 4.9 nm measured for the 4 nm (nominal) Nb_2O_5 which will result in a higher electric field in the Nb_2O_5 layer and increased depth of potential well. As seen in Figure 6.12 (a), the forward current is enhanced when the applied voltage reaches ~1 V indicating strong evidence of resonance.

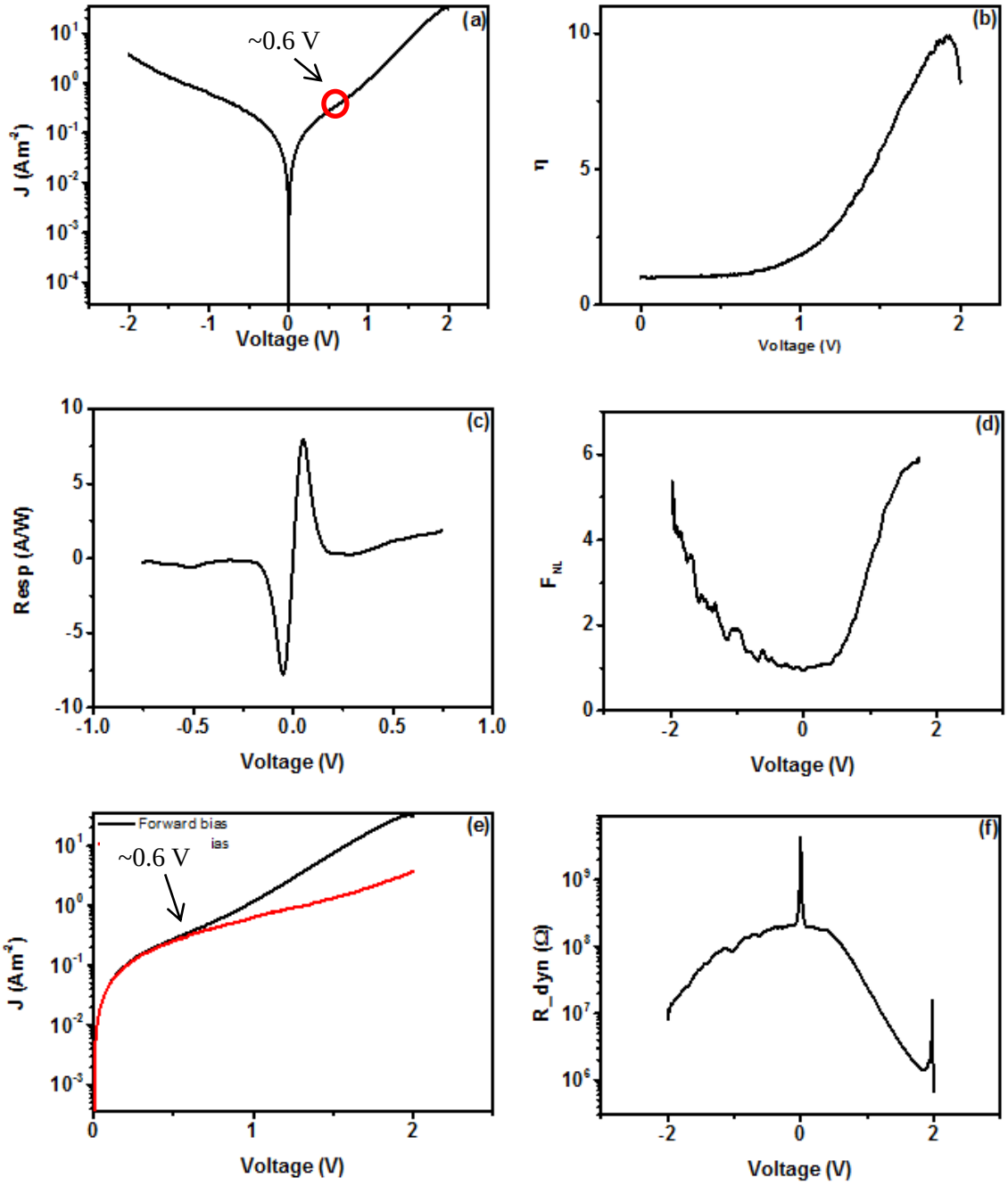

Figure 6.12: Device (a) JV Characteristics, (b) asymmetry, (c) responsivity, (d) non-linearity, (e) rectification reversal and (f) dynamic resistance for Al/1.6 nm AlO_x/1 nm Al_2O_3/4 nm Nb_2O_5/Al. The device area = 1×10^{-8} m^2.

In the case of reverse bias, a potential well was not created in the structure. Therefore the conduction in reverse bias is dominated by DT and FNT processes. The electrons have to traverse through both oxides when the applied bias was smaller than -0.9 V (Figure 6.11 (e)). However the electrons overcome the CB edge of Nb_2O_5 when the applied bias is larger than -0.9 V, reaching the step tunnelling regime (Figure 6.11 (f)). Higher forward bias currents can be observed compared to reverse bias currents due to dominance of resonant tunnelling.

A peak device asymmetry of 9.95 was recorded at 1.9 V (Figure 6.12 (b)). A peak responsivity of 7.8 A/W at 0.06 V can be seen in Figure 6.12 (c). A peak device non-linearity of 5.8 at 1.7 V and a rate of change of non-linearity of 5.18 V^{-1} are illustrated in Figure 6.12 (d). The rectification reversal, the point where forward bias current started to dominate the reverse bias current occurred at 0.6 V as shown Figure 6.12 (e)). The extracted dynamic resistance values at zero bias and 1.9 V were 300 MΩ and 1.3 MΩ respectively as shown in Figure 6.12 (f).

In summary of this section, the dominance of resonance at lower voltages was experimentally evident for Al/Nb_2O_5/Al_2O_3/Al device in contrast to the Al/Ta_2O_5/Al_2O_3/Al structure. The native AlO_x layer caused a reduction in the electric field applied on either Ta_2O_5 or Nb_2O_5 based devices. Therefore an approach has been carried out to investigate the rectification properties by replacing Al with metals such as Nb and Ta and also using different metal electrodes for Ta_2O_5/Al_2O_3 and Nb_2O_5/Al_2O_3 based MIIM devices.

6.2.2 MIIM structures with different metal electrodes

The effect of native AlO_x can be minimised if the MIIM structures are fabricated using metals such as Ta or Nb as the bottom metal electrode. Although Ta and Nb react with air and create native oxides, it is assumed that the overall thickness of either Ta_2O_5 or Nb_2O_5 becomes larger, resulting in an increase of the potential applied to Ta_2O_5 or Nb_2O_5 instead of Al_2O_3. The gradient of the CB edge will be increased by the increasing applied voltage. Therefore the potential well is created at lower bias leading to rectification reversal at smaller voltages. The work function of Ta and Nb were found to be 4.17 eV and 4.11 eV respectively. Another set of experiments was carried out by changing the electrode adjacent to Al_2O_3 in order to tune the rectification reversal to larger/smaller voltages. The metals used in this series of experiments were Ag, Cr and W with the work function values of 4.26 eV, 4.5 eV and 4.64 eV respectively. It is worth mentioning that the work function values of Ag, Cr and W are larger than the work function values of Ta and Nb. Therefore the rectification reversal is shifted towards larger values and this will be explained with the aid of energy band diagrams. In this section the oxides, Al_2O_3, Ta_2O_5 and Nb_2O_5 were deposited by RF sputtering whereas the metals Nb, Ta, Cr and W were deposited using DC sputtering at University of Southampton. Moreover, Ag was deposited by thermal evaporation process.

The measurements were repeated at least five times to verify the consistency and repeatability of the results obtained. Although there are nine devices on each Corning glass slide, the yield was between two and eight. This was as a consequence of the fluorescent light source used in the probe station which led to break down of the devices. It was assumed that the light source generated an instantaneous pulse of ~1 V.

6.2.2.1 Ta/4 nm Ta_2O_5/1 nm Al_2O_3/Ta device

The MIIM structure was fabricated using Ta as the top and bottom metal electrodes. The effect of Ta native oxide was negligible based on the VASE measurements performed. The metal electrodes were patterned by shadow mask process. Moreover, the oxides, 4nm (nominal) Ta_2O_5 and 1 nm (nominal) Al_2O_3 were deposited by RF sputtering process. The device cross-section is illustrated in Figure 6.13 (a).

The barrier height of 0.63 eV at the Ta/Ta_2O_5 is smaller in contrast to the Al/Ta_2O_5, hence it is expected to observe the dominance of resonance at a smaller voltage which will be explained with theoretical and experimental analysis performed on this MIIM structure. Moreover in this structure the fraction of potential which falls on Ta_2O_5 and Al_2O_3 is 0.67:0.33.

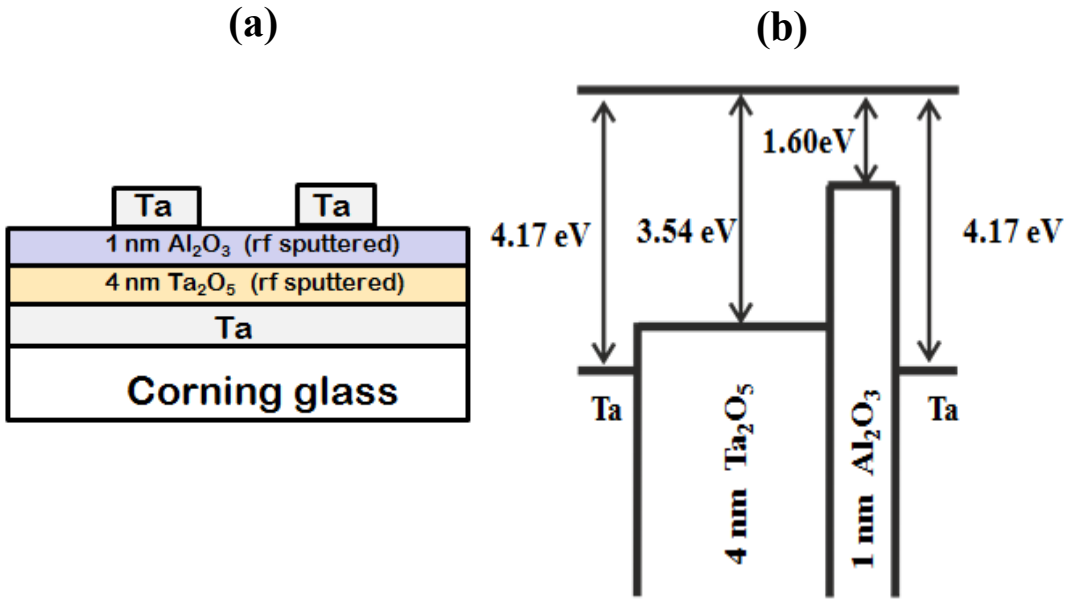

Figure 6.13: Device (a) cross-section and (b) energy band diagram for Ta/1 nm Al_2O_3/4 nm Ta_2O_5/Ta.

As can be seen in Figure 6.14 (a), the device is in the flat band condition when the applied bias is zero due to the zero work function difference between left and right metal electrodes. After simulating the device structure, it was found that a bound state can be obtained at 0.45 eV above the Fermi level of Ta at the applied voltage of 0.55 V [7, 9]. However, resonant tunnelling is not pronounced in DC characteristics due to the 0.63 eV barrier height at the Ta/Ta_2O_5 interface, therefore the number of electrons which occupy the energy state of 0.45 eV above the Fermi level of Ta is small. As shown in Figure 6.14 (b), conduction is dominated by DT when the applied bias was smaller than 0.9 V. The dominance of resonance cannot not be observed although Ta_2O_5 reaches FNT regime at 0.9 V - see Figure 6.14 (c). However, strong evidence of resonant tunnelling is observed at 1.3 V, as a result of the small energy difference of 0.13 eV and 0.37 eV between the energy levels of the bound states and the Fermi level of Ta (Figures 6.14 (d) and 6.15 (a)).

The conduction in reverse bias is dominated by a combination of DT and FNT (Figure 6.14 (e)). The electrons inject to the CB of Ta_2O_5 when the applied voltage increased beyond -1.2 V (step tunnelling), resulting in the 1 nm thin Al_2O_3 to limit the conduction by DT as shown in Figure 6.14 (f).

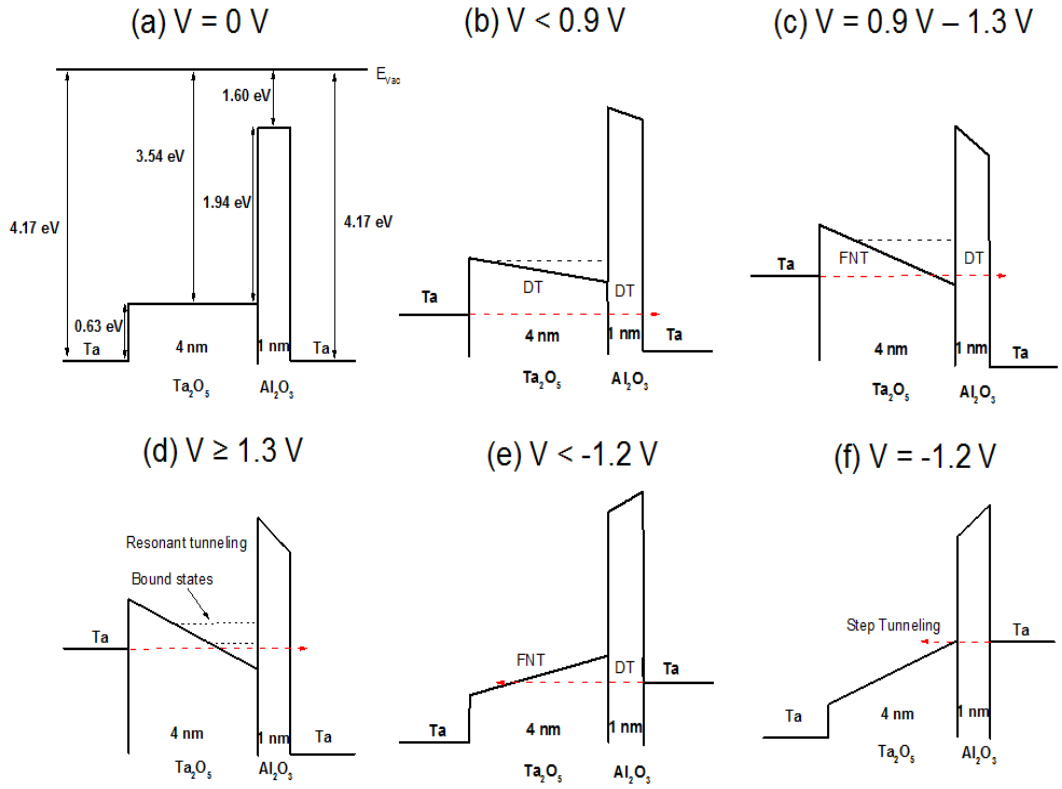

Figure 6.14: Energy band diagrams of Ta/1 nm Al_2O_3/4 nm Ta_2O_5/Ta MIIM tunnel rectifier depicting various conduction scenarios being dependent on external bias: (a) flat band condition (b)-(d) positive voltages; (e)-(f) negative voltages.

The *IV* measurements were performed with a step voltage of 2 mV. The *IV* characteristics of this MIIM structure are shown in Figure 6.15 (a). The device asymmetry was calculated considering the ratio of forward to reverse bias current and a peak device asymmetry of 1.6 was extracted at 1.8 V due to resonant tunnelling (Figure 6.15 (b)). The asymmetry was not large as a result of observing resonant tunnelling at 1.3 V and the voltage sweep was limited to 2 V. A peak device responsivity of 8.3 A/W was extracted at 0.1 V and a zero bias responsivity was 0.1 A/W as can be seen in Figure 6.15 (c). As per Figure 6.15 (d), a peak device non-linearity of 3.6 at 1.3 V and a rate of change of non-linearity of 2 V^{-1} were extracted. The rectification reversal occurred at 1.3 V due to the dominance of resonant

tunnelling (Figure 6.15 (e)). The dynamic resistance of this structure was recorded as 9 GΩ at zero bias reducing to 90 MΩ at 1.5 V (Figure 6.15 (f)).

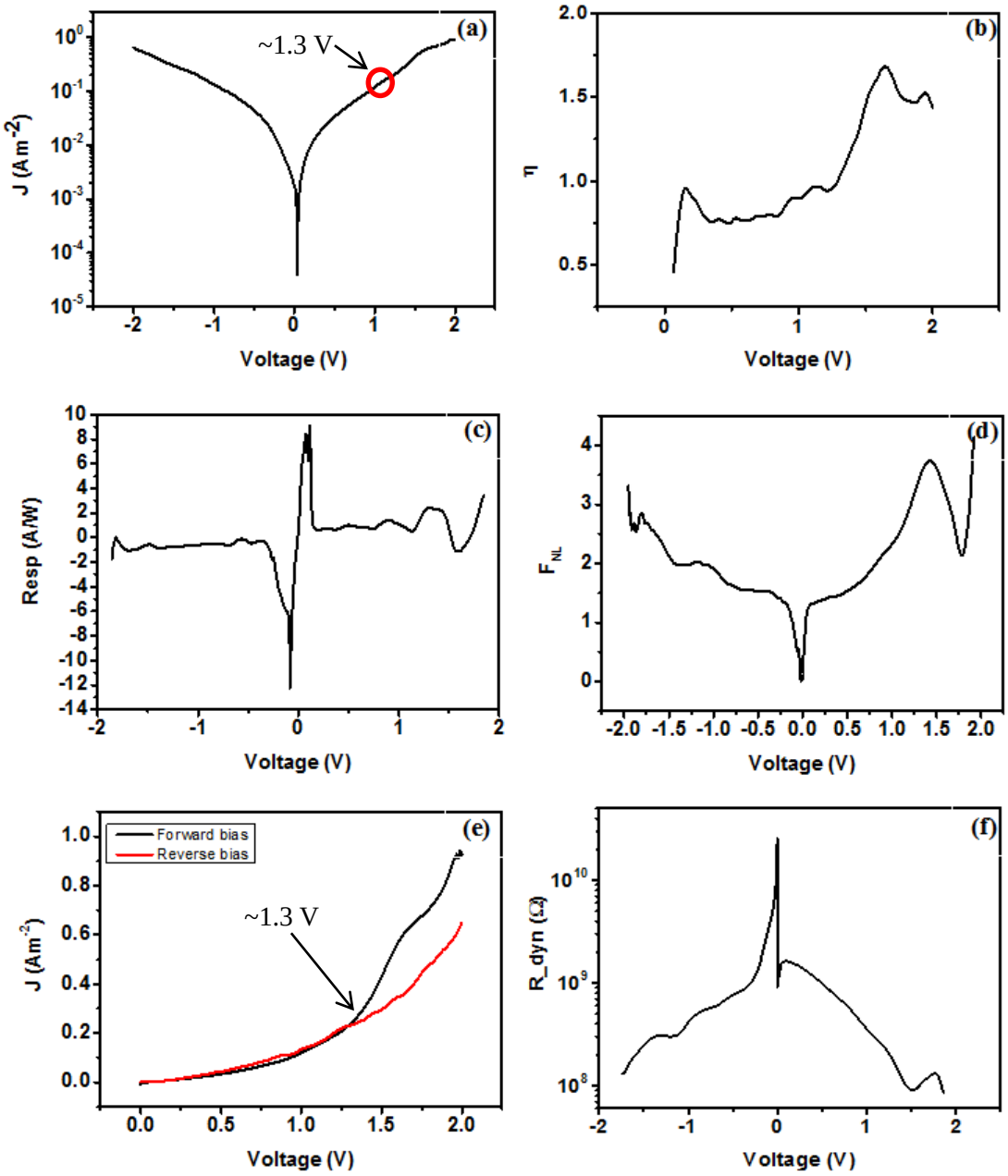

Figure 6.15: Device (a) JV Characteristics, (b) asymmetry, (c) responsivity, (d) non-linearity, (e) rectification reversal and (f) dynamic resistance for Ta/4 nm Ta_2O_5/1 nm Al_2O_3/Ta. The device area = 1×10^{-8} m^2.

6.2.2.2 Ta/4 nm Ta_2O_5/1 nm Al_2O_3/Ag device

The MIIM structure discussed in section 6.2.2.1 can be used as a reference and allows investigation of the rectification reversal point. It can be used to investigate the possibility of tuning rectification reversal by changing the work function of the top metal electrode. In this device, Ag was used as the top metal electrode with the motivation of shifting the onset of resonant tunnelling towards larger voltages as the work function of Ag (4.26 eV) is larger than that of Ta (4.17 eV) (Figure 6.16 (b)). The oxides, 4 nm (nominal) Ta_2O_5 and 1 nm (nominal) Al_2O_3 were used in this structure. The cross-section of the completed device is shown in Figure 6.16 (a).

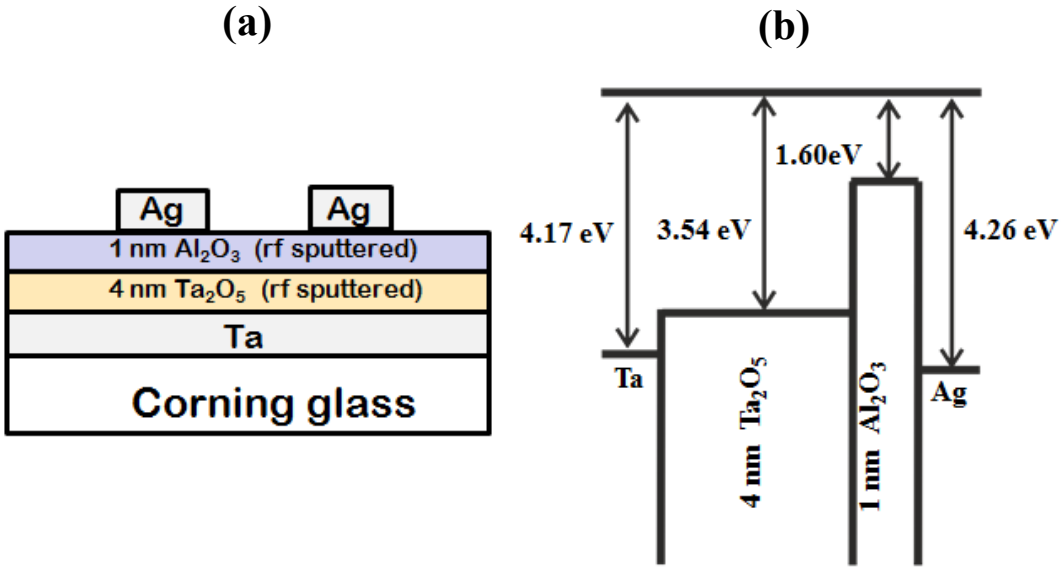

Figure 6.16: Device (a) cross-section and (b) energy band diagram for Ta/1 nm Al_2O_3/4 nm Ta_2O_5/Ag.

The work function difference between the metal electrodes was 0.09 eV. The device is not in the flat band condition when applied bias is zero as the conduction bands were bent to the left side since the metal Fermi levels align at zero bias (Figure 6.17 (a)). A voltage of 0.13 V has to be applied on the Ag electrode to reach the flat band condition. This will be discussed in detail and related to the shift observed in the rectification reversal.

The voltage dropped across each oxide layer was calculated using Eqn. 6.18. The same potential division is applied on this structure due to the use of same oxide combination.

A bound state at 0.7 V was obtained from theoretical simulations [7, 9]. However the resonance is not observed as a result of the large energy difference of 0.46 eV between the Fermi energy level of Ta and the energy level of the bound state. This is due to the number of electrons at energy levels above the metal Fermi level is small, therefore the transmittance, the product of Fermi-Dirac-like distribution and tunnelling probability is reduced significantly. The Ta_2O_5 reaches FNT regime when the applied bias is increased to 1 V (Figure

6.17 (d)). Eventually the dominance of resonant tunnelling can be observed when the applied bias increases to 1.39 V as shown in Figure 6.17 (e) due to the small energy difference of 0.18 eV and 0.40 eV between the Fermi level of Ta and the energy level of two bound states.

The conduction in reverse bias is dominated by DT and FNT when the applied bias was smaller than -0.7 V as seen in Figure 6.17 (f). However, the electrons will be injected to the CB edge or CB of Ta_2O_5 from Al_2O_3 when the applied is increased beyond -0.7 V as shown in Figure 6.17 (g).

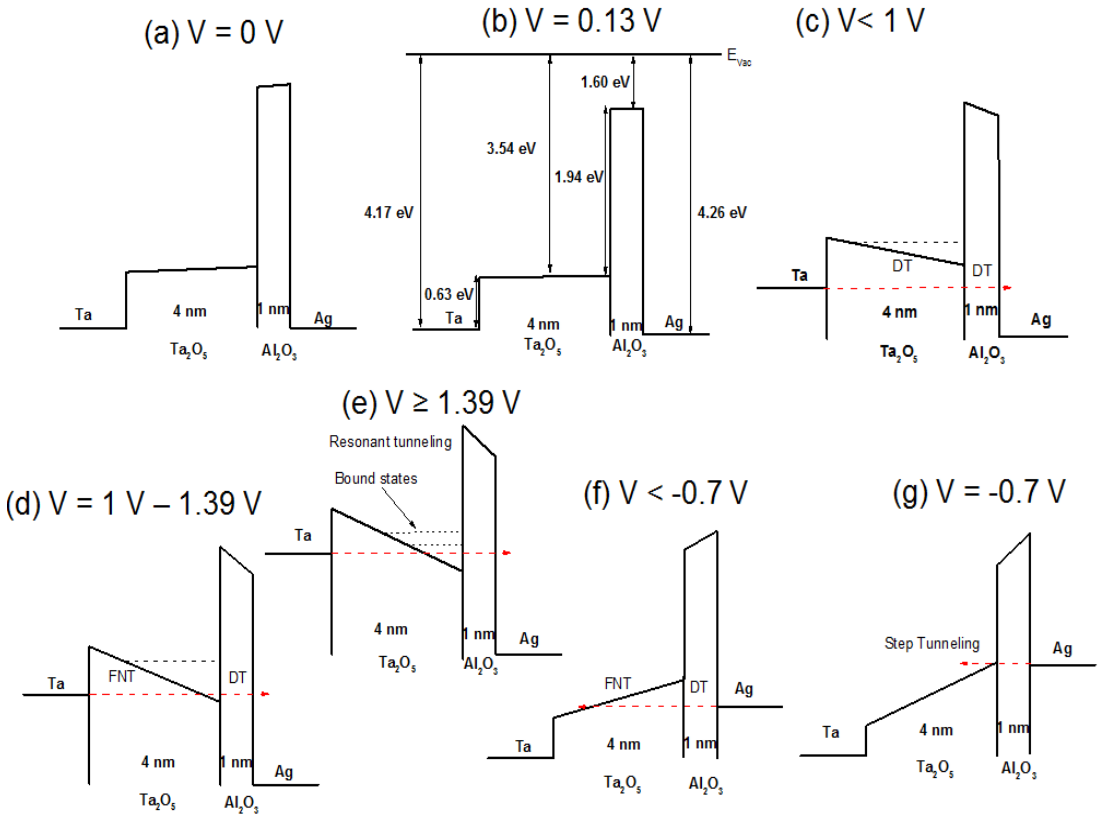

Figure 6.17: Energy band diagrams of Ta/1 nm Al_2O_3/4 nm Ta_2O_5/Ag MIIM tunnel rectifier depicting various conduction scenarios being dependent on external bias: (a) zero bias (b) flat band condition (c)-(e) positive voltages; (f)-(g) negative voltages.

The next step is to analyse the rectification properties of this MIIM structure. A peak device asymmetry of 2.1 was recorded at 1.6 V for the forward to reverse current ratio as shown in Figure 6.18 (b). This was obtained due to resonant tunnelling. However, it was evident an asymmetry of 3.2 at 0.56 V due to step tunnelling as shown in the inset of Figure 6.18 (b). Furthermore, as per Figure 6.18 (c), a peak device responsivity of 7.7 A/W was recorded at 0.2 V. A peak device non-linearity of 5.7 at 1.38 V and a rate of change of non-linearity of 7.41 V^{-1} were extracted by analysing the Figure 6.18 (d). The rectification reversal occurred

at 1.39 V as consequence of resonant tunnelling (Figure 6.18 (e)). The dynamic resistance at zero bias and at 1.5 V were 2 TΩ and 20 MΩ respectively as can be seen in Figure 6.18 (f).

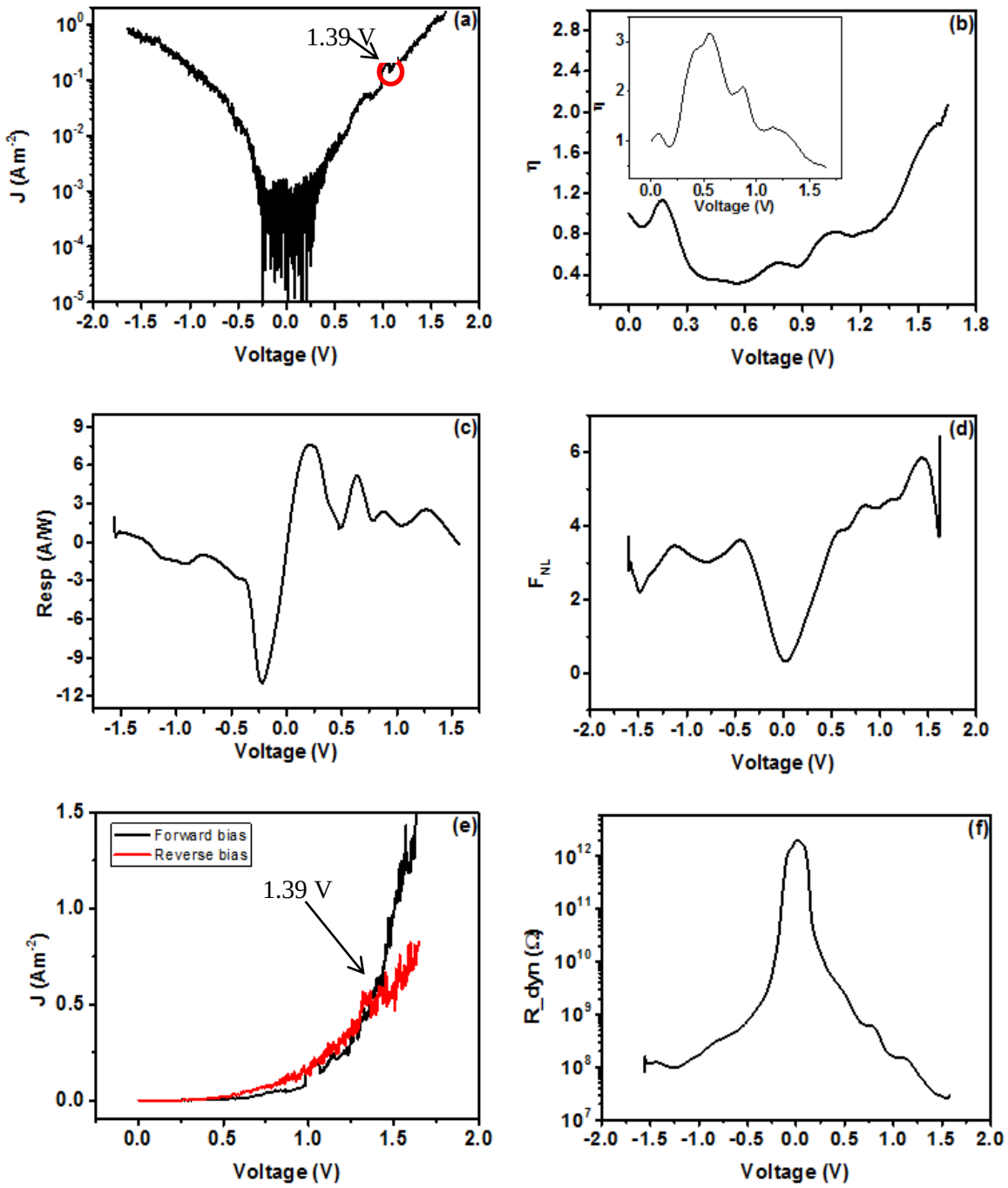

Figure 6.18: Device (a) JV characteristics, (b) asymmetry, (c) responsivity, (d) non-linearity, (e) rectification reversal and (f) dynamic resistance for Ta/1 nm Al_2O_3/4 nm Ta_2O_5/Ag. The device area = 1×10^{-8} m^2.

6.2.2.3 Ta/4 nm Ta_2O_5/1 nm Al_2O_3/Cr device

In this case the top metal electrode was replaced with Cr to observe if the rectification could be shifted further. The completed MIIM structure can be seen in Figure 6.19 (a).

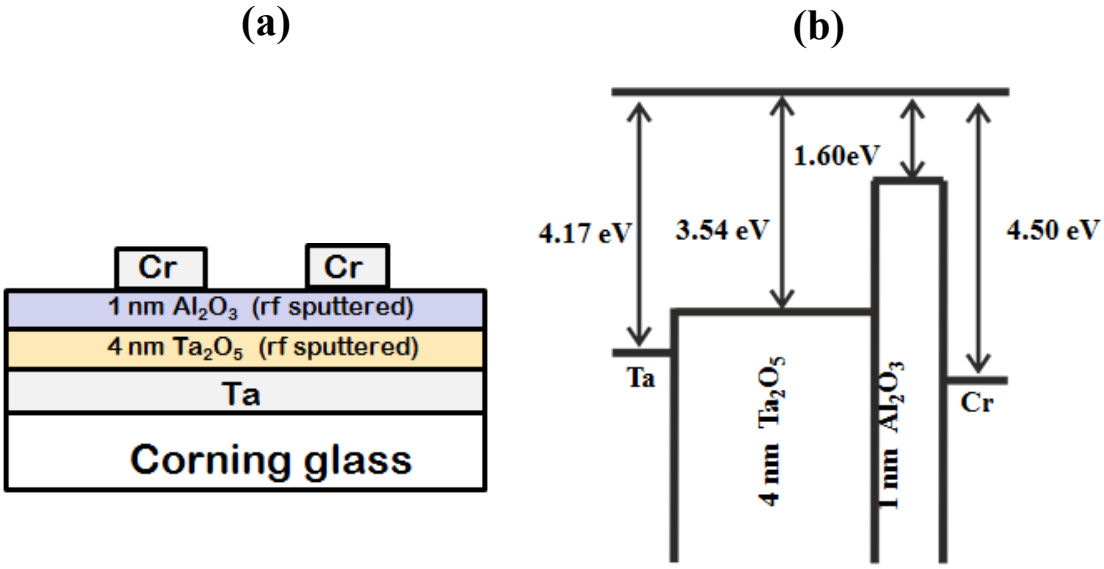

Figure 6.19: Device (a) cross-section and (b) energy band diagram for Ta/1 nm Al_2O_3/4 nm Ta_2O_5/Cr.

The work function of Cr is 4.5 eV, creating a metal work function difference of 0.33 eV as illustrated in Figure 6.19 (b). This caused the CB edges to slope towards left at zero bias as seen in Figure 6.20 (a); therefore a voltage of 0.49 V must be applied on the Cr electrode to reach the flat band condition (Figure 6.20 (b)). The potential divided across the oxides is identical to the previous two devices due to the same thickness and oxide combination.

A triangular quantum well is formed when the CB edge of Ta_2O_5 slopes right as shown in Figure 6.20 (c-e). The CB slope can be estimated precisely using the portion of applied voltage on Ta_2O_5. It is possible to obtain a bound state in the triangular quantum well if a voltage bias of 0.8 V was applied on the structure. However, the conduction in forward bias is dominated by DT process up to 1.25 V (Figure 6.20 (c)). This is a consequence of the large energy difference of 0.32 eV between the Fermi level of Ta and the energy level of the bound state. Furthermore, if the applied bias is increased beyond 1.25 V, Ta_2O_5 reaches FNT regime as shown in Figure 6.20 (d). Nevertheless, the dominance of resonant tunnelling can be observed when the applied bias is further increased beyond 1.6 V as per Figure 6.20 (e). The energy difference between the Fermi level of Ta and the bound states are 0.19 eV and 0.38 eV respectively. Note that the device broke down at 1.7 V. Therefore the *IV* measurements were performed in the voltage range of -1.6 V to 1.6 V. As a consequence, it was not possible to observe the dominance of forward bias current due to resonance.

In the case of reverse bias, when the applied bias was smaller than -0.6 V, the electron transport is limited by DT in both Ta_2O_5 and Al_2O_3 oxides. The conduction mechanism in Al_2O_3 was always dominated by DT whereas in Ta_2O_5, DT and FNT at smaller voltages as shown in Figure 6.20 (f). If the applied bias is further increased beyond -0.6 V, the electrons will travel through Al_2O_3 by DT and injected to the CB edge or CB of Ta_2O_5 as illustrated in Figure 6.20 (g)).

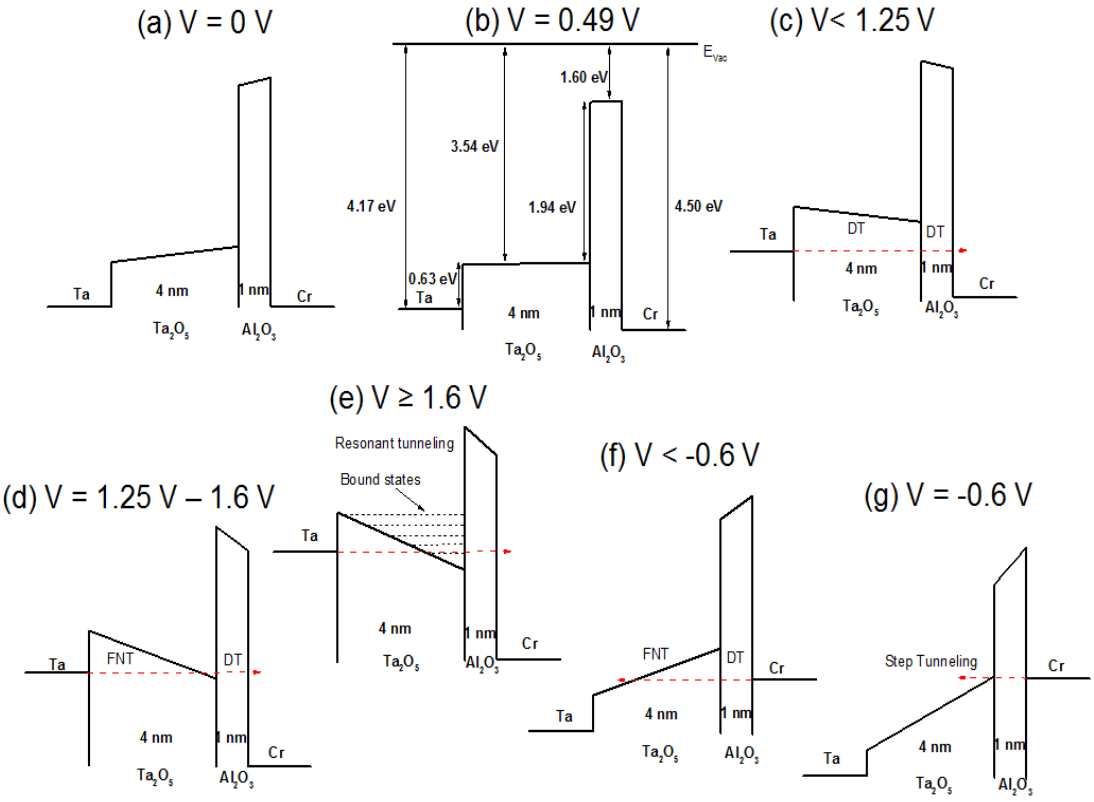

Figure 6.20: Energy band diagrams of Ta/1 nm Al_2O_3/4 nm Ta_2O_5/Cr MIIM tunnel rectifier depicting various conduction scenarios being dependent on external bias: (a) zero bias, (b) flat band condition, (c)-(e) positive voltages, (f)-(g) negative voltages.

The *JV* characteristics of this MIIM structure are shown in Figure 6.21 (a). The device asymmetry was calculated by considering the ratio of reverse to forward bias current as the dominance of resonance could not be observed. A peak device asymmetry of 1.9 was recorded at 0.75 V (Figure 6.21 (b)). A peak device responsivity of 2.5 A/W at 0.2 V (Figure 6.21 (c)) and a peak non-linearity of 5.5 at 1.4 V (Figure 6.21 (d)) were obtained. The rate of change of non-linearity was 4.8 V^{-1}. It could be anticipated that the rectification reversal occurred around 1.6 V as shown in Figure 6.21 (e). The zero bias dynamic resistance was 15.4 MΩ whereas the dynamic resistance at 1.6 V was 88 kΩ as shown in Figure 6.21 (f).

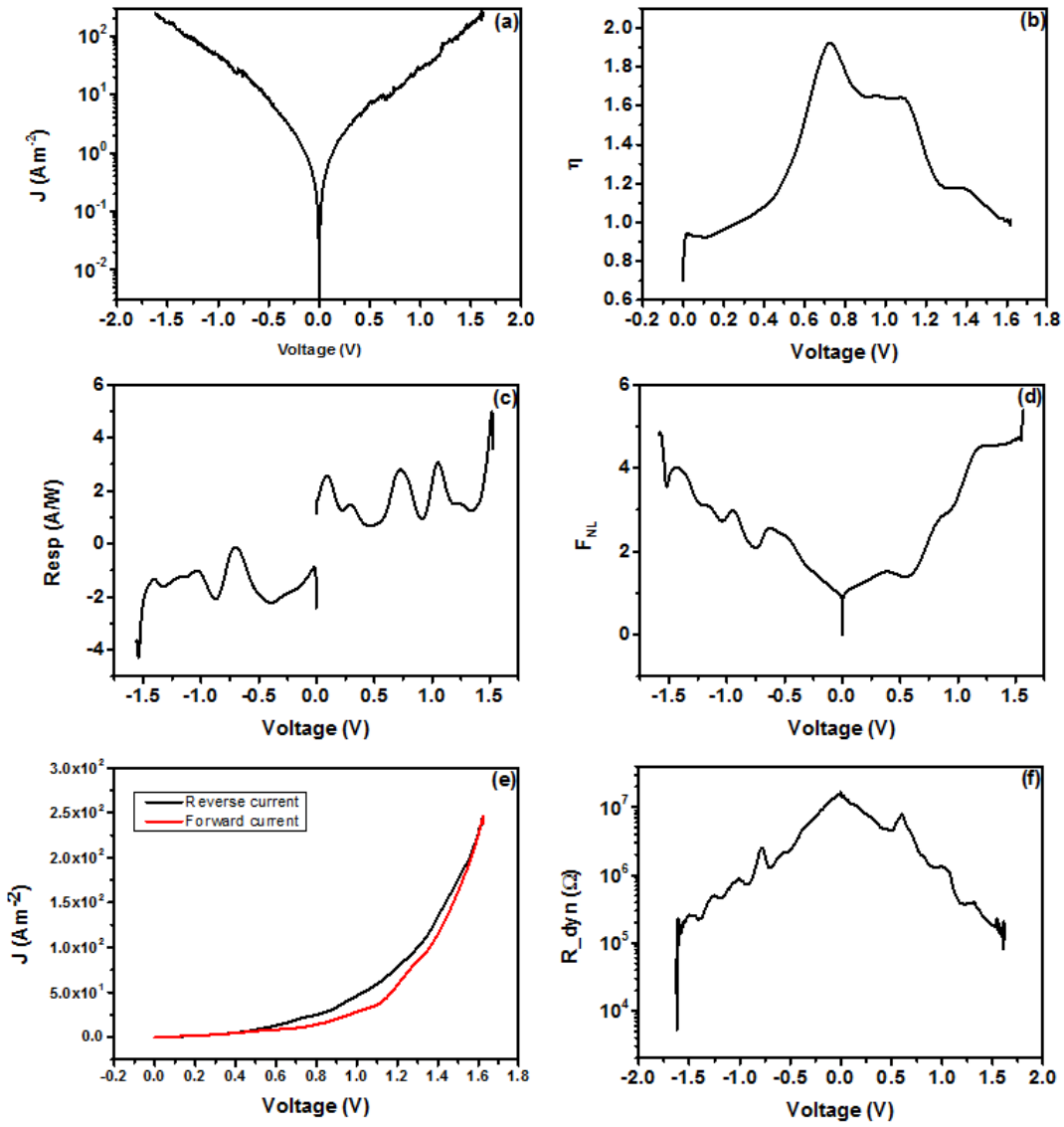

Figure 6.21: Device (a) JV characteristics, (b) asymmetry, (c) responsivity, (d) non-linearity, (e) rectification reversal and (f) dynamic resistance for Ta/1 nm Al_2O_3/4 nm Ta_2O_5/Cr. The device area = 1×10^{-8} m^2.

It can be deduced that the rectification reversal point has been shifted towards larger voltages > 1.6 V with the increase in the work function of the top metal electrode (adjacent to Al_2O_3). This result indicates a proof of concept that changing the work function difference from Ta/Ta to Ta/Ag and to Ta/Cr, allows the tuning of the onset of resonant tunnelling. The same study has been conducted by replacing Ta with Nb and using the oxide combination of Nb_2O_5 and Al_2O_3 and this is described in the next section.

6.2.2.4 Nb/4 nm Nb_2O_5/1 nm Al_2O_3/Nb device

In this device, Nb_2O_5 was chosen as the first oxide due to its larger electron affinity value of 3.72 eV in contrast to Ta_2O_5 (3.54 eV). This resulted in a barrier height of 0.39 eV at the Nb/Nb_2O_5 interface and a conduction band offset between the dielectrics of 2.12 eV (Figure 6.22 (b)). The energy band diagram with the corresponding work function values of Nb and electron affinities of Nb_2O_5 and Al_2O_3 is shown in Figure 6.22 (b). The 4 nm (nominal) Nb_2O_5 and 1 nm (nominal) Al_2O_3 were deposited by RF sputtering. The device cross-section of the completed MIIM structure is shown in Figure 6.22 (a).

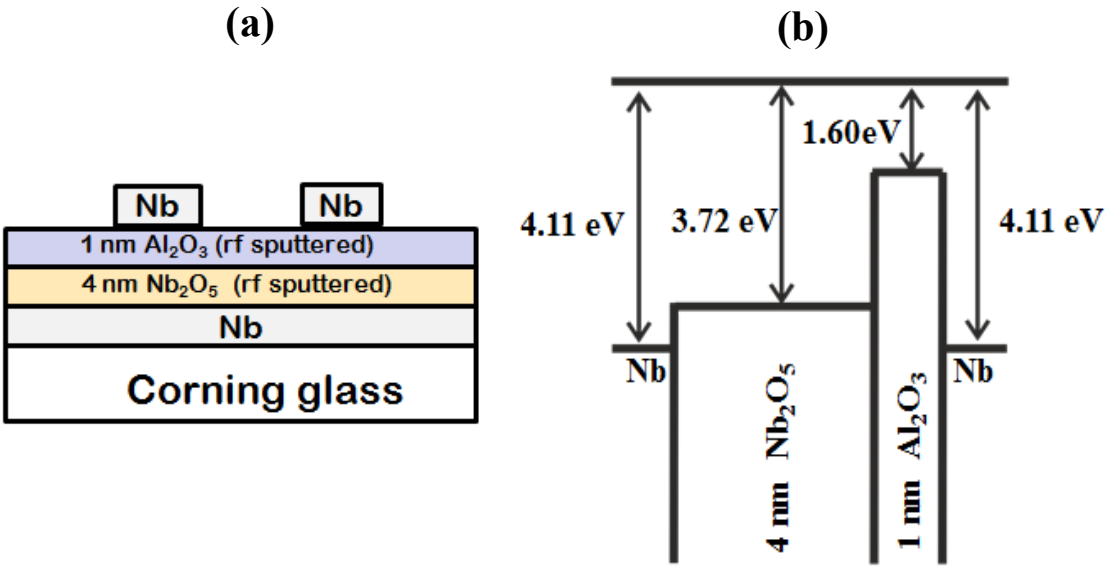

Figure 6.22: Device (a) cross-section and (b) energy band diagram for Nb/1 nm Al_2O_3/4 nm Nb_2O_5/Nb.

As can be seen in Figure 6.22 (b), the work function difference between the metal electrodes is zero, therefore the structure is in the flat band condition at zero bias (Figure 6.23 (a)). The dominance of resonance can be observed at smaller voltages in contrast to the previously discussed devices due to the smaller barrier height of 0.39 eV. This will be explored by analysing the conduction process and the DC characteristics of this MIIM structure.

The portion of voltage dropped across Nb_2O_5 and Al_2O_3 is 0.61:0.39.The first bound state was created when the applied bias reached 0.38 V at the energy of 0.40 eV. However, as shown in Figure 6.23 (b), the conduction in this structure is dominated by DT even with the presence of a bound state due to the large energy gap of ~0.40 eV between the Fermi level of Nb and the bound state energy level. Moreover, Nb_2O_5 reaches FNT regime when the applied voltage reaches 0.57 V (Figure 6.23 (c)). The dominance of resonant tunnelling can be observed around 0.7 V (Figures 6.23 (d) and 6.24 (e)) due to the narrow energy difference of 0.12 eV and 0.34 eV between the Fermi level and the energy state of two bound states.

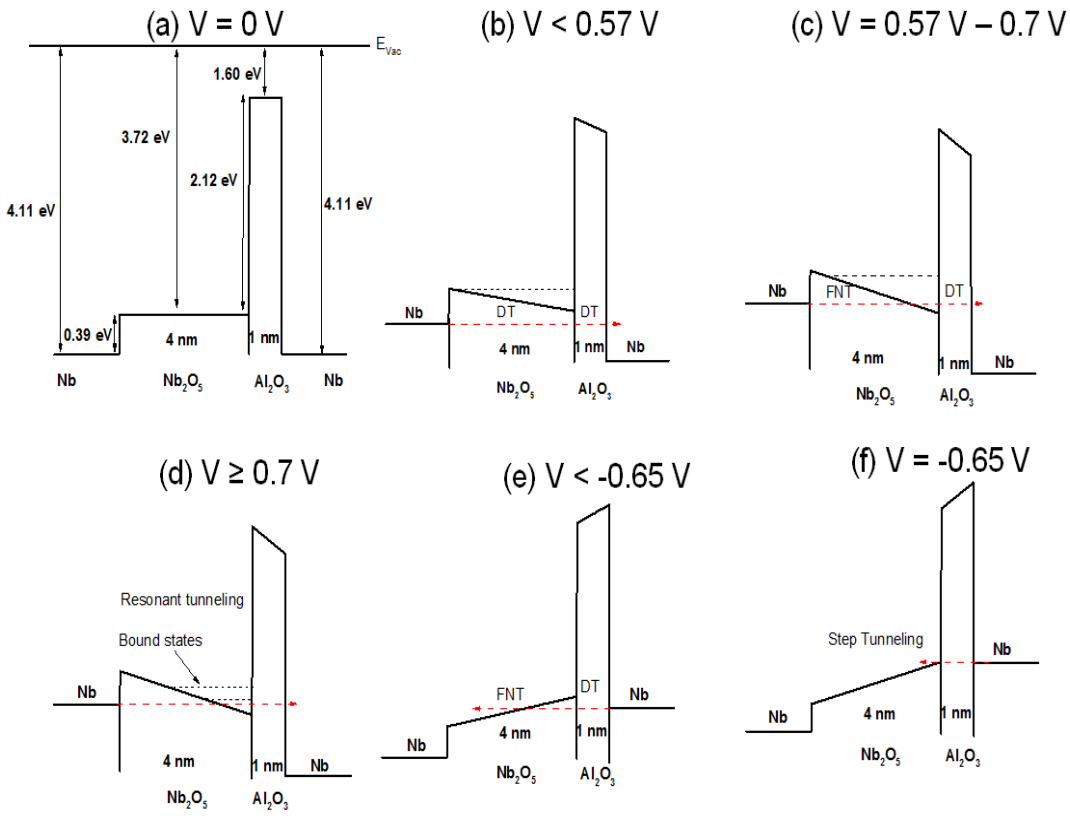

Figure 6.23: Energy band diagrams of Nb/1 nm Al_2O_3/4 nm Nb_2O_5/Nb (a) flat band condition, (b), (c) and (d) conduction in forward bias (e), (f) conduction in reverse bias.

The conduction in reverse bias is dominated by a combination of DT and FNT when the applied bias is smaller than -0.65 V as shown in Figure 6.23 (e). The electron transport in Al_2O_3 is limited by DT, and then these electrons will be injected to the CB edge of Nb_2O_5 when the applied bias is increased beyond -0.65 V as shown in Figure 6.23 (f).

Next, the rectification properties of this structure was analysed based on the *IV* measurements in Figure 6.24 (a). Peak device asymmetries of 2.2 and 1.4 were extracted at 0.03 V and 1 V respectively as seen in Figure 6.24 (b). The asymmetry extracted at 0.03 V can be ascribed to noise. The device asymmetry obtained due to resonance was not significant as a result of the small change in the magnitudes for forward bias current. This is in agreement with the ratio between forward to reverse current extracted from the theoretical model which is 1.5 at 1 V. A peak device responsivity of 7.9 A/W was recorded at 0.1 V as shown in Figure 6.24 (c). It was possible to observe another peak (2.4 A/W at 0.7 V) in the responsivity which could be in correspondence with the regime where resonant tunnelling is dominant. A peak device non-linearity of 3.9 at 0.9 V and a rate of change of non-linearity of 4.34 V^{-1} were extracted from non-linearity plot shown in Figure 6.24 (d). The rectification reversal occurred around 0.7 V as can be seen in Figure 6.24 (e). The dynamic resistance at zero bias was 35 MΩ reducing to 19 kΩ at 1.29 V (Figure 6.24 (f)).

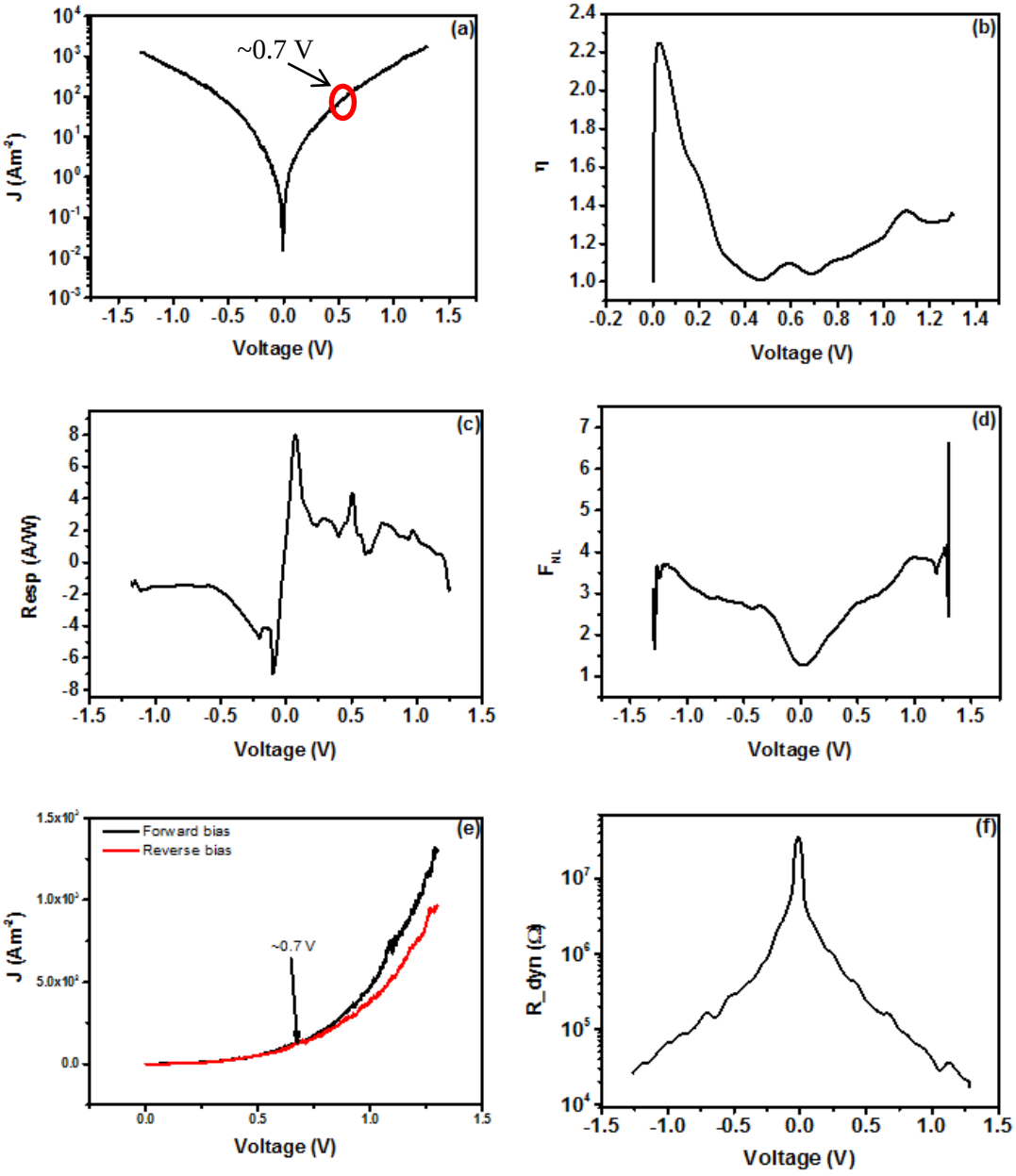

Figure 6.24: Device (a) JV characteristics (logarithmic scale), (b) asymmetry, (c) responsivity, (d) non-linearity, (e) rectification reversal and (f) dynamic resistance for Nb/1 nm Al_2O_3/4 nm Nb_2O_5/Nb. The device area = 1×10^{-8} m^2.

6.2.2.5 Nb/4 nm Nb_2O_5/1 nm Al_2O_3/Ag device

The Nb/Nb_2O_5/Al_2O_3/Nb MIIM structure can be used as a reference. The top electrode is replaced with Ag in order to tune the rectification reversal and to observe its effect on rectification properties. The cross-section of the completed device structure is shown in Figure 6.25 (a).

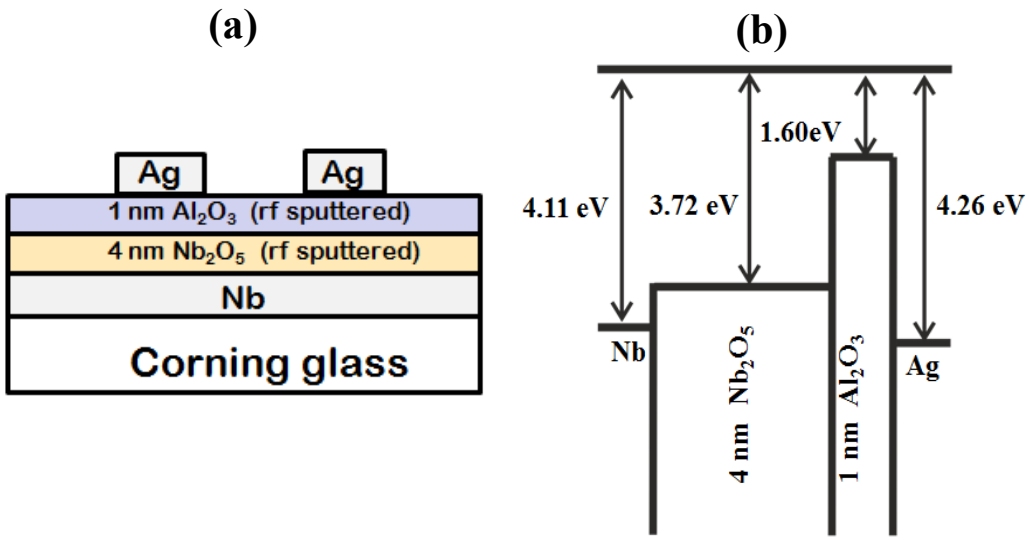

Figure 6.25: Device (a) cross-section and (b) energy band diagram for Nb/1 nm Al_2O_3/4 nm Nb_2O_5/Ag.

As can be seen in Figure 6.25 (b), the work function of Ag is 0.15 eV larger than that of Nb. The portion of applied voltage across 4 nm Nb_2O_5 and 1 nm Al_2O_3 was the same as in section 6.2.2.4 as a result of the identical oxide combination and the thicknesses. Hence this MIIM structure is not in the flat band condition at zero bias (Figure 6.26 (a)). However, if the applied bias is increased to 0.18 V, the structure reaches the flat band condition as shown in Figure 6.26 (b). Therefore a larger voltage must be applied on this structure to form a quantum well compared to the case where both metal electrodes were Nb. The first bound state forms when the applied bias is increased to 0.49 V at the energy of 0.41 eV. However, there is no evidence of resonant tunnelling observed in Figure 6.27 (a) at 0.49 V due to the large energy difference of 0.41 eV between the Nb Fermi level and the bound state as per Figure 6.26 (c). The conduction dominates by DT when the applied voltage bias is smaller than 0.8 V as shown in Figure 6.26 (c). Moreover, Nb_2O_5 reaches FNT regime at voltages beyond 0.8 V (Figure 6.26 (d)). The forward bias current starts to dominate the reverse bias current at ~0.9 V as shown in Figure 6.26 (e) and Figure 6.27 (a). This can be ascribed to the small energy difference of 0.07 eV and 0.27 eV between the Fermi level of Nb and the energy level of two bound states. It is evident that the rectification reversal is shifted towards larger voltages (0.9 V) comparing to Nb/Nb_2O_5/Al_2O_3/Nb structure (0.7 V).

The conduction in reverse bias is a combination of DT and FNT when the applied bias is smaller than -0.6 V (Figure 6.26 (f)). Nevertheless, if the reverse bias is further increased beyond -0.6 V, the structure reaches step tunnelling regime as shown in Figure 6.26 (g).

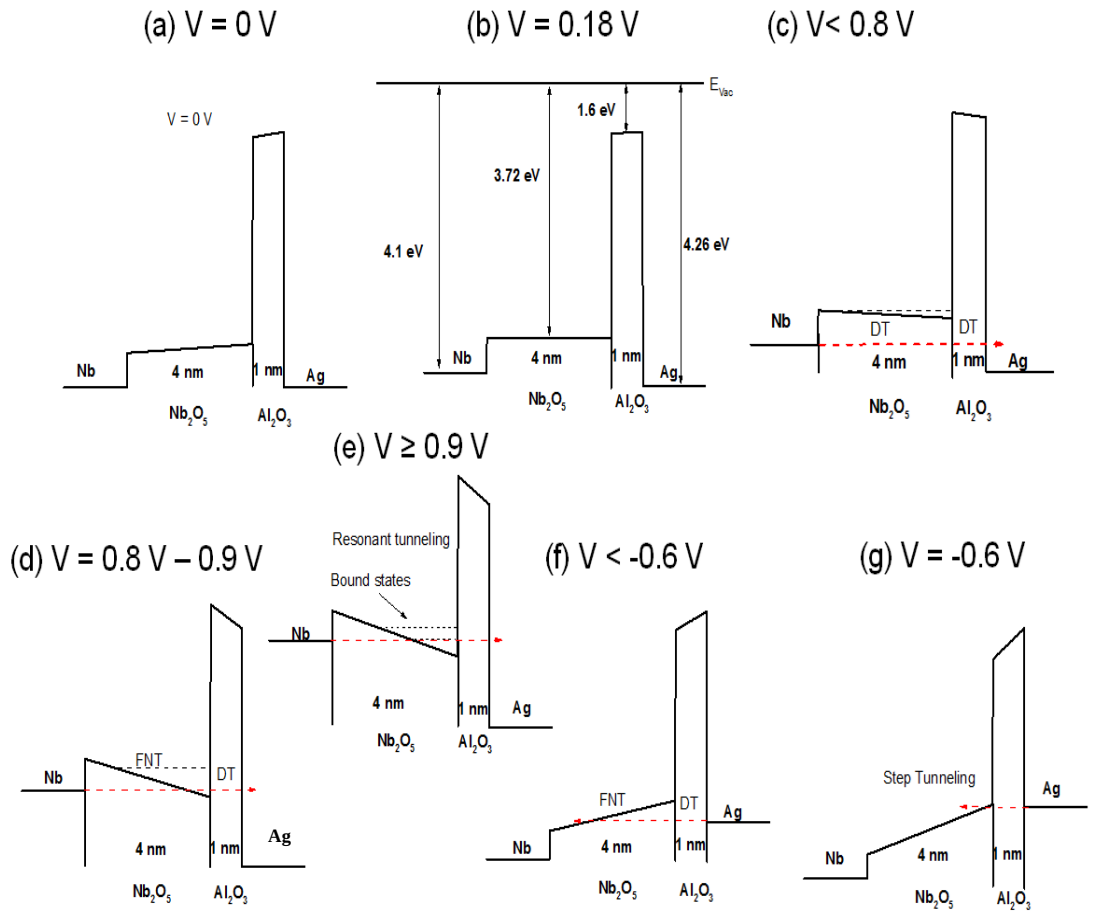

Figure 6.26: Energy band diagrams of Nb/1 nm Al_2O_3/4 nm Nb_2O_5/Ag MIIM tunnel rectifier depicting various conduction scenarios being dependent on external bias: (a) zero bias, (b) flat band condition, (c)-(e) positive voltages, (f)-(g) negative voltages.

The experimentally measured *JV* characteristics can be seen in Figure 6.27 (a). The device asymmetry was calculated by considering both the reverse to forward bias current ratio and the forward to reverse bias current ratio. When the forward to reverse current ratio was considered a peak device asymmetry of 10.5 was recorded at 1.2 V due to resonant tunnelling as shown in Figure 6.27 (b). A peak asymmetry of 35 at 0.06 V was observed if the reverse to forward bias current ratio was considered (inset of Figure 6.27 (b)). It was evident that large reverse bias currents have been observed near 0 V as a result of the band line up as shown in Figure 6.26 (a). As can be seen in Figure 6.27 (c), peak device responsivity value of 9 A/W at 0.45 V was extracted. Furthermore, as shown in Figure 6.27 (d), a peak device non-linearity of 6 at 0.9 V and a rate of change of non-linearity of 6.33 V^{-1} were extracted for this MIIM structure. The rectification reversal occurred at 0.9 V as shown in Figure 6.27 (e),

demonstrating the dominance of resonant tunnelling. The zero bias dynamic resistance was 100 MΩ whereas the lowest resistance was 1.8 kΩ at 1.2 V (Figure 6.27 (f)).

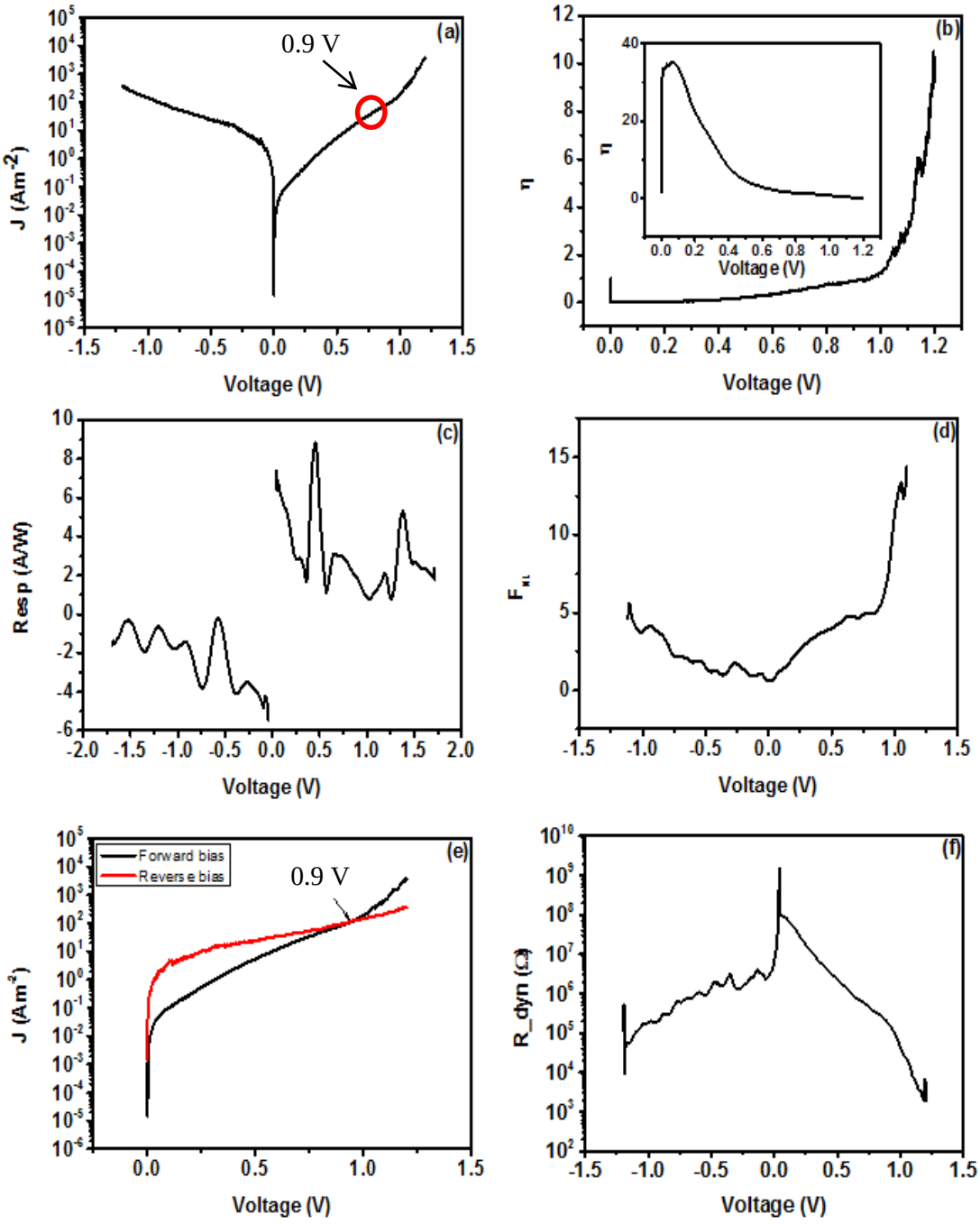

Figure 6.27: Device (a) JV characteristics (logarithmic scale), (b) asymmetry, (c) responsivity, (d) non-linearity, (e) rectification reversal and (f) dynamic resistance for Nb/1 nm Al_2O_3/4 nm Nb_2O_5/Ag. The device area = 1×10^{-8} m^2.

6.2.2.6 Nb/4 nm Nb_2O_5/1 nm Al_2O_3/W device

The top metal electrode was replaced with W with the intention of further shifting the onset of resonant tunnelling. The cross-section of the completed device structure can be seen in Figure 6.28 (a).

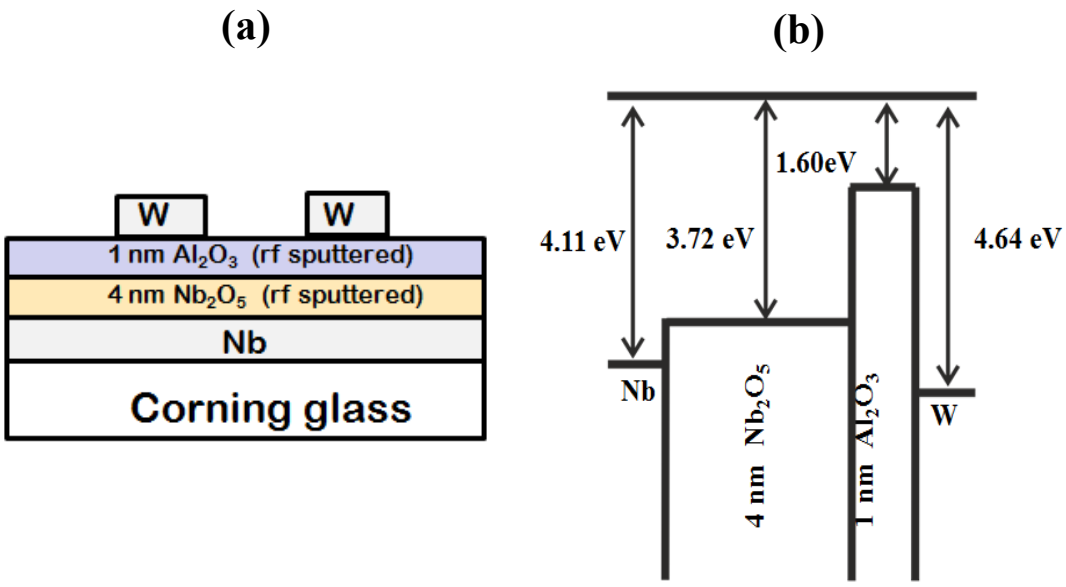

Figure 6.28: Device (a) cross-section and (b) energy band diagram for Nb/1 nm Al_2O_3/4 nm Nb_2O_5/W.

As can be seen in Figure 6.28 (b), the work function of W is 4.64 eV, resulting in a work function difference of 0.53 eV between the metal electrodes. Therefore the onset of resonant tunnelling is expected to be shifted towards larger voltages. The portion of voltage applied on each oxide layer was the same as in sections 6.2.2.4 and 6.2.2.5 due to the use of same oxide configuration. The conduction process in both forward and reverse bias are analysed with the aid of energy band diagrams as shown in Figure 6.29.

The conduction bands of Nb_2O_5 and Al_2O_3 have a slope to the left as a result of the large difference in work function values of the left and right metal electrodes (Figure 6.29 (a)). A 0.79 V bias is to be applied on the W electrode to reach the flat band condition (Figure 6.29 (b)). When the applied potential is smaller than 1 V, DT is the most pronounced conduction in both layers as shown in Figure 6.29 (c). When the applied bias is increased beyond 1 V, Nb_2O_5 reaches FNT regime (Figure 6.29 (d)). The rectification reversal in this structure occurred at 1.09 V as shown in Figure 6.30 (e) due to the energy difference between the Nb Fermi level and the bound states is 0.25 eV and 0.42 eV. This occurred 0.35 V smaller than the theoretically anticipated value in Figure 6.32 (b). This could be ascribed to a soft breakdown event. It was not possible to conduct voltage sweeps beyond 1.3 V as the device broke down.

In the case of reverse bias the structure reaches step tunnelling at small voltages, ~-0.3 V as a result of the work function offset between the metal electrodes as illustrated in Figures 6.29 (f) and (g).

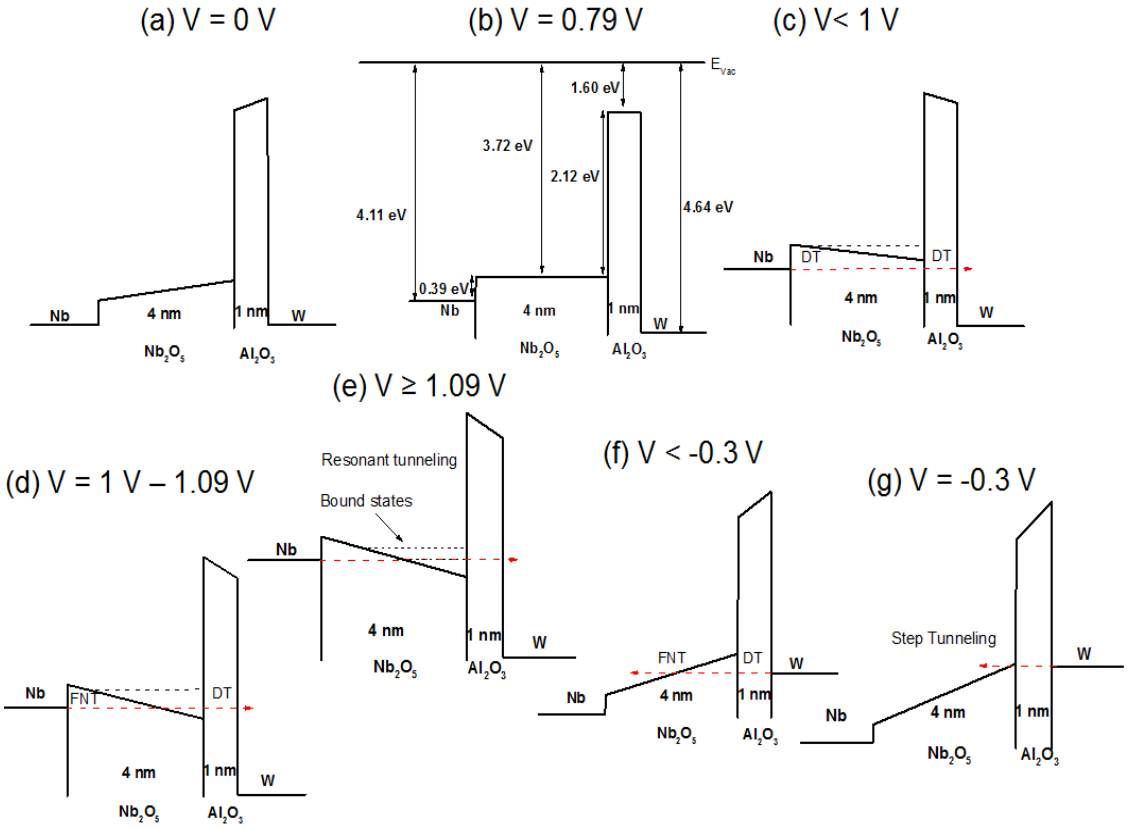

Figure 6.29: Energy band diagrams of Nb/1 nm Al_2O_3/4 nm Nb_2O_5/W MIIM tunnel rectifier depicting various conduction scenarios being dependent on external bias: (a) zero bias, (b) flat band condition, (c)-(e) positive voltages and (f)-(g) negative voltages.

The *JV* characteristics are shown in Figure 6.30 (a) and a significant increase in current magnitudes can be clearly observed at ~1.09 V. Presumably, this could be ascribed to a soft breakdown. The device asymmetry was calculated considering the ratio of forward bias to reverse bias current. A peak device asymmetry of 2.4 was recorded at 1.15 V from Figure 6.30 (b) as a result of soft breakdown. Moreover a peak responsivity of 9 A/W at 0.04 V (Figure 6.30 (c)) and a peak non-linearity of 2.8 at 0.7 V (Figure 6.30 (d)) were extracted. The rate of change of non-linearity was 6.20 V^{-1}. Furthermore, the shape of the *IV* curve was closely analysed in order to study the effect of resonance and the soft breakdown. It was evident that a slight change in curvature was observed in the forward bias current before the soft breakdown occurred (Figure 6.30 (e)). Possibly this could be due to resonance however the rectification reversal occurs at 1.09 V as a result of the soft breakdown (Figure 6.30 (e)). The zero bias resistance was 2.4 MΩ whereas the lowest resistance was 230 Ω at 1.1 V (Figure 6.30 (f)).

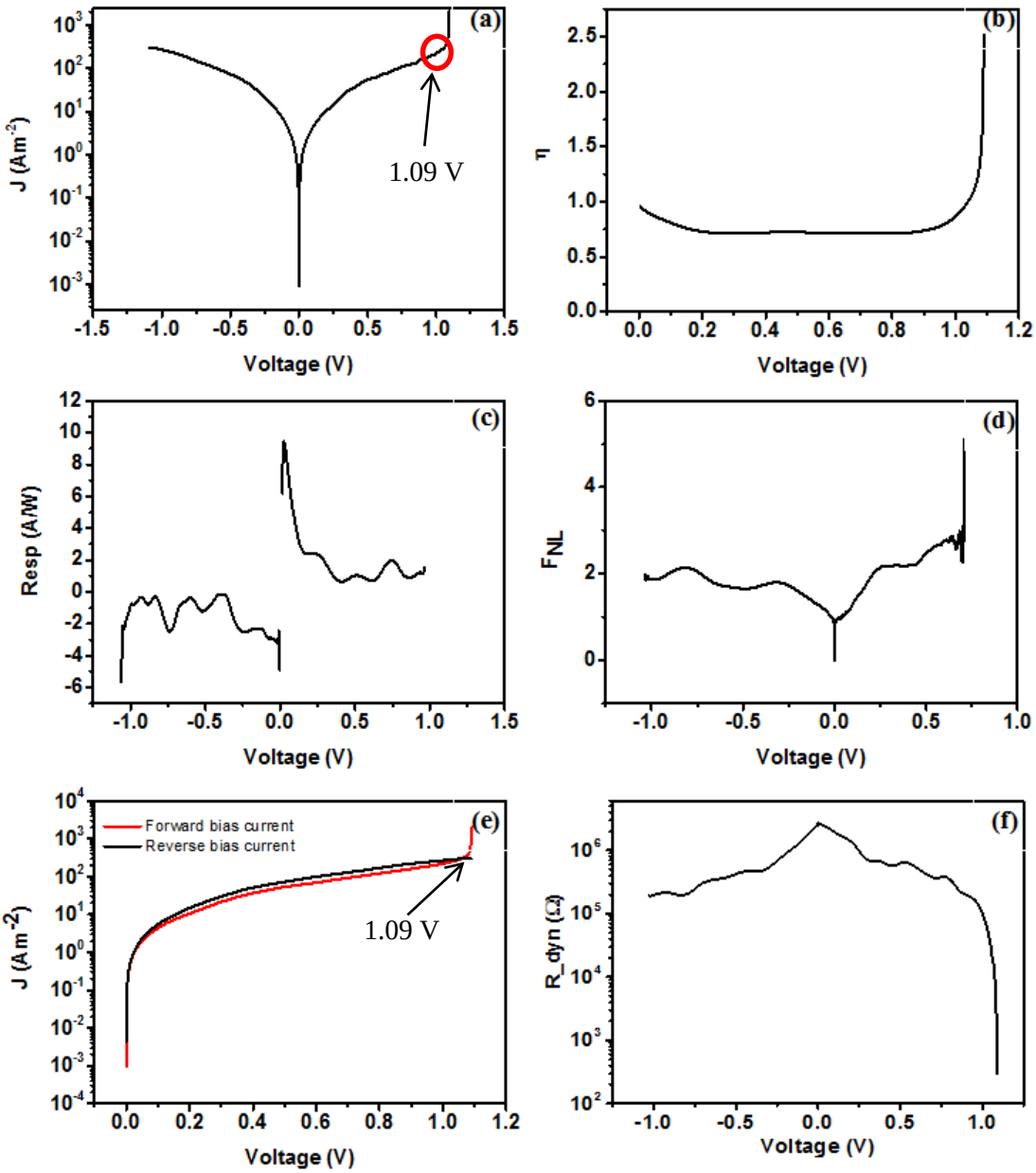

Figure 6.30: Device (a) JV characteristics (logarithmic scale), (b) asymmetry, (c) responsivity, (d) non-linearity, (e) rectification reversal and (f) dynamic resistance for Nb/1 nm Al_2O_3/4 nm Nb_2O_5/W. The device area = 1×10^{-8} m^2.

In summary, the metals Ag, W with larger work function values than Nb were used as the electrode adjoining Al_2O_3 and caused the rectification reversal to shift towards larger voltages from 0.7 V (Nb/Nb) to 0.9 V (Nb/Ag) and 1.1 V (Nb/W).

6.3 Discussion and summary

The main objective of the experimental work in this chapter was to observe the effect of resonant tunnelling by engineering the band structure of MIIMs with the right choice of metal and oxide combinations. The first step was to simulate the potential structures using the model explained in [7, 9, 10]. The fabrication process was done by using the deposition techniques such as thermal evaporation (Al, Ag and Cr), DC sputtering (Ta, Nb, and W), ALD (Nb_2O_5, Ta_2O_5, and Al_2O_3) and/or RF sputtering (Nb_2O_5, Ta_2O_5, and Al_2O_3). The bottom and top metal electrodes were patterned by either shadow masks or photolithography.

The MIIM structures were fabricated considering the oxide combination of Ta_2O_5/Al_2O_3 and Nb_2O_5/Al_2O_3. The electron affinity of Nb_2O_5 (3.72 eV) was larger than that of Ta_2O_5 (3.54 eV), therefore the barrier height at the metal/oxide interface was smaller if Nb_2O_5 was used. A broad range of metals (Al, Ag, Cr, Nb, Ta and W) were chosen with different work function values in order to tune the barrier height at the metal/oxide interface.

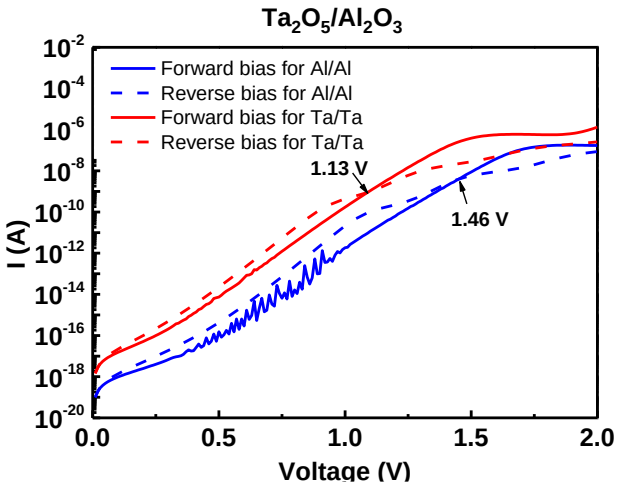

Figure 6.31: Rectification reversal point (*IV* characteristics) of Al/4 nm Ta_2O_5/1 nm Al_2O_3/Al and Ta/4 nm Ta_2O_5/1 nm Al_2O_3/Ta.

As can be seen in Figure 6.31, the simulated Al/4 nm Ta_2O_5/1 nm Al_2O_3/Al MIIM structure demonstrated smaller currents compared to the Ta/4 nm Ta_2O_5/1 nm Al_2O_3/Ta structure. The rectification reversal occurred at 1.13 V for the Ta based MIIM structure whereas this occurred at 1.46 V for the Al based structure (Figure 6.31) [7, 9, 10]. The experimentally observed rectification reversal points for Ta and Al based devices were 1.27 V and 1.5 V respectively as shown in Figures 6.15 (e) and 6.9 (a). This could be ascribed to the smaller barrier height of 0.63 eV at the interface of Ta/Ta_2O_5 in contrast to the 0.74 eV obtained for Al/Ta_2O_5. The other drawback of using Al was an Al-native oxide layer which caused the onset of resonant tunnelling to shift towards larger voltages due to the increase in overall Al_2O_3 thickness; hence

it was mandatory to replace Al with other metals in order to eliminate the effect of native oxide layer.

The MIIM structures with the same metal electrodes and also with an offset of metal work function values to tune the rectification reversal point were fabricated. It was assumed that the dominance of resonance was observed around the potential where rectification reversal occurred. The theoretically extracted rectification reversal of Ta/4 nm Ta_2O_5/1 nm Al_2O_3/M (Ta, Cr and Ag) and Nb/4 nm Nb_2O_5/1 nm Al_2O_3/M (Nb, Ag, W) are illustrated in Figures 6.32 (a) and (b) respectively.

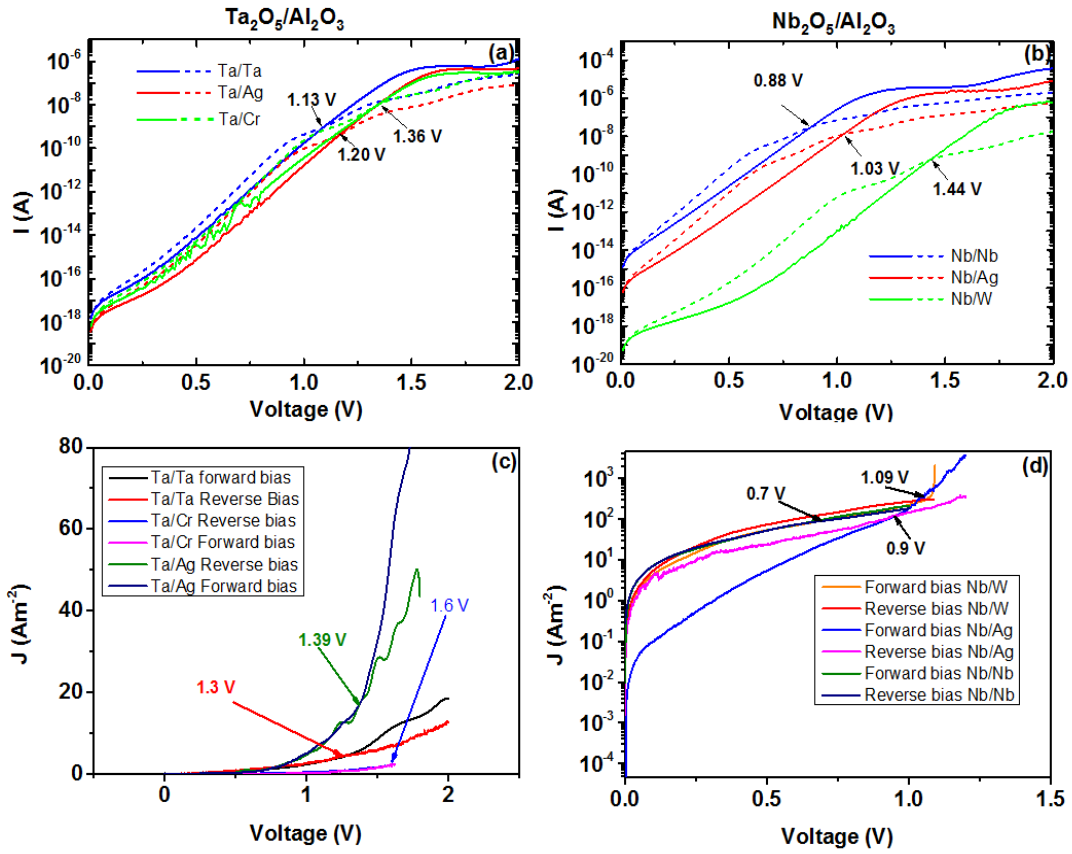

Figure 6.32: Rectification reversal (a) Simulated Ta/4 nm Ta_2O_5/1 nm Al_2O_3/M (Ta, Cr and Ag) (b) Simulated Nb/4 nm Nb_2O_5/1 nm Al_2O_3/M (Nb, W, and Ag) (c) experimental Ta/4 nm Ta_2O_5/1 nm Al_2O_3/M (Ta, Cr, and Ag) (d) experimental Nb/4 nm Nb_2O_5/1 nm Al_2O_3/M (Nb, W, and Ag).

It was evident that a shift in rectification reversal can be observed when the metal electrode adjoining Al_2O_3 was replaced with a different metal electrode (Figure 6.32). The rectification reversal in experimental MIIM structure shifted toward larger voltages as shown in Figures 6.32 (c) and (d). A summary of the theoretical and experimental rectification reversal points can be seen in Table 6.2.

As seen in Figure 6.32 and Table 6.2, the trend of the experimental observations was in agreement with the simulated results extracted from the models [7, 9, 10]. It is worth

mentioning that the simulations have been carried out assuming the nominal oxide thicknesses, 4 nm for Ta_2O_5 and Nb_2O_5 and 1 nm for Al_2O_3. As illustrated in Table 6.2, the rectification reversal points in experimental MIIM structures that were fabricated with the oxide combination of Nb_2O_5 and Al_2O_3 observed about ~0.1 - 0.3 V shift to lower voltages than the theoretical results. This is because the thickness of Nb_2O_5 was 0.4 - 0.5 nm higher than the nominal value of 4 nm; hence the portion of potential applied on Nb_2O_5 becomes larger, resulting to form the quantum well at smaller voltages with respect to the 4 nm Nb_2O_5 structure. Meanwhile, in the case of Ta_2O_5/Al_2O_3 MIIM structures, the rectification reversal was experimentally observed at ~0.1 – 0.2 V larger values than theoretically predicted (Table 6.2). This is due to a smaller thickness of Ta_2O_5 ~3.65 nm measured by VASE instead of the nominal 4 nm Ta_2O_5.

Table 6.2: Summary of theoretical and experimental rectification reversal values for MIIM structures.

Structure	Theoretical rectification reversal (V)	Experimental rectification reversal (V)
$Ta/Ta_2O_5/Al_2O_3/Ta$	1.13	1.3
$Ta/Ta_2O_5/Al_2O_3/Ag$	1.20	1.39
$Ta/Ta_2O_5/Al_2O_3/Cr$	1.36	1.60
$Nb/Nb_2O_5/Al_2O_3/Nb$	0.88	0.7
$Nb/Nb_2O_5/Al_2O_3/Ag$	1.03	0.90
$Nb/Nb_2O_5/Al_2O_3/W$	1.44	1.09

Many research groups have performed experimental and theoretical analysis on metal-insulator-insulator-metal structures. Alimardani *et al*. reported an asymmetry of 10 at 0.45 V and a maximum asymmetry of 187 at 1.2 V, and a non-linearity of 6.5 at 0.45 V for $ZrCuAlNi/Al_2O_3/Ta_2O_5/Al$ Metal-insulator-insulator-metal (MIIM) device structures [21]. In their previous work they concluded that in Ta_2O_5 layers Schottky emission dominates at lower electric fields and Poole-Frenkel emission dominates at higher electric fields, however in the case of Al_2O_3 the conduction is dominated by DT and FNT. Therefore they reported that the dominant conduction mechanism in metal-double insulator structure is 'Defect Enhanced Direct Tunnelling' since it is a combination of Poole-Frenkel and Schottky emission in Ta_2O_5 and DT in Al_2O_3 [21]. Alimardani *et al*. further reported an asymmetry of 10 at 0.8 V and a non-linearity of 5 at 0.8 V for $ZCAN/HfO_2/Al_2O_3/Al$ MIIM device [13]. Maraghechi *et al.* performed experiments on MIIM ($Cr/HfO_2/Al_2O_3/Cr$) devices and reported an asymmetry of 10 at 3 V, a peak device responsivity of 2.5 A/W at 0.5 V and a non-linearity of 6 at 1.4 V [22]. Grover *et al.* obtained a responsivity of 11 A/W at 0.02 V by simulations for $W/Nb_2O_5/Al_2O_3/W$ structure is ascribed to a resonant tunnelling in MIIM structure [2].

Aydinoglu *et al.* reported an asymmetry of 3 at 1.6 V and also a non-linearity of 3 at 0.8 V for $Cr/TiO_2/Al_2O_3/Ti$ MIIM structure [4]. Moreover, Singh *et al.* performed experiments on an ALD fabricated Ni/NiO/ZnO/Cr MIIM structure and obtained an asymmetry of 16 at 0.5 V and a peak device responsivity of 8 A/W at 0.25 V [23]. However, all the MIIM devices that have been fabricated or simulated have demonstrated large dynamic resistance values.

Table 6.3: Summarised rectification properties of MIIM structures fabricated in this work.

Device	Rectification reversal (V)	Peak asymmetry	Responsivity (A/W)	Non-linearity	Dynamic resistance
$Al/Al_2O_3/Ta_2O_5/Al$	1.50	6 at 1.75 V (due to RT) 18 at 0.3 V (due to ST)	6.7 at 0.27 V	6.2 at 1.5 V	15.6 MΩ at 0 V 24 Ω at 2.3 V
$Ta/Ta_2O_5/Al_2O_3/Ta$	1.3	1.6 at 1.8 V	8.3 A/W at 0.1 V	3.6 at 1.3 V	9 GΩ at 0 V 90 MΩ at 1.5 V
$Ta/Ta_2O_5/Al_2O_3/Ag$	1.39	2.1 at 1.6 V (due to RT) 3.2 at 0.56 V (due to ST)	7.7 A/W at 0.2 V	5.7 at 1.38 V	2 TΩ at 0 V 20 MΩ at 1.5 V
$Ta/Ta_2O_5/Al_2O_3/Cr$	1.60	1.9 at 0.75 V (due to ST)	2.5 A/W at 0.2 V	5.5 at 1.4 V	15.4 MΩ at 0 V 88 kΩ at 1.6 V
$Al/Al_2O_3/Nb_2O_5/Al$	0.60	9.95 at 1.9 V	7.8 A/W at 0.06 V	5.8 at 1.7 V	300 MΩ at 0 V 1.3MΩ at 1.9 V
$Nb/Nb_2O_5/Al_2O_3/Nb$	0.7	1.4 at 1 V (due to RT) 2.2 at 0.03 V	7.9 A/W at 0.1 V 2.4 A/W at 0.7 V	3.9 at 0.9 V	35 MΩ at 0 V 19 kΩ at 1.29 V
$Nb/Nb_2O_5/Al_2O_3/Ag$	0.90	10.5 at 1.2 V (due to RT) 35 at 0.06 V (due to ST)	9 A/W at 0.45 V	6 at 0.9 V	100 MΩ at 0 V 1.8 kΩ at 1.2 V
$Nb/Nb_2O_5/Al_2O_3/W$	1.09	2.4 at 1.15 V	9 A/W at 0.04 V	2.8 at 0.7 V	2.4 MΩ at 0 V 230 Ω at 1.1 V

The rectification properties of all the MIIM structures that were fabricated in this work are summarised in Table 6.3. It was shown that the dominant conduction process of these MIIM structures is quantum mechanical tunnelling (see chapter 5). Moreover, it is evident that large device asymmetries were obtained for certain devices at the low voltage regime due to large currents in reverse bias. As illustrated in Table 6.3, the devices, Al/1 nm Al_2O_3/4 nm Ta_2O_5/Al and Nb/4 nm Nb_2O_5/1 nm Al_2O_3/Ag illustrated large device asymmetries of 18 at 0.3 V and 35 at 0.06 V respectively in advance to the state-of-the-art. However, the obtained asymmetries as a result of resonant tunnelling were generally smaller and also observed at larger voltages as seen in Table 6.3. The reason for this was that the resonant tunnelling did not happen at zero bias as a result of large metal/oxide barrier heights. It can also be observed large responsivity and non-linearity values at low voltage regime in advance to reported values (Table 6.3). The MIIM devices have large capacitance around 0.4 nF as a result of the large device area. Furthermore, the dynamic resistance extracted on all the structures demonstrated large values, resulting in a large RC time constant. For efficient rectification in THz regime or ideally ultraviolet/infrared region in the electromagnetic spectrum it is crucial to obtain a time constant in the order of ~10^{-15} seconds. This can be potentially achieved by engineering the metal oxide barrier height to be around 0.2 eV or smaller by selecting appropriate materials to obtain a resistance around $100\ \Omega$ and also by reducing the device area substantially to 100 nm $\times$ 100 nm. This will result in a time constant of 0.4×10^{-13} seconds.

In conclusion, it has been shown that the device rectification properties can be significantly improved by reducing the barrier height at the metal/insulator interface, scaling down the device, using oxides with small dielectric constants and also by further reduction of insulator thicknesses. State-of-the-art values of asymmetry and responsivity were achieved in fabricated Nb_2O_5/Al_2O_3 devices with Al/Al and Nb/Ag electrodes at low voltage regime < 0.5 V. It is important to maintain the same ratio 1:4 of thicknesses of the oxides, large insulator conduction band offset to form the quantum well, and the conduction to be dominated by quantum mechanical tunnelling for femto-second fast tunnelling transit times.

References

[1] A New Technology for Terahertz Electronics, Phiar Corporation, Np 1.0 (2013)

[2] S. Grover, G. Moddel, "Engineering the current-voltage characteristics of metal-insulator-metal diodes using double-insulator tunnel barriers", Solid State Electron., 67(1), 94 (2012)

[3] P. Maraghechi, A. Foroughi-Abari, K. Cadien, A.Y. Elezzabi, "Enhanced rectifying response from metal-insulator-insulator-metal junctions", Appl. Phys. Lett., 99, 253503 (2011)

[4] F. Aydinoglu, M. Alhazmi, B. Cui, O. Ramahi, M. Irannejad, A. Brzezinski, M. Yavuz, "Higher performance metal-insulator-metal diodes using multiple insulator layers", Austin J. Nanomed. Nanotechnol., 1, 3 (2013)

[5] M. Alhazmi, F. Aydinoglu, B. Cui, O.M. Ramahi, M. Irannejad, A. Brezezinski, M. Yavuz, "Comparison of the effects of varying of metal electrode in metal-insulator-metal diodes with multi-layer dielectric layers", Austin J. Nanomed. Nanotechnol., 2 (2014)

[6] S. Grover, "Diodes for optical rectennas", PhD thesis, Boulder: University of Colorado at Boulder (2011)

[7] N. Sedghi, J. F. Ralph, I. Z. Mitrovic, P. R. Chalker, S. Hall, "Electron trapping at the high-κ/GeO_2 interface: The role of bound states", Appl. Phys. Lett., 102, 092103 (2013)

[8] S. M. Sze, Kwok K. Ng., "Tunnel device in physics of semiconductor devices", 3rd edition. John Willey & Sons, 2007, Ch. 8, sec 8.4, 454

[9] N. Sedghi, J. W. Zhang, J. F. Ralph, Y. Huang, I. Z. Mitrovic, S. Hall, "Towards rectenna for solar energy harvesting", Proc: European Solid-State Device Research Conference (ESSDERC), Romania, 131 (2013)

[10] S. Hall, I. Z. Mitrovic, N. Sedghi, Y. C. Shen, Y. Huang, J. F. Ralph, "Energy Harvesting using THz electronics", in:A. Nazarov *et al.*, Functional nanomaterials and devices for electronics, Sensors and energy harvesting, Engineering materials, Springer, Switzerland, 241 (2014)

[11] Bart Van Zeghbroeck, "Principles of Semiconductor Devices", University of Colorado, 2007

[12] David J. Griffiths, "The time-independent Schrödinger equation" in Introduction to quantum mechanics, New Jersey, USA, Prentice Hall, 1995, Ch 2, sec 2.2, 24-27

[13] N. Alimardani, J. Conley Jr. ''Step tunneling enhanced asymmetry in asymmetric electrode metal insulator-insulator-metal tunnel diodes'' Appl. Phys. Lett., 102, 143501 (2013)

[14] Y. Matsumoto, T. Hanajiri, T. Toyabe, T. Sugano, "Single electron device with assymetric tunnel barriers", Jpn. J. Appl. Phys., 35, 1126 (1996)

[15] S. Vaziri, M. Belete, E. Dentoni Litta, A.D. Smith, G. Lupina, M.C. Lemme, M. Östling, "Bilayer insulator tunnel barriers for graphene-based vertical hot-electrons transistors", Nanoscale, 7(30), 13096 (2015)

[16] I.Z. Mitrovic, Y. Lu, O. Buiu, S. Hall, "Current transport mechanisms in $(HfO_2)_x(SiO_2)_{1-x}/SiO_2$ gate stacks", Microelec Eng., 84, 2306 (2007)

[17] A. Sanchez, C. F. Davis Jr., K.C. Liu, A. Javan, "The MOM tunnelling diode: Theoretical estimate of its performance at microwave and infrared frequencies", Jnl. Appl. Phys., 49(10). 5270 (1978)

[18] B. Elisson, "Metal-insulator-metal diodes for solar energy conversion", PhD thesis, Boulder: University of Colorado at Boulder (2001)

[19] J. Robertson, "High dielectric constant gate oxides for metal oxide Si transistors", Rep. Prog. Phys.69, 328 (2006)

[20] P. D. Ye, B. Yang, K. K. Ng, J. Bude., "GaN metal-oxide-semiconductor high-electron-mobility-transistor with atomic layer deposited Al_2O_3 as gate dielectric", Appl. Phys. Lett., 86, 063501 (2005)

[21] N. Alimardani, J. Conley Jr., ''Enhancing metal-insulator-insulator-metal tunnel diodes via defect enhanced direct tunnelling'' J. Appl. phys., 105, 082902-1 (2014)

[22] P. Maraghechi, A. Foroughi-Abari, K. Cadien, A. Y. Elezzabi, "Enhanced rectifying response from metal-insulator-insulator-metal junctions," Appl. Phys. Lett., 99, 253503 (2011)

[23] A. Singha, R. Ratnadurai, R. Kumar, S. Krishnana, Y. Emirovc, S. Bhansali, “Fabrication and current-voltage characteristics of NiO_x/ZnO based MIIM tunnel”, Appl.Surf. Science, 334, 197 (2015)

Chapter 7

7. Metal-Insulator-Insulator-Insulator-Metal (MIIIM) structures

The MIIIM structures were fabricated with the aim of achieving better rectification properties in contrast to the MIM and MIIM structures presented in chapters 5 and 6. The structures were engineered to obtain a bound state at zero bias in the rectangular quantum well which was created in the conduction band (CB) of Nb_2O_5 as can be seen in Figure 7.1. Three novel structures were fabricated by varying the thicknesses of Ta_2O_5 and Nb_2O_5 with the intention of studying the effect of resonant tunnelling.

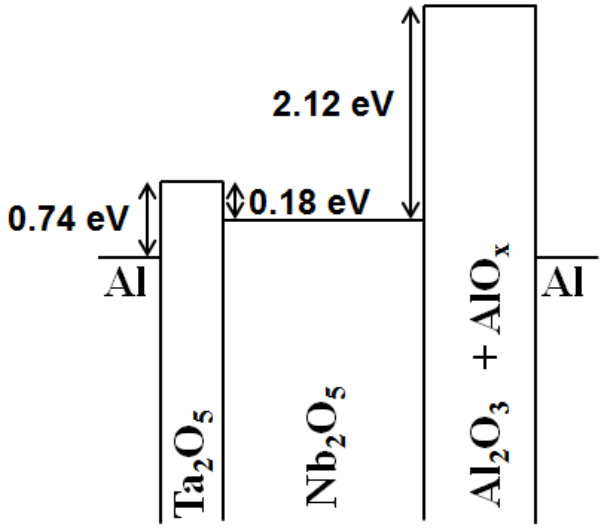

Figure 7.1: Energy band diagram of the MIIIM structure

The metal, Al with a work function of 4.28 eV was chosen as the top and bottom metal electrodes and then three dielectrics were selected with different electron affinity and band gaps. The oxide in the middle has the smallest band gap of 3.76 eV and the largest electron affinity of 3.72 eV. The first oxide, Ta_2O_5 has a larger band gap of 4.40 eV and a smaller electron affinity of 3.54 eV compared to Nb_2O_5, however the third oxide Al_2O_3 has the largest band gap of ~6.43 eV and the smallest electron affinity of 1.60 eV. The conduction band offsets (CBO) between Ta_2O_5 and Nb_2O_5, and Al_2O_3 and Nb_2O_5 are 0.18 eV and 2.12 eV respectively. A rectangular potential well can be expected with a bound state in the CB of Nb_2O_5 at zero bias due to the conduction band offsets as illustrated in Figure 7.1. Moreover, a triangular potential well can be expected in the CB of Nb_2O_5 if a positive voltage is applied to right electrode as the CB edge bends with the increase in voltage applied.

The barrier height at the Al/Nb_2O_5 interface is 0.56 eV (see section 4.3.2, Figure 4.19), resulting in a large energy difference between the Fermi level of Al and the energy level of the bound state. Therefore the dominance of resonance at or near zero bias would not be apparent, however it could be if a small bias of ~0.35 V is applied to the right metal electrode.

This is due to the decrease in energy difference between the Al Fermi level and the energy level of the bound state(s). This phenomenon will be further explained using the experimental and theoretical analysis performed for these structures.

Another MIIIM diode structure was fabricated with the same oxides, but with a different configuration of 1 nm of Nb_2O_5 as the first and 3 nm Ta_2O_5 as the second oxide. This configuration does not result in a rectangular quantum well but a triangular quantum well forms as voltage is applied. The fabricated MIIIM structures are listed in Table 7.1.

Table 7.1: Sample specifications with nominal thickness values for MIIIM devices.

Sample	Bottom electrode	First oxide	Second oxide	Third oxide	Top electrode
$Al/Al_2O_3/Nb_2O_5/Ta_2O_5/Al$ (1:3:1)	~60 nm Al (thermally evaporated)	1 nm Al_2O_3 (ALD) + native AlO_x	3 nm Nb_2O_5 (ALD)	1 nm Ta_2O_5 (ALD)	~60 nm Al (thermally evaporated)
$Al/AlO_x/ Al_2O_3/ Nb_2O_5/Ta_2O_5/Al$ (1:2.5:1.5)	~60 nm Al (thermally evaporated)	1 nm Al_2O_3 (ALD) + native AlO_x	2.5 nm Nb_2O_5 (ALD)	1.5 nm Ta_2O_5 (ALD)	~60 nm Al (thermally evaporated)
$Al/AlO_x/Al_2O_3/Nb_2O_5/Ta_2O_5/Al$ (1:2:2)	~60 nm Al (thermally evaporated)	1 nm Al_2O_3 (ALD) + native AlO_x	2 nm Nb_2O_5 (ALD)	2 nm Ta_2O_5 (ALD)	~60 nm Al (thermally evaporated)
$Al/AlO_x/Al_2O_3/ Ta_2O_5/Nb_2O_5/Al$ (1:3:1)	~60 nm Al (thermally evaporated)	1 nm Al_2O_3 (ALD) + native AlO_x	~3 nm Ta_2O_5 (ALD)	1 nm Nb_2O_5 (ALD)	~60 nm Al (thermally evaporated)

In this chapter, the conduction process and the rectification properties are investigated and finally compared to the extracted results with previously discussed MIM and MIIM devices in chapters 5 and 6 respectively.

7.1 Theoretical calculations

The theoretical model explained in chapter 6 [1, 2] has been modified to simulate the MIIIM structures presented in this chapter. The Al/1 nm Al_2O_3+1.6 nm AlO_x /3 nm Ta_2O_5/1 nm Nb_2O_5/Al was simulated and it was found that rectification reversal occurs at ~0.5 V although the experimentally observed value was 0.35 V. Moreover it was shown experimentally in chapter 4 that the Nb_2O_5 thickness is larger than the nominal value whereas that the Ta_2O_5 was smaller. Variable angle spectroscopic ellipsometry (VASE) was performed on reference samples to measure the thickness of the ALD oxide layer. The thickness of Nb_2O_5 was found to be 3.6 $\pm$ 0.07 nm compared to the nominal 3 nm and whereas the nominal 1nm Ta_2O_5 layer was ~0.8 $\pm$ 0.06 nm.

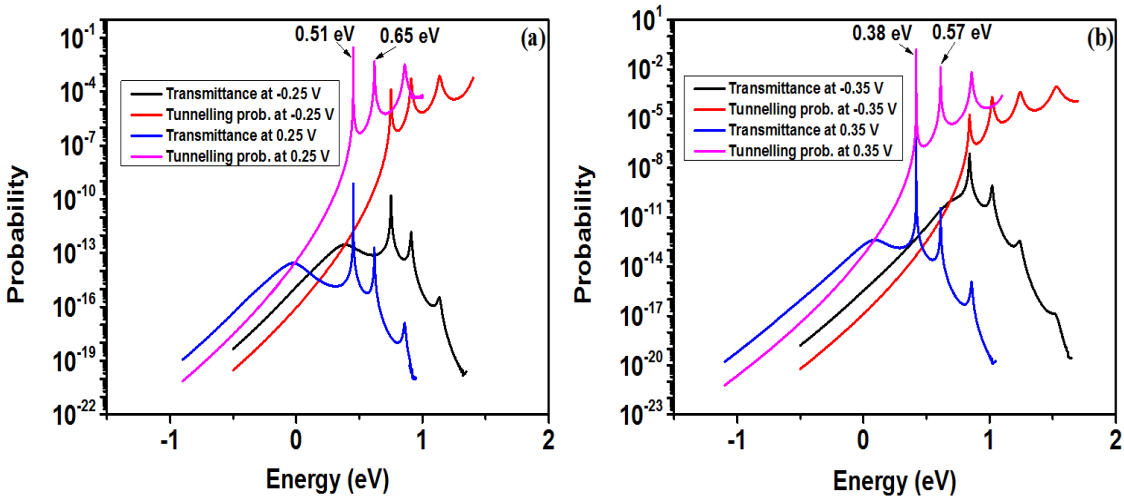

Figure 7.2: Transmittance peaks at (a) 0.25 V and -0.25 V, (b) 0.35 V and -0.35 V for Al/0.8 nm Ta_2O_5/3.6 nm Nb_2O_5/1 nm Al_2O_3/Al.

The simulations were performed considering the experimentally extracted thicknesses for the structure Al/1 nm Al_2O_3+1.6 nm AlO_x/3.6 nm Nb_2O_5/0.8 nm Ta_2O_5/Al. It was found that, a bound state can be expected in the CB of Nb_2O_5 at zero bias (at the energy of 0.56 eV) although the effect of resonance could not be observed presumably due to the large energy difference of 0.56 eV between the Al Fermi level and the CB of Nb_2O_5. The area under the transmittance curve is directly proportional to the device current as explained in chapter 6, section 6.1. As can be seen in Figure 7.2 (a), if the applied voltage to the Al/0.8 nm Ta_2O_5/3.6 nm Nb_2O_5/1 nm Al_2O_3+1.6 nm AlO_x/Al is increased up to 0.25 V, the area under the transmittance plot is smaller compared to the curve under reverse bias of -0.25 by a factor of 1.9. Although resonance occurs through two bound states positioned at 0.51 eV and 0.65 eV at the applied

potential of 0.25 V (Figure 7.2 (a)), the number of electrons occupying these energy levels is low based on the Fermi-Dirac statistics. Hence the transmittance is considerably smaller (~10^{-11}) although the tunnelling probability is large (~10^{-3}) as shown in Figure 7.2 (a). Therefore the effect on DC characteristics due to resonance is expected to be weak.

As illustrated in Figure 7.2 (b), if a voltage of 0.35 V is applied to the right electrode of the MIIIM structure, the area under the transmittance curve become identical to that under the transmittance at -0.35 V. The closest bound state in this case appears at 0.38 eV having a smaller energy difference to the Al Fermi level compared to the difference of 0.51 eV when the applied voltage is 0.25 V. Hence the transmittance at 0.35 V is higher than in the case where the applied voltage is 0.25 V. The forward bias current will start to dominate the reverse bias current at a voltage close to 0.35 V. However, a pronounced change of curvature in DC characteristics due to resonance could not be observed at the low voltage regime < 0.5 V although the rectification reversal occurred at 0.35 V (see Figure 7.7 (a)). This can be ascribed to the large barrier height at the Al/Nb_2O_5 interface; therefore the transmittance is smaller as a consequence of the small magnitude of Fermi-Dirac-like distribution. As can be seen in Figure 7.3, the dominance of resonance can be observed after 1.2 V due to the smaller energy of 0.01 eV, 0.21 eV and 0.41 eV between the Fermi level of Al and three bound states. Moreover, based on the simulations the current magnitudes at 1.2 V is 3.8 times larger comparing to the reverse bias current as shown in Figure 7.3.

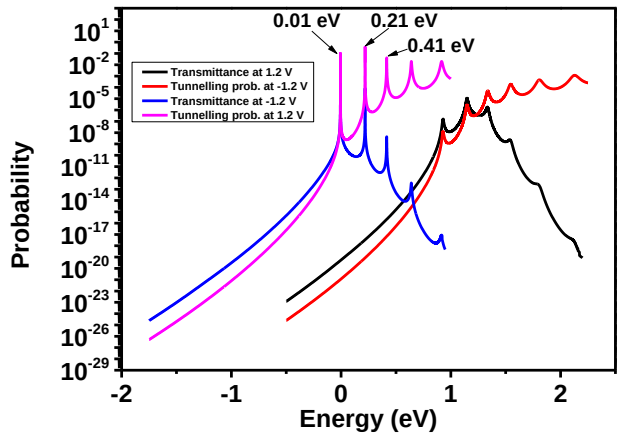

Figure 7.3: Transmittance peaks at 1.2 V for Al/0.8 nm Ta_2O_5/3.6 nm Nb_2O_5/1 nm Al_2O_3/Al device.

The theoretical model was then used to simulate the structure, Nb/1 nm Ta_2O_5/4 nm Nb_2O_5/1 nm Al_2O_3/Nb shown in Figure 7.4. This was done with the aim of observing a possible rectification reversal point at zero bias.

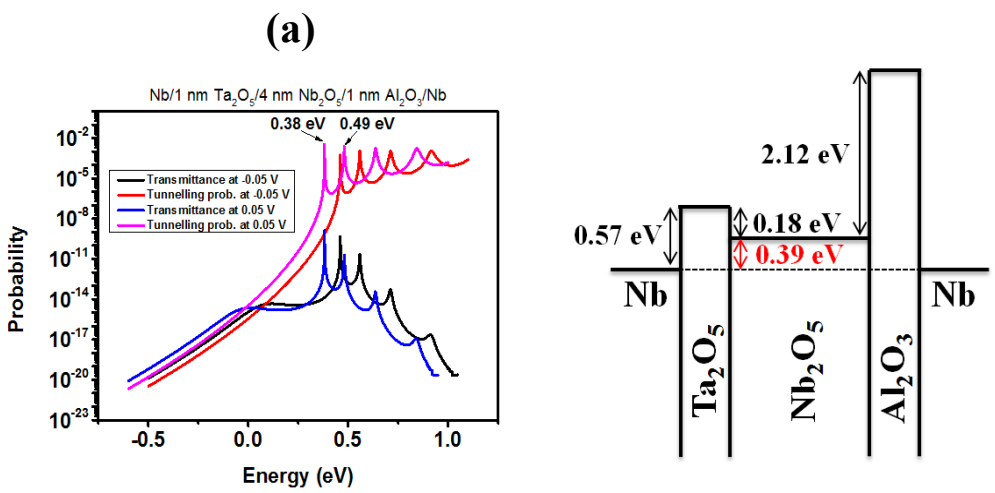

Figure 7.4: (a) Transmittance peaks at 0.05 V, (b) band diagram for Nb/1 nm Ta_2O_5/4 nm Nb_2O_5/1 nm Al_2O_3/Nb device.

The theoretical results suggest the dominance of resonant tunnelling and the rectification reversal can be observed at zero bias if a small barrier height of 0.39 eV at the Nb/Nb_2O_5 interface is used as shown in Figure 7.4 (b). Note that the bound state is in the CB of Nb_2O_5. The current at 0.05 V is larger by a factor of 1.18 in comparison to the current at -0.05 V as shown in Figure 7.4 (a).

An experiment has been carried out to investigate resonant tunnelling phenomena in these MIIIM structures. The thicknesses of the first two oxides that are Nb_2O_5 and Ta_2O_5 were varied in order to study the effect of resonance. Another MIIIM structure was engineered with the intention of obtaining bound states in both conduction bands of Nb_2O_5 and Ta_2O_5. The thicknesses of the oxides were chosen in such a way to obtain bound states at the same applied bias in conduction bands of both Ta_2O_5 and Nb_2O_5 simultaneously.

7.2 Experimental

The MIIIM structures were fabricated on 2.5 cm × 2.5 cm Corning glass slides with root mean square (RMS) surface roughness of 0.32 nm. In this series of experiments, Al with a work function = 4.28 eV was used as the top and bottom metal electrodes. The optimum deposition conditions while evaporating Al were used as explained in chapters 4-6. The metal electrodes were patterned by shadow mask process. Then the oxides, Al_2O_3, Ta_2O_5 and Al_2O_3 were deposited by ALD. The structure was completed by depositing the Al top metal electrodes which were then patterned using the shadow mask process. The oxides were not patterned due to the use of ultra-thin oxides (< 5 nm), resulting in no complications while probing the devices. It must be noted that the inevitable growth of native AlO_x on the bottom metal electrode could affect the device performance as the electric field in the intentionally grown oxides is decreased. The value of AlO_x measured by VASE was found to be 1.6 nm.

The fabricated MIIIM diodes were electrically characterised by performing DC current-voltage (*IV*) sweeps. These measurements were done in a dark probe station with the aid of Agilent B1500 semiconductor parameter analyser. The step voltages used varied from 1-3 mV depending on the voltage range considered. The continuous (negative to positive voltages or vice versa) and discontinuous (zero to positive voltages or zero negative voltages) *IV* sweeps were performed to check if the origin of the *IV* curve is shifted due to any charging effect. Moreover, in each case at least five devices out of nine on the substrate were measured and each measurement was repeated five times in order to confirm the consistency and the repeatability of the results.

The voltage drop across each capacitor was calculated using Eqn. 6.18. The number of bound states created in the quantum well at certain voltages was estimated using the theoretical model.

The diode structures with the non-cascaded configuration ($Al/Ta_2O_5/Nb_2O_5/Al_2O_3$) are discussed first and then the cascaded structure ($Al/Nb_2O_5/Ta_2O_5/Al_2O_3/Al$) is presented. In each case, the conduction process is analysed followed by the rectification properties results.

7.2.1 Non-Cascaded MIIIM structures

7.2.1.1 Al/ 1 nm Al_2O_3/3 nm Nb_2O_5/1 nm Ta_2O_5/Al device

The cross-section of the completed device structure is illustrated in Figure 7.5 (a). The VASE measured thicknesses of Nb_2O_5 was 0.6 nm thicker than the nominal value of 3 nm whereas the measured thickness for Ta_2O_5 was ~0.2 nm thinner than the nominal 1 nm.

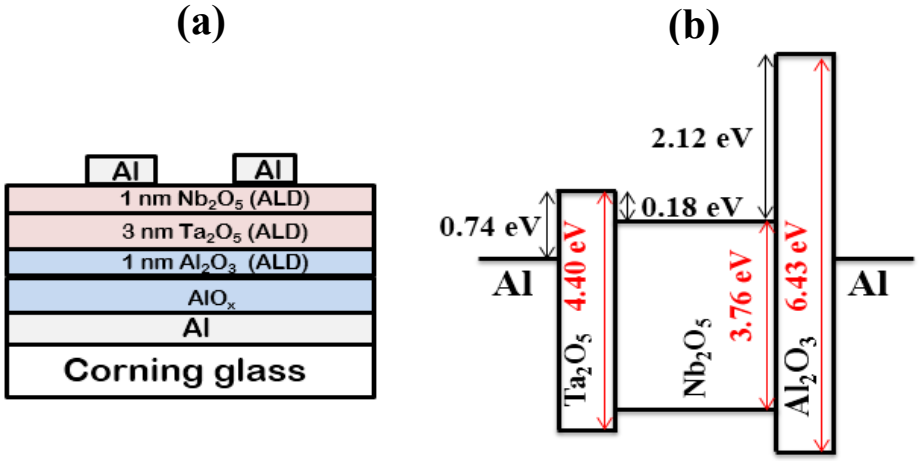

Figure 7.5: (a) A device cross-section and (b) energy band diagram of Al/native AlO_x/1 nm Al_2O_3/3 nm Nb_2O_5/1 nm Ta_2O_5/Al.

The energy band diagram for this structure is shown in Figure 7.5 (b). The CBO between Nb_2O_5 and Ta_2O_5, and Nb_2O_5 and Al_2O_3 are 0.18 eV and 2.12 eV respectively, leading to a quantum well in the CB of Nb_2O_5 at zero bias.

The ratio of potential applied across oxides, 1 nm Al_2O_3 + native AlO_x, 0.8 nm Ta_2O_5 and 3.6 nm Nb_2O_5 was found to be 0.6:0.1:0.3 from Eqn. 6.18.

The required electric field for the 3.6 nm Nb_2O_5 film to reach FNT regime is 3.15 $MVcm^{-1}$ which corresponds to a voltage of 0.42 V. However, a voltage of 1.2 V needs to be applied to this MIIIM structure as the portion of voltage applied on Nb_2O_5 is only 33% of the total bias. An applied voltage of 1.6 V needs to be applied for the Ta_2O_5 to reach the Fowler-Nordheim tunnelling (FNT) regime.

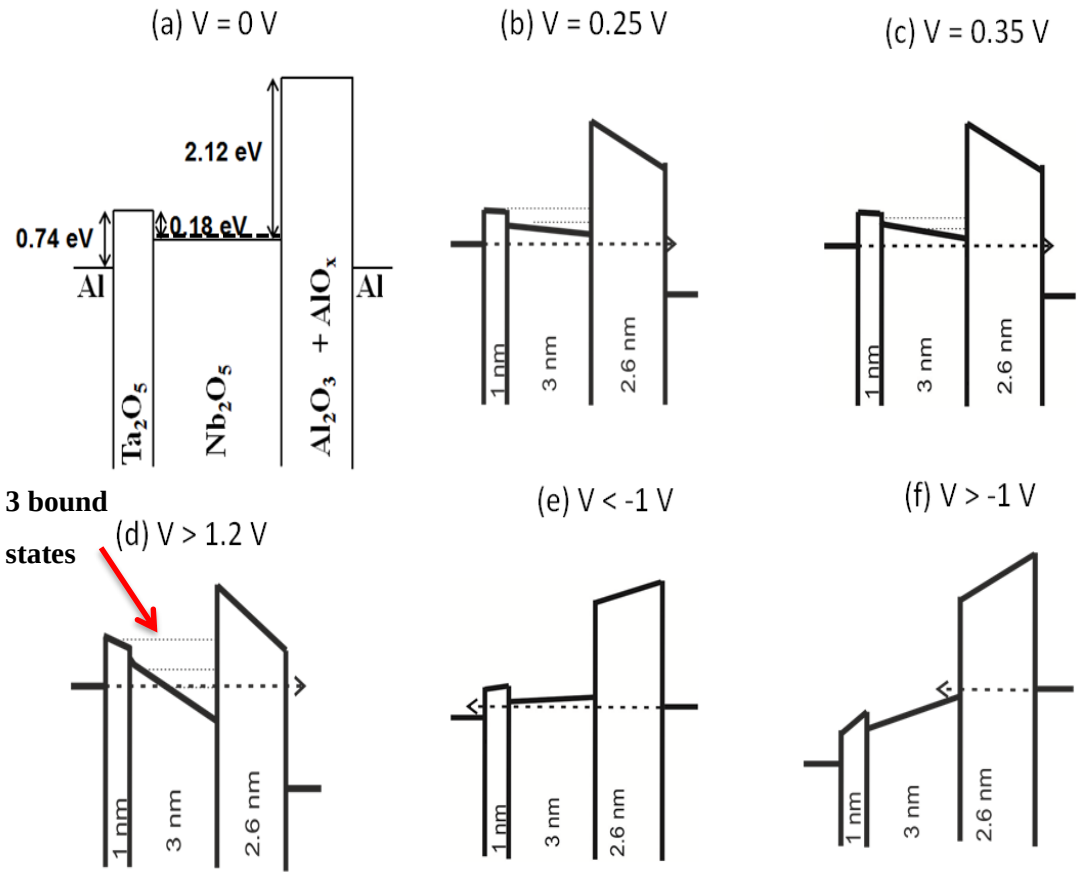

Figure 7.6: Conduction (a) at flat band condition, (b), (c) and (d) forward bias, (e) and (f) in reverse bias for Al/native AlO_x/1 nm Al_2O_3/3 nm Nb_2O_5/1 nm Ta_2O_5/Al device.

As stated before, there is a possibility of observing the dominance of resonant tunnelling at zero bias via the bound state in the rectangular quantum well. The other possibility is that the bound state is formed in a triangular well under applied bias. This is further explained with the aid of energy band diagrams in Figure 7.6 which serve to aid the explanation of the experimental results in Figure 7.7. Figure 7.6 (a) indicates a bound state (0.56 eV above the Fermi level of Al) in the CB of Nb_2O_5 at zero bias, however the *IV* results of Figure 7.7 (a) do not show such resonance as explained in the theoretical section. Figure 7.6 (b) indicates the likelihood of another bound state with potential of 0.25 V; the current is small due to the large energy difference of 0.51 eV and 0.65 eV between the metal Fermi level and the bound states.

Figure 7.6 (c) shows the situation for a potential of 0.35 V and resonance is seen in Figure 7.7 (a). As shown in Figure 7.7 (e), the rectification reversal occurs at 0.35 V as explained in section 7.1. Furthermore, if the applied voltage was further increased to 1.2 V as indicated in Figure 7.6 (d), Nb_2O_5 reaches the FNT regime. Figure 7.3 indicates the likelihood of resonance and indeed the results of Figure 7.7 (b) show that the forward bias current is larger than the reverse bias current by a factor of 3.3 at 1.2 V.

For reverse bias, conduction through all oxide films was dominated by direct tunnelling (DT) if the applied bias < 1 V as shown in Figure 7.6 (e). A quantum well was created in the CB of Nb_2O_5 due to CB edge bending. However, as a result of the small CBO of 0.18 eV between Nb_2O_5 and Ta_2O_5, the bound state leaked to the left, resulting in the conduction to be dominated only by DT and FNT. A potential of -1 V must be applied for the electrons to reach the step tunnelling regime as shown in Figure 7.6 (f). Although large reverse bias currents are expected when the device is in the step tunnelling regime, the forward bias currents are much higher due to resonant tunnelling.

The *IV* measurements were performed from -1.8 V to 1.8 V considering a step voltage of 1.8 mV. The *JV* characteristics are shown in Figure 7.7 (a) and as can be seen the effect of charging is negligible as the origin of the *JV* curve was not shifted. A peak device asymmetry of 5.3 was achieved at 1.8 V after considering the forward to reverse bias current ratio as shown in Figure 7.7 (b). Furthermore, the device asymmetry of 3.3 extracted at 1.2 V is in agreement with the asymmetry of 3.8 obtained from simulations. Therefore the obtained device asymmetry can be ascribed to the effect of resonant tunnelling in forward bias. Moreover, the larger asymmetry from simulated results could be due to many reasons such as slight variations in oxide thicknesses, metal work function, oxide electron affinity, effective electron mass used in accordance with the reported data and the relative dielectric constant values. Figure 7.7 (c) shows a peak device responsivity of 4.3 A/W at 0.35 V. This presumably corresponds to the change in curvature of the *IV* curve due to resonance. It was evident that the forward bias current starts to dominate the reverse bias current from 0.35 V as illustrated in the rectification reversal plot of Figure 7.7 (e). The Figure 7.7 (d) shows non-linearity vs. voltage with a peak non-linearity of 4.5 at 0.54 V and a rate of change of non-linearity of 6.48 V^{-1}. A smaller dynamic resistance of 580 Ω was estimated at 1.77 V; however the zero bias resistance was 2.9 MΩ as can be seen in Figure 7.7 (f).

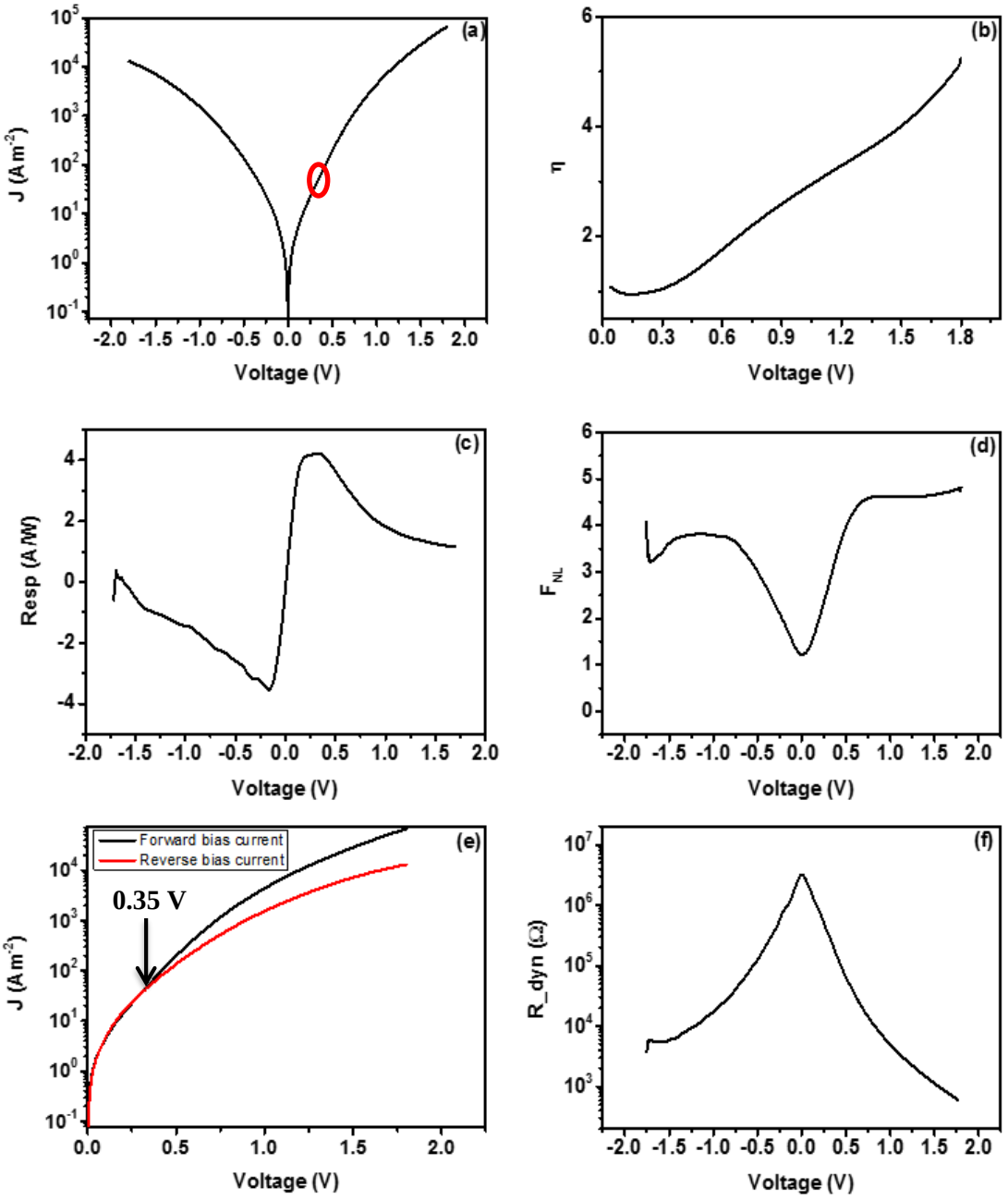

Figure 7.7: Device (a) JV characteristics, (b) asymmetry, (c) responsivity, (d) non-linearity, (e) rectification reversal and (f) dynamic resistance for Al/~1.6 nm AlO_x/1 nm Al_2O_3/3 nm Nb_2O_5/1 nm Ta_2O_5/Al. The device area = 1×10^{-8} m^2.

The dominance of resonance was not evident at zero bias. This could be ascribed to the large barrier of 0.56 eV at the Al/Nb_2O_5 interface. The effect of resonance at 0 V can be achieved by reducing the barrier height at the metal dielectric interface as shown theoretically using the Nb/Ta_2O_5/Nb_2O_5/Al_2O_3/Nb structure (Figure 7.4).

7.2.1.2 Al/1 nm Al_2O_3/2.5 nm Nb_2O_5/1.5 nm Ta_2O_5/Al device

In this device, the thicknesses of the ALD deposited oxides were slightly varied. The first oxide, Ta_2O_5 was chosen to be 1.5 nm (nominal) whereas the thickness of the second oxide (Nb_2O_5) was chosen to be 2.5 nm. The ratio of voltage applied across oxides, 1 nm Al_2O_3 + native AlO_x, 2.5 nm Nb_2O_5 and 1.5 nm Ta_2O_5 was found to be 0.59:0.19:0.22 from Eqn. 6.18.The rectification reversal can be shifted towards larger voltages due to the smaller field in the Nb_2O_5 in comparison to the structure where the thickness of Nb_2O_5 was 3 nm. Moreover, a bias of 1.41 V must be applied to the structure to reach the FNT regime for the Nb_2O_5. The energy band diagrams of Figure 7.8 are used to help explain the experimental data of Figure 7.9.

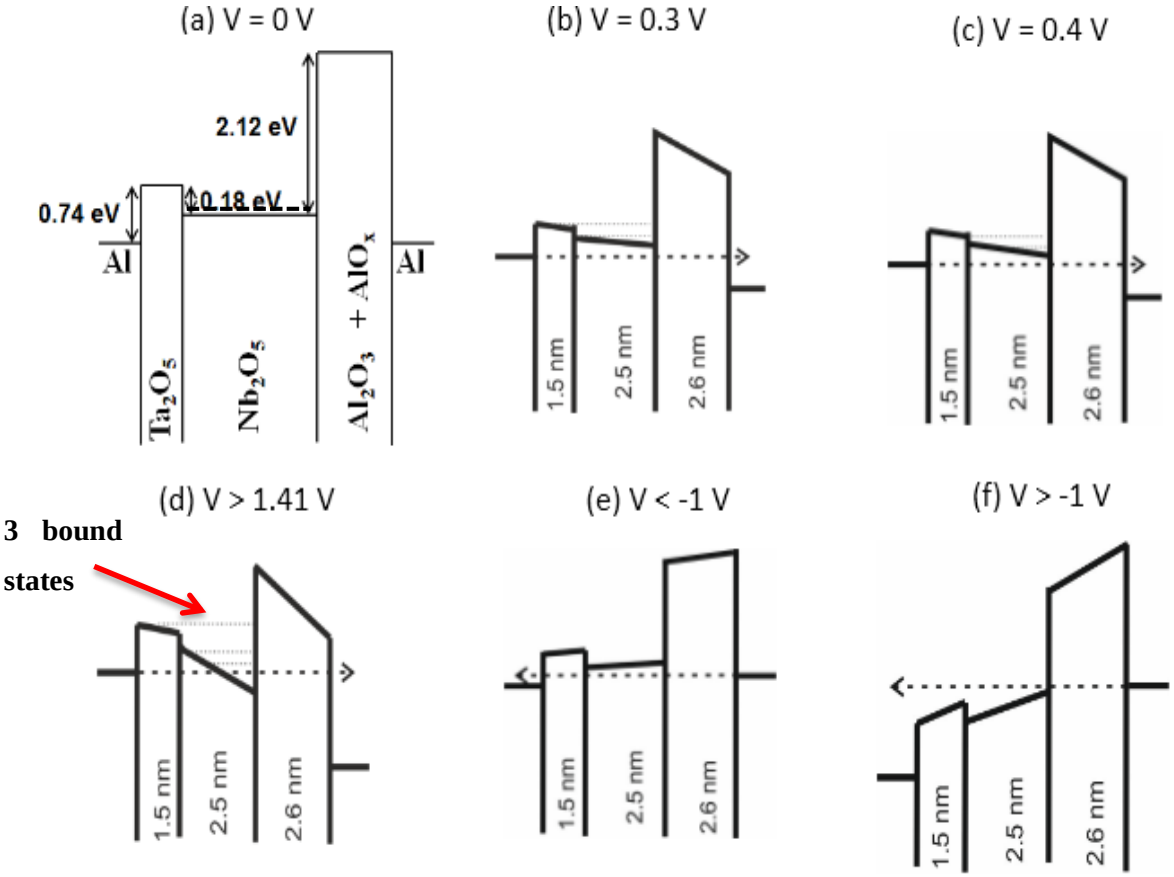

Figure 7.8: Conduction in Al/1.6 nm AlO_x/1 nm Al_2O_3/2.5 nm Nb_2O_5/1.5 nm Ta_2O_5/Al (a) Flat band condition, (b), (c) and (d) conduction in forward bias, (d) and (e) conduction in reverse bias.

Figure 7.8 (a) shows a bound state in a rectangular quantum well for 0 V applied as a result of the CBO between Nb_2O_5 and Ta_2O_5 and Nb_2O_5 and Ta_2O_5. An applied voltage of 0.3 V results in two bound states, as shown in Figure 7.8 (b). The current is not expected to be enhanced as the barrier height is large with the difference between the Fermi level of Al and the bound states being 0.41 eV and 0.54 eV. Figure 7.8 (c) shows the case of applied voltage of 0.4 V

resulting in a reduction of energy difference between the Al Fermi level and the energy level of bound states to 0.35 eV and 0.49 eV. The forward current level has now increased as shown in Figure 7.9 (e), due to resonant tunnelling. The Nb_2O_5 reaches the FNT regime when the applied bias is 1.41 V as shown in Figure 7.8 (d). Moreover, the energy differences between the Fermi level of Al and the bound states at 1.41 V are 0.02 eV, 0.23 eV and 0.44 eV, resulting in large currents.

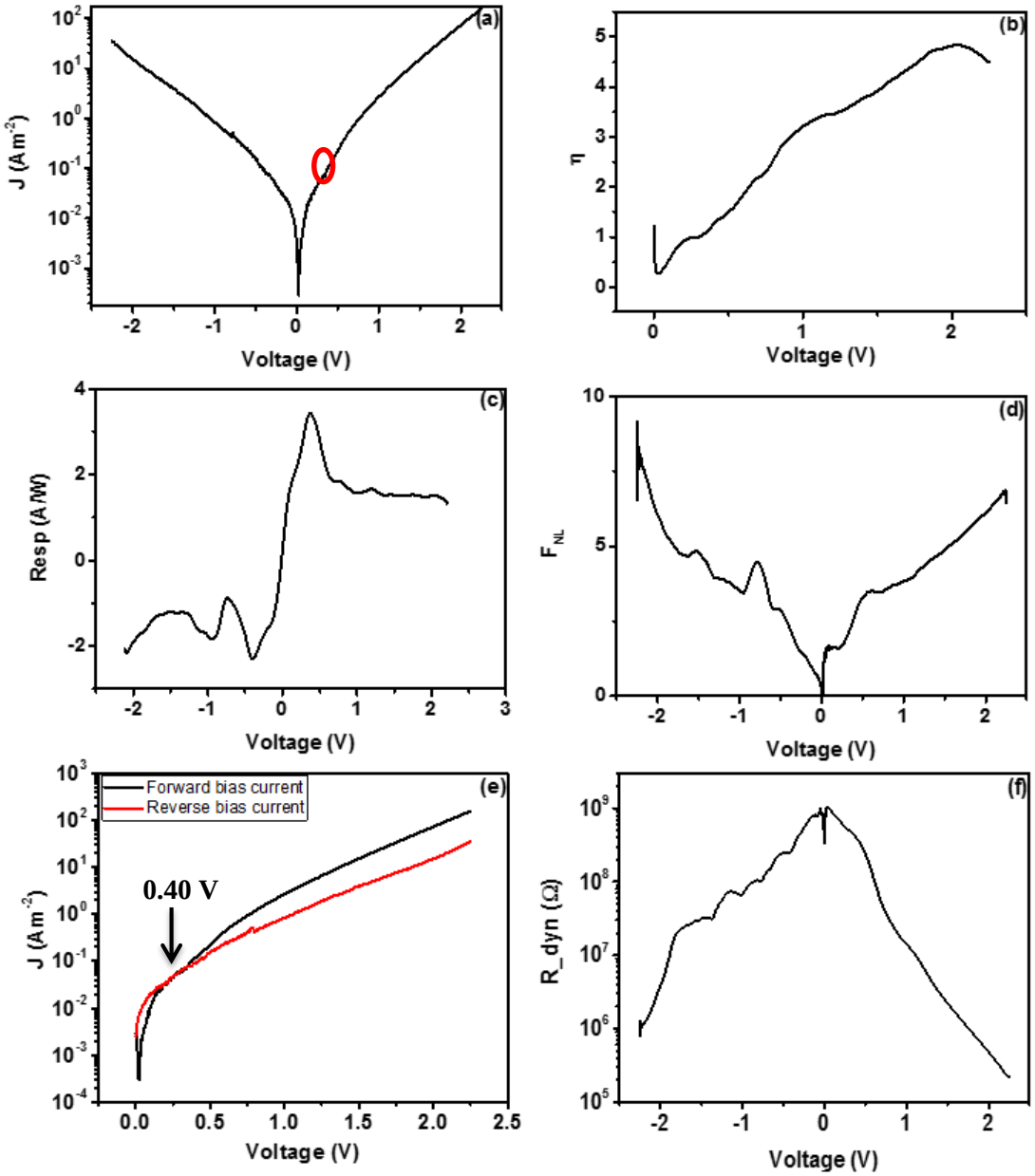

Figure 7.9: Device (a) JV characteristics, (b) asymmetry, (c) responsivity, (d) non-linearity, (e) rectification reversal and (f) dynamic resistance for Al/~1.6 nm AlO_x/1 nm Al_2O_3/2.5 nm Nb_2O_5/1.5 nm Ta_2O_5/Al. The device area = 1×10^{-8} m^2.

In the case of reverse bias, initially there was a bound state when the applied bias is zero. Increasing the voltage causes this state to disappear due to the small CBO between Nb_2O_5 and Ta_2O_5. Therefore the dominant conduction process is expected to be DT and FNT under this

polarity, as shown in Figure 7.8 (e). However, the structure reaches the step tunnelling regime for -1 V as can be seen in Figure 7.8 (f).

The *IV* measurements were performed from -2.2 V to 2.2 V with a voltage step of 2.2 mV. The effect of charging was negligible as seen in the *JV* characteristics in Figure 7.9 (a). A peak device asymmetry of 4.85 was recorded at 2 V as demonstrated in Figure 7.9 (b). This asymmetry was achieved as a result of resonant tunnelling. Figure 7.9 (c) indicates a peak device responsivity of 3.45 A/W at 0.4 V. Figure 7.9 (d) shows a peak device non-linearity of 6.5 at 2.1 V and rate of change of non-linearity of 6 V^{-1}. Figure 7.9 (e) shows rectification reversal at 0.4 V, indicating the dominance of resonant tunnelling. Figure 7.9 (f) shows a dynamic resistance of 650 MΩ at zero bias and 230 kΩ at 2.1 V.

The rectification reversal point was shifted towards larger voltages in this structure when compared to Al/native AlO_x/1 nm Al_2O_3/3 nm Nb_2O_5/1 nm Ta_2O_5/Al. This is due to the variation of oxide thicknesses, which leads to a smaller electric field in the Nb_2O_5. Therefore a larger voltage must be applied to increase the depth of the triangular quantum well.

7.2.1.3 Al/1 nm Al_2O_3/2 nm Nb_2O_5/2 nm Ta_2O_5/Al device

The same oxide combination with a slight variation of the thicknesses of the first two oxides to 2 nm was used in this MIIIM structure. The ratio of potential applied across oxides, Al_2O_3, Nb_2O_5 and Ta_2O_5 was found to be 0.58:0.17:0.25 from Eqn. 6.18.

It can be seen that the voltage across the Ta_2O_5 is larger than that of Nb_2O_5 in comparison to the previous two devices. This is due to the smaller capacitance of Ta_2O_5 in comparison to Nb_2O_5. The impact of this modification is investigated by analysing the conduction process and also the rectification properties of this structure.

Figure 7.10 (a) predicts a single bound state from zero bias up to 0.7 V and Figure 7.10 (b) indicates DT conduction. Figure 7.10 (c) shows another bound state for voltages beyond 0.7 V, about 0.42 eV above the fermi level of Al; however this is a free running state. The experimental results of Figure 7.11 (a) show evidence of resonant tunnelling at voltages > 1 V, in fact the magnitude of reverse bias currents are always larger than that of the forward bias current. The Nb_2O_5 reaches FNT regime at voltage 1.6 V. As shown in Figure 7.10 (d), increasing the applied voltage to 1.7 V, results in a bound state 0.21 eV, 0.39 eV and 0.57 eV above the Fermi level of the Al.

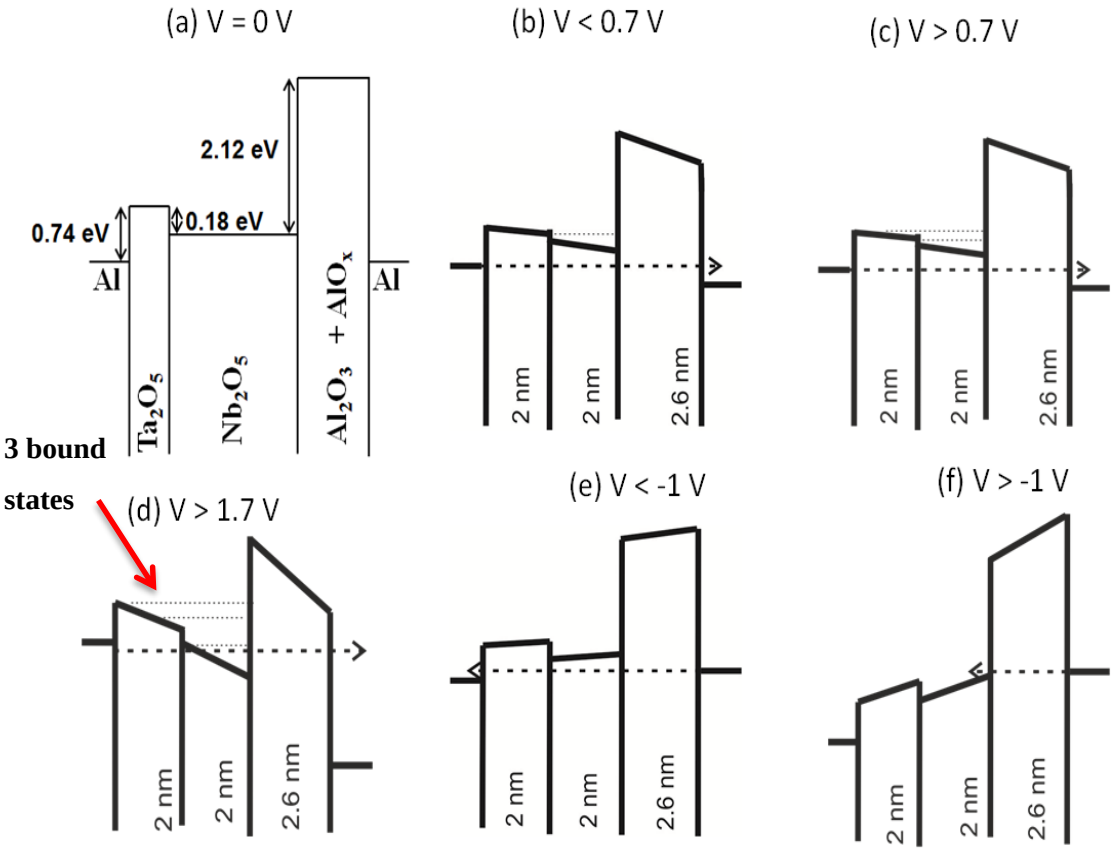

Figure 7.10: Conduction in Al/1.6 nm AlOx/1 nm Al_2O_3/2 nm Nb_2O_5/2 nm Ta_2O_5/Al (a) flat band condition, (b), (c) and (d) conduction in forward bias, (e) and (f) conduction in reverse bias.

For negative bias, there is a bound state at zero bias; however this disappears at the voltage of -0.18 V due to the small CBO between Nb_2O_5 and Ta_2O_5. Figure 7.10 (e) indicates that the conduction in all three layers should be DT and FNT for voltages smaller than -1 V. Electrons may overcome the Nb_2O_5 and Ta_2O_5 CB at the voltage of -1 V, leading to step tunnelling as seen in Figure 7.10 (f).

The *IV* measurements were taken from -2.2 V to 2.2 V with voltage step of 2.2 mV. Figure 7.11 (a) shows the magnitudes of the reverse bias currents are larger in comparison to forward bias. This is a consequence of not observing resonant tunnelling at smaller voltages < 1 V; however a change in curvature of the forward bias current and also a decrease in slope were visible toward large positive voltages, ~1.8 V. This could be ascribed to resonant tunnelling (Figure 7.10 (d)). A larger voltage must be applied so that the Nb_2O_5 CB edge to slope as the voltage drop on Nb_2O_5 is significantly smaller due to the chosen thickness of 2 nm. In this case device asymmetry was calculated by considering the ratio of reverse bias current to the forward bias current. As shown in Figure 7.11 (b), a peak device asymmetry of 11.5 occurs at 0.1 V. The peak device responsivity of 5.1 A/W occurs at 0.24 V from Figure 7.11 (c). Furthermore, it is possible to observe a change in device responsivity caused by a change in

curvature of the *IV* curve from 1.75 V. This can be considered as further evidence of resonant tunnelling around 1.8 V. A peak device non-linearity of 4.5 at 0.6 V and -0.6 V, and a rate of change of non-linearity of 7.3 V^{-1} were extracted from Figure 7.11 (d). Moreover, a large change in non-linearity is visible from 1.8 V as shown in Figure 7.11 (d). Figure 7.11 (e) shows dynamic resistance at zero bias of 70 MΩ, 760 Ω at -2 V and 1.2 kΩ at 2 V.

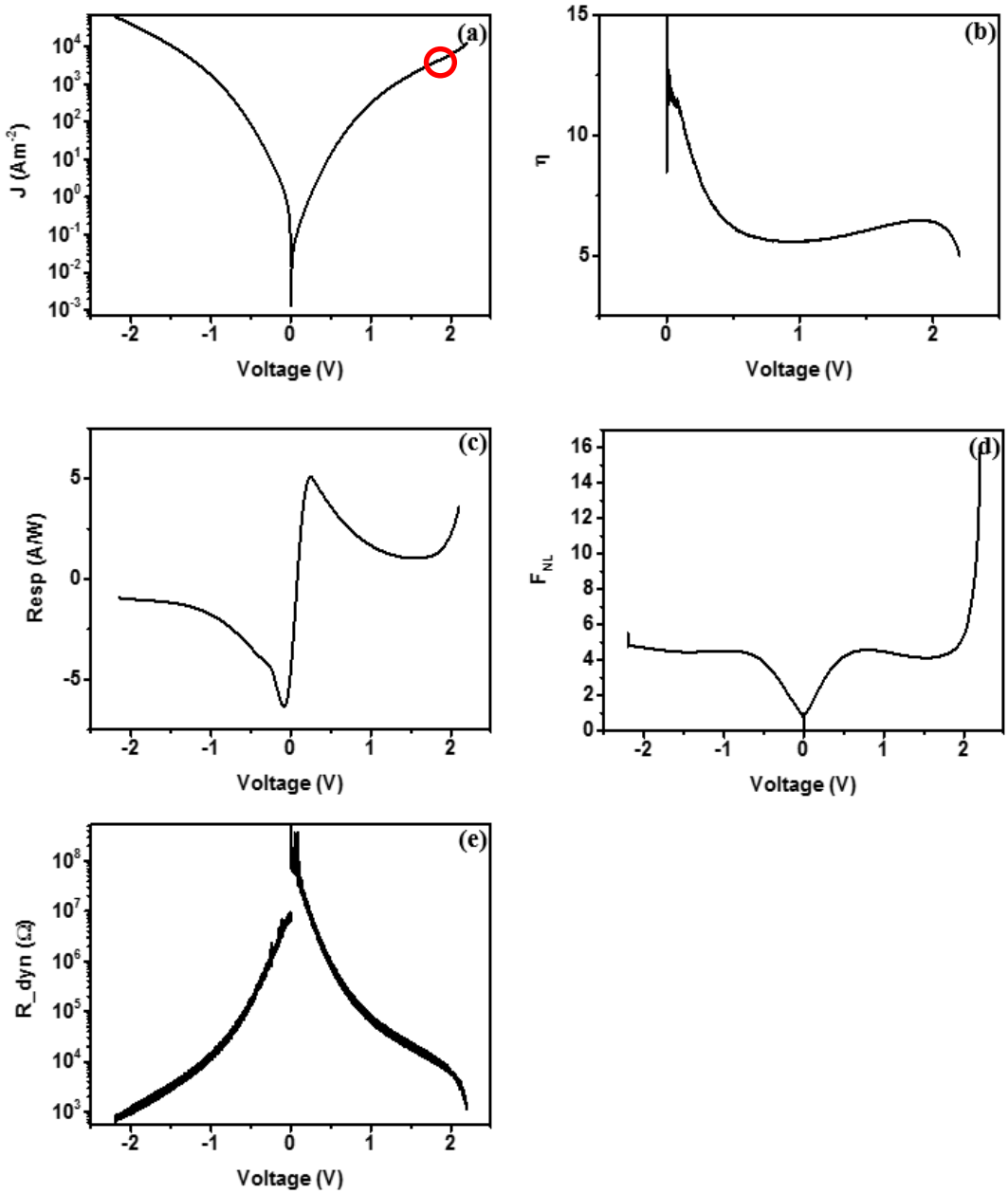

Figure 7.11: Device (a) JV characteristics, (b) asymmetry, (c) responsivity, (d) non-linearity and (e) dynamic resistance for Al/~1.6 nm AlO_x/1 nm Al_2O_3/2 nm Nb_2O_5/2 nm Ta_2O_5/Al. The device area = 1 $\times 10^{-8}$ m^2.

It is proposed that resonant tunnelling in this MIIIM structure occurs at larger voltages (~1.8 V). This could be due to the bound states formed in the CB of Ta_2O_5 or the bound state created

in the CB of Nb_2O_5. It should be noticed that the potential required on Nb_2O_5 to form a triangular quantum well is larger in comparison to the previous two devices.

The observed trend from these three MIIIM structures is the dominance of resonant tunnelling which shifts towards applied larger voltages with decreasing thickness of the Nb_2O_5 layer. The experimental results are in good agreement with the theoretical predictions.

7.3.2 Cascaded MIIM structures

7.3.2.1 Al/1 nm Al_2O_3/3 nm Ta_2O_5/1 nm Nb_2O_5/Al

The cross-section of the completed device structure can be seen in Figure 7.12 (a).

The motivation of fabricating this device was to create bound states in the triangular quantum wells formed in the CB of Nb_2O_5 and Ta_2O_5. It is possible to create two triangular quantum wells with the application of voltage in both conduction bands (Nb_2O_5 and Ta_2O_5) simultaneously as a result of the chosen thicknesses of the oxides.

It can be seen that the portion of voltage applied across Nb_2O_5 is only 0.08 V for a bias of 1 V. Moreover, the largest fraction of voltage falls across Ta_2O_5. The barrier height at the interface of Al/Nb_2O_5 is 0.56 eV which is 0.18 eV smaller than that of Al/Ta_2O_5. This structure was engineered in such a way for Nb_2O_5 and Ta_2O_5 to reach the FNT regime at the same voltage of 1.2 V.

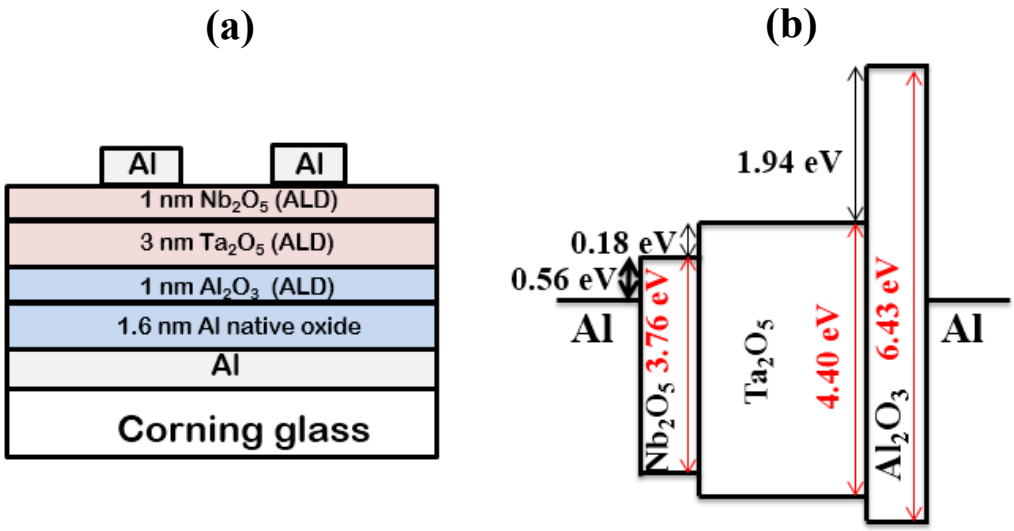

Figure 7.12: (a) A device cross-section and (b) **e**nergy band diagram for Al/1.6 nm AlO_x/1 nm Al_2O_3/3 nm Ta_2O_5/1 nm Nb_2O_5/Al.

The ratio of voltage drop across each oxide, Al_2O_3, Ta_2O_5 and Nb_2O_5 is 0.44:0.48:0.08.

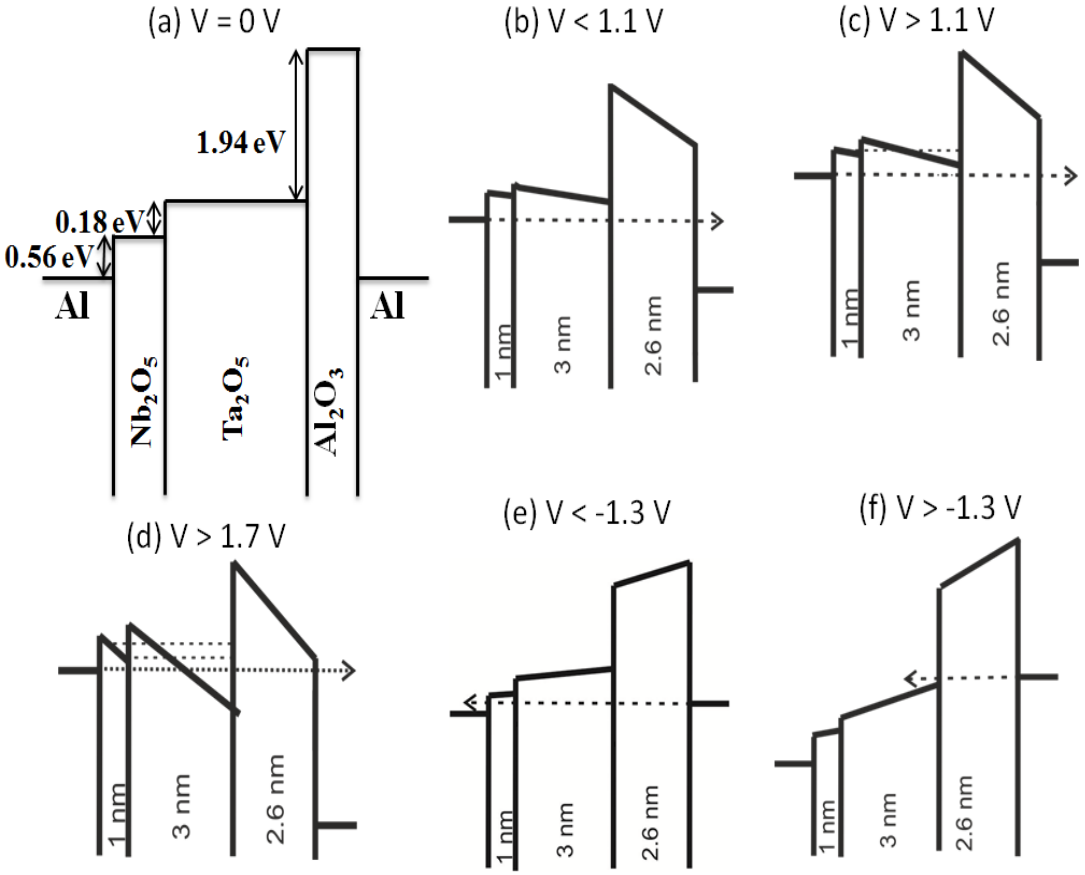

Figure 7.13: Conduction in Al/1.6 nm AlOx/1 nm Al_2O_3/3 nm Ta_2O_5/1 nm Nb_2O_5/Al (a) flat band condition, (b), (c) and (d) conduction in forward bias, (e) and (f) conduction in reverse bias.

As can be seen in Figure 7.13 (a), it was not possible to obtain any bound states in the structure when the applied bias was zero. The conduction process will thus be dominated by DT in all three oxides for applied bias voltages less than 1.1 V as shown in Figure 7.13 (b). A bound state in the CB of both Nb_2O_5 and Ta_2O_5 is created beyond 1.1 V as shown in Figure 7.13 (c). This is 0.24 eV above the Fermi level of Al. The conduction at this voltage should be dominated by resonant tunnelling as shown in Figure 7.15 (a). The second bound state can be expected ~0.20 eV above the Fermi level of Al at the voltage of 1.7 V as can be seen in Figure 7.13 (d).

In the case of reverse bias, no bound states are apparent. Therefore the conduction below -1.3 V will be dominated ideally by DT and FNT in all three layers as shown in Figure 7.13 (e). However, it is possible for the structure to reach the step tunnelling regime by overcoming the Ta_2O_5 and Nb_2O_5 CB edge by applying a voltage bias of -1.3 V as shown in Figure 7.13 (f).

The *IV* measurements were performed from 1.6 V to -1.6 V with step voltage of 1.6 mV. Figure 7.14 (a) indicates that a charging effect is evident for this MIIIM structure when a continuous measurement was performed from 1.6 V to -1.6 V. This could be due to ionic contamination in the oxide films. Their transport lags behind the rate of increase of applied voltage [3, pages 42-43]. If the forward to reverse bias current ratio is considered for these *IV* characteristics, the resultant asymmetry values may reach artificially high values of ~10^3 as shown in Figure 7.14 (b).

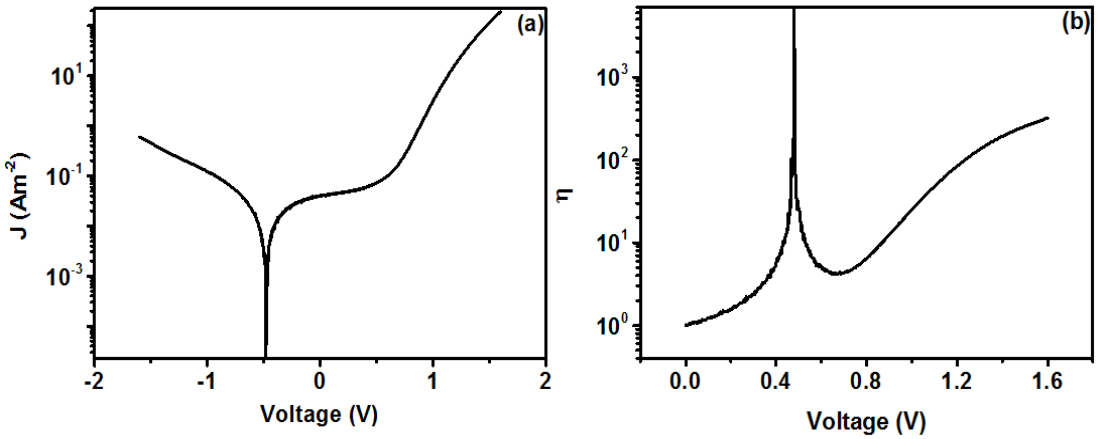

Figure 7.14: Device (a) JV characteristics, and (b) asymmetry for Al/~1.6 nm AlOx/1 nm Al_2O_3/3 nm Ta_2O_5/1 nm Nb_2O_5/Al.

It was possible to compensate for this effect by performing discontinuous measurements from zero to a positive voltage and/or from zero to a negative voltage.

The compensated *JV* characteristics are shown in Figure 7.15 (a). It is evident that the forward bias current is larger than the reverse bias current due to resonant tunnelling at 1.1 V. Figure 7.15 (b) shows a peak device asymmetry of 117 at 1.6 V. Although the device asymmetry was significantly larger in comparison to the previously presented MIIIM structures; it was not possible to observe the dominance of resonant tunnelling at lower voltages (< 0.5 V). This is one of the main drawbacks of this structure. A device asymmetry of 6.5 was extracted at 0.1 V when considering the reverse to forward bias current ratio as shown in the inset of Figure 7.15 (b). Figure 7.15 (c) shows a peak device responsivity of 5 A/W at the voltage of ~1 V. Figure 7.15 (d) indicates a peak device non-linearity of 11.8 at 1.1 V and a rate of change of non-linearity of 6.98 V^{-1}. Figure 7.15 (e) illustrates that the forward bias current starts to dominate the reverse bias current at 1.1 V. The dynamic resistance extracted at zero bias is 3.4 GΩ reducing to 309 kΩ at the voltage of 1.6 V as shown in Figure 7.15 (f).

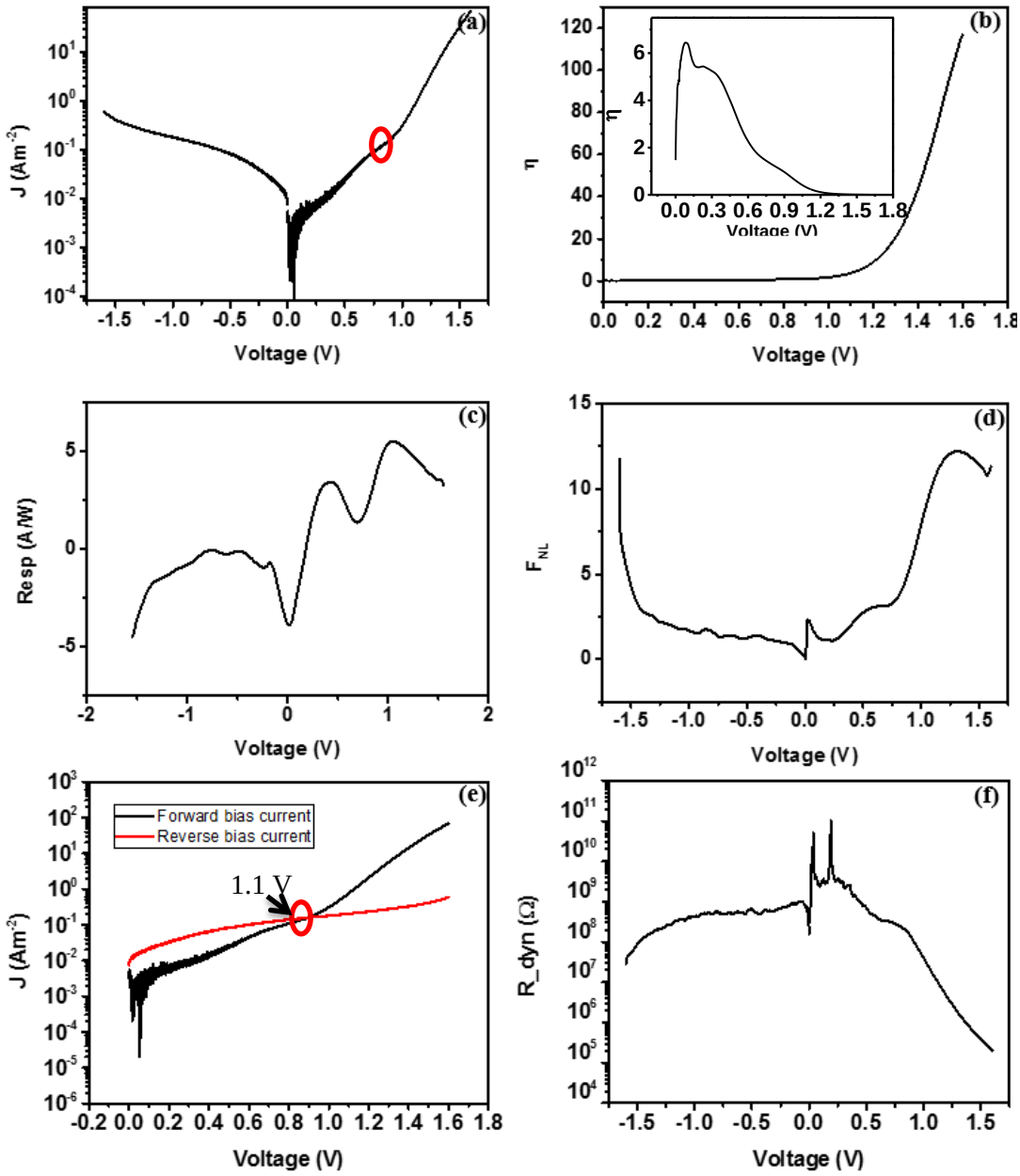

Figure 7.15: Device (a) JV Characteristics, (b) asymmetry, (c) responsivity, (d) non-linearity, (e) rectification reversal and (f) dynamic resistance for Al/~1.6 nm AlO_x/1 nm Al_2O_3/3 nm Ta_2O_5/1 nm Nb_2O_5/Al. The inset of (b) represents the asymmetry considering the ratio of reverse to forward bias current. The device area = 1×10^{-8} m^2.

The charging effect of this structure was immense due to the likely ionic charge in the oxides. Then the other drawback was the dominance of resonant tunnelling observed at larger voltages in contrast to the previously analysed structures. However, a large device asymmetry of 117 was recorded at 1.6 V.

7.4 Discussion and summary

The rectification properties of the experimentally fabricated MIIIM structures are summarised in Table 7.2.

Table 7.2: Summary of rectification properties of the MIIIM structures.

Device	Reversal point (V)	Peak Asymmetry	Responsivity (A/W)	Non-linearity	Dynamic resistance
Al/Al_2O_3/Nb_2O_5/Ta_2O_5/Al (1:3:1)	035 V	5.3 at 1.8 V	4.3 at 0.35 V	4.5 at 0.54 V	2.9 MΩ at 0 V 580 Ω at 1.77 V
Al/AlO_x/ Al_2O_3/ Nb_2O_5/Ta_2O_5/Al (1:2.5:1.5)	0.40 V	4.85 at 2 V	3.45 at 0.4 V	6.5 at 2.1 V	650 MΩ at 0 V 230 kΩ at 2.1 V
Al/AlO_x/Al_2O_3/ Nb_2O_5/Ta_2O_5/Al (1:2:2)	~1.8 V	11.5 at 0.1 V	5.1 at 0.24 V	4.5 at 0.6 V	70 MΩ at 0 V 1.2 kΩ at 2 V, 0.76 kΩ at -2 V
Al/AlO_x/Al_2O_3/ Ta_2O_5/Nb_2O_5/Al (1:3:1)	1.1 V	117 at 1.6 V 6.5 at 0.1 V (ST)	5 at 1 V	11.8 at 1.1 V	3.4 GΩ at 0 V 309 kΩ at 1.6 V

As can be seen in Table 7.2, the best rectification properties were obtained on the structure Al/native AlO_x/1 nm Al_2O_3/3 nm Ta_2O_5/1 nm Nb_2O_5/Al. A device asymmetry of 117 was recorded at 1.6 V due to resonant tunnelling. The evidence of resonance was visible at 1.1 V. This was further substantiated by observing a large responsivity of 5 A/W and a non-linearity of 11.8 at ~1 V. Nevertheless, better rectification properties can be anticipated in the low voltage regime if the structure is slightly modified considering the following steps, i.e.

I. Replacing Al with a metal that has a smaller work function (ideally ~3.7 eV)
II. Eliminating the effect of Al-native oxide by choosing a less reactive metal (Nb or Ta)
III. Reducing the oxide thicknesses whilst maintaining the same thickness ratio (1:3:1)

The device, Al/1 nm Al_2O_3/3 nm Ta_2O_5/1 nm Nb_2O_5/Al demonstrated the effect of charging; hence the origin of the *IV* curve was shifted towards negative voltages as explained in section 7.3.2.1. Maraghechi *et al* [4] reported an asymmetry of 10^5 for a similar structure. Presumably, this could be a result of the charging effect as shown in the analysis in this chapter (see Figure 7.14 (b)). Note, in this work the charging effect was eliminated by performing discontinuous measurements (zero to positive voltages and zero to negative voltages) [3, page 42, 43]. Furthermore, Yavuz *et al.* reported enhanced electrical charachtersitics on a metal-insulator-insulator-insulator-metal device [5]. They demonstrated a higher asymmetry of ~75 at 1 V and a non-linearity of 6 at 0.7 V [5].

The dominance of resonant tunnelling was observed in the low voltage regime < 0.5 V for non-cascaded MIIIM diodes presented in section 7.3.1. The device Al/1 nm Al_2O_3/2 nm Nb_2O_5/2 nm Ta_2O_5/Al demonstrated a large asymmetry of 11.5 at 0.1 V and a responsivity of 5.1 A/W at 0.2 V due to enhanced tunnelling for reverse (negative) bias; in advance on the state-of-the-art. No values were reported below 0.5 V for MIIIM devices.

All the diode structures presented in this work demonstrated large dynamic resistance values. It is crucial to have a diode with a very small dynamic and series resistance and a capacitance in order to obtain large coupling efficiencies [6, page 49]. This could be achieved by fabricating nano-scale devices with small barrier heights of ~0.1 - 0.2 eV at the metal/oxide interface.

References

[1] N. Sedghi, J. F. Ralph, I. Z. Mitrovic, P. R. Chalker, S. Hall, "Electron trapping at the high-κ/GeO_2 interface: The role of bound states", Appl. Phys. Lett., 102, 092103 (2013).

[2] N. Sedghi, J. W. Zhang, J. F. Ralph, Y. Huang, I. Z. Mitrovic, S. Hall, "Towards rectenna for solar energy harvesting", Proc: European Solid-State Device Research Conference (ESSDERC), Romania, 131 (2013)

[3] B. Eliasson, "Metal-insulator-metal diodes for solar energy conversion" PhD thesis, Boulder: University of Colorado at Boulder (2001)

[4] P. Maraghechi, A. Foroughi-Abari, K. Cadien, A. Y. Elezzabi, "Observation of resonant tunnelling phenomenon in metal-insulator-insulator-insulator metal electron tunnel devices", Appl. Phys. Lett., 100, 092103 (2012)

[5] F.M Alhazmi, O.M. Ramahi, M. Irannejad, A. Brzezinski, M. Yavuz., "Comparison of the effects of varying of metal electrode in metal-insulator-metal diodes with multi-dielectric layers." Austin J Nanomed Nanotechnol., 2 (2), 4 (2014)

[6] S. Grover, "Diodes for optical rectennas" PhD thesis, Boulder: University of Colorado at Boulder (2011)

Chapter 8

8. Conclusion and future work

The research work presented in this thesis primarily focused on two emerging applications of high-k dielectrics, that are metal oxide semiconductor field effect transistors (MOSFET) and metal insulator metal (MIM) diodes. The device fabrication process, material selection process and novel findings from physical and electrical characterisation techniques used underpinned by analytical modelling are addressed in this thesis.

Extensive research is conducted on non-silicon channel materials to replace Si to enhance the device performance. One way this can be achieved is to allow scaling down of the supply voltage of transistors by using high mobility channel materials. Nevertheless it is critical to obtain a good interface between the gate oxide and the channel material as an unstable interface may result in degradation of carrier mobility and poor control of threshold voltage. Therefore with the aim of achieving a stable interface between the gate oxide and Ge, materials such as GeO_2, Tm_2O_3, Y_2O_3 (deposited at 225 ^oC and 400 ^oC) and Al_2O_3 were chosen to deposit on Ge. These have been characterised extensively by our collaborators regarding the material and interfacial properties, to confirm their compatibility for future Ge-based MOSFET applications. The main contribution to the work, reported in this thesis, was the optical characterisation undertaken using variable angle spectroscopic ellipsometry (VASE) measurements and analysis. These data were correlated with the other studies. In addition to the extraction of band gap values, the sub-band gap absorption features were analysed for the above stated structures. Urbach tailing for Y_2O_3/Ge structure deposited at 400 ^oC was less apparent compared to the Y_2O_3/Ge structure deposited at 225 ^oC which was ascribed to defect reduction and temperature induced crystallisation. The VASE analysis was found to be in agreement with X-ray photoelectron spectroscopy (XPS) analysis as the presence of GeO_x was evident only for the Y_2O_3/Ge structure deposited at 225 ^oC. The poly-crystalline nature of Y_2O_3 was further observed by X-ray diffraction (XRD). Furthermore, the electrical characterisation techniques suggested the superiority of the 400 ^oC deposited Y_2O_3/Ge structure due to its low leakage current and enhanced capacitance voltage (*CV*) characteristics. The 225 ^oC deposited Y_2O_3/Ge structure demonstrated high-frequency dispersion with notable humps in the weak inversion regime. The band gap of Y_2O_3 was extracted to be 5.99 eV from absorption coefficient method using VASE analysis. The offsets at the valence band (VBO) and conduction band (CBO) extracted after combining XPS and VASE analysis at the Y_2O_3/Ge interface were 2.68 eV and 2.35 eV respectively. The band gap values extracted for Tm_2O_3 and GeO_2 were in the range of 5.65 - 5.95 eV and 5.3 - 5.77 eV respectively. The presence of GeO_x at the interface of GeO_2/Ge was evident from both VASE and XPS analysis whereas this was not the case for Tm_2O_3/Ge. The large CBO and VBO extracted at the

interfaces of GeO_2/Ge and Tm_2O_3/Ge are favourable for potential MOSFET applications, to achieve acceptable gate leakage current. Furthermore, Urbach tailing for Tm_2O_3 layer suggested the poly-crystalline nature of the film. The band gap extracted for Al_2O_3 was in the range of 6.1 – 6.4 eV. It was not possible to observe Urbach tailing for Al_2O_3, implying negligible sub-band gap absorption. The presence of an interfacial layer was not evident from XPS analysis, proving the consistency with VASE analysis. Thus Al_2O_3 was found to act as a barrier layer on Ge.

Comprehensive research has been conducted on the experimental study of the MIM structures with enhanced DC characteristics at low voltage regime (< 1 V) for energy harvesting (infrared, visible light) applications. The MIM diode concept has captured the attention of many researchers due to its potential for replacing conventional diodes in these high frequency regimes. These structures can overcome the limitations caused by semiconductor technology in frequency regimes beyond > 12 THz. The MIM structures were fabricated with an ultra-thin (1-5 nm) high-k dielectric film sandwiched in between two metal electrodes; so that the carriers can traverse through thin oxide from one metal electrode to the other depending on the polarity of the applied bias. For THz operation, the dominant conduction must occur by quantum mechanical tunnelling due to its fast transit times of the order of 10^{-15} seconds. Consequently, the time constant of the diode must also be in the femto-seconds regime; thus the device resistance (differential/dynamic resistance and series resistance) and capacitance has to be as small as possible. In addition to this, the diode resistance which is the combination of dynamic and series resistances significantly affects the coupling efficiency between the antenna and the diode. If the antenna resistance is increased to match the resistance of the diode, then the overall efficiency of the rectenna circuit will increase, resulting in an increase in time constant. A smaller dynamic resistance is achievable by engineering the barrier height at the metal/oxide interface to be as small as possible. Therefore the materials (oxides and metals) were chosen carefully to achieve a smaller resistance at lower biasing voltages. Ta_2O_5 and Nb_2O_5 were chosen as the high-k dielectrics to fabricate the single insulator MIM structures due to their large electron affinity values of 3.54 eV and 3.72 eV respectively. The metals, Al, Nb and Ta were chosen as the metal electrodes due to their work function values of 4.28 eV, 4.11 eV and 4.17 eV respectively. The electron affinity and work function values of the oxides and metals were estimated by performing XPS, VASE and electrical measurements. The temperature independent behaviour of their current-voltage (*IV*) characteristics suggested the dominance of quantum mechanical tunnelling, hence the barrier heights at the metal/oxide interfaces were extracted by Fowler-Nordheim analysis. The rectification properties of the MIM structures were assessed by analysing the *IV*

characteristics. Nevertheless, as discussed in chapter 5, the MIM devices demonstrated poor rectification properties due to the symmetric nature of the band structure.

A diode with sufficiently large non-linearity is critical for efficient rectification of analogue signals. The metal insulator insulator metal (MIIM) structures were identified as a potential route to improve the low-voltage (< 0.5 V) rectification properties compared to MIM structures. The MIIM structures were fabricated by introducing another thin dielectric layer with a smaller electron affinity of 1.6 eV to the MIM structure with a conduction band offset > 1.94 eV to form a quantum well in the conduction band of the oxide which has the large electron affinity value (Nb_2O_5 or Ta_2O_5). The electrons may tunnel through the discrete energy levels formed within the quantum well, leading to the presence of a third conduction mechanism known as resonant tunnelling (RT) in addition to the conventional direct and Fowler-Nordheim tunnelling mechanisms. RT was expected to improve the rectification properties compared to the MIM structures. The metals, Al, Nb, Ta, Cr, W and Ag were selected as the electrodes while fabricating these MIIM structures. In addition to the MIIM structures with similar metal electrodes, the experiments have been carried out by applying work function offset between the metal electrodes up to 0.6 eV in order to investigate the shift in rectification reversal point where resonance becomes dominant.

It was possible to observe a shift in rectification reversal towards smaller voltages when the barrier height at the metal/oxide interface is reduced (see chapter 6, Figure 6.31). Also a shift towards larger voltages was evident if a metal with a relatively larger work function is used at the Al_2O_3 compared to the metal work function of Ta_2O_5 or Nb_2O_5 (see chapter 6, Figure 6.32). These experimental observations were found to be in agreement with the quantum-mechanical calculations. Therefore as a conclusion from this thesis, it can be said that the rectification reversal point can be shifted towards smaller voltages (at/near 0 V) by replacing the metal electrode adjacent to the Al_2O_3 with a metal that has a smaller work function with respect to the other metal electrode. In comparison to MIM structures, MIIM structures demonstrated superior rectification properties. For example, $Nb/Nb_2O_5/Al_2O_3/Ag$ structure demonstrated large device asymmetries of 10.5 at 1.2 V due to resonant tunnelling and 35 at 0.06 V due to the enhanced tunnelling mechanism for reverse (negative) bias. Furthermore, large device responsivity values of 9 A/W at 0.45 V, 8.3 A/W at 0.1 V and 7.7 A/W at 0.2 V were observed for $Nb/Nb_2O_5/Al_2O_3/Ag$, $Ta/Ta_2O_5/Al_2O_3/Ag$ and $Ta/Ta_2O_5/Al_2O_3/Ag$ structures respectively (see chapter 6, Table 6.3) than the state-of-the-art 8 A/W at 0.25 V for Ni/NiO/ZnO/Cr device.

The rectification properties of metal insulator insulator insulator metal (MIIIM) structures were studied with the aim of achieving enhanced rectification properties compared to MIM and MIIM structures. As discussed in chapter 7, the oxides Ta_2O_5, Nb_2O_5 and Al_2O_3 were

configured in such a way to form a rectangular potential well in the conduction band of Nb_2O_5 at zero bias. The barrier height of 0.56 eV was observed at the Al/Nb_2O_5 interface. Therefore the dominance of resonance at zero bias was not observed; however the devices were fabricated with motivation of observing the dominance of resonance at low voltage regime (< 0.5 V). Three novel non-cascaded MIIIM structures with a variation of thicknesses for first two oxides (Ta_2O_5 and Nb_2O_5) were investigated in this thesis in addition to the cascaded MIIIM structure. The rectification reversal for Al/1 nm Ta_2O_5/3 nm Nb_2O_5/1 nm Al_2O_3/Al and Al/1.5 nm Ta_2O_5/2.5 nm Nb_2O_5/1 nm Al_2O_3/Al were evident at 0.35 V and 0.4 V respectively whereas resonance was observed at ~1.8 V for Al/2 nm Ta_2O_5/2 nm Nb_2O_5/1 nm Al_2O_3/Al MIIIM structure. However, Al/1 nm Ta_2O_5/2 nm Nb_2O_5/2 nm Al_2O_3/Al structure demonstrated a large asymmetry of 11.5 at 0.1 V due to the larger negative bias current. Although the dominance of resonant tunnelling can be observed at smaller voltages < 0.5 V, the DC *IV* characteristics were not found to be improved in the low voltage regime. Enhanced characteristics can be achieved by the step tunnelling process; from the experimental results in this thesis the enhanced tunnelling current was observed at small negative bias, at ~ -0.1 V. Moreover, the cascaded structure demonstrated strong evidence of charging as the origin of the *IV* curve was shifted during a continuous *IV* sweep (positive to negative voltages). This is likely to be due to ionic contamination in the oxide films. However, this shift was compensated by performing discontinuous measurements (from zero to positive voltages and zero to negative voltages). The rectification reversal was observed at 1 V and a large device asymmetry of 117 due to resonance was observed at 1.6 V. Moreover, the theoretical study conducted on MIIIM structures suggested the dominance of resonant tunnelling for non-cascaded MIIIM structures can be observed at zero bias if the Nb/1 nm Ta_2O_5/4 nm Nb_2O_5/1 nm Al_2O_3/Nb device structure is used (see chapter 7, Figure 7.4).

The fabricated MIM, MIIM and MIIIM structures demonstrated large device resistance due to the large barrier heights at the metal/oxide interfaces. This problem was addressed by finding suitable metal and oxide combinations to reduce the barrier height. A small resistance-area product of 1 $\Omega(\mu m^2)$ for the Ni/NiO/Ni based MIM structure with a barrier height of 0.2 eV at the interface of Ni/NiO was achieved. The device capacitance of 310 pF could be greatly improved by reducing the device area from $100 \times 100\ \mu m^2$ to ideally $100 \times 100\ nm^2$, however this will increase the device resistance. Nevertheless, if the band structure of the diode is engineered with a small barrier height, of the order 0.2 eV (Ni/NiO interface), it should be possible to have a good control over the resistance.

The material selection process was found to have a large impact on the device performance. For example, the effect of RT can be observed at zero bias if the barrier height was tuned as

elaborated in this work. Therefore, the MIIM devices should be fabricated by using two high-k oxides that result in a large conduction band offset and the metal(s) must be selected to form a small barrier height of < 0.2 eV at the metal/oxide interface. Furthermore, the conduction through oxides must be limited by quantum mechanical tunnelling for femto-second fast transit times. The dielectric constants of the oxides must be small as possible in high frequency regime in order to obtain a small device capacitance. The MIIIM structures demonstrated state-of-the-art rectification properties at low voltage regime < 0.5 eV, however this can be further improved by replacing Al contacts with Nb as explained in chapter 7. This is due to the small barrier height of 0.39 eV formed at the interface of Nb/Nb_2O_5. Next step would be to fabricate the rectifier by electron beam lithography to achieve nano-scale device dimensions to achieve a small device capacitance. The rectifier can be then combined with the broad-band antenna to complete the rectenna circuit. Then both direct current and alternating current measurements and analysis will be performed in order to evaluate their potential to be used in future energy harvesting applications in infrared regime.